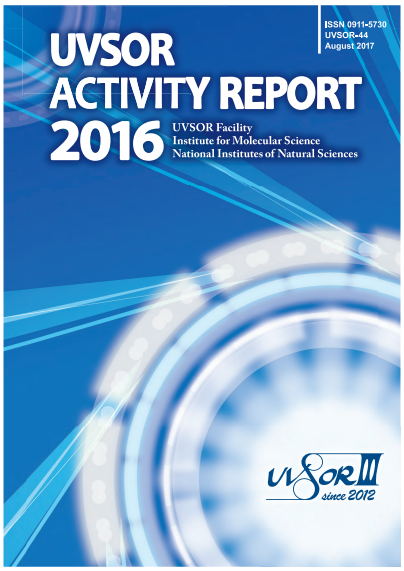
ISSN 0911-5730
UVSOR-44
August 2017
UVSOR
ACTIVITY REPORT
2016
UVSOR Facility
Institute for Molecular Science
National Institutes of Natural Sciences
UVSOR III
since 2012

Preface

This Activity Report covers scientific and technological activities carried out using the UVSOR-III Synchrotron in FY2016 (April 2016-March 2017). This is the fourth volume in the blue series for the fourth decade of the UVSOR Synchrotron Facility. We are proud of our successful progress in the fourth year after the second major upgrade project UVSOR-III in 2012.

The UVSOR Synchrotron Facility belongs to the Institute for Molecular Science (IMS), one of the inter-university research institutes fully supported by MEXT (the Ministry of Education, Culture, Sports, Science and Technology in Japan), and has been leading chemical applications of synchrotron radiation(SR)-based VUV and soft X-rays since 1983, the very beginning of the second generation SR facilities in Japan. Molecular science is growing up as an interdisciplinary science combined with meso- and nano-scale spectroscopic approaches covering not only chemical and physical sciences but also biosciences, and is one of the most important targets of the low emittance synchrotron radiation.

The present UVSOR-III Synchrotron is one of the most advanced low energy SR facilities of the third generation in the world and is now one of the critical resources in doing molecular science. The UVSOR-III Synchrotron has a small electron storage ring but has powerful 6 undulator beamlines (3 VUV and 3 in-vacuum soft X-ray undulators) with 8 dipole beamlines. We never stop improving and upgrading our micro- and nano-scale photoabsorption and photoemission approaches and in situ/operando measurements in the VUV and soft X-ray regions, based on our strategic international collaboration program in molecular science.

We are grateful to all the people who use our facility and support our efforts. In late November 2016, we encountered a serious water leak inside the storage ring, but we could restart steady-state top-up operation for users just after New Year. To continue high-level achievements in science and technology at the UVSOR-III Synchrotron, we in-house staff are always working hard to maintain and improve our high-performance accelerators and beamlines.

We hope many users will perform excellent work by fully utilizing the UVSOR-III Synchrotron as a unique international hub for the SR research in advanced molecular science.

April 2017
Nobuhiro Kosugi
Director of the UVSOR-III Synchrotron

Morino Foundation for Molecular Science (2016)

Prof. Masanari Nagasaka

Pioneering Research on Local Structure Analysis of Intermolecular Interaction Systems by Soft X-ray Absorption Spectroscopy

Dr. Nagasaka has awarded Morino Foundation for Molecular Science (2016) for his pioneering work of soft X-ray absorption spectroscopy (XAS) of liquid samples and application to in operando observations of electrochemical reactions. Morino foundation is established in 1985 by the donation of Prof. Yonezo Morino at the University of Tokyo, and is celebrated young researchers in the field of molecular science.

Dr. Nagasaka has developed a liquid flow cell for XAS of liquid in transmission mode at the soft X-ray undulator beamline BL3U at UVSOR-III Synchrotron. Soft X-ray region below 1 keV has many important absorption edges, such as C, N, and O K-edges, and 3d metal L-edges. However, it is difficult to measure XAS of liquid in transmission mode because soft X-ray is strongly absorbed by solvent water. He has achieved XAS of liquid in transmission mode by controlling the liquid thickness from 20 nm to 2000 nm, in which the liquid layer is sandwiched between two silicon nitride membranes with the thickness of 100 nm. By using the developed liquid cell, local structures of several aqueous solutions are investigated by XAS in C, N, and O K-edges. Furthermore, he has applied XAS of liquid samples to in operando observation of electrochemical reaction by developed a liquid flow cell with built-in electrodes. He also developed a potential modulation method that is able to measure XAS of electrochemical reaction at the same scan rate as in cyclic voltammetry (typically 100 mV/s). The change in valence of Fe ions at different potentials in the Fe redox reaction is successfully investigated by Fe L-edge XAS of aqueous solutions at a scan rate of 100 mV/s. It is a pioneering work about the application of XAS in soft X-ray region to electrochemical reaction.

Awarding ceremony by Morino Foundation at Koshiba Hall, the University of Tokyo.

I

Organization and Staff List

UVSOR Organization

May 2017

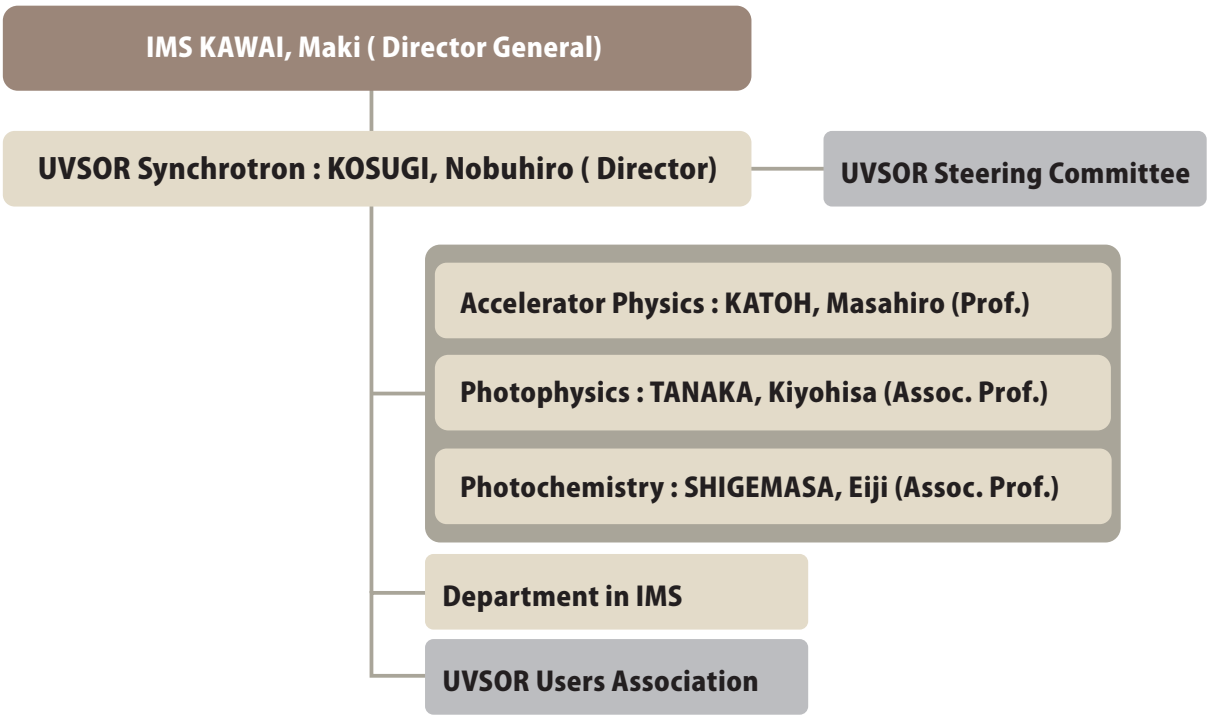

Staff List

UVSOR Staff

Director

KOSUGI, Nobuhiro	Professor	kosugi@ims.ac.jp	

Light Source Division (Accelerator Physics)

KATOH, Masahiro	Professor	mkatoh@ims.ac.jp	
FUJIMOTO, Masaki	Assistant Professor	mfmoto@ims.ac.jp	
MIRIAN, Najmeh Sadat	Research Fellow	mirian@ims.ac.jp	(until May 2016)
YAMAZAKI, Jun-ichiro	Unit Chief Engineer	yamazaki@ims.ac.jp	
HAYASHI, Kenji	Unit Chief Engineer	h-kenji@ims.ac.jp	
TESHIMA, Fumitsuna	Assistant Unit Chief Engineer	tetsu@ims.ac.jp	
MINAKUCHI, Aki	Supporting Engineer	minakuchi@ims.ac.jp	

Light Source Division (X-ray Imaging Optics)

OHIGASHI, Takuji	Assistant Professor	ohigashi@ims.ac.jp	
INAGAKI, Yuichi	Engineer	yinagaki@ims.ac.jp	

Beamline Division (Photophysics)

TANAKA, Kiyohisa	Associate Professor	k-tanaka@ims.ac.jp
HIRAHARA, Toru	Visiting Associate Professor	
IDETA, Shin-ichiro	Assistant Professor	idetas@ims.ac.jp
HASUMOTO, Masami	Unit Chief Engineer	hasumoto@ims.ac.jp
SAKAI, Masahiro	Assistant Unit Chief Engineer	sakai@ims.ac.jp
TOKUSHI, Tetsuzyo	Supporting Engineer	tetsuzyo@ims.ac.jp

Beamline Division (Photochemistry)

SHIGEMASA, Eiji	Associate Professor	sigemasa@ims.ac.jp
IWAYAMA, Hiroshi	Assistant Professor	iwayama@ims.ac.jp
NAKAMURA, Eiken	Facility Chief Engineer	eiken@ims.ac.jp
KONDO, Naonori	Assistant Unit Chief Engineer	nkondo@ims.ac.jp
YANO, Takayuki	Assistant Unit Chief Engineer	yano@ims.ac.jp
HORIGOME, Toshio	Senior Engineer	horigome@ims.ac.jp
HAYASHI, Kenichi	Supporting Engineer	khayasi@ims.ac.jp

Secretary

HAGIWARA, Hisayo	hagiwara@ims.ac.jp	
MASUDA, Michiko	masuda@ims.ac.jp	(until Mar. 2017)
INAGAKI, Itsuko	itsuko@ims.ac.jp	(since Apr. 2017)

UVSOR Steering Committee (* Chair)

KOSUGI, Nobuhiro *	UVSOR, IMS
KATOH, Masahiro	UVSOR, IMS
SHIGEMASA, Eiji	UVSOR, IMS
TANAKA, Kiyohisa	UVSOR, IMS
HIRAHARA, Toru	UVSOR, IMS (Tokyo Institute of Technology)
YOKOYAMA, Toshihiko	IMS
KERA, Satoshi	IMS
AKIYAMA, Shuji	IMS
FUJI, Takao	IMS
ADACHI, Shin-ichi	KEK-IMSS
DAIMON, Hiroshi	NAIST
OHASHI, Haruhiko	JASRI
SASAKI, Shigemi	Hiroshima Univ.
KITAURA, Mamoru	Yamagata Univ.
KOMORI, Fumio	Univ. of Tokyo
OKABAYASHI, Jun	Univ. of Tokyo

UVSOR Users Association Board (* Chair)

FUKUI, Kazutoshi *	Fukui Univ.
HIRAHARA, Toru	Tokyo Institute of Technology
ITO, Takahiro	Nagoya Univ.
KITAURA, Mamoru	Yamagata Univ.
YOSHIDA, Tomoko	Osaka City Univ.

Departments in IMS (* Group Leader)

KOSUGI, Nobuhiro *	Department of Photo-Molecular Science	
NAGASAKA, Masanari	Department of Photo-Molecular Science	
YAMANE, Hiroyuki	Department of Photo-Molecular Science	
YUZAWA, Hayato	Department of Photo-Molecular Science	
CARLIER, Andy	Department of Photo-Molecular Science	
KERA, Satoshi *	Department of Photo-Molecular Science	
UEBA, Takahiro	Department of Photo-Molecular Science	
YONEZAWA, Keiichiro	Department of Photo-Molecular Science	(until Mar. 2017)
MEISSNER, Matthias	Department of Photo-Molecular Science	
SUN, Zhengyi	Department of Photo-Molecular Science	
SHIRAISHI, Ryo	Department of Photo-Molecular Science (SOKENDAI)	
KIMURA, Kentaro	Department of Photo-Molecular Science (SOKENDAI)	(until Mar. 2017)
YAMAGUCHI, Takuma	Department of Photo-Molecular Science (SOKENDAI)	
YOKOYAMA, Toshihiko *	Department of Materials Molecular Science	
TAKAGI, Yasumasa	Department of Materials Molecular Science	
UEMURA, Yohei	Department of Materials Molecular Science	

Graduate Students

FUJISE, Hikaru	SOKENDAI	
FUJITA, Taishi	Nagoya Univ.	(until Sep. 2016)
FUKUE, Syuhei	Nagoya Univ.	(until Sep. 2016)
MITAUCHI, Tomohiro	Nagoya Univ.	(until Sep. 2016)
NAGASAKI, Kazuya	Nagoya Univ.	(until Sep. 2016)
YAMAGUCHI, Kenta	Nagoya Univ.	(until Sep. 2016)
YAMAMOTO, Kouki	Nagoya Univ.	(until Sep. 2016)
YAMAMURA, Kouhei	Nagoya Univ.	(until Sep. 2016)
HASEGAWA, Jun	Nagoya Univ.	(since Oct. 2016)
IMAO, Kenta	Nagoya Univ.	(since Oct. 2016)
KUSUNOKI, Naohiro	Nagoya Univ.	(since Oct. 2016)

Visiting Scientists

WIGGERS, Frank	Univ. of Twente	May 2016

DE JONG, Michel	Univ. of Twente	May 2016
CHIU, Chao-Wen	National Univ. of Kaohsiung	Jun. 2016
DONG, Chung-Li	Tamkang Univ.	Jun. 2016, Feb. 2017
WANG, Yu-Fu	Tamkang Univ.	Jun. 2016, Feb. 2017
LU, Ying-Jui	National Chiao Tung Univ. Taiwan	Jun. 2016
KHODABANDEH, Aminreza	Univ. of Tasmania	Jun. 2016
CHEN, Qiuyun	Fudan Univ.	Jun. 2016
YAO, Qi	Fudan Univ.	Jun. 2016
XU, Difei	Fudan Univ.	Jun. 2016
WANG, Qi	Soochow Univ.	Jul. 2016
JI, Ruru	Soochow Univ.	Jul. 2016
DUHM, Steffen	Soochow Univ.	Jul. 2016, Jan 2017
JUNG, Sun Won	Pohang Univ. of Scienceand Technolog	Jul. 2016
KIM, Jinkwang	Pohang Univ. of Scienceand Technolog	Jul. 2016
OH, Kyung Hoon	Pohang Univ. of Scienceand Technolog	Jul. 2016
FISHER, Henry	Freie Univ. Berlin	Jul. 2016
RÜHL, Eckart	Freie Univ. Berlin	Jul. Sep. Dec. 2016
GLANS, Anders	LBNL	Aug. 2016, Mar. 2017
LIU, Yi-Sheng	LBNL	Aug. 2016
LAI, Yu Ling	NSRRC	Aug. 2016
LIN, Ming-Wei	NSRRC	Aug. 2016, Feb. 2017
SHIU, Hung-Wei	NSRRC	Aug. 2016, Feb. 2017
KLOSSEK, Andre	Freie Univ. Berlin	Sep. 2016
YAMAMOTO, Kenji	Freie Univ. Berlin	Sep. 2016, Jan. 2017
RADBRUCH, Moritz	Freie Univ. Berlin	Jan. 2017
SALZMANN, Ingo	Humboldt Uni Berlin	Jan. 2017
YU, Li-Chung	NSRRC	Feb. 2017
HUANG, Yu-Cheng	National Chiao Tung Univ.	Feb. 2017
LAI, Chun-Yen	National Chiao Tung Univ.	Feb. 2017
HSU, Wei-Hao	Academia Sinica Taiwan	Feb. 2017
CHUANG, Cheng-Hao	Tamkang Univ.	Feb. 2017
JUNG, Jiwon	Pohang Univ. of Scienceand Technolog	Feb. 2017
STANIA,Roland	Institute for Basic Science Korea	Feb. 2017
FUKUTANI, Keisuke	Institute for Basic Science Korea	Feb. 2017
HUTTULA, Marko	Univ. of Oulu	Feb. 2017
MICHAILOUDI, Georgia	Univ. of Oulu	Feb. 2017
PATANEN, Minna	Univ. of Oulu	Feb. 2017
PRISLE, Nonne	Univ. of Oulu	Feb. 2017
ISMAIL, Mostafa	Univ. of Oulu	Feb. 2017
REN, Jian	Helmholz-Zentrum Berlin	Mar. 2017
WEI, Xueqin	Sichuan Univ.	Mar. 2017

II

Current Status of Light Sources and Beamlines

Light Source in 2016

1. Status of UVSOR Accelerators

In the fiscal year 2016, we had scheduled to operate UVSOR-III from May to March, for 38 weeks for users as usual. However, due to a vacuum leakage trouble at the frontend of a beamline and the following recovery works, we canceled the user runs for four weeks and a half in November and December. We had a scheduled shutdown period in April and May for about 6 weeks. This was for the scheduled maintenance works and for replacing the RF power amplifier of the storage ring and the power supply for the injection septum of the booster-synchrotron.

We operated the machine for 31 weeks and a half in the multi-bunch top-up mode, in which the beam current was kept at 300 mA, and 1 week in the single-bunch mode, in which the machine was operated in single-bunch top-up mode with the beam current of approximately 40 mA. The monthly statistics of the operation time and the integrated beam current are shown in Fig. 1. The deep dip around December was due to the vacuum trouble and the recovery work.

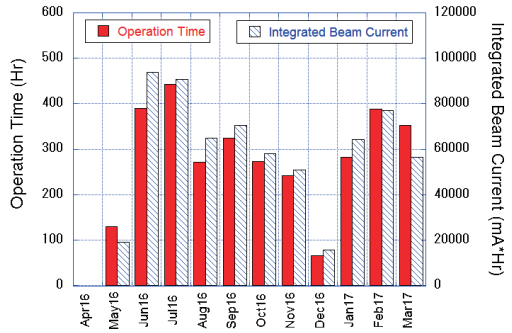

Fig. 1. Monthly statistics in FY2016.

The weekly operation schedule is as follows. On Monday, from 9 am to 9 pm, the machine is operated for machine studies. On Tuesday and Wednesday, from 9 am to 9 pm, the machine is operated for users. From Thursday 9 am to Friday 9 pm, the machine is operated for 36 hours continuously for users. Therefore, the beam time for users in a week is 60 hours. We had 3 weeks dedicated for machine studies, in November, just after the New Year vacation and the last week in March. The machine study week in November is mainly dedicated for the accelerator conditioning after the annual planned power outage.

As described above, the most serious trouble in this year was the vacuum leakage that happened on 23th Nov. Just after the scheduled beam dump at 9 pm, the vacuum of the storage ring steeply rose. From the record of the vacuum pressure around the ring, it was suspected that a leakage took place around the frontend of a beam-line, BL3U. This was confirmed by opening the vacuum system on 25th Nov. We found that the cooling water of a mask in the frontend of the beam-line was leaking out to the ultrahigh vacuum. We separated the beam-line from the storage ring by a gate valve and started the recovery work, which involved the baking of the entire ring. After the preparation works, we started the baking of a half of the ring on 5th Dec. and another half on 12th Dec., both of which we continued for one week. We started the machine operation for the vacuum conditioning by synchrotron radiation on 19th Dec. We restarted the user operation on 17th Jan. The beam lifetime recovery during the vacuum conditioning run is shown in Fig. 2.

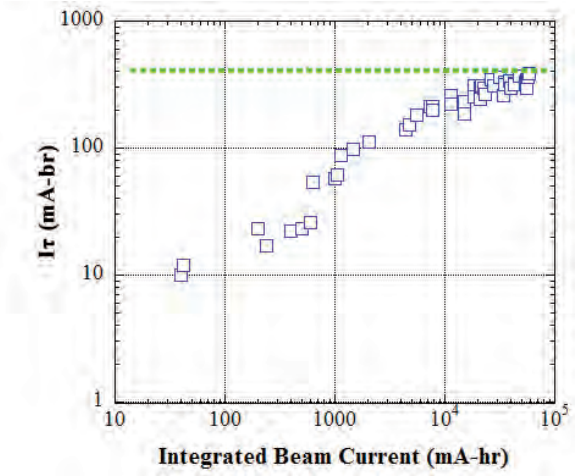

Fig. 2. The lifetime recovery during the vacuum conditioning runs in Dec. 2016 and Jan. 2017. The horizontal axis is the integrated beam current and the vertical axis is the life time multiplied by the beam current ($I\tau$). The lifetime just before the vacuum accident is shown by a blue dotted line.

In this year, other than the vacuum trouble described above, we had a few minor troubles on the power supplies of the injection/extraction magnets. However, fortunately, in all cases the beam time for users was not lost. The water leakages from a quadrupole magnet in the booster synchrotron happened but it was recovered by replacing the water cooling pipe during the shut-down period.

2. Improvements and Developments

The solid state 90 MHz RF power amplifiers of the booster synchrotron and of the storage ring had been used for about 20 years. They had been working well without any serious problem. However it became difficult to maintain them because of the outage of

electronic parts. We decided to replace the amplifiers with new ones which have basically same performances but much smaller sizes and are water cooled. We expect that the water cooling would be beneficial to stabilize the accelerator room temperature and also to reduce the sound noise in the experimental hall. In the spring shut down 2015, we replaced the amplifier for the booster synchrotron. It had been working well without any serious problem for one year. Then, in this year, we have replaced that of the storage ring. The new RF amplifier had an electric noise problem, however, it was soon improved by adding some filters.

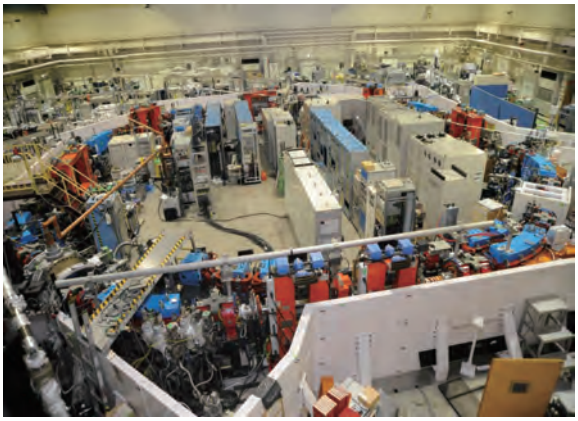

Fig. 3. An open space appeared in the storage ring after removing the old RF power amplifier.

Light Source Developments and Beam Physics Studies

We continue the efforts to develop light sources technologies and their applications such as free electron lasers, coherent harmonic generation, coherent synchrotron radiation, laser Compton scattering gamma-rays, intense polarized and vortex UV radiation at the new source development station BL1U, which was constructed under the support of Quantum Beam Technology Program by MEXT/JST. This beam-line is dedicated to develop light source technologies and to explore their applications.

This year, we continued studying the optical vortex beam from a helical undulator in collaboration with Hiroshima U., Nagoya U. and other institutes. Since the UVSOR electron beam is diffraction-limited in the UV range, we could precisely investigate the optical properties of the vortex beams from undulators in this wavelength range using conventional optical components such as a UV-CCD camera, bandpass filters and so on. In the spring shut down 2016, we collaborated with the beamline staffs, and installed a mirror and a monochromator at BL1U, which would be used for exploring the applications of novel light sources. By using this beam-line, we continued the experimental study on the interaction between optical vortex VUV light and atoms in collaboration with Saga LS and Niigata U. [1]. As a theoretical work, we have successfully shown that the origin of the vortex nature of the undulator radiation was in the radiation from an electron in circular motion [2].

We are continuing the effort to reconstruct the optical cavity for the resonator free electron laser at BL1U, which has been investigated for many years at UVSOR. This time, the main objective is the high flux intra-cavity gamma-ray production for the nuclear resonance fluorescence imaging in cooperation with Kyoto University. Currently gamma-rays are produced by using conventional fiber laser for the proof-of-principle study [3]. The gamma-rays are also used for investigating the origin of the homo-chirality of biomolecules in nature in collaboration with Hiroshima U., Yokohama N. U. and others.

Irradiation experiments using polarized ultraviolet light are being carried out in corporation with Tokyo U. Sci. and with Yokohama N. U and Hiroshima U. In the latter case, the circularly polarized UV-VUV light was used for the study on the origin of homo-chirality [4]

A spin polarized electron gun is being developed in collaboration with Nagoya U. and KEK. This year, the temporal response of the photocathode was investigated by using femto-second laser system at BL1U [5].

We continued designing a new harmonic cavity in collaboration with Nagoya U., to replace the present cavity which has a vacuum trouble. For this design study, we have started investigating present beam instabilities at UVSOR-III [6].

[1] T. Kaneyasu *et al.*, in these reports
[2] M. Katoh *et al.*, in these reports
[3] H. Zen *et al*., in these reports
[4] K. Matsuo *et al*., in these reports
[5] N. Yamamoto *et al.*, in these reports
[6] A. Mochihashi *et al*., in these reports

Masahiro KATOH (UVSOR Facility)

UVSOR Accelerator Complex

Injection Linear Accelerator

Energy	15 MeV
Length	2.5 m
Frequency	2856 MHz
Accelerating RF Field	2π/3 Traveling Wave
Klystron Power	1.8 MW
Energy Spread	~1.6 MeV
Repetition Rate	2.6 Hz

UVSOR-III Storage-Ring

Energy	750 MeV
Injection Energy	750 MeV
Maximum Storage Current	500 mA (multi bunch) 100 mA (single bunch)
Normal operation current (Top-up mode)	300 mA (multi bunch) 50 mA (single bunch)
Natural Emittance	17.5 nm-rad
Circumference	53.2 m
RF Frequency	90.1 MHz
Harmonic Number	16
Bending Radius	2.2 m
Lattice	Extended DBA × 4
Straight Section	(4 m × 4)+(1.5 m × 4)
RF Voltage	120 kV
Betatron Tune	
Horizontal	3.75
Vertical	3.20
Momentum Compaction	0.030
Natural Chromaticity	
Horizontal	-8.1
Vertical	-7.3
Energy Spread	5.26×10^{-4}
Coupling Ratio	1%
Natural Bunch Length	128 ps

Booster Synchrotron

Energy	750 MeV
Injection	15 MeV
Frequency	32 mA (uniform filling)
Circumference	26.6 m
RF Frequency	90.1 MHz
Harmonic Number	8
Bending Radius	1.8m
Lattice	FODO × 8
Betatron Tune	
Horizontal	2.25
Vertical	1.25
Momentum Compaction	0.138
Repetition Rate	1 Hz (750 MeV)

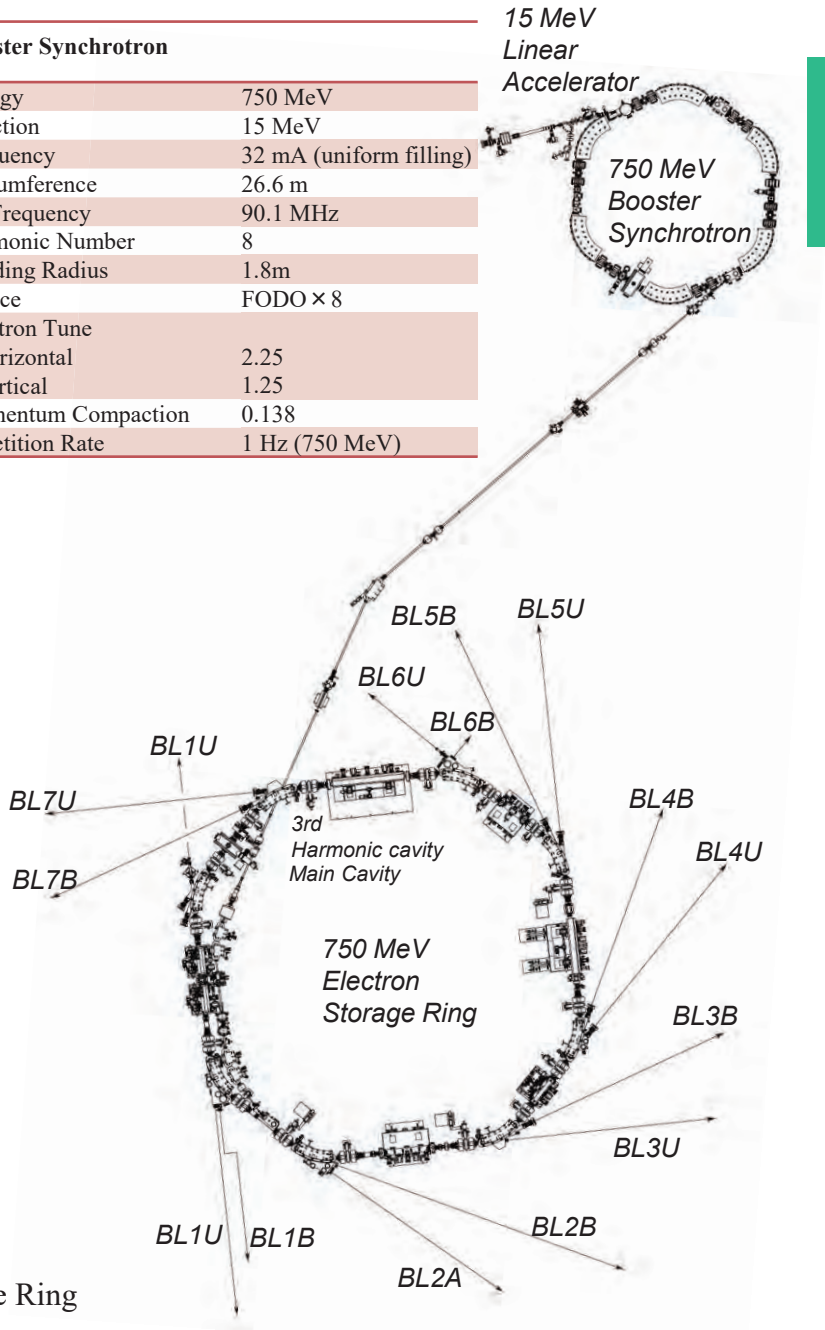

Electron Beam Optics of UVSOR-III Storage Ring

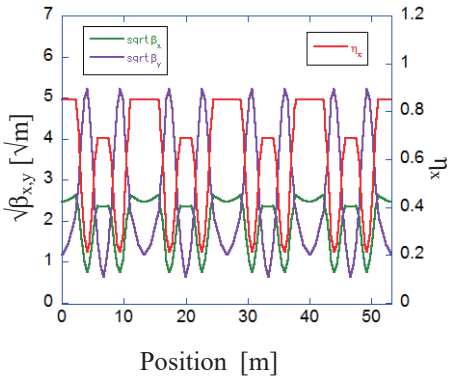

Horizontal/vertical betatron functions and dispersion function

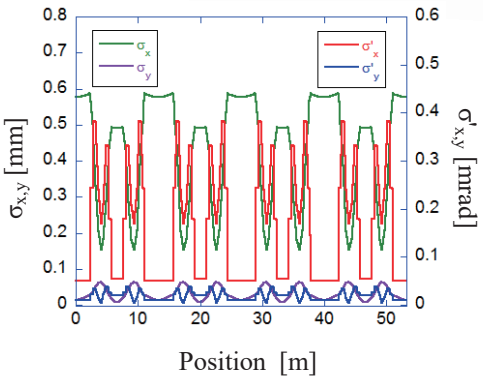

Horizontal/vertical electron beam size and beam divergences

Insertion Device

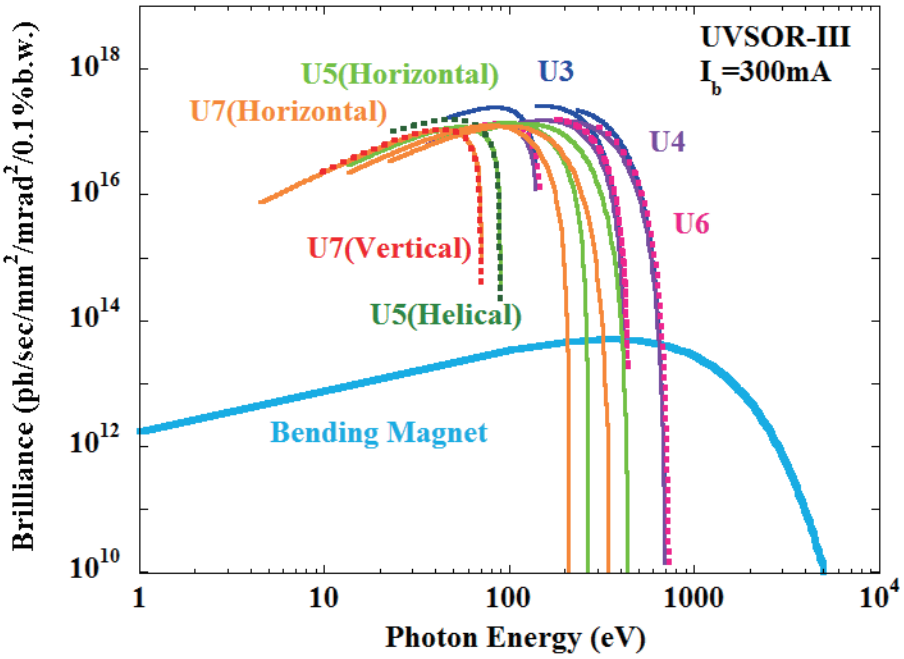

Brilliance of radiation from the insertion devices (U3, U4, U5, U6 and U7) and a bending magnet of UVSOR-III

U1 Apple-II Undulator /

Optical Klystron

Number of Periods	10+10
Period length	88 mm
Pole Length	0.968 m + 0.968 m
Pole Gap	24-200 mm
Deflection Parameter	7.36 (Max. Horizontal) 4.93 (Max. Vertical) 4.06 (Max. Herical)

U3 In-vacuum Undulator

Number of Periods	50
Period length	38 mm
Pole Length	1.9 m
Pole Gap	15-40 mm
Deflection Parameter	2.0-0.24

U4 In-vacuum Undulator

Number of Periods	26
Period length	38 mm
Pole Length	0.99 m
Pole Gap	13-40 mm
Deflection Parameter	2.4-0.19

U5 Apple-II

Variable Polarization Undulator

Number of Periods	38
Period length	60 mm
Pole Length	2.28 m
Pole Gap	24-190 mm
Deflection Parameter	3.4 (Max. Horizontal) 2.1 (Max. Vertical) 1.8 (Max. Helical)

U6 In-vacuum Undulator

Number of Periods	26
Period length	36 mm
Pole Length	0.94 m
Pole Gap	13-40 mm
Deflection Parameter	1.78 - 0.19

U7 Apple-II

Variable Polarization Undulator

Number of Periods	40
Period length	76 mm
Pole Length	3.04 m
Pole Gap	24-200 mm
Deflection Parameter	5.4 (Max. Horizontal) 3.6 (Max. Vertical) 3.0 (Max. Helical)

Bending Magnets

Bending Radius	2.2 m
Critical Energy	425 eV

Beamlines in 2016

Kiyohisa TANAKA
UVSOR Facility, Institute for Molecular Science

Among the synchrotron radiation facilities with electron energies of less than 1 GeV, UVSOR is one of the highest-brilliance light sources in the extreme-ultraviolet region. The natural emittance of the UVSOR-III storage ring is as low as 17.5 nm-rad after the successful completion of the storage ring upgrade project (the UVSOR-III project) in 2012.

Eight bending magnets and five insertion devices are available as synchrotron light sources at UVSOR. As of 2015 there are a total of fourteen operational beamlines, which are classified into two categories. Eleven of them are the so-called "Open beamlines", which are open to scientists from universities and research institutes belonging to the government, public organizations, private enterprises and also those from foreign countries. The remaining three beamlines are the "In-house beamlines", and are dedicated to the use of research groups within Institute for Molecular Science (IMS).

There is one soft X-ray station equipped with a double-crystal monochromator, seven extreme ultraviolet and soft X-ray stations with grazing incidence monochromators, three vacuum ultraviolet (VUV) stations with normal incidence monochromators, two infrared (IR) stations equipped with Fourier-Transform interferometers, and one free electron laser beamline with no monochromator, as shown in the appended table (next page) for all available beamlines at UVSOR in 2016.

In November 2016, there was a serious vacuum leakage accident from water cooling line at a four-quadrant copper mask located at upstream of BL3U. It was installed 10 years ago, and cooling water made a hole through 1 mm thick copper pipe. Since the accident occurred just after user operation, all upper most valves of beamlines were closed and the effect was limited to the storage ring. The whole storage ring has been baked after the four-quadrant copper mask was removed. User operation was restarted from 17th January, which means users lost beamtime for five weeks. The pipe which made leakage will be modified to 3 mm thickness one and will be installed during the shutdown of 2017. There are three more similar type of masks installed in the storage ring, and they will be also replaced during the shutdown. Users who lost beamtime were reassigned to the open beamtime according to their request. If there was no beamtime left, users lost beamtime. The loss of beamtime will be considered during the peer review process of the next beamtime request in FY 2017. In BL4U, where there are many users from companies and minimum beamtime is one day, the rest of the whole beamtime was rescheduled.

BL2A equipped with a double-crystal monochromator, where users can use the highest energy photons in UVSOR (~4 keV), has been used mainly for photoabsorption spectroscopy. Since there are users who want to evaluate the sample surface, a new chamber for X-ray photoemission spectroscopy (XPS) has been prepared offline. This system will be attached to BL2A during the shutdown of 2017.

In BL3B, to achieve high efficiency VUV emission spectroscopy, a new endstation chamber has been designed and manufactured in 2016. It will be available from FY 2017.

BL6B is an Infrared-THz beamline which has confocal type micro-spectroscope station, reflection/transmission station, and IR microscope imaging station. To solve serious long term drift of beam path caused by M0 magic mirror thermal load, the feedback control system of M0 mirror angle by monitoring the reflection of visible laser from M0 mirror has been developed. This feedback control system has been routinely operated and successfully provide stable beam for users from this year.

BL5U has been officially opened for users from 2016 as high energy resolution angle-resolved photoemission spectroscopy (ARPES) beamline. It became one of the most popular beamline in UVSOR, whose beamtime requests are about three times more than the beamtime. Space-resolved and spin-resolved function will be developed and installed in one year.

All users are required to refer to the beamline manuals and the UVSOR guidebook (the latest revision in PDF format uploaded on the UVSOR web site in June 2010), on the occasion of conducting the actual experimental procedures. Those wishing to use the open and in-house beamlines are recommended to contact the appropriate beamline master (see next page). For updated information on UVSOR, please see http://www.uvsor.ims.ac.jp.

Beamlines at UVSOR

Beamline	Monochromator / Spectrometer	Energy Range	Targets	Techniques	Contact
BL1U	Free electron laser	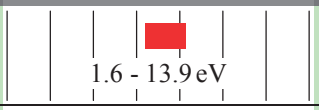			M. Katoh mkatoh@ims.ac.jp
BL1B	Martin-Puplett FT-FIR	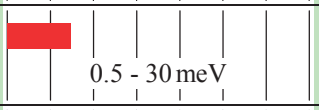	Solid	Reflection Absorption	F. Teshima tetsu@ims.ac.jp
BL2A	Double crystal	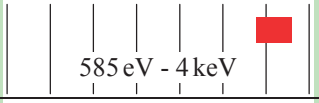	Solid	Reflection Absorption	N. Kondo nkondo@ims.ac.jp
BL2B	18-m spherical grating (Dragon)	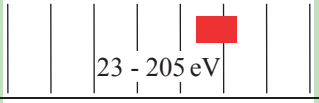	Solid	Photoemission	S. Kera kera@ims.ac.jp
BL3U*	Varied-line-spacing plane grating (Monk-Gillieson)	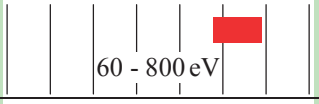	Gas Liquid Solid	Absorption Photoemission Photon-emission	N. Kosugi kosugi@ims.ac.jp
BL3B	2.5-m off-plane Eagle	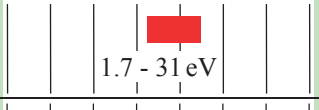	Solid	Reflection Absorption Photon-emission	M. Hasumoto hasumoto@ims.ac.jp
BL4U	Varied-line-spacing plane grating (Monk-Gillieson)	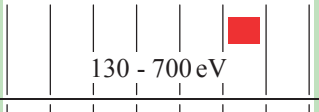	Gas Liquid Solid	Absorption (Microscopy)	T. Ohigashi ohigashi@ims.ac.jp
BL4B	Varied-line-spacing plane grating (Monk-Gillieson)	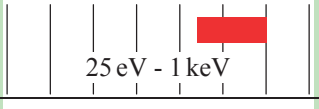	Gas Solid	Photoionization Photodissociation Photoemission	E. Shigemasa sigemasa@ims.ac.jp
BL5U	Varied-line-spacing plane grating (Monk-Gillieson)	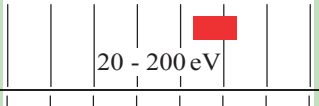	Solid	Photoemission	M. Sakai sakai@ims.ac.jp
BL5B	Plane grating	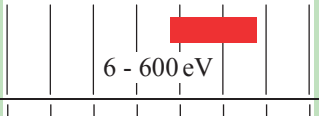	Solid	Calibration Absorption	M. Hasumoto hasumoto@ims.ac.jp
BL6U*	Variable-included-angle varied-line-spacing plane grating	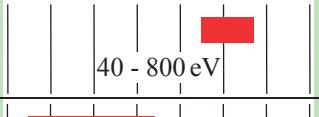	Gas Solid	Photoionization Photodissociation Photoemission	E. Shigemasa sigemasa@ims.ac.jp
BL6B	Michelson FT-IR	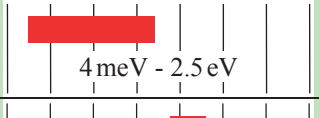	Solid	Reflection Absorption IR microscope	F. Teshima tetsu@ims.ac.jp
BL7U	10-m normal incidence (modified Wadsworth)	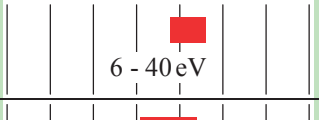	Solid	Photoemission	S. Ideta idetas@ims.ac.jp
BL7B	3-m normal incidence	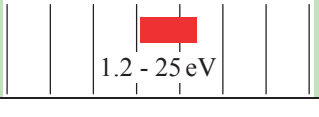	Solid	Reflection Absorption Photon-emission	M. Hasumoto hasumoto@ims.ac.jp

Yellow columns represent undulator beamlines.
* In-house beamline.

BL1U

Light Source Development Station

▼Description

BL1U has being constructed for developments and applications of various photon sources including free electron laser in the range from visible to deep UV, coherent harmonic generation in the deep UV and VUV, laser Compton scattering gamma-rays and undulator radiation with various polarization properties including optical vortices.

The beam-line is equipped with a dedicated twin polarization variable undulator system with a buncher section, which can be used for a FEL oscillator and a VUV CHG. It is also equipped with a femto-second laser system synchronized with the accelerator, which is used for CHG, slicing, LCS and coherent THz radiation generation.

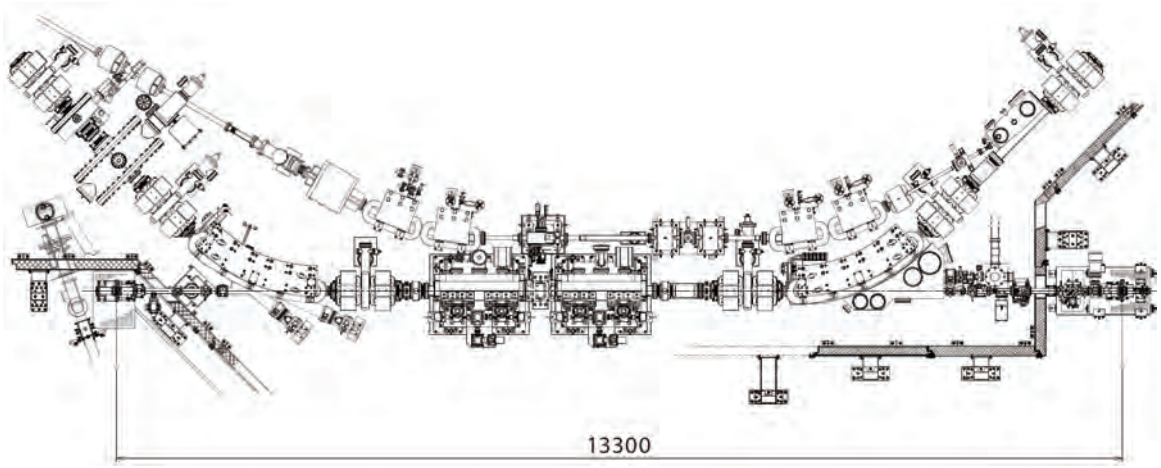

Fig. 1. Configuration of the free electron laser (under reconstruction)

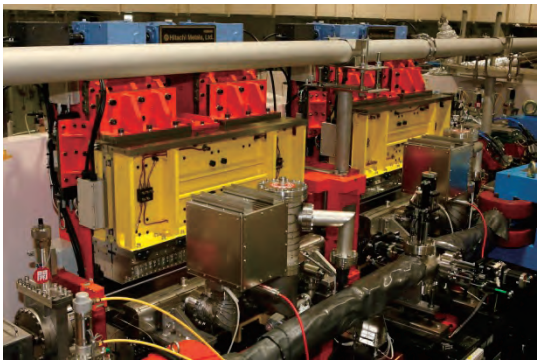

Fig. 2. Twin Apple-II Undulator

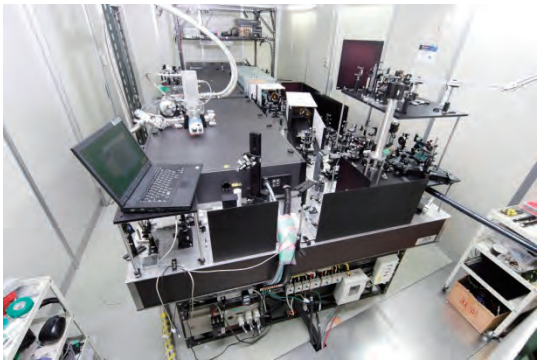

Fig. 3. Accelerator synchronized Laser System

▼Technical Data of FEL

Wave Length	199-800 nm
Spectral Band Width	~10^{-4}
Polarization	Circular/Linear
Pulse Rate	11.26 MHz
Max. Ave. Power	~1W

▼Technical Data of Ti:Sa Laser

Wave Length	800 nm		
Pulse Length	130 fsec		
Oscillator	90.1 MHz		
Pulse Energy	2.5mJ	10mJ	50mJ
Repetition Rate	1kHz	1kHz	10Hz

BL1B

Terahertz Spectroscopy Using Coherent Synchrotron Radiation

▼Description

Coherent synchrotron radiation (CSR) is a powerful light source in the terahertz (THz) region. This beamline has been constructed for basic studies on the properties of THz-CSR. However, it can be also used for measurements of reflectivity and transmission spectra of solids using conventional synchrotron radiation.

The emitted THz light is collected by a three-dimensional magic mirror (3D-MM, M0) of the same type as those already successfully installed at BL43IR in SPring-8 and BL6B in UVSOR-II. The 3D-MM was installed in bending-magnet chamber #1 and is controlled by a 5-axis pulse motor stage (x, z translation; θ_x, θ_y, θ_z rotation). The acceptance angle was set at 17.5-34 degrees (total 288 mrad) in the horizontal direction. The vertical angle was set at ±40 mrad to collect the widely expanded THz-CSR.

The beamline is equipped with a Martin-Puplett type interferometer (JASCO FARIS-1) to cover the THz spectral region from 4 to 240 cm^{-1} ($h\nu$ = 500 μeV-30 meV). There is a reflection/absorption spectroscopy (RAS) end-station for large samples (~ several mm). At the RAS end-station, a liquid-helium-flow type cryostat with a minimum temperature of 4 K is installed.

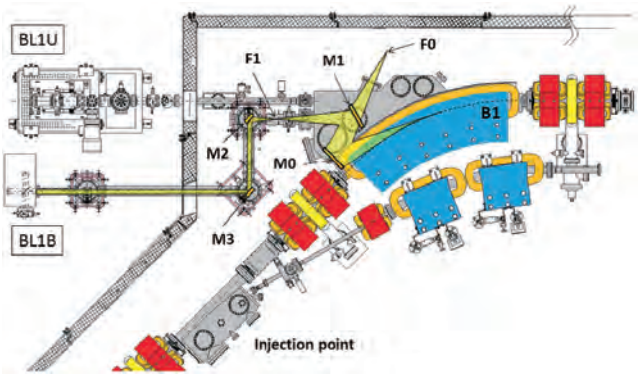

Fig. 1. Schematic top view of the beam extraction part of the THz-CSR beamline, BL1B. The three-dimensional magic mirror (3D-MM, M0) and a plane mirror (M1) are located in the bending-magnet chamber. A parabolic mirror (M2) is installed to form a parallel beam. The straight section (BL1U) is used for coherent harmonic generation (CHG) in the VUV region.

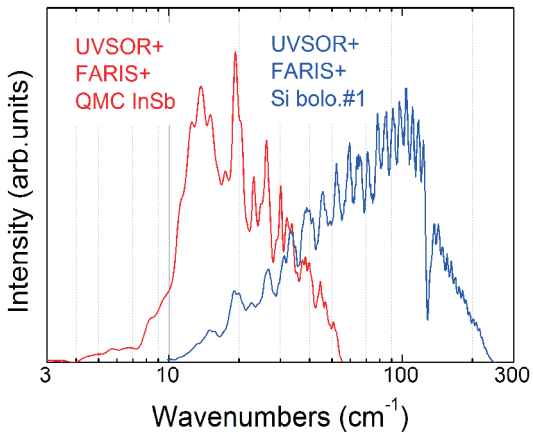

Fig. 2. Obtained intensity spectra with the combination of a light source (UVSOR), interferometer (FARIS-1), and detectors (Si bolometer and InSb hot-electron bolometer).

▼Technical Data

Interferometer	Martin-Puplett (JASCO FARIS-1)
Wavenumber range (Energy range)	4-240 cm^{-1} (500 μeV-30 meV)
Resolution in cm^{-1}	0.25 cm^{-1}
Experiments	Reflection/transmission spectroscopy
Miscellaneous	Users can use their experimental system in this beamline.

BL2A

Soft X-Ray Beamline for Photoabsorption Spectroscopy

▼Description

BL2A, which was moved its previous location as BL1A in 2011, is a soft X-ray beamline for photoabsorption spectroscopy. The beamline is equipped with a focusing premirror and a double-crystal monochromator [1]. The monochromator serves soft X-rays in the energy region from 585 to 4000 eV using several types of single crystals, such as β-A l_2O_3, beryl, KTP ($KTiOPO_4$), quartz, InSb, and Ge. The throughput spectra measured using a Si photodiode (AXUV-100, IRD Inc.) are shown in Fig. 1. The typical energy resolution (E / ΔE) of th e monochromator is approximately 1500 for beryl and InSb.

A small vacuum chamber equipped with an electron multiplier (EM) detector is available. Photoabsorption spectra for powdery samples are usually measured in total electron yield mode, with the use of the EM detector. A silicon drift detector is also available for measuring partial fluorescence yields from solid samples.

[1] Hiraya *et al.*, Rev. Sci. Instrum. **63** (1992) 1264.

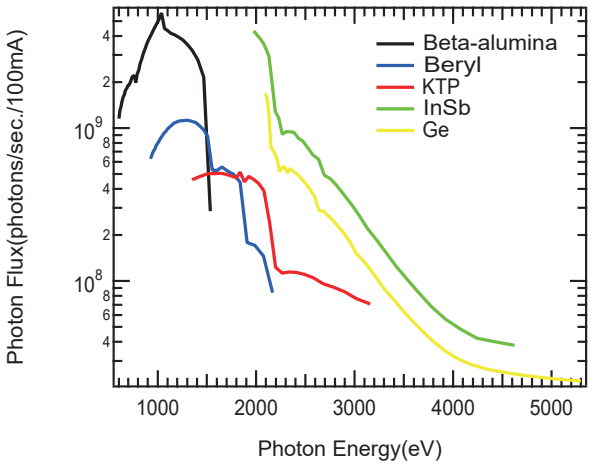

Fig. 1. Throughput spectra of the double-crystal monochromator at BL2A.

Fig. 2. Side view of BL2A.

▼Technical Data

Monochromator	Double crystal monochromator
Monochromator crystals: (2d value, energy range)	β-Al_2O_3 (22.53 Å, 585-1609 eV), beryl (15.965 Å, 826-2271 eV), KTP (10.95 Å, 1205-3310 eV), quartz (8.512 Å, 1550-4000 eV), InSb (7.481 Å, 1764-4000 eV), Ge (6.532 Å, 2094-4000 eV)
Resolution	E / ΔE = 1500 for beryl and InSb
Experiments	Photoabsorption spectroscopy (total electron yield using EM and partial fluorescence yield using SDD)

BL2B

Photoelectron spectroscopy of molecular solids

▼Description

This beamline previously dedicated for experiments in the field of gas phase photoionization and reaction dynamics. Then, the beamline has been reconstructed for photoelectron spectroscopy of molecular solids with a new end station, and experiments can be performed from May 2014. The monochromator is a spherical grating Dragon type with 18-m focal length. High throughput (1×10^{10} photons s^{-1}) and high resolution ($E/\Delta E$ = 2000 - 8000) are achieved simultaneously under the condition of the ring current of 100 mA [1]. The optical system consists of two pre-focusing mirrors, an entrance slit, three spherical gratings (G1 - G3), two folding mirrors, a movable exit slit, and a refocusing mirror [2]. The monochromator is designed to cover the energy range of 23–205 eV with the three gratings: G1 (2400 lines mm^{-1}, R = 18 m) at 80–205 eV; G2 (1200 lines mm^{-1}, R = 18 m) at 40–100 eV; G3 (2400 lines mm^{-1}, R = 9.25 m) at 23–50 eV. The percentage of the second-order light contamination at $h\nu$ = 45.6 eV is 23% for G2 or 7% for G3.

A UHV chamber is placed downstream of the refocusing mirror chamber and equipped silicon photodiode, sapphire plate Au mesh and filters for absolute photon flux measurement, monitor the photon-beam position, relative photon flux measurements and attenuate higher order light, respectively.

The new end station consists of a main chamber with a hemispherical analyzer (SCIENTA R3000) and a liquid-He-cooled cryostat (temperature range of 15-400 K) with 5-axis stage, a sample preparation chamber with a fast-entry load-lock chamber and a cleaning chamber with LEED, ion gun for sputtering and IR heating unit.

[1] M. Ono, H. Yoshida, H. Hattori and K. Mitsuke, Nucl. Instrum. Meth. Phys. Res. A **467-468** (2001) 577.
[2] H. Yoshida and K. Mitsuke, J. Synchrotron Radiation **5** (1998) 774.

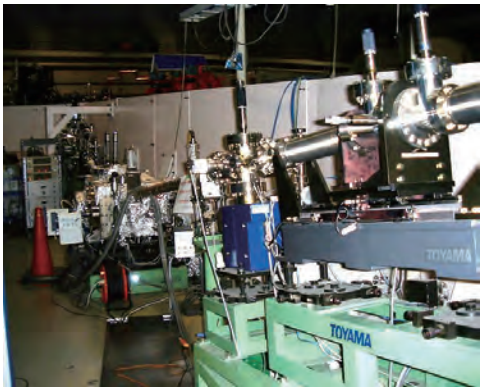

Fig. 1. 18 m spherical grating monochromator at BL2B.

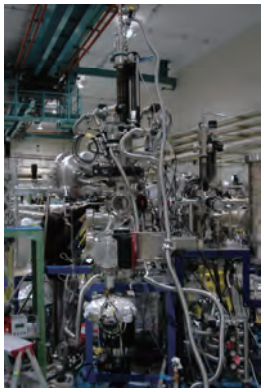

Fig. 2. End station of BL2B for photoelectron spectroscopy of molecular solids.

▼Technical Data

Monochromator	18 m spherical grating Dragon-type
Wavelength Range	23-205 eV
Resolution	2000-8000 depending on the gratings
Experiments	Angle-resolved ultraviolet photoemission spectroscopy

BL3U

Varied-Line-Spacing Plane Grating Monochromator for Molecular Soft X-Ray Spectroscopy

▼Description

The beamline BL3U is equipped with an in-vacuum undulator composed of 50 periods of 3.8 cm period length. The emitted photons are monochromatized by the varied-line-spacing plane grating monochromator (VLS-PGM) designed for various spectroscopic investigations in the soft X-ray range including soft X-ray emission studies. Three holographically ruled laminar profile plane gratings are designed to cover the photon energy range from 60 to 800 eV. The beamline has two endstations, namely, XES setup and multi-purpose setup. The XES setup is used for soft X-ray emission spectroscopy. The beam is horizontally focused onto the sample position by a plane-elliptical mirror, M2X. In the multi-purpose setup, the beam is focused by the toroidal mirror M2. Between the sample position and M2, the differential pumping is placed. XAS of liquid samples and the application of in operando observations are performed at the experimental stage of the multi-purpose setup.

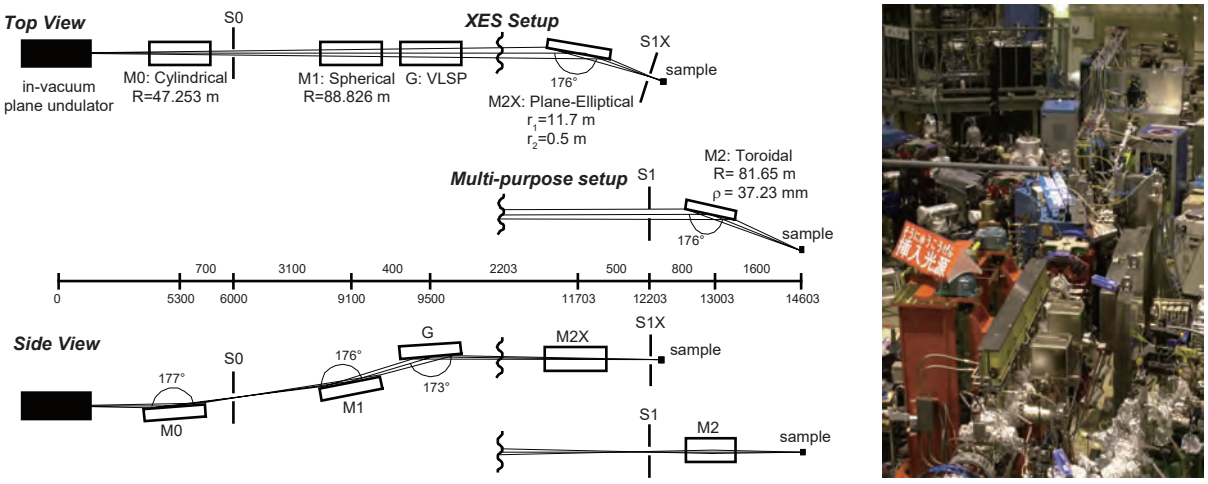

Fig. 1. Schematic layout (left) and the photography (right) of the BL3U. The distances along the beam from the center of the in-vacuum plane undulator are shown in millimeters. S1X and M2X can be replaced with the other exit slit S1 so that experiments can be carried out at either the XES or the multipurpose endstation. In the XES setup, the sample is placed 5–10 mm downstream of S1X.

▼Technical Data

Monochromator	Varied-line-spacing plane grating monochromator
Energy Range	60-800 eV
Resolution	$E / \Delta E > 10\,000$
Experiments	Soft X-ray spectroscopy (XPS, XES, XAS)
Beam Size (XES Endstation)	Gaussian shape Vertical 5-20 μm; Horizontal 41 μm (FWHM)

BL3B (HOTRLU)

VIS-VUV Photoluminescence and Reflection/Absorption Spectroscopy

▼Description

BL3B has been constructed to study photoluminescence (PL) in the visible (VIS) to vacuum ultraviolet (VUV) region. This beamline consists of a 2.5 m off-plane Eagle type normal-incidence monochromator, which covers the VUV, UV, and VIS regions, i.e., the energy (wavelength) region of 1.7-31 eV (40-730 nm), with three spherical gratings having constant grooving densities of 1200, 600, and 300 l/mm optimized at the photon energies of ~20, ~16, and ~6 eV, respectively. The schematic side view and top view layouts are shown in Figs. 1(a) and 1(b), respectively. The FWHM of the beam spot at the sample position is 0.25 mm (V) × 0.75 mm (H). Low energy pass filters (LiF, quartz, WG32, OG53) can be inserted automatically to maintain the optical purity in the G3 (300 l/mm) grating region (1.7~11.8 eV). Figure 2 shows the throughput spectra (photon numbers at a beam current of 300 mA) for each grating with entrance and exit slit openings of 0.1 mm (resolving power E / ΔE of ~2000 (G3, ~6.8 eV)). Since both slits can be opened up to 0.5 mm, a monochromatized photon flux of 10^{10} photons/s or higher is available for PL measurements in the whole energy region.

The end station is equipped with a liquid-helium-flow type cryostat for sample cooling and two detectors; one of which is a photomultiplier with sodium salicylate and the other a Si photodiode for reflection/absorption measurement. For the PL measurements in the wide energy region from VIS to VUV, two PL monochromators, comprising not only a conventional VIS monochromator but also a VUV monochromator with a CCD detector, are installed at the end station.

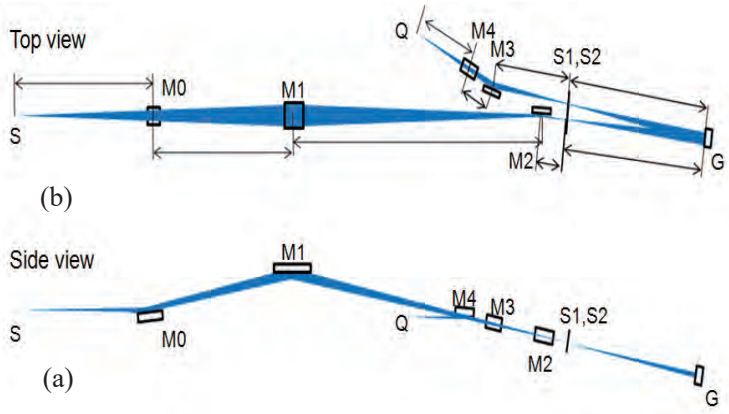

Fig. 1. Schematic layout of the BL3B (a) side view and (b) top view.

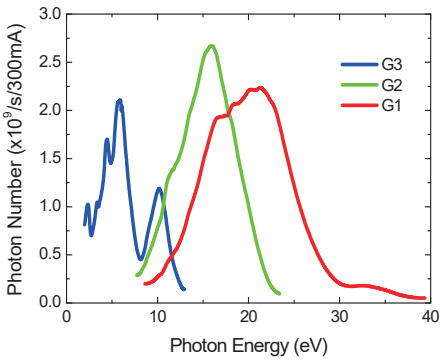

Fig. 2. Throughput spectra for each grating (G1:1200 l/mm, G2:600 l/mm and G3:300 l/mm) with S1 = S2 = 0.1 mm.

▼Technical Data

Monochromator	-2.5 m normal-incidence monochromator
Energy range	1.7-31 eV (40-730 nm)
Resolution (Δhν/ hν)	≥ 12000 (at ~ 6.9 eV, 0.02 mm slits, G1 (1200 l/mm)
Experiments	Photoluminescence, reflection, and absorption spectroscopy, mainly for solids

BL4U

Scanning Transmission X-ray Microscopy in the Soft X-ray Region

▼Description

In the soft x-ray region, there are several absorption edges of light elements and transition metals. The near edge X-ray absorption fine structure (NEXAFS) brings detailed information about the chemical state of target elements. A scanning transmission X-ray microscope (STXM) in the soft X-ray region is a kind of extended technique of the NEXAFS with high spatial resolution. The STXM has a capability of several additional options, for example, in-situ observations, 3-dimensional observation by computed tomography and ptychography, by utilizing the characteristics of the X-rays. The STXM can be applied to several sciences, such as polymer science, material science, cell biology, environmental science, and so on.

This beamline equips an in-vacuum undulator, a varied-line-spacing plane grating monochromator and a fixed exit slit. The soft X-ray energy range from 100 to 770 eV with the resolving power (E/ΔE) of 6,000 is available. The aperture size of the fixed exit slit determines not only the resolving power but also the size of a microprobe. A Fresnel zone plate is used as a focusing optical device through an order select aperture and its focal spot size of ~30 nm is available at minimum. An image is acquired by detecting intensities of the transmitted X-rays by a photomultiplier tube with scintillator with scanning a sample 2-dimensionally. By changing the energy of the incident beam, each 2-dimensional NEXAFS image is stacked. A main chamber of STXM is separated from the beamline optics by a silicon nitride membrane of 100-nm thickness; therefore, sample folders can be handled in vacuum or in helium.

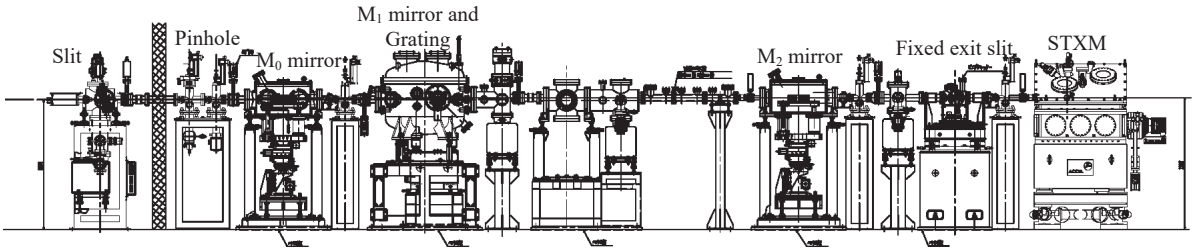

Fig. 1. Schematic image of BL4U

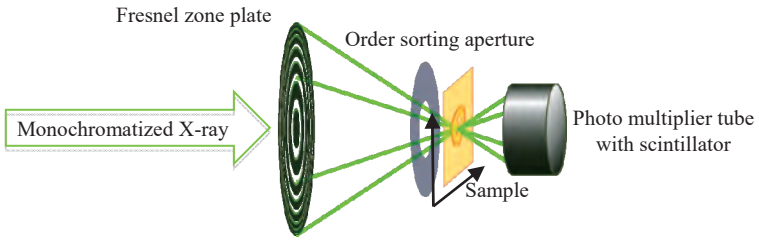

Fig. 2. Schematic image of the STXM

▼Technical Data

Energy range (E)	100-770 eV
Resolving power (E/ΔE)	~6,000
Focusing optical element	Fresnel zone plate
Spatial resolution	~30 nm
Experiments	2-dimensinal absorption spectroscopy
Measurement environment	standard sample folder in vacuum or in helium, specially designed sample cell in ambient condition

BL4B

Varied-Line-Spacing Plane Grating Monochromator for Molecular Soft X-Ray Spectroscopy

▼Description

The beamline BL4B equipped with a varied-line-spacing plane grating monochromator (VLS-PGM) was constructed for various spectroscopic investigations in a gas phase and/or on solids in the soft X-ray range. Three holographically ruled laminar profile plane gratings with SiO_2 substrates are designed to cover the photon energy range from 25 to 800 eV. The gratings with groove densities of 100, 267, and 800 l/mm cover the spectral ranges of 25–100, 60–300, and 200-1000 eV, respectively, and are interchangeable without breaking the vacuum. Fig. 1 shows the absolute photon flux for each grating measured using a Si photodiode (IRD Inc.), with the entrance- and exit-slit openings set at 50 and 50 μm, respectively. The maximum resolving power ($E/\Delta E$) achieved for each grating exceeds 5000.

There is no fixed endstation on this beamline. A small vacuum chamber equipped with an electron multiplier (EM) detector is available. Soft X-ray absorption spectra of solid samples are usually measured by means of the total electron yield method using EM, and the partial fluorescence yield method using a silicon drift detector (SDD).

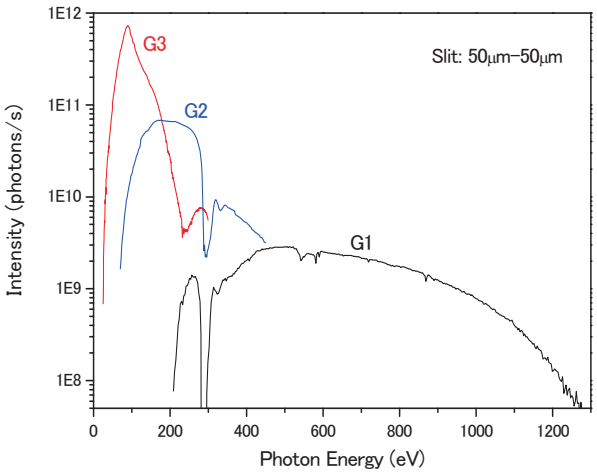

Fig. 1. Throughput from the VLS-PGM monochromator on BL4B.

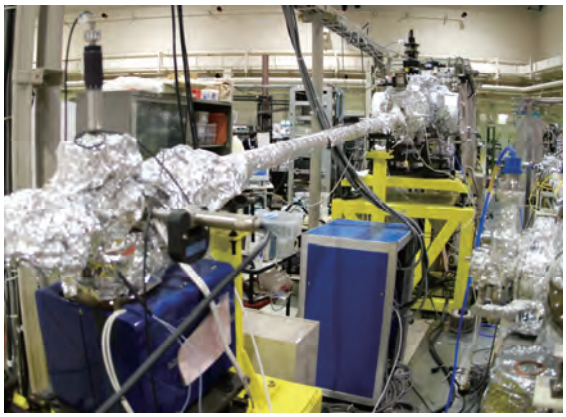

Fig. 2. Photo of BL4B.

▼Technical Data

Monochromator	Varied-line-spacing Plane Grating Monochromator
Energy range	25-1000 eV
Resolution	$E / \Delta E > 5000$ (at maximum)
Experiments	Soft X-ray spectroscopy (mainly, photoabsorption spectroscopy for solid targets by means of total electron yield method using EM and partial fluorescence yield method using SDD)

BL5U

Photoemission Spectroscopy of Solids and Surfaces

▼Description

This beamline was originally used for angle-resolved photoemission spectroscopy (ARPES) study of solids and surfaces. After Jan 2014, the beamline had been shutdown for upgrade. The whole beamline, including the undulator and the endstation, is renewed to perform higher energy resolution ARPES experiments. This beamline will also have new capability to obtain spin- and spatial-dependence of the electronic structure of solids using new spin detector and micro-focused beam. This beamline is opened for users from 2016.

Fig. 1. Pictures of BL5U on May 2014.

▼Technical Data (Expected Performance)

Monochromator	Monk-Gillieson VLS-PGM
Energy Range	20-200 eV
Resolution	$h\nu$ / ΔE > 10,000 for < 10 μm slits
Experiment	ARPES, Spin-resolved ARPES, Space-resolved ARPES
Flux	$<10^{12}$ photons/s for <10 μm slits (at the sample position)
Beam spot size	400 (H) x 5-20 (V) μm, 10 (H) x 4-6 (V) μm (microscope)
Main Instruments	Hemispherical photoelectron analyzer (MBS A-1), Liq-He flow cryostat with 5-axis manipulator (5-400 K)

BL5B

Calibration Apparatus for Optical Elements and Detectors

▼Description

BL5B has been constructed to perform calibration measurements for optical elements and detectors. This beamline is composed of a plane grating monochromator (PGM) and three endstations in tandem. The most upstream station is used for the calibration measurements of optical elements, the middle one for optical measurements for solids, and the last for photo-stimulated desorption experiments. The experimental chamber at the most downstream station is sometimes changed to a chamber for photoemission spectroscopy. The calibration chamber shown in Fig. 2 is equipped with a goniometer for the characterization of optical elements, which has six degrees of freedom, X-Y translation of a sample, and interchanging of samples and filters. These are driven by pulse motors in vacuum. Because the polarization of synchrotron radiation is essential for such measurements, the rotation axis can be made in either the horizontal or vertical direction (s- or p-polarization).

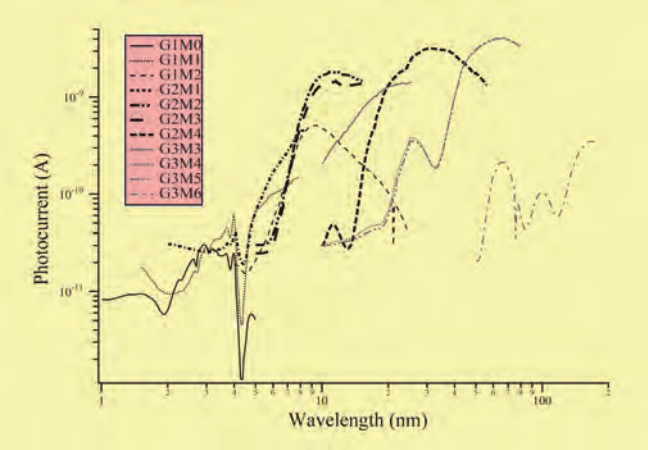

Fig. 1. Throughput spectra for possible combinations of gratings and mirrors at BL5B measured by a gold mesh.

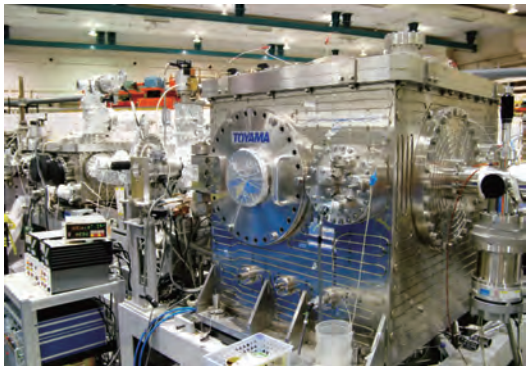

Fig. 2. A side view of the experimental chamber for calibration measurements.

▼Technical Data

Monochromator	Plane Grating Monochromator
Energy range	6-600 eV (2-200 nm)
Resolution	E / ΔE~500
Experiments	Calibration of optical elements, reflection and absorption spectroscopy mainly for solids

BL6U

Variable-Included-Angle VLS-PGM for Molecular Soft X-Ray Spectroscopy

▼Description

The beamline BL6U equipped with a variable-included-angle Monk-Gillieson mounting monochromator with a varied-line-spacing plane grating was constructed for various spectroscopic investigations requiring high-brilliance soft X-rays in a gas phase and/or on solids. Through a combination of undulator radiation and sophisticated monochromator design (entrance slit-less configuration and variable-included-angle mechanism), using a single grating, the monochromator can cover the photon energy ranging from 30 to 500 eV, with resolving power of greater than 10000 and photon flux of more than 10^{10} photons/s. Figure 1 shows an example of the monochromator throughput spectra measured using a Si photodiode, with the exit-slit opening set at 30 μm, which corresponds to the theoretical resolving power of 10000 at 80 eV.

There is no fixed endstation on this beamline.

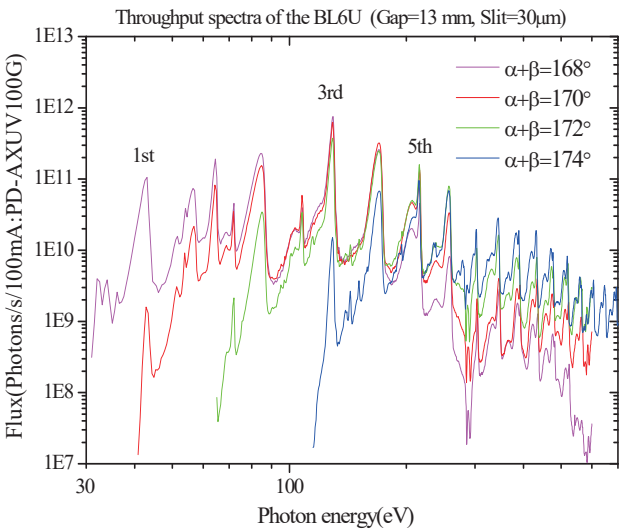

Fig. 1. Throughput spectra of the BL6U monochromator at various included angles.

Fig. 2. Photo of BL6U

▼Technical Data

Monochromator	Variable-included-angle Varied-line-spacing Plane Grating Monochromator
Energy range	40-500 eV
Resolution	E / ΔE > 10000 (at maximum)
Experiments	High-resolution soft X-ray spectroscopy (mainly photoelectron spectroscopy for gaseous and solid targets)

BL6B
Infrared and Terahertz Spectroscopy of Solids

▼Description

Synchrotron radiation (SR) has good performance (high brilliance and high flux) not only in the VUV and soft X-ray (SX) regions but also in the infrared (IR) and THz regions. BL6B covers the IR and THz regions. The previous beamline, BL6A1, which was constructed in 1985, was the pioneer in IRSR research. The beamline was deactivated at the end of FY2003 and a new IR/THz beamline, BL6B (IR), was constructed in FY2004. The front-end part including bending duct #6 was replaced with a new part having a higher acceptance angle (215 (H) × 80 (V) mrad^2) using a magic mirror, as shown in Fig. 1.

There are two Michelson type interferometers in this endstation; with first one (Bruker Vertex70v), which covers a wide spectral region from 30 to 20,000 cm^{-1} ($h\nu$ = 4 meV-2.5 eV), reflection/absorption spectroscopy measurements of large samples (up to several mm) and IR/THz microscopy measurements of tiny samples (up to several tens of μm) can be performed. For reflection/absorption spectroscopy measurements, a liquid-helium-flow type cryostat with a minimum temperature of 4 K is installed. The other interferometer (Jasco FT/IR-6100), which covers 350 to 15,000 cm^{-1} ($h\nu$ = 45 meV-1.8 eV), has been available for IR microscopy imaging measurements from FY2014. One can also perform ATR measurements using diamond ATR prism.

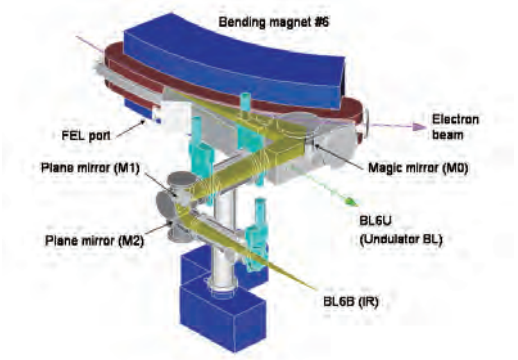

Fig. 1. Design of the optics and front end of BL6B.

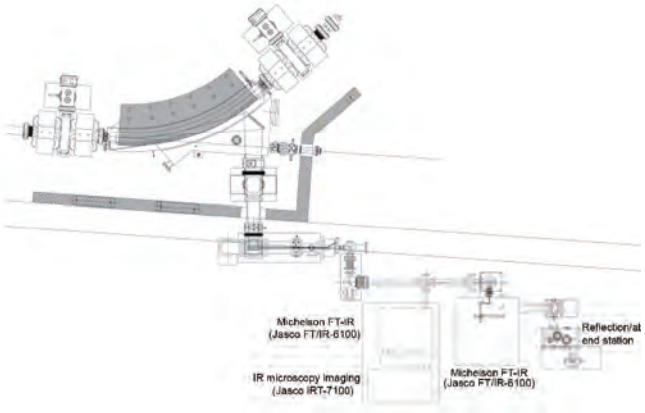

Fig. 2. Schematic top view of BL6B.

▼Technical Data

Interferometer	Michelson (Bruker Vertex70v)	Michelson (Jasco FT/IR-6100)
Wavenumber Range (Energy range)	30-20,000 cm^{-1} (4 meV-2.5 eV)	350-15,000 cm^{-1} (45 meV-1.8 eV)
Resolution in cm^{-1}	0.1 cm^{-1}	0.5 cm^{-1}
Experiments	Reflectivity and transmission spectroscopy THz Microspectroscopy	IR microscopy imaging (JASCO IRT-7000) ATR spectroscopy

BL7U (SAMRAI)

Angle-Resolved Photoemission of Solids in the VUV Region

▼Description

Beamline 7U, named the Symmetry- And Momentum-Resolved electronic structure Analysis Instrument (SAMRAI) for functional materials, was constructed to provide a photon flux with high energy resolution and high flux mainly for high-resolution angle-resolved photoemission spectroscopy, so-called "ARPES", of solids [1]. An APPLE-II-type variable-polarization undulator is installed as the light source. The undulator can produce intense VUV light with horizontal/vertical linear and right/left circular polarization. The undulator light is monochromatized by a modified Wadsworth type monochromator with three gratings (10 m radius; 1200, 2400, and 3600 lines/mm optimized at hv = 10, 2 0, and 33 eV). The energy resolution of the light ($hv/\Delta hv$ is more than 10^4 with a photon flux of 10^{11}-10^{12} ph/s or higher on samples in the entire energy region. The beamline has a photoemission end-station equipped with a 200 mm-radius hemispherical photoelectron analyzer (MB Scientific AB, A-l analyzer) with a wide-angle electron lens and a liquid-helium-cooled cryostat with 6-axis pulse motor control (AVC Co., Ltd., i-GONIO). The main function of the beamline is to determine the electronic structure of solids and its temperature dependence in order to reveal the origin of their physical properties.

[1] S. Kimura, T. Ito, M. Sakai, E. Nakamura, N. Kondo, K. Hayashi, T. Horigome, M. Hosaka, M. Katoh, T. Goto, T. Ejima and K. Soda, Rev. Sci. Instrum. **81** (2010) 053104.

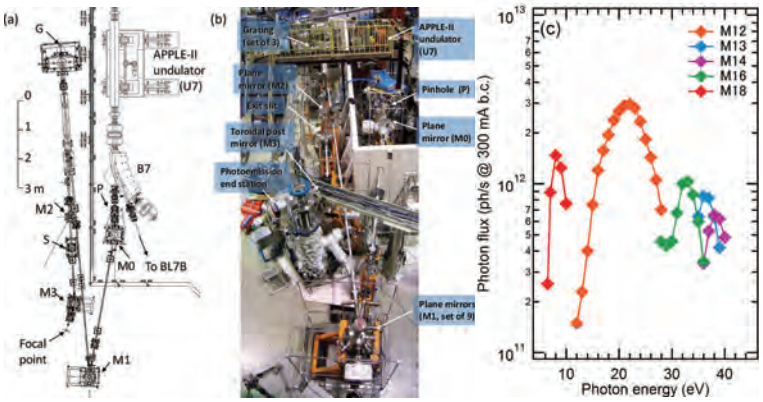

Fig. 1. SAMRAI beamline [(a), (b)] consisting of an APPLE-II type undulator (U7), a modified Wadsworth type monochromator (M0-S), and a high-resolution photoemission analyzer at the focal point. The monochromator has five major optical components: two plane mirrors (M0 and M1) with water cooling, one set of three spherical gratings (G), an exit slit (S), and one toroidal refocusing mirror (M3). (c) Example of flux intensity *versus* photon energy [1].

▼Technical Data

Light source	APPLE-II type undulator (λ_u = 76 mm, N = 36) vertical/horizontal, right/left circular (depending on hv)
Monochromator	10 m normal-incidence monochromator (modified Wadsworth type)
Photon energy range	6-40 eV (λ = 30-200 nm)
Resolution ($hv/\Delta hv$)	E / ΔE > 10000-50000
Photon flux on sample	≥ 1012-1011 ph/s (depending on hv)
Beam size on sample	200 (H) × 50 (V) μm^2
Experiments	Angle-resolved photoemission of solids (MV Scientific A-1 analyzer, acceptance angle: ± 18 deg)

BL7B

3 m Normal-Incidence Monochromator for Solid-State Spectroscopy

▼Description

BL7B has been constructed to provide sufficiently high resolution for conventional solid-state spectroscopy, sufficient intensity for luminescence measurements, wide wavelength coverage for Kramers–Kronig analyses, and minimum deformation to the polarization characteristic of incident synchrotron radiation. This beamline consists of a 3-m normal incidence monochromator, which covers the vacuum ultraviolet, ultraviolet, visible, and infrared, i.e., the wavelength region of 50–1000 nm, with three gratings (1200, 600, and 300 l/mm). Two interchangeable refocusing mirrors provide two different focusing positions. For the mirror with the longer focal length, an LiF or a MgF_2 window valve can be installed between the end valve of the beamline and the focusing position. Figure 1 shows the absolute photon intensity for each grating with the entrance and exit slit openings of 0.5 mm. A silicon photodiode (AXUV-100, IRD Inc.) was utilized to measure the photon intensity and the absolute photon flux was estimated, taking the quantum efficiency of the photodiode into account.

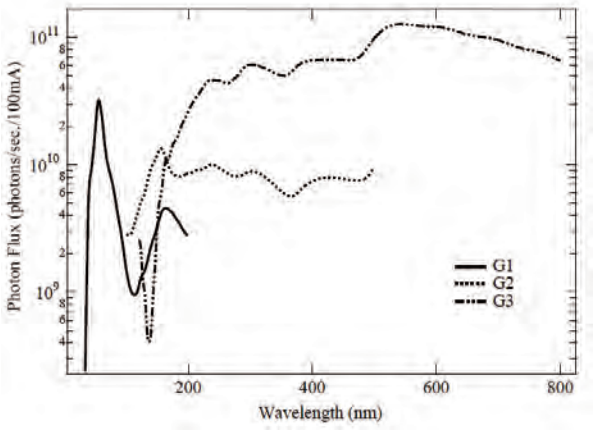

Fig. 1. Throughput spectra of BL7B measured using a silicon photodiode.

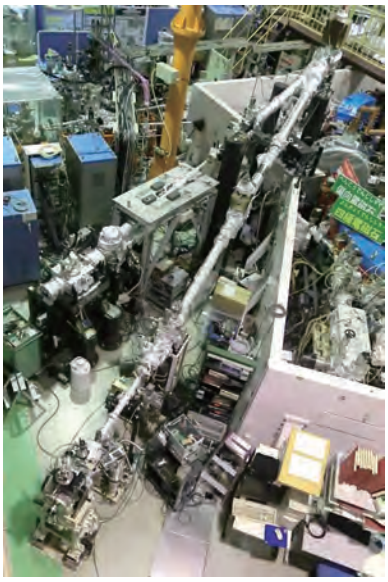

Fig. 2. Photo of BL7B.

▼Technical Data

Monochromator	3 m Normal-Incidence Monochromator
Wavelength Range	50-1000 nm (1.2-25 eV)
Resolution	$E / \Delta E$ = 4000-8000 for 0.01 mm slits
Experiments	Absorption, reflection, and fluorescence spectroscopy, mainly for solids

UVSOR User 1

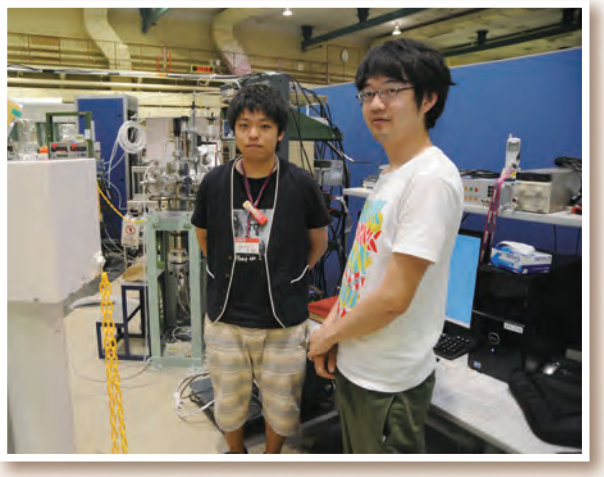

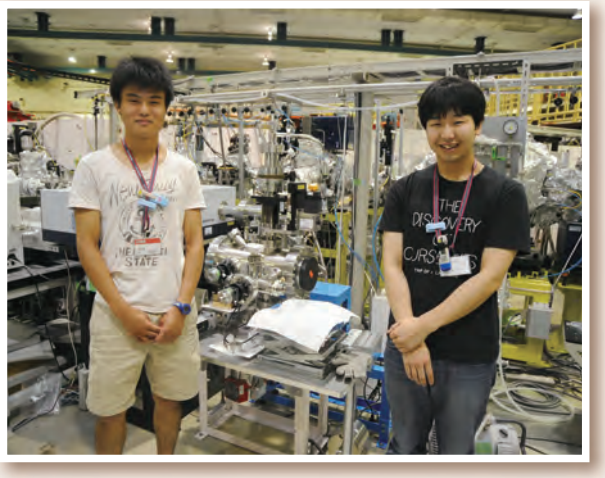

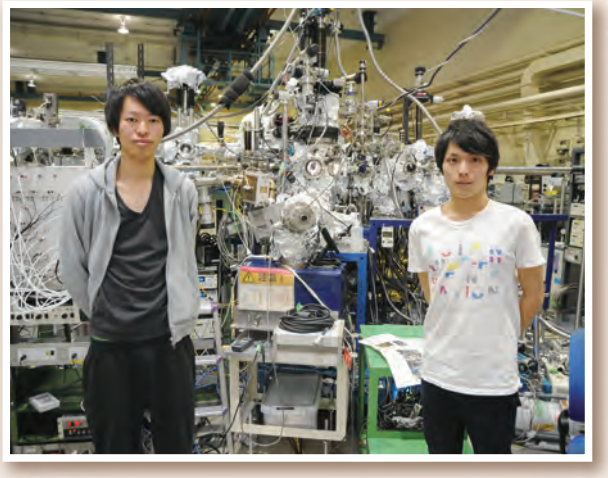

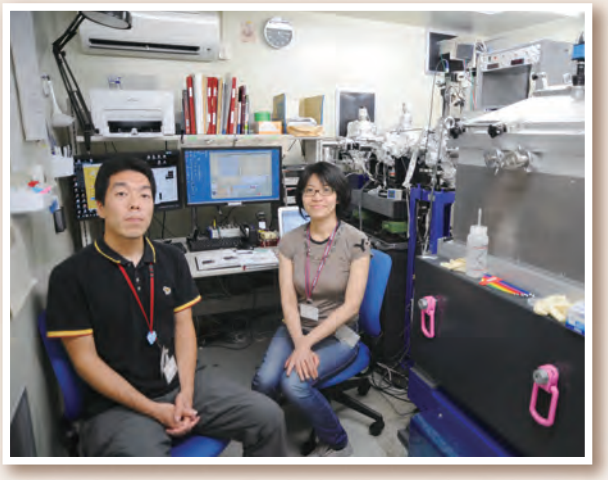

UVSOR User 2

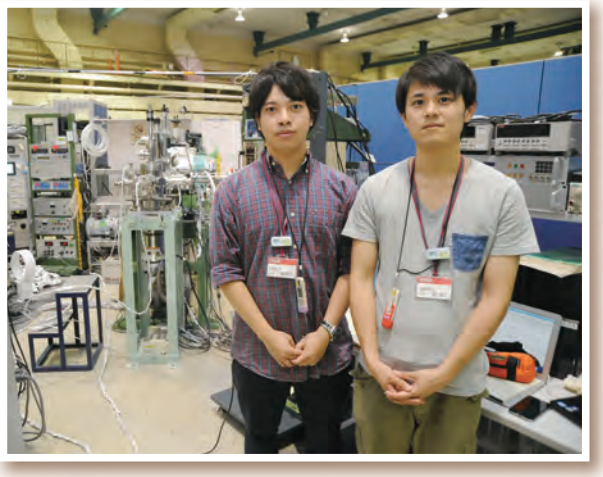

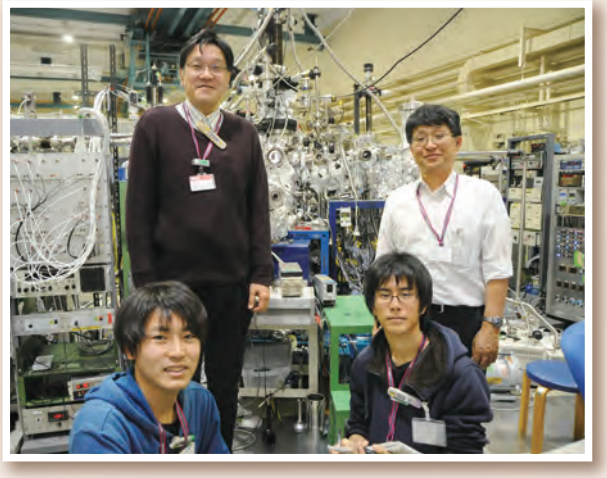

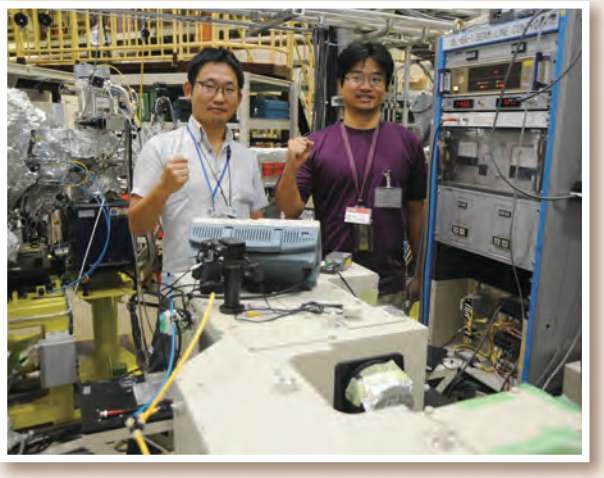

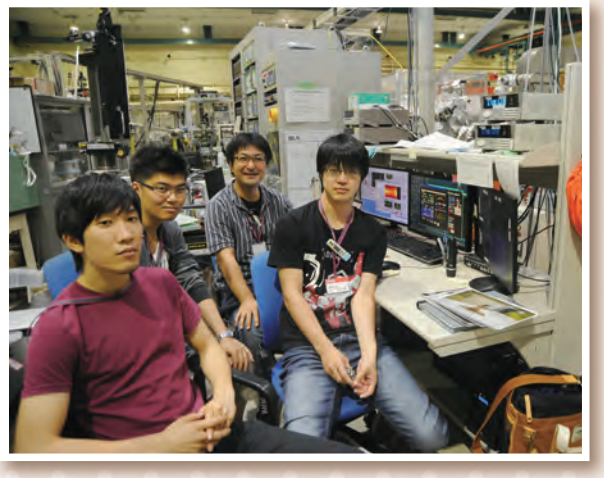

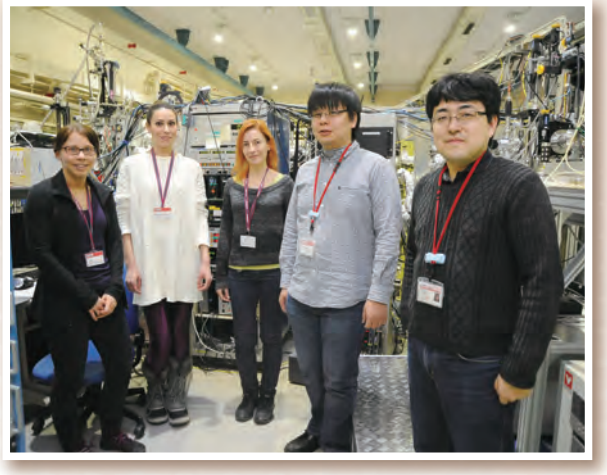

III-1

Accelerators and Instruments

Light sources

Measurement of Temporal Response of Transmission-type Spin-Polarized Photocathodes （PCs） -II

N. Yamamoto[1], K. Yamaguchi[2], A. Mano[2], M. Hosaka[2], X. G. Jin[1], Y. Takashima[2] and M. Katoh[3, 2]

[1] *High Energy Accelerator Research Organization (KEK), Tsukuba 305-0801, Japan*
[2]*Nagoya University, Nagoya 464-8601, Japan*
[3]*UVSOR Facility, Institute for Molecular Science, Okazaki 444-8585, Japan*

In order to study the temporal response directly and precisely, A radio-frequency (rf) deflection cavity was designed and constructed [1].

The measurement system consists of a pump laser system, a 20-kV DC electron gun, a 2.6-GHz rf deflection cavity [2] and a beam profiling system (shown in Fig. 1). A mode-locked Ti:Sapphire laser (COHERENT, MIRA) with 90.1 MHz pulse reputation rate was used to illuminate the PC. A screen monitor with a thin fluorescent coating was located 0.6 m downstream of the deflection cavity.

For synchronizing the electron bunch with the rf phase of the deflection cavity, the rf signal was passively generated from pump laser signals by using a silicon photodetector (EOS, ET-2030A) and a band pass filter. The obtained rf signal was converted to 2612.9 MHz by using a 29-times frequency multiplier. Finally, the rf signal passing through a phase shifter to adjust between the beam and rf phases was amplified up to 50 W and was fed to the deflection cavity. The laser pulse length convoluted with the timing jitter of synchronization system was measured by a streak camera and was confirmed to around 0.6 ps in root-mean-square.

The temporal distribution of the electron beam extracted from the transmission-type GaAs/GaAsP strained-SL PC [3] was shown in Fig. 2, where the data points with open circles and a solid line indicate the experimental data and fitted curve with assumed the convolution integral of the laser pulse length and transverse beam size at the screen monitor and electron retardation mechanisms with the decay constant τ in the semiconductor. [4]. It is found that the intensity increases exponentially at earlier time around the zero reference time then decays with relative slow time constants. The characteristic time of 90 and 98 % of the pulse charge are contained, were evaluated to be 14.0 ± 0.2 ps and 27.0 ± 0.2 ps, respectively.

The decay constant of 4.6 ps ± 0.2 ps was derived by the fitting procedure. This value could be understood by assuming the electron diffusion constant of 7 cm^2/s [5]. Then it is confirmed that the electron emission process from the PC is mainly dominated by the electron diffusion process in the semiconductor.

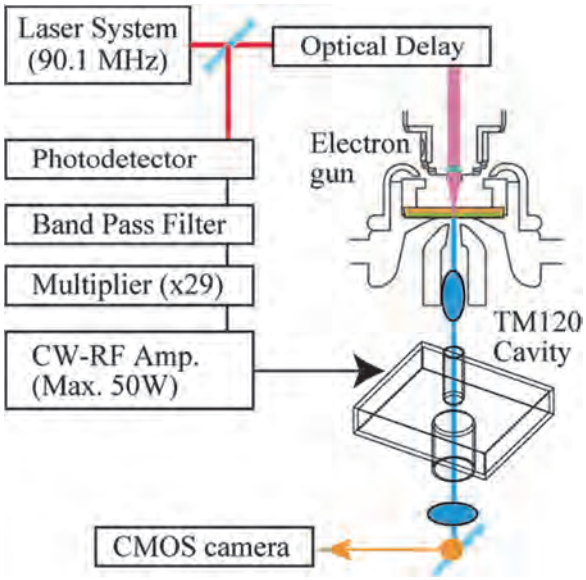

Fig. 1. Schematic view of the measurement system and timing diagram.

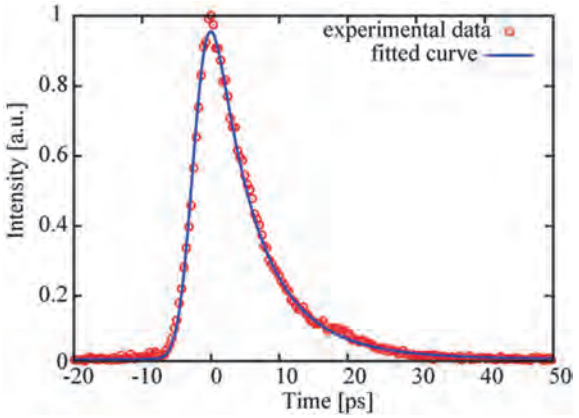

Fig. 2. Measured temporal charge distribution and the fitted decay curve (solid line).

[1] T. Inagaki, UVSOR Activiy Report **42** (2014) 33.
[2] T. Niwa, master's thesis, Nagoya University (2013).
[3] X. G. Jin, F. Ichihashi, A. Mano, *et. al*., JJAP **51** (2012) 108004.
[4] N. Yamamoto *et. al*., Proc. of the 13th Annual Meeting of PASJ (2016) WEPMY039.
[5] X. G. Jin *et. al*., Ultramicroscopy **130** (2013) 44.

Light sources

Angular Momentum Carried by Radiation from an Electron in Circular Motion

M. Katoh[1, 2], M. Fujimoto[1, 2], H. Kawaguchi[3], K. Tsuchiya[4], K. Ohmi[4], T. Kaneyasu[5], Y. Taira[6], M. Hosaka[7], A. Mochihashi[7] and Y. Takashima[7]

[1]*Institute for Molecular Science, Okazaki 444-8585, Japan*
[2]*Sokendai (the Graduated University for Advanced Studies), Okazaki 444-8585, Japan*
[3]*Muroran Institute of Technology, Muroran 050-8585, Japan*
[4]*High Energy Accelerator Research Organization (KEK), Tsukuba 305-0801, Japan*
[5]*Saga Light Source, Tosu 841-0005 Japan*
[6]*National Institute of Advanced Industrial Science and Technology (AIST), Tsukuba 305-8568, Japan*
[7]*Nagoya University, Nagoya 464-0814, Japan*

Optical vortex or twisted photons possess spiral phase structure and carry orbital angular momentum other than spin angular momentum [1]. In these years, such strange photons can be produced by using lasers and special filters in laboratories and they are widely investigated towards applications on nano-, imaging, and information/communication technologies [2]. On the other hand, it was theoretically predicted that the harmonic components of helical undulator radiation has vortex nature possessing helical phase structures [3]. Later, this was experimentally verified [4, 5]. However, the origin of this interesting phenomenon has not been clearly discussed in these previous works.

Electrons in a helical undulator undergo a spiral motion in its periodic magnetic field. This motion can be decomposed to a drift motion with a relativistic velocity along the undulator and a circular motion. In this sense, the undulator radiation can be considered as radiation from an electron in circular motion but Lorentz-transformed to the laboratory frame. Because the phase of the electromagnetic field is Lorentz-invariant, the spiral phase structure seen in the undulator radiation should be found in the radiation from an electron in circular motion.

We have recently re-analyze the radiation from an electron in circular motion [6]. This is one of the most fundamental radiation processes as the basis of various important processes, such as cyclotron radiation, synchrotron radiation or electron scattering of circularly polarized light. This process has been addressed in many scientific papers and textbooks. However, its vortex nature has not been discussed explicitly in these literatures.

We started from the retarded potential. For the radiation from an electron in circular motion, we obtained the Fourier component of the vector potential as follows;

$$\vec{A}_l(\vec{r},t) = e\frac{e^{i(kr-l\omega t+l\phi)}}{r}\begin{pmatrix} J_l(l\beta\sin\theta) \\ \cot\theta J_l(l\beta\sin\theta) \\ i\beta J_l'(l\beta\sin\theta) \end{pmatrix}_{r\theta\phi} + o\left(\frac{1}{r^2}\right)$$

where J_l is the Bessel function, l is the harmonic number, k and ω the wave number and angular frequency, r, θ and φ the position of the observer in a spherical coordinate, β the electron velocity divided by the light velocity, e the elementary charge. It should be noted that the vector potential has a spiral phase term.

By using this result, we could obtain the ratio between the angular momentum and the energy carried by the radiation field. The result can be expressed as follows;

$$\frac{\left\langle \frac{dJ_{lz}}{dt} \right\rangle}{\left\langle \frac{dU_l}{dt} \right\rangle} = \frac{\frac{kl}{4\pi}\int r^2 d\Omega\left(A_{l\theta}^{(1)}A_{l\theta}^{(1)*} + A_{l\phi}^{(1)}A_{l\phi}^{(1)*}\right)}{\frac{ck^2}{4\pi}\int r^2 d\Omega\left(A_{l\theta}^{(1)}A_{l\theta}^{(1)*} + A_{l\phi}^{(1)}A_{l\phi}^{(1)*}\right)} = \frac{N_p\hbar l}{N_p\hbar l\omega}$$

where the denominator is the energy and the numerator is the angular momentum carried away by the radiation field for unit time. N_p the number of photons and $\hbar$ the reduced Plank constant. This equation indicates that n-th harmonic photon carries well-defined energy and angular momentum which are given by $\hbar\omega$ and $\hbar l$, respectively. Since the angular momentum along the axis of the drift motion is Lorentz invariant, the radiation field in the laboratory frame also possesses the well-defined angular momentum.

[1] L. Allen, M. W. Beijersbergen, R. J. C. Spreeuw and J. P. Woerdman, Phys. Rev. A. **45** (1992) 8185.
[2] G. Molina-Terriza, J. P. Torres and L.Torner, Nat. Phys. **3** (2007) 305.
[3] S. Sasaki and I. McNulty, Phys. Rev. Lett. **100** (2008) 124801.
[4] J. Bahrdt *et al*., Phys. Rev. Lett. **111** (2013) 034801.
[5] M. Hosaka *et al*., Proc. IPAC2016 (2016) 2036.
[6] M. Katoh *et al*., Phys. Rev. Lett. **118** (2017) 094801.

Others

Development of Large Grain Size Nuclear Emulsion for Cosmic-ray Radiography

A. Nishio[1], M. Moto[1], Y. Manabe[1], K. Kuwabara[1], K. Morishima[1, 2] and M. Nakamura[1, 3]
[1]*Graduate School of Science, Nagoya University, Nagoya 464-8602, Japan*
[2]*Institute for Advanced Research, Nagoya University, Nagoya, 464-8602, Japan*
[3]*Institute of Materials and Systems for Sustainability, Nagoya Universuty, Nagoya, 464-8602, Japan*

Cosmic ray radiography is the a new non-destructive inspection technique of large-scale constructions with cosmic ray muon. Cosmic ray muon has high penetrating power and it always comes from the whole sky. In the same way of taking a X-ray photograph, we can obtain integrated density of constructions which thickness are several tens to several hundreds. We had ever applied this technique to pyramids, nuclear reactors, volcanos, and so on [1].

In these observations, we used nuclear emulsion as a detector. Nuclear emulsion is a kind of photographic film and has sensitivity for ionizing radiation. The film record tracks of charged particle with angular accuracy under several mrad. Nuclear emulsion is made by coating emulsion gel on plastic base. In Nagoya University, started a emulsion gel production machine in 2010. It was enable us to develop new-type emulsion gel by ourself. Emulsion gel is mainly consisted by silver bromide crystal and gelatin.

We developed a Large Crystal Nuclear Emulsion for the purpose of improving sensitivity, contrast, and long-term characteristics. We have succeeded in producing nuclear emulsion with the diameter of silver bromide crystals at 350, 450, 800 nm, in addition to the conventional 200 nm one. Electron microscopic image of the silver bromide crystal are shown in Fig. 1. Optimum gold-sulfur sensitization was performed to each crystal size [2]. For the developing solution, XAA developer (FUJIFILM Co., Ltd.) was used. pH of the developing solution was optimally adjusted to each crystal size. Figure 2 shows the optical microscopic image of minimum ionized particle tracks. Table 1 shows the evaluation results of sensitivity (Grain Density) and noise (Fog Density). The volume occupancy of silver bromide was 30%.

We succeeded in increasing the sensitivity without changing the noise level compared to the conventional 200 nm one. Furthermore, as contrast improved as the crystal size was larger, it is suitable for future low magnification / wide field scanning.

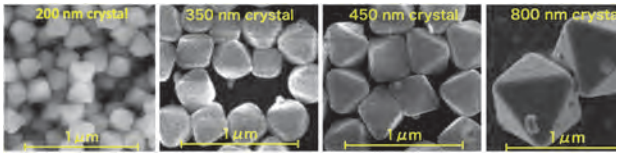

Fig. 1. Electron microscopic image of the conventional 200 nm silver bromide crystal and new-type 350, 450, 800 nm crystal (SEM image).

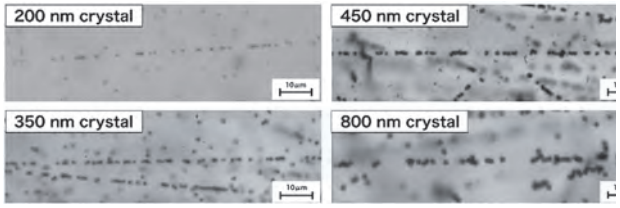

Fig. 2. Optical microscopic image of minimum ionized particle tracks. The larger the silver bromide crystals, the higher the contrast.

Crystal Size (nm)	200	350	450	
Grain Density (/100μm)	33.6 ± 2.6	42.0 ± 2.9	46.6 ± 3.1	(34.1 ±
Number of Crystal (/100μm)	225	129	100	
Crystal Sensitivity	0.15 ± 0.01	0.33 ± 0.02	0.47 ± 0.03	(0.61 ±
Fog Density(/1000μm³)	1.1 ± 0.2	0.9 ± 0.2	0.5 ± 0.1	0.7

Table 1. Sensitivity and noise of large crystal size nuclear emulsion. Sensitivity is evaluated by Grain Density (G.D) which is linear density of developed crystals. Noise is evaluated by Fog Density which is volume density of randomly developed crystals. G.D of 800 nm crystals was shown with parenthesis due to reproducibility problem.

[1] K. Morishima *et al.*, RADIATION DETECTORS AND THEIR USES (2012) 30.
[2] M. Moto *et al.*, 2nd Fall meeting of Federation of Imaging Societies (2015) 29.

BL1U

Design of NRF-CT Experimental Setup for 2D Isotope Imaging at BL1U

H. Zen[1], H. Ohgaki[1], Y. Taira[2], T. Hayakawa[3], T. Shizuma[3], I. Daito[4], J. Yamazaki[5], T. Kii[1], H. Toyokawa[2] and M. Katoh[5, 6]

[1]*Institute of Advanced Energy, Kyoto University, Uji 611-0011, Japan*
[2]*National, Institute of Advanced Industrial Science and Technology, Tsukuba 305-8560, Japan*
[3]*National Institutes for Quantum and Radiological Science and Technology, Tokai 319-1195, Japan*
[4]*Nippon Advanced Technology Co., Ltd., Amagasaki 661-0001, Japan*
[5]*UVSOR Facility, Institute for Molecular Science, Okazaki 444-8585, Japan*
[6]*School of Physical Sciences, The Graduate University for Advanced Studies (SOKENDAI), Okazaki 444-8585, Japan*

Three-dimensional isotope imaging is an emerging technology which has very wide applications in areas of nuclear security, non-destructive inspection, nuclear plant decommissioning and so on. A novel method named as Nuclear Resonance Fluorescence Computer Tomography (NRF-CT) which will enable us to measure the three-dimensional isotope image of a shielded target has been proposed [1-3]. Most nuclei can be resonantly excited by the absorption of a gamma-ray. The excited nucleus de-excites to the ground state by the emission of a gamma-ray with the same energy. This sequential process is called NRF. Because each isotope has characteristic NRF energy levels, the isotopes can be identified by measuring NRF energies. The proposed method in [1-3] utilizes the resonance attenuation induced by photon- absorption in a sample target and thus available for imaging application directly. In this study, we designed a setup for the first demonstration experiment of the two-dimensional isotope imaging of ^{208}Pb by the NRF-CT method at BL1U.

At first, we designed a test sample target as shown in Fig. 1. The test target consists of an 8-mm-diameter natural lead rod and a 10-mm-diameter iron rod wrapped by a 30-mm-diameter aluminum cylinder and a 35-mm-diameter iron cylinder.

Next, the imaging measurement setup was designed as shown in Fig. 2. The flux of the incident and transmitted gamma-rays will be monitored by a plastic scintillation detector (PL) and a $LaBr_3$(Ce) scintillation detector (LB), respectively. The NRF gamma-rays from a witness target (WT) with a ^{208}Pb excitation energy of 5292 keV will be measured by two high purity germanium detectors (HPGe). When the same isotopes in the witness target (^{208}Pb in this case) exist on the gamma-ray beam path between the gamma-ray source and the witness target, the gamma-ray with the energy of 5292 keV is resonantly attenuated by the photon-absorption. The amount of the resonant attenuation can be evaluated from the variation of the NRF yield measured by the HPGe detectors and the transmittance of non-resonant gamma-rays measured by the $LaBr_3$(Ce) detector [1]. The sample target is placed on a three-axis movable stage which can change the horizontal position, vertical position, and rotation angle. To obtain a CT image, the amount of the resonant attenuation will be measured by changing the position and angle of the sample target.

By using the designed sample target and experimental setup, a 2D image of the ^{208}Pb contained in the lead rod shielded by the iron cylinder and the aluminum cylinder will be measured in forthcoming experiment.

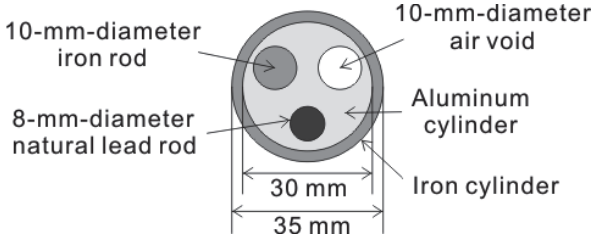

Fig. 1. Schematic diagram of the designed sample target.

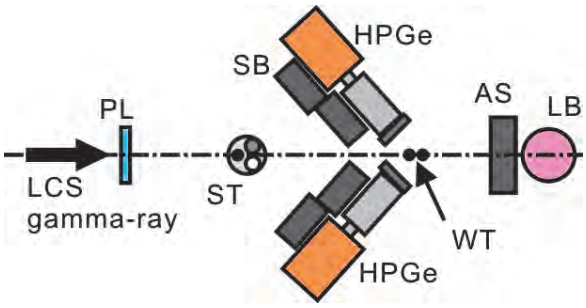

Fig. 2. Designed setup of the NRF-CT 2D isotope imaging experiment. PL: Plastic scintillation detector, ST: Sample target, SB: Shielding block, HPGe: High purity germanium detector, WT: Witness target, AS: Absorber, LB: $LaBr_3$(Ce) scintillation detector.

[1] C. P. Barty *et al*., LLNL-CONF-515893 (2011).
[2] W. Bertozzi and R. J. Ledoux, US Patent 8180019 B2 (2012).
[3] I. Daito *et al*., Energy Procedia **89** (2016) 389.

BL1U

Observation of Longitudinal Coupled Bunch Instability in UVSOR Storage Ring

A. Mochihashi[1], J. Hasegawa[2], M. Hosaka[1], M. Fujimoto[4, 5], Y. Takashima[1, 2], K. Imao[2], K. Takahashi[3] and M. Katoh[4, 5]

[1]*Synchrotron Radiation Research Center, Nagoya University, Nagoya 464-0814, Japan*
[2]*Graduate School of Engineering, Nagoya University, Nagoya 464-0814, Japan*
[3]*School of Engineering, Nagoya University, Nagoya 464-0814, Japan*
[4]*UVSOR Facility, Institute for Molecular Science, Okazaki 444-8585, Japan*
[5]*School of Physical Sciences, The Graduate University for Advanced Studies (SOKENDAI), Okazaki 444-8585, Japan*

In UVSOR electron storage ring, we have longitudinal coupled bunch instability in multi-bunch operation. To suppress the instability, we have used a 3rd harminic cavity (HCV) whose resonant frequency is 270.3 MHz, and almost Landau-damped the harmful instability. However, the source of the instability has not yet been completely understood. Moreover, we now plan to fabricate a new HCV because of overage problem such as vacuum failure. For the new HCV, we have started to investigate the source of the beam instability and estimate systematically the Landau damping effect of HCV. As one of the leading candidates of an impedance source for the londitudinal coupled bunch instability, we have pointed out a higher order mode (HOM) in the HCV. According to the 2-demensional electromegnetic simulation by Superfish [1], R/Q value for TM010 mode is 149; on the other hand, the R/Q for TM020 mode (780 MHz) is 13 which is not negligible value.

To investigate this, we have observed the longitudinal coupled bunch instability in multi-bunch operation (uniform filling). In the experiment, we have used BL1U mirror port and observed a visible edge radiation from the bending magnet BM8 which is just upstream of the undulator U1. To observe temporal beam oscillation, we have used a dual time based streak camera (Hamamatsu, C5680). In the experiment, we have stored 300 mA beam and gradually decreased the beam current by a beam scraper. Because of the Landau damping of the passive HCV, the instability was suppressed up to about 150 mA; however, below 150 mA the beam induced voltage in the HCV decreased and the instability started. When the beam current was decreased further, the instability ceased below the beam current of 7.4 mA. Figure 1 shows the longitudinal profile of the bunches by the streak camera at the beam current of 300, 100 and 7.4 mA. In the experiment, the HCV was tuned moderately to suppress the instability in the higher beam current, and the tuner position was fixed. In the higher beam current, the Laudau damping by the beam induced voltage in the HCV overcomes the growth of the longitudinal coupled bunch instability; the balance turns over below 150 mA because the voltage in the HCV decreases and the Laudau damping effect becomes weak. In the weak beam current condition, the Laudau damping already becomes negligible but the growth rate of the instability also becomes small and comparable to the longitudinal radiation damping rate. We have estimated the growth rate of the longitudinal coupled bunch instability due to the HOM of the HCV at the weak beam edge of 7.4 mA. In the calculation we have applied LCR resonant cavity impedance model. The Q factor and the shunt impedance value were estimated by Superfish [1] calculation. The growth rate of the instability was estimated to be 64.3 [sec^{-1}] at 7.4 mA; on the other hand, the longitudinal radiation damping rate is 60.3 [sec^{-1}] which is comparable to the instability growth rate. From above estimation, it is supposed that the longitudinal coupled bunch instability at lower beam current condition is caused by the HOM in the HCV; however, we are now considering a possibility that the cause of the instability in higher beam current condition is different from that in lower beam current condition. To investigate this, we now plan systematic measurements for the characteristics of the Laudau damping by the HCV. Based on these measurements we plan to design and fabricate new HCV which can overcome the longitudinal coupled bunch instability in the wide range of the beam current condition.

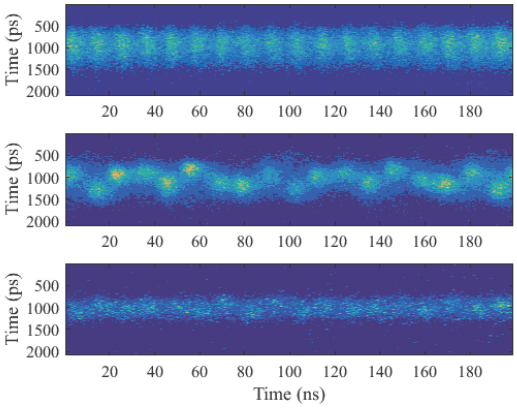

Fig. 1. Longitudinal coupled bunch instability in (upper)300 mA, (middle)100 mA and (lower)7.4 mA.

[1] K. Halbach and R. F. Holsinger, Particle Accelerators **7** (1976) 213.

BL2B

Evaluation of Photon Counting Capability of a High-Speed Back-Illuminated CMOS Sensor in a Soft X-ray Range of 0.8 keV – 4.5 keV

N. Narukage[1] and S. Ishikawa[2]

[1]*National Astronomical Observatory of Japan, Mitaka 181-8588, Japan*

[2]*Institute of Space and Astronautical Science, Japan Aerospace Exploration Agency, Sagamihara 252-5210, Japan*

The solar corona is full of dynamic phenomena. They are accompanied by interesting physical processes, namely, magnetic reconnection, particle acceleration, shocks, waves, flows, evaporation, heating, cooling, and so on. The understandings of these phenomena and processes have been progressing step-by-step with the evolution of the observation technology in EUV and X-rays from the space. But, there are fundamental questions remain unanswered, or haven't even addressed so far. Our scientific objective is to understand underlying physics of dynamic phenomena in the solar corona, covering some of the long-standing questions in solar physics such as particle acceleration in flares and coronal heating. In order to achieve these science objectives, we identify the imaging spectroscopy (the observations with spatial, temporal and energy resolutions) in the soft X-ray range (from ~0.5 keV to ~10 keV) is a powerful approach for the detection and analysis of energetic events [1]. This energy range contains many lines emitted from below 1 MK to beyond 10 MK plasmas plus continuum component that reflects the electron temperature.

The soft X-ray imaging spectroscopy is realized with the following method. We take images with a short enough exposure to detect only single X-ray photon in an isolated pixel area with a fine pixel Silicon sensor. So, we can measure the energy of the X-ray photons one by one with spatial and temporal resolutions. When we use a high-speed soft X-ray camera that can perform the continuous exposure with a rate of 1,000 times per second, we can count the photon energy with a rate of several 10 photons / pixel / second. This high-speed exposure is enough to track the time evolution of spectra generated by dynamic phenomena in the solar corona, whose lifetimes are about form several ten seconds to several minutes.

In this time, we evaluated the photon counting performance of a back-illuminated high-speed CMOS sensor, which is a key device of the high speed camera, in a soft X-ray range from 0.8 keV to 4.5 keV using the BL-2A as shown in Fig. 1. On the basis of this evaluation, we confirmed that this CMOS sensor has the enough photon counting (2D imaging spectroscopic) capability. So, we decided to use this sensor for the imaging spectroscopic observations of the solar corona in the soft X-ray range. This observation will be executed with the NASA's sounding rocket (FOXSI-3 project) in the summer of 2018.

[1] T. Sakao, N. Narukage, M. Shimojo, K. Watanabe, Y. Suematsu, S. Imada and S. Ishikawa, Proc. SPIE **8862** (2013) 12.

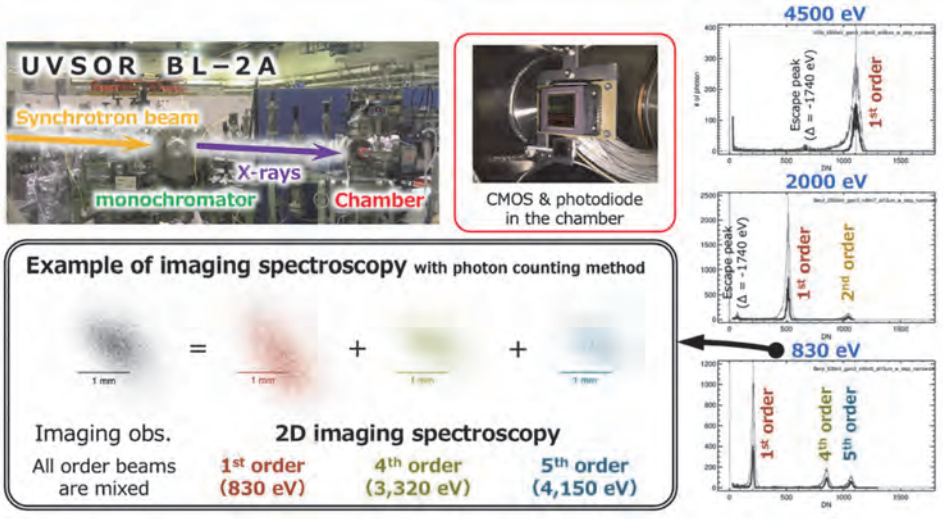

Fig. 1. Evaluation of the back-illuminated CMOS sensor. The CMOS was illuminated by the monochromatic X-rays (including higher-order diffraction lights). The right plots are the measured X-ray spectrum with the CMOS sensor using photon counting methods. The bottom panel is an example of imaging spectroscopy for 830 eV X-ray light. These results show that this CMOS has a capability of 2D imaging spectroscopy.

BL4U

Development of a 3-Dimensional Quantitative Observation Method in Scanning X-ray Transmission Microscopy

T. Ohigashi[1], Y. Inagaki[1], A. Ito[2], K. Shinohara[2] and N. Kosugi[1]
[1]*UVSOR Synchrotron, Institute for Molecular Science, Okazaki 444-8585, Japan*
[2]*School of Engineering, Tokai University, Hiratsuka 252-1292, Japan*

Computed Tomography (CT) is a powerful method by using X-rays to observe 3-dimensional internal structure of a sample without any destructive process. A reconstructed image of CT shows distributions of liner absorption coefficients (LACs). In the soft X-ray region, CT can be combined with X-ray microscopic techniques regarding the relationship between relatively short penetration depth of the soft X-rays and high spatial resolution. Generally, full-field imaging X-ray microcopy is used for performing CT because of its short measurement time. On the other hand, scanning transmission X-ray microscopy (STXM) has an advantage in tuning of the X-ray energy and is typically used to perform CT with limited-angle rotation to reduce the measurement time [1, 2] though this method loses quantitative values on the reconstructed images. We have been developing CT by using STXM with full-rotation (180° or 360°) to get quantitative values and performing 3-dimensional spectromicroscopy, though the working distance, which is defined by distance between an order select aperture and sample, is too short. We have overcome this difficulty by developing a special sample cell and adjusting an optical system of STXM and performed a feasibility test of CT.

A sample cell for full-rotation CT developed (Fig. 1) is equipped with a small two-phase stepping motor (AM-1020, Faulhaber) and a spur gearhead (12/5, Faulhaber) for the rotation of the sample. The samples are set on a tip of a needle and the needle is fixed by a clamp. Motion of the sample is controlled by a programmable stepping driver (AD PM 00, Faulhaber) via a feedthrough. Shape of the sample cell is compatible with ALS-based STXM systems.

Polystyrene spheres of diameter of 5 μm as a test sample were attached on a tip of a tungsten needle by glue. 50 STXM images (100×100 pixels, 150 nm step) were acquired with rotating the sample 3.6° each (180° rotation in total). Then, the X-ray energy of 280 eV, below the C K-edge, was used and dwell time was 3 ms. The STXM images were aligned manually and sinograms were extracted. 2-dimensional cross sectional image was reconstructed by using homemade convolution-backprojection algorithm with assuming parallel beam projection. The reconstructed cross sectional image and 3-dimensional volume image are shown in Figs. 2(a) and (b), respectively. The 3-dimensional volume image was obtained by stacking the cross sectional images. A histogram of LACs of the reconstructed image is shown in Fig. 2(c). A main peak at 0.173 μm^{-1} shows polystyrene and its FWHM is 0.016 μm^{-1}, 9.3% of the peak LAC. That FWHM degrades quality of spectrum in spectroscopy so it should be decreased. As perspective, a Fresnel zone plate with proper parameter should be used to obtain the STXM images with good quality and a number of the STXM images will be increased [3].

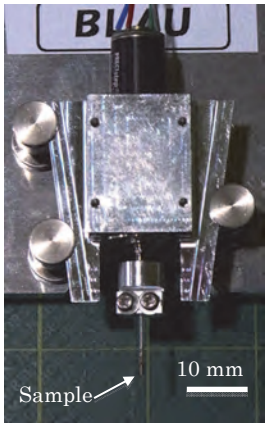

Fig. 1. The sample cell for CT

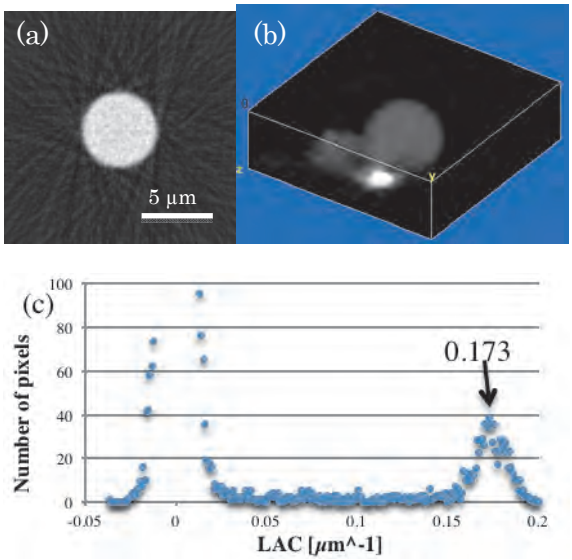

Fig. 2. Tomographic reconstructed images of polystyrene spheres, (a) a cross sectional image, (b) 3-dimensional volume image and (c) a histogram of LACs of the cross sectional image

[1] M. Obst, J. Wang and A. P. Hitchcock, Geobiol. **7** (2009) 577.
[2] V. Berejnov, D. Susac, J. Stumper and A. P. Hitchcock, ECS Transac. **50** (2012) 361.
[3] T. Ohigashi *et al.*, accepted.

BL5B

Performance Evaluation of C/Al/C Metallic Thin Filters for Observation of the Earth's Plasmasphere

M. Kuwabara[1], R. Hikida[2], F. Suzuki[2], K. Yoshioka[1, 2] and I. Yoshikawa[1]

[1]*Department of Complexity Science and Engineering, Graduate School of Frontier Sciences, The University of Tokyo, Chiba 277-8561, Japan*

[2]*Department of Earth and Planetary Science, Graduate School of Science, The University of Tokyo, Tokyo 113-0033, Japan*

A small telescope in extreme ultraviolet (EUV) named PHOENIX (Plasmaspheric Helium ion Observation by Enhanced New Imager in eXtreme ultraviolet) will be boarded on the world's smallest spacecraft to explore the Earth-Moon Lagrange point.

By flying far from the Earth, PHOENIX can obtain the entire image of the Earth's plasmasphere. The image from the equatorial plane helps us to understand the dynamics of plasmas along the magnetic field. The behavior of plasmas which is related to the solar activity is the key for understanding physics and evolution of the Earth's environment.

PHOENIX consists of an entrance mirror, metallic thin filter, photon counting detector (microchannel plates and resistive anode encoder), and electronics. The optical system is optimized for the emission line of He ion (wavelength of 30.4 nm), which is the important component of the Earth's plasmasphere. The column density of He ion along the field of view of the instrument can be obtained because the intensity of the emission is proportional to it under the assumption that observational region is optically thin. Therefore, the accuracies of the efficiencies of the optical system of the instrument are critical for estimation of the density and to achieve the scientific goals of our mission.

The contaminations from other sources (He I 58.4 nm, O II 83.4 nm, H I 121.6 nm and etc.) should be eliminated by the metallic thin filter. Therefore, the filter materials which provide high transmittance at the target wavelength of 30.4 nm, while attenuating the unwanted emissions are required. For the reason noted above, the C/Al/C (15 nm/165.2 nm/15 nm) filter was chosen for the PHOENIX mission [3].

In this experiment, we evaluated the transmittances of two C/Al/C filters (No.1 and 2) at the wavelengths of 30.4 nm and 58.4 nm by using the photo diode and the microchannel plates. In order to achieve the pure 30.4 nm and 58.4 nm lights, we installed an Al/Mg/Al filter and an Sn filter at the entrance of the SOR beam [1, 2, 4, 5].

The results are shown in Fig. 2 and the transmittances of C/Al/C filters are 16% and 2% at the wavelengths of 30.4 nm and 58.4 nm, respectively.

For the next step, in addition to the 30.4 nm line and 58.4 nm line, we plan to measure the transmittance at 83.4 nm line. O ion has an emission line at 83.4 nm and is known as one of the main components in the Earth's plasmasphere.

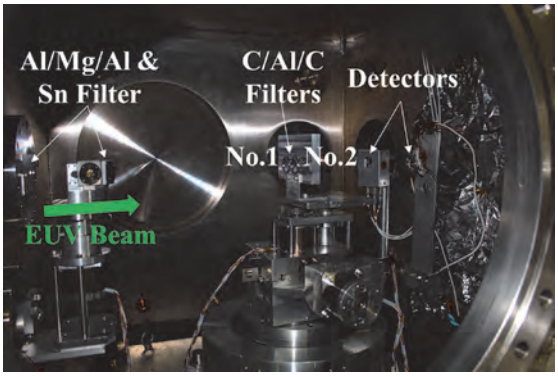

Fig. 1. The setup of the measurements. C/Al/C filters are installed on the central stage.

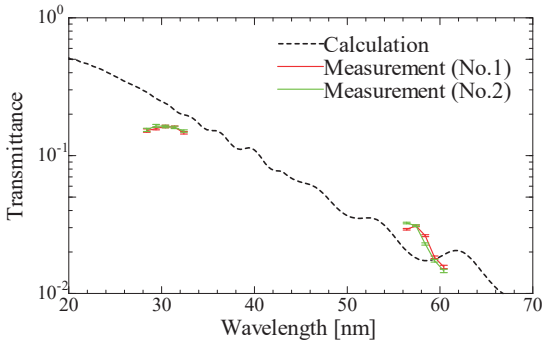

Fig. 2. The transmittances of two C/Al/C filters. The solid lines with dots show the results of the measurements and the dashed line shows the calculation.

[1] K. Yoshioka *et al.*, UVSOR Activity Report **35** (2007) 55.
[2] G. Ogawa *et al.*, UVSOR Activity Report **36** (2008) 127.
[3] I. Yoshikawa *et al.*, Earth Planets Space **60** (2008) 407.
[4] G. Murakami *et al.*, UVSOR Activity Report **37** (2009) 47.
[5] K. Sakai *et al.*, UVSOR Activity Report **38** (2010) 45.

BL6B

Feedback Stabilization of Synchrotron Radiation Beam Path at BL6B

H. Zen[1], T. Iizuka[2], F. Teshima[3], E. Nakamura[3] and K. Tanaka[3, 4]

[1]*Institute of Advanced Energy, Kyoto University, Uji 611-0011, Japan*

[2]*Toyota Technological Institute, Nagoya 468-8511, Japan*

[3]*UVSOR Facility, Institute for Molecular Science, Okazaki 444-8585, Japan*

[4]*School of Physical Sciences, The Graduate University for Advanced Studies (SOKENDAI), Okazaki 444-8585, Japan*

Beamline 6B (BL6B) is an Infrared-THz beamline which has confocal type micro-spectroscope station, reflection/transmission station, and IR microscope imaging station. This beamline can provide measurement techniques which are not available in conventional IR sources, utilizing the characteristics of synchrotron radiation (SR) such as high brilliance, polarization, or broad spectrum.

After the introduction of top-up operation of the UVSOR storage ring, serious long term drift of SR beam path in BL6B has been recognized. Our group has been investigated the cause of this long term drift of the SR beam path and found that the long-term drift of the M0 magic mirror angle is the main source of the drift [1]. In this study, a feedback control system of M0 mirror angle was developed for stabilizing the SR beam path in BL6B.

The schematic diagram of the feedback control system of the M0 mirror angle is shown in Fig. 1. A visible laser is injected into the vacuum chamber of bending magnet and reflected by the M0 mirror. The position of reflected laser light is monitored by a CCD camera. The CCD camera image is processed in a PC and the position of laser light is calculated from the image. The angle variation of the M0 mirror can be evaluated from the measured position of the reflected laser light. The angle of the M0 mirror can be controlled by stepping motors to keep the readout value of real-time angle monitor constant.

The feedback control system has been developed and demonstration experiments were conducted. The results are shown in Fig. 2 and Fig. 3. As shown in Fig. 2, the reflected laser light position, i.e. the M0 mirror angle, can be stabilized by using the developed feedback control during the 300-mA top-up operation of UVSOR. The small oscillation in Y direction was caused by the backlash. And then the SR intensity which is measured by an FT-IR spectrometer and an MCT detector can be also stabilized by using the feedback control as shown in Fig. 3.

After the successful demonstration, the developed feedback control system is routinely operated to supply stable SR beam for user experiments. This feedback system has already significantly increased the usability of BL6B beamline.

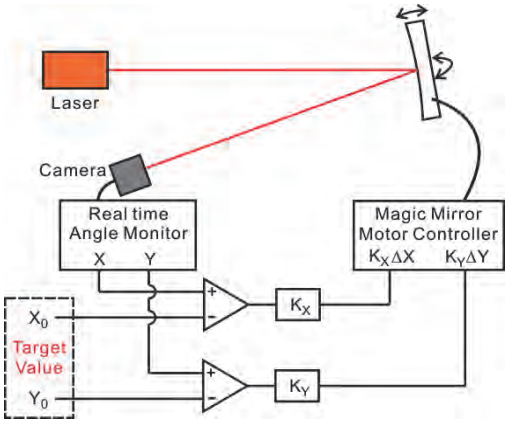

Fig. 1. Schematic diagram of the feedback control system of M0 mirror angle.

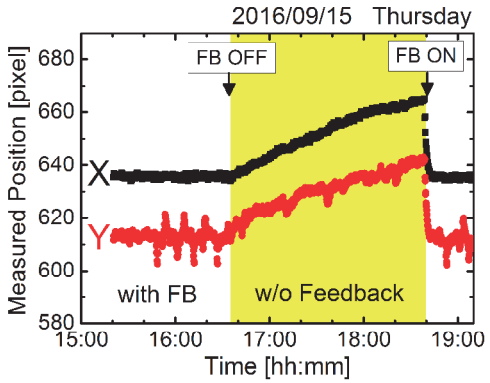

Fig. 2. The stability of the reflected laser position with and without feedback control.

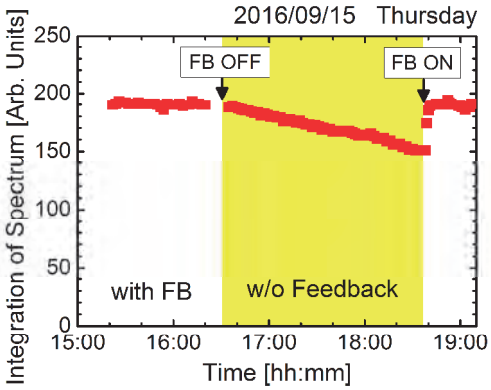

Fig. 3. The stability of SR intensity with and without feedback control.

[1] T. Iizuka *et al.*, UVSOR Activity Report **43** (2016) 38.

BL7B

Characterization of Optical Components for Polarization Spectroscopy at the Large Helical Device

M. Goto[1, 2, 3], N. Nimavat[2], R. Makino[1, 2], T. Oishi[1, 2] and R. Kano[3]
[1]*National Institute for Fusion Science, Toki 509-5292, Japan*
[2]*Department of Fusion Science, SOKENDAI, Toki 509-5292, Japan*
[3]*National Astronomical Observatory of Japan, Mitaka 181-8588, Japan*

Excitation due to anisotropic collisions gives rise to an inhomogeneous population distribution over the magnetic sublevels of ions in plasma, and emission lines from those ions are generally polarized. When Larmor motion of electrons in a plasma for the nuclear fusion research of magnetic confinement are selectively accelerated by means of microwave injection, electrons could have a velocity distribution function (VDF) different in the parallel and perpendicular directions regarding the magnetic field. Because the confinement characteristics of electrons depend on their pitch angle with the magnetic field direction, the anisotropic VDF of electrons is one of the key issues which govern the performance of plasma confinement. However, no reliable method has been established for measuring the anisotropy in the electron VDF to date.

We launched a project to earn information on the anisotropy in the electron VDF in the Large Helical Device (LHD) at the National Institute for Fusion Science through detection of polarization in emission lines. The first observation target was the Lyman-α line of neutral hydrogen, the dominant constituent of the nuclear fusion plasma. It was fortunate that we could borrow optical components such as a 1/2-waveplate, a high reflectivity mirror, and a polarization analyzer developed and elaborately characterized in CLASP (Chromospheric Lyman- Alpha SpectroPolarimeter) project led by a group of National Astronomical Observatory of Japan [1]. These optics were incorporated into an existing spectrometer at LHD and actual measurements were started from February in 2017.

Some preliminary results have been already obtained and the measurement itself looks successful. However, there is a limitation in the Lyman-α line that its emissions are localized at the outermost boundary of the plasma and hence the results do not reflect the state in the plasma core region that is more important for the plasma confinement study. Therefore, in the next stage of our project, we plan to use a CIV line ($1s^2 2s\ ^2S_{1/2}$ - $1s^2 2p\ ^2P_{1/2,\ 3/2}$) at 154.9 nm instead of Lyman-α.

The best solution is naturally replacing all the optical components with those optimized at 154.9 nm, but that is unfortunately difficult with the presently available budget for the project. Instead, we only prepare a 1/2-waveplate for 154.9 nm and the high reflectivity mirror and the polarization analyzer optimized for Lyman-α are tentatively used for the CIV line measurement. In this case, characterization of these optical components at 154.9 nm is required.

We have therefore made measurements of the polarization-resolved reflectivity of the high reflectivity mirror and the polarization analyzer for 154.9 nm at BL7B of UVSOR. An example of the results is given in Fig. 1, which shows the dependence of the reflectivity on the incident angle of the p- and s-polarized lights at 154.9 nm for the polarization analyzer. It is found that Brewster's angle at this wavelength is approximately 56° while the incident angle in our measurement is 68°. The extinction ratio at 68° is approximately 0.2, which is rather large when it is recalled that linear polarizers available as a commercial product for visible light typically realize an extinction ratio of 10^{-4}. However, this relatively large extinction ratio just reduces the sensitivity and does not deny the possibility of the polarization detection. As for the high reflectivity mirror, the result shows that their reflectivity is about 0.8 at 154.9 nm and at the incident angle 23° used in our measurement.

We conclude from these results that a polarization measurement at 154.9 nm with using the optical components for Lyman-α is possible although the condition is not optimized. After detecting any sign of polarization in the CIV line at the LHD experiment, we will consider preparing a high reflectivity mirror and a polarization analyzer optimized at 154.9 nm.

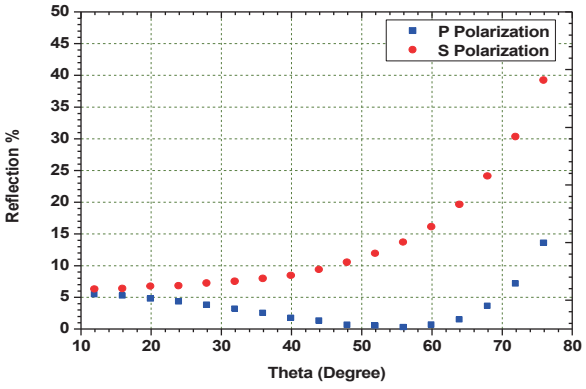

Fig. 1. Incident angle dependence of the reflectivity of p- and s-polarized lights at 154.9 nm for the polarization analyzer.

[1] UVSOR Activity Reports from 2009 to 2015.

BL7B

Axis Measurement of Polarizer and Waveplate for CLASP2 Light Source

R. Ishikawa, K. Shinoda, H. Hara, R. Kano and N. Narukage
National Astronomical Observatory of Japan, Mitaka 181-8588, Japan

The Chromospheric LAyer Spectro-Polarimeter 2 (CLASP2) is the second flight of the CLASP (Chromospheric Lyman-Alpha Spectro-Polarimeter, CLASP) sounding rocket experiment [1], which succeeded in the first measurement of the linear polarization signals in the hydrogen Lyman-α line (121.6 nm) emitted from the Sun (e.g., [2]). In CLASP2, we will measure all four Stokes parameters (i.e., intensity, two linear polarizations, and one circular polarization) in the Mg II h & k lines around 280 nm to obtain the magnetic field information in the upper solar chromosphere by refitting the existing CLASP instrument. After the integration, the polarization calibration of the instrument will be performed with a well-calibrated light source by feeding purely polarized light at least six different polarization states (four for linear polarization and two for circular polarization). The input light for the linear polarization will be produced with a linear polarizer of the transmissive type same as the sample that we tested before [3]. The input light for the circular polarization will be produced via a 1/4-waveplate installed immediately after the polarizer. The polarizer and waveplate are installed on the rotating motor and rotated to emit the different polarization state. For the precise polarization calibration, the direction of the principle axes of the polarizer and waveplate with respect to the instrument has to be known precisely.

We measured a relative angle between the polarizer (or waveplate) and motor at the UVSOR BL7B in the wavelength of 280 nm. Our goal is to measure the angle with the precision better than 0.1-degree. Figures 1 and 2 show the experimental setups for the polarizer and waveplate, respectively. Using a high-reflective (Hi-R) polarizer, the linearly polarized 280 nm beam in the horizontal direction was directed on to the waveplate/polarizer, and intensity modulation induced by rotating the waveplate/polarizer was measured with a photodiode. One example of the intensity modulation for the polarizer is shown in Fig. 3, where the measurement was done every 5-degree step of rotating motor. The principle axis of the analyzer can be represented by the angle where the intensity becomes minimum (vertical dashed line in Fig. 3), and the relative angle with respect to the motor is estimated to be 45.0-degree. We performed the same measurement at several times, and found that the repeatability is quite good (the angle differences between the measurements are less than 0.1-degree). The waveplate axis was also measured with the same accuracy. Therefore, we conclude that the waveplate and polarizer angles are successfully measured with the accuracy less than our requirement.

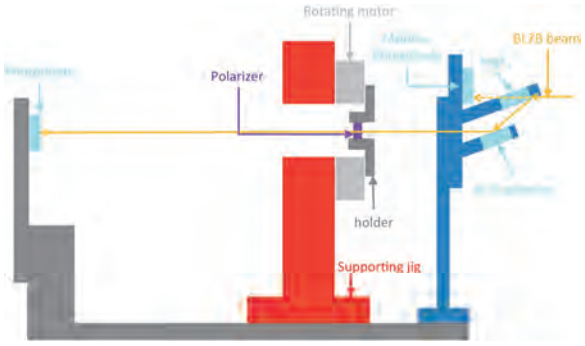

Fig. 1. Experimental setup for the polarizer axis measurement.

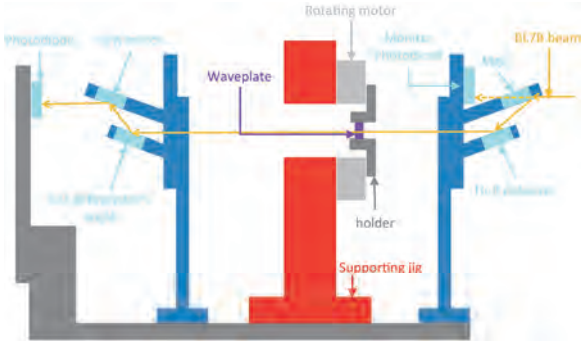

Fig. 2. Experimental setup for the waveplate axis measurement.

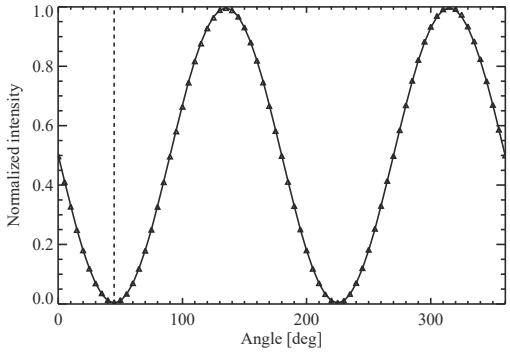

Fig. 3. Example of the intensity modulation for the polarizer axis measurement. Triangles show the measurement and solid line shows the result of fitting.

[1] N. Narukage *et al.*, UVSOR Activity Report **43** (2016) 31.
[2] R. Kano *et al.*, ApJ, in press
[3] R. Ishikawa *et al.*, UVSOR Activity Report **43** (2016) 40.

BL7B

Stokes Parameters Measurements of the Beamline BL7B by Using VUV Ellipsometry

Y. Fujii[1], Y. Nasu[1], K. Fukui[1], K. Yamamoto[2], T. Saito[3] and T. Horigome[4]
[1]*Department of Electrical and Electronics Engineering, University of Fukui, Fukui 910-8507, Japan*
[2]*Far-infrared region Development Research Center, University of Fukui, Fukui 910-8507, Japan*
[3]*Department of Environment and Energy, Tohoku Institute of Technology, Sendai 982-8577, Japan*
[4]*UVSOR Facility, Institute for Molecular Science, Okazaki 444-8585, Japan*

Ellipsometers are known as powerful tools to determine optical constants of materials. However, because no solid materials can have transparency in the vacuum ultraviolet (VUV) region, an ellipsometer in VUV region must consist of both reflection type polarizer and analyzer in vacuum. Since these requirements make it difficult to construct VUV ellipsometers, there exists only one beamline (at BESSY) equipped with VUV spectroscopic ellipsometer (SE) [1] in the world to our knowledge. Saito et al. proposed the other idea for VUV SE, which is dedicated to the synchrotron radiation (SR) and used an oblique incidence detector [2, 3]. Although this type of SE requires much longer measuring time than that of the standard SE, this type of SE has an advantage in obtaining not only optical constants of the sample through the sample ellipsometric parameters, Ψ and Δ, but also both detector Ψ and the Stokes parameters of the incident beam, which are completely independent of the ellipsometric parameters of the sample. In this report, we focus on the photon energy dependence of these sample independent parameters at each sample measurement, specifically an Au mirror (standard sample), two bulk AlN substrates with different surface roughness.

Figure 1 shows ellipsometric angles Ψ and Δ of Au mirror. Multiple measurement results are plotted and each color corresponds to the BL7B conditions: the combination of the grating (G_1 - G_3) and low energy pass filter (blank, LiF_2 crystal, Quartz plate, Pyrex glass, 530nm-cut LPF). Figure 1 represents that the reproducibility of this SE is within a few percentage except for G_2 region where there is a known problem and it will be fixed in the near future. Figure 2 shows the normalized S_1 at Au mirror and two bulk AlN substrates measurements as a function of the photon energy. Although noted variation in S_1 among samples is found in G_1 region, the very good fits are observed in G_3 region. The variation in short wavelength (G_1) region may be attributed to the scattering due to the surface roughness of samples. In contrast, good fits on S_1 in G_3 region independent of different samples prove not only the high measurement accuracy for the Stokes parameters, but also the reliability of the ellipsometric parameters of the sample.

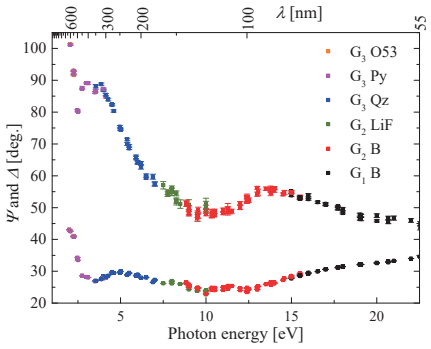

Fig. 1. Photon energy dependences of ellipsometric parameters of Au mirror.

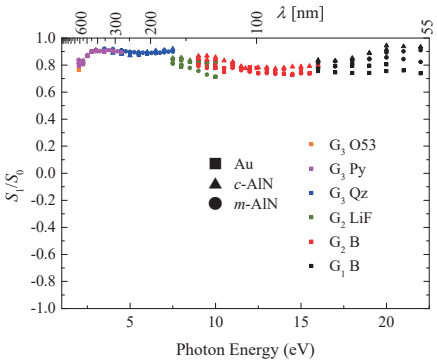

Fig. 2. Photon energy dependences of S_1/S_0 of multiple samples.

[1] W. Budde and R. Dittmann, PTB-Mitt. **83** (1973) 1.
[2] T. Saito, M. Yuri and H. Onuki, Rev. Sci. Instrum. **66** (1995) 1570.
[3] T. Saito, K. Ozaki, K. Fukui, H. Iwai, K. Yamamoto, H. Miyake and K. Hiramatsu, Thin Solid Films **571** (2014) 517.

UVSOR User 3

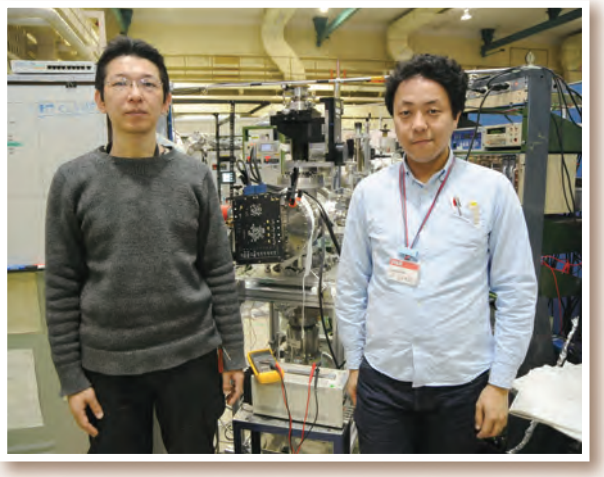

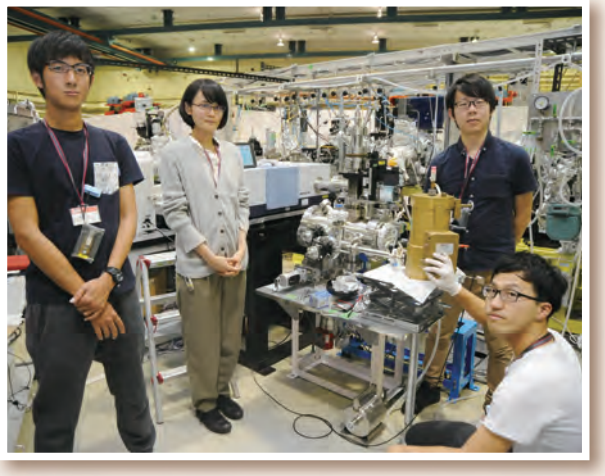

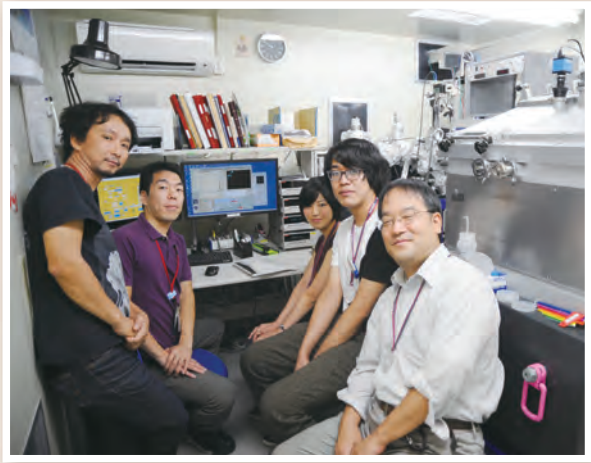

UVSOR User 4

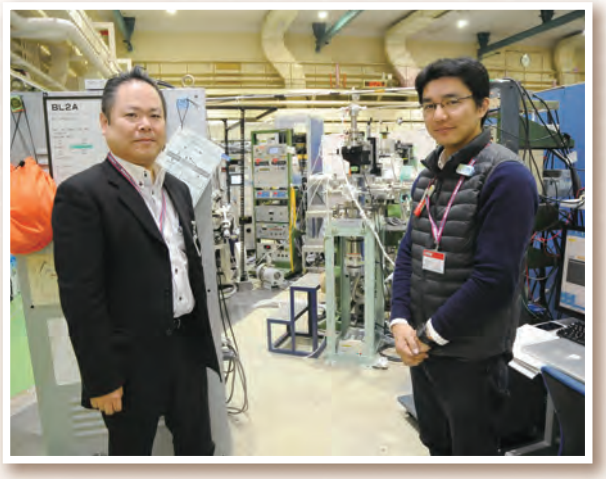

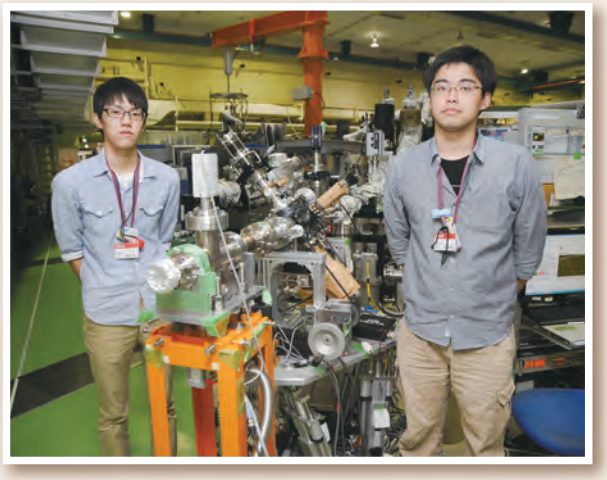

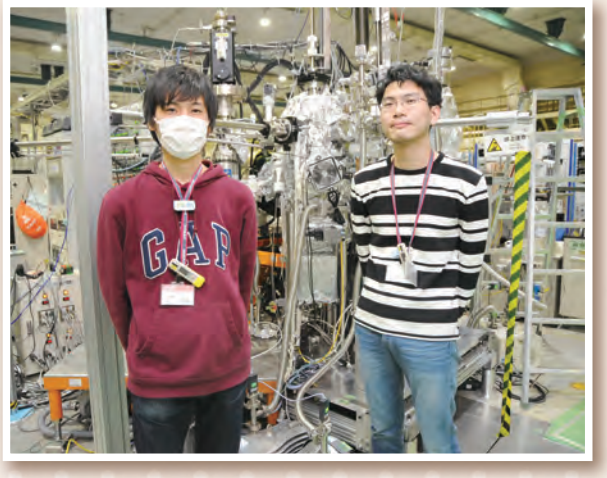

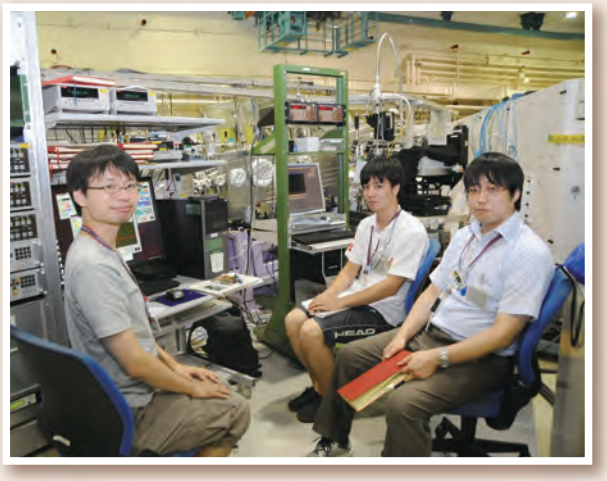

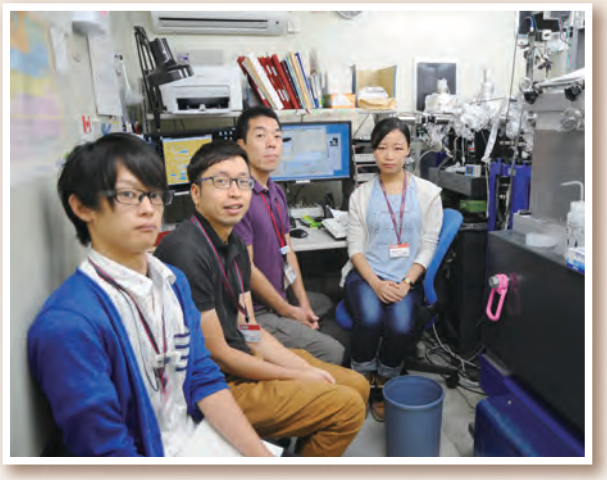

Ⅲ-2

Materials Sciences

BL1B

Terahertz Spectroscopy of Ionic Liquids

T. Awano
Faculty of Engineering, Tohoku Gakuin University, Tagajo 985-8537, Japan

We have observed millimeter wave absorption bands in AgI-superionic conductive glasses previously [1,2]. These bands were also observed in CuI-superionic glasses at slight different peak positions[3]. These bands seems to be due to collective motion of conductive ions, although how conduction ions moves in correlation is not clear.

Ionic liquid is molten salt at room temperature because of large radius of component ions. Figure 1 shows molecular structures of [DEME] (a) and [Tf_2N] (b). It is interesting to compare ionic motion in ionic liquids with those in superionic conductor for investigation of dynamics of mobile ions. In superionic conducting glasses, only cation is movable.

Temperature dependence of absorption spectra of ionic liquids in spectral range between 20 to 60 cm^{-1} have measured to investigate change of dynamics of ions in process of change of state from liquid to solid. Transmittance spectra of one and two filter papers with the ionic liquid of the same quantity per the paper were measured. Absorption spectra were obtained by subtracting each other. To eliminate interference structure remaining in the spectra, absorption difference spectra between each spectrum and that at 86 K are shown in Figs. 2 and 3.

There observed some slight structures in the absorption spectra in terahertz region contrary to the previously reported THz-TDS result[4]. Temperature dependence of the absorption spectra showed similar tendency as the results in the millimeter wave region, that were obtained using coherent millimeter wave at the LINAC of the Kyoto University Research Reactor Institute[5]. Absorption intensity of [DEME][BF_4], which becomes solid (crystal) under 282 K, drastically decreased at that temperature. On the other hand, that of [DEME][Tf_2N], which becomes solid (glass) under 182 K decreased gradually. Absorption intensity of all other ionic liquids measured in this study decreased like these ones, concerning with the transition temperature of melting point or glass transition temperature.

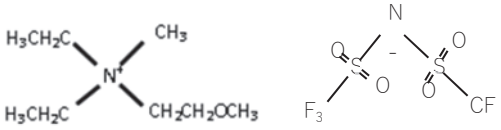

Fig. 1. Ionic structures of [DEME] (a) and [Tf2N] (b).

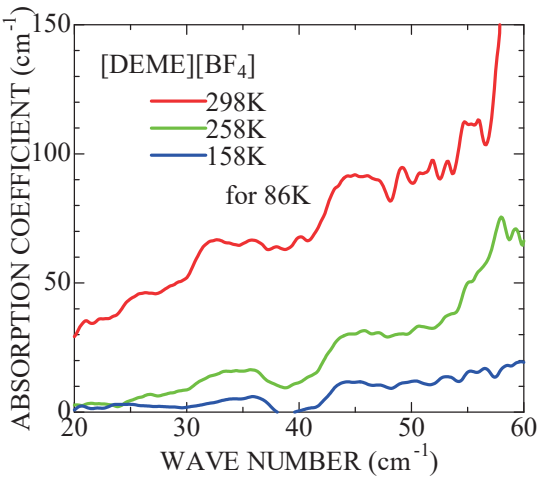

Fig. 2. Absorption increment spectra of [DEME] [BF_4] against the absorption spectrum at 86 K.

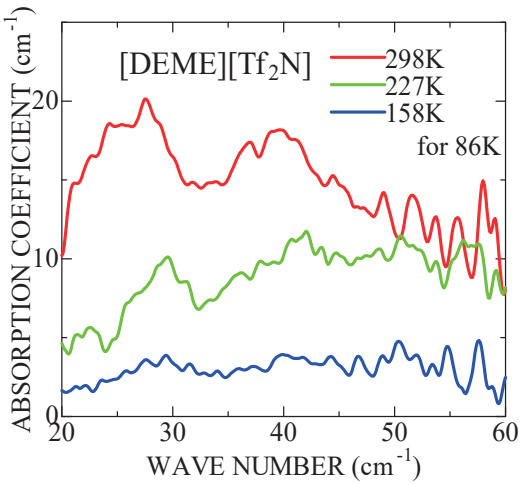

Fig. 3. Absorption increment spectra of [DEME] [Tf_4N] against the absorption spectrum at 86 K.

[1] T. Awano and T. Takahashi, J. Phys. Conf. Ser. **148** (2009) 012040.
[2] T. Awano and T. Takahashi, J. Phys. Soc. Jpn. **79** (2010) Suppl. A, 118.
[3] T. Awano and T. Takahashi, Proc. 13th Asian Conf. Solid State Ionics (2012) 569.
[4] T. Yamada, Y. Tominari, A. Tanaka and M. Mizuno, J. Phys. Chem. B **119** (2015) 15696.
[5] T. Awano and T. Takahashi, KURRI Prog. Rep. 2015, CO4-1.

BL1B

Optical Conductivity Spectra of Electron- and Hole-doped Anisotropic Kondo Semiconductor $CeOs_2Al_{10}$ in the THz Region

S. Kimura[1, 2], H. Takao[2], J. Kawabata[3], Y. Yamada[3] and T. Takabatake[3, 4]

[1]*Graduate School of Frontier Biosciences, Osaka University, Suita 565-0871, Japan*
[2]*Department of Physics, Graduate School of Science, Osaka University, Toyonaka 560-0043, Japan*
[3]*Department of Quantum Matter, ADSM, Hiroshima University, Higashi-Hiroshima 739-8530, Japan*
[4]*Institute for Advanced Materials Research, Hiroshima University, Higashi-Hiroshima 739-8530, Japan*

An anisotropic Kondo semiconductor $CeOs_2Al_{10}$ exhibits an unusual antiferromagnetic order at rather high transition temperature T_0 of 28.5 K [1]. Two possible origins of the magnetic order have been proposed so far, one is the Kondo coupling of the hybridization between the conduction (c) and the 4f states and the other is the charge-density wave/charge ordering along the orthorhombic b axis [2,3]. To clarify the origin of the magnetic order, we have investigated the electronic structure of hole- and electron-doped $CeOs_2Al_{10}$ [$Ce(Os_{1-y}Re_y)_2Al_{10}$ and $Ce\sigma$ $(Os_{1-x}Ir_x)_2Al_{10}$, respectively] by using optical conductivity [$\sigma(\omega)$] spectra along the b axis.

$\sigma(\omega)$ spectra, which were derived from the Kramers-Kronig analysis of reflectivity spectra, along the b axis at $T = 10$ K in $\hbar\omega < 100$ meV are shown in Fig. 1(a). In this region, it should be noted that a very sharp peak owing to a transverse optical phonon is observed at around 25 meV in all samples. Except for the sharp peak, one Drude component owing to carriers and three interband transition peaks are observed in all samples.

To clarify the change of the spectra by increasing x and y, we adopt the Drude-Lorentz fitting method. The $\sigma(\omega)$ spectra are fitted by using the combination of one Drude and three Lorentz functions. The obtained values of the effective electron number N^* together with T_0 and γ are plotted in Fig. 1(b) as functions of Re (y) and Ir (x) concentrations. Firstly, the carrier density (N^* of Drude component) is almost proportional to the electron specific heat coefficient γ. Secondly, the intensity of the c-f hybridization gap (N^* of $\Delta_{c\text{-}f}$) at $\hbar\omega$ ~ 50 meV continuously decreases from $y = 0.10$ to $x = 0.12$ via $x = y = 0$. On the other hand, the intensity of the charge excitation (N^* of Δ_0) observed at $\hbar\omega$ ~ 20 meV has the maximum at $x = y = 0$ as similar with the doping dependence of T_0. The fact that the charge excitation is strongly related to the magnetic order strengthens the possibility of the charge density wave/charge ordering as the origin of the magnetic order [4].

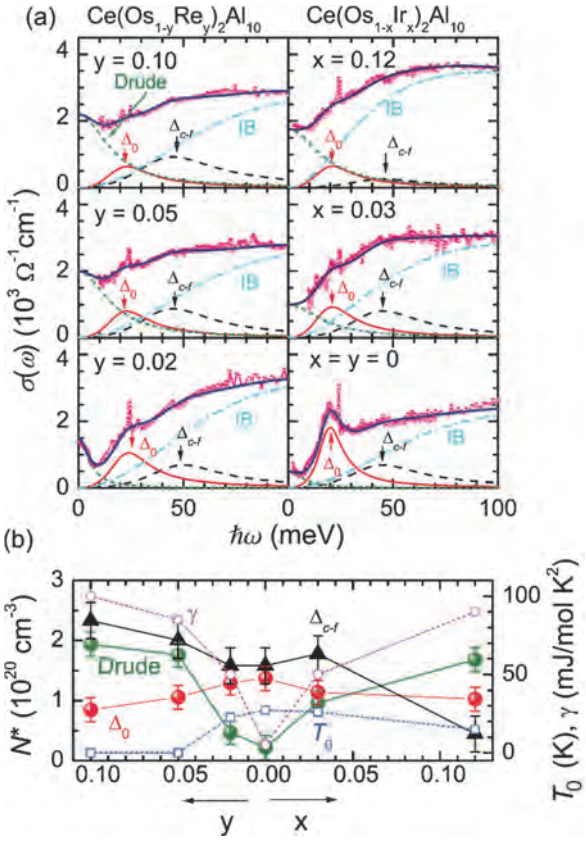

Fig. 1. (a) $\sigma(\omega)$ spectra along the b axis at $T = 10$ K and the fitted lines of one Drude and three Lorentz functions. The three Lorentz functions are assumed as a peak (Δ_0, solid line) appearing below the magnetic ordering temperature T_0, the interband transition in the c-f hybridization gap ($\Delta_{c\text{-}f}$, dashed line), and higher interband transition from lower energy side (IB, dot-dashed line). (b) Obtained effective electron numbers (N^*s) of the Drude, Δ_0, and $\Delta_{c\text{-}f}$ components, which are plotted together with T_0 and the electronic specific heat coefficient as functions of the Re (y) and Ir (x) concentrations.

[1] A. M. Strydom, Physica B **404** (2009) 2981.
[2] S. Kimura, T. Iizuka, H. Miyazaki, A. Irizawa, Y. Muro and T. Takabatake, Phys. Rev. Lett. **106** (2011) 056404.
[3] S. Kimura, T. Iizuka, H. Miyazaki, T. Hajiri, M. Matsunami, T. Mori, A. Irizawa, Y. Muro, J. Kajino and T. Takabatake, Phys. Rev. B **84** (2011) 165125.
[4] T. Yoshida, T. Ohashi and N. Kawakami, J. Phys. Soc. Jpn. **80** (2011) 064710.

BL2A

Local Structural Evaluation of Alloy Nitrides Extracted by Electrolytic Extraction Method

M. Sato
Institute for Materials Research, Tohoku University, Sendai 980-8577, Japan

It is well known that the martensite phase obtained by quenching is hard but brittle. Therefore the balance between hardness and toughness is adjusted by the subsequent tempering treatment. At that time, cementite is precipitated in case carbon steel, and Fe_4N is precipitated in case of nitrogen steel [1, 2].

Although it is known that alloying elements partially dissolve in solid solution in these precipitates, there is little knowledge on the chemical state of these substitution elements in the precipitates. In this study, changes in the chemical state of the substitutional elements before and after tempering treatment were investigated by XAFS measurement.

Fe-1mass%Si and Fe-1mass%Mo alloys were used as starting materials. They were homogenized at 1523 K for 24h and furnace-cooled until room temperature. Fe-1Mo-0.3N and Fe-1Si-0.3N alloys were prepared by nitriding and quenching process using NH_3/H_2 mixed gas at 1273 K for 1 h. Then Fe-1Mo-0.3N and Fe-1Si-0.3N alloys were tempered at 773 K for 1 h. and precipitates generated during tempering were extracted using Iodine-alcohol procedure. The Si K-edge and Mo $L_{Ⅲ}$-edge XANES spectra were corrected by fluorescence method using InSb double crystal monochrometer and silicon drift detector (SDD) at BL-2A in UVSOR, respectively. Obtained data were analyzed using Athena software.

Figure 1 shows Si K-edge XANES spectra of (a) ~ (c) references and (d) ~ (f) samples. Since the obtained spectrum from the as-quenched sample mainly had the similar shape with that of the Si powder (see Fig 1(a) and (d)), and it was suggested that Si atoms are substituted into the Fe structure. However, peak was observed around 1844 eV, which is consistent with the white line of SiO_2, suggesting a partial oxidation of sample. In case of the tempered sample, a new peak appeared around 1842 eV consistent with the white line of Si3N4 in addition to the above peaks. On the other hand, the spectrum of the extracted residue showed two peaks around 1842 and 1844 eV, and these peak positions were consistent with the white line of Si_3N_4 and SiO_2, respectively.

Figure 2 shows Mo $L_{Ⅲ}$-edge XANES spectra of (a) reference and (b) ~ (d) samples. No change in spectral shape was observed before and after tempering. This result indicate that local structure around Mo atom does not change by tempering treatment. However, the spectrum of the extracted powder sample showed chemical shift to the high energy side, implying the precipitation of Mo compounds. From this result, it was suggested that a trace amount of Mo is precipitating as compounds such as Mo nitrides etc. In the future, detailed examination will be carried out by analysis of the EXAFS region and calculation using FEFF code.

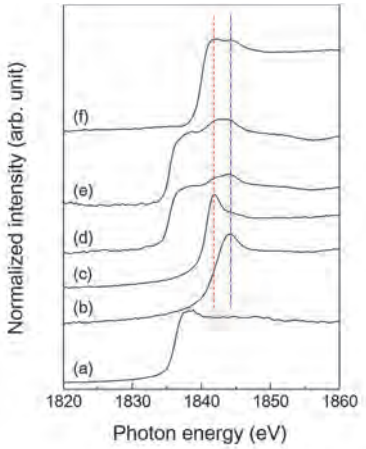

Fig. 1. Si K-edge XANES spectra of samples. (a) Si, (b) SiO_2, (c) Si_3N_4, (d) as quenched Fe-1Mo-0.3N alloy, (e) tempered Fe-1Mo-0.3N alloy and (f) extracted residue.

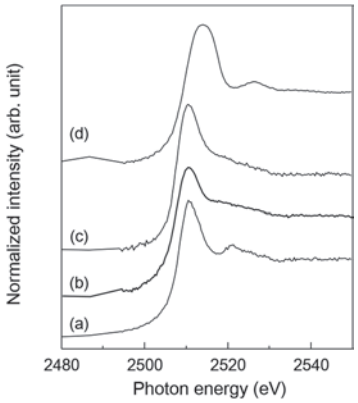

Fig. 2. Mo $L_{Ⅲ}$-edge XANES spectra of samples. (a) Mo foil, (b) as quenched Fe-1Mo-0.3N alloy, (c) tempered Fe-1Mo-0.3N alloy and (d) extracted residue.

[1] L. Cheng and E. J. Mittemeijer, Met. Trans. A **21A** (1990) 13.
[2] L. Cheng, A. Bottger and E. J. Mittemeijer, Met. Trans. A **23A** (1992) 1129.

BL2A

Characterization of MTB-Active Mo-Carbide Species Supported on H-MFI Catalysts by Mo L_{III}-edge XANES

H. Aritani[1], S. Mogi[1], R. Yamazaki[1], M. Akutsu[1], K. Kawashima[1], M. Tsutsumi[1] and A. Nakahira[2]

[1]*Graduate School of Engineering, Satama Institute of technology, Fukaya 369-0293 Japan*
[2]*Graduate School of Engineering, Osaka Prefecture University, Sakai 599-8531 Japan*

For direct conversion of LNG (Liquified natural gas) to useful organic compounds, Mo-modified H-MFI is a typical catalyst for MTB (Methane to Benzene) reaction, *i.e.*, methane dehydroarimatization. The MTB reaction is very unique and useful for industrial methane conversion, however, coke deposition over the catalyst cannot be avoided during the reaction.[1] At the same time, active Mo species should be changed structurally because of excess carburizaiton on both Mo species and acid sites of H-MFI.[2] For obtaining the durable MTB reactivity, the deactivation process over the catalysts is one of an important point to develop the industrial MTB catalysts. In this study, time course of the characterization of active Mo species for MTB (manly Mo_2C species) on H-MFI zeolites in various Si./Al_2 ratios is investigated by means of Mo L_{III}-edge XANES.

Catalyst samples were prepared by impregnation of each H-MFI (Si/Al_2=28 and 40) support with $MoO_2(acac)_2$–$CHCl_3$ solution (in 5wt% as MoO_3), and followed by dried and calcined at 773 K. The H-MFI supports were synthesized hydrothermally at 413 K for a week, and followed by ion-exchanging with NH_4Cl and calcined at 873 K. The catalytic MTB reactivity was evaluated by means of fixed-bed flow reaction at 1023 K, as described in a separate paper [1]. Mo L_{III}-edge XANES spectra were measured in BL2A of UVSOR-IMS in a total- electron yield mode using InSb double-crystal monochromator. Photon energy was calibrated by using Mo metal-foil, and normalized XANES spectra and their derivatives are presented. REX-2000 (Rigaku Co.) software was used by normalization of each XANES spectrum.

Figure 1 shows the time course of the Mo L_{III}-edge XANES spectra over MTB-active Mo/H-MFI (in Si/Al_2 ratios are 28 and 40) catalysts during the reaction. For Mo/H-MFI in Si/Al_2=28, higher MTB activity and lower deactivation are shown than in Si/Al_2=40. For these catalysts, edge energy of L_{III}-XANES becomes lower by proceeding the MTB reaction. This result indicates that a carbonization of molybdenum species advanced according to the reaction time. On the other hand, the MTB reactivity has been maximized at 30-55 minutes over Mo/H-MFI (Si/Al_2=28-40) catalysts. For the XANES spectrum, metallic Mo species can be seen at 30-90 minutes over these catalysts. The result suggests the formation of active Mo species as well-dispersed metallic ones. For Mo/H-MFI (Si/Al_2=40), the XANES spectra at 180 minutes (well-deactivated) shows the formation of α-Mo_2C species with higher edge energy than that of metallic one. In contrast, the XANES spectra of Mo/H-MFI (Si/Al_2=28) shows excess carbonized Mo species at 180 minutes. These results suggest the relationship between the formation of α-Mo_2C species and deactivation of Mo species for MTB reaction. For obtaining more details, metal-ion promoted Mo/H-MFI catalysts have been employed to characterize the highly active Mo species for MTB. This study is now in progress.

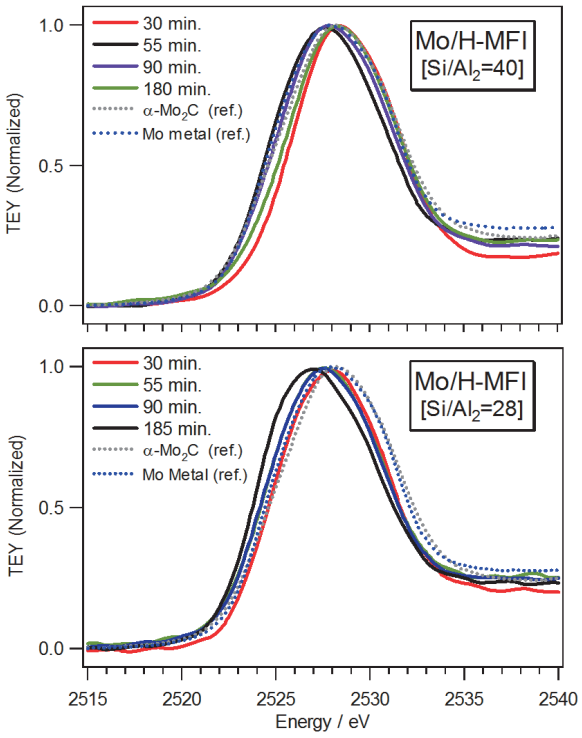

Fig. 1. Time course of the Mo L_{III}-edge XANES spectra over Mo/H-MFI [Si/Al_2 ratios are 28 (top) and 40 (bottom)] catalysts during the MTB reaction.

[1] H. Aritani, H. Shibasaki, H. Orihara and A. Nakahira, J. Environm. Sci. **21** (2009) 736.
[2] H. Aritani, S. Mogi, N. Naijo, T. Sugawara, A. Akutsu, K. Kawashima and A. Nakahira, UVSOR Activity Report **43** (2016) 49.

BL2A

XAS Analysis of Charge State of Eu in $Ba_2Eu_xBi_{(2-x)}O_6$ Double Perovskite

A. Kamata[1] and T. Yamamoto[1, 2]

[1]*Faculty of Science and Engineering, Waseda University, Tokyo 169-8555, Japan*

[2]*Institute of Condensed-Matter Science, Waseda University, Tokyo 169-8555, Japan*

Bithmus is an interesting elements, which can stably exist as various charge states, 3+ and 5+ for Bi. Especially, both of Bi^{3+} and Bi^{5+} can exist in one material, e.g., in $BaBiO_3$ with the ratio of Bi^{3+}:Bi^{5+} = 1:1. This is simply because of keeping the charge neutrality in the material. When the Bi^{3+} and Bi^{5+} exist periodically, say 3+,5+,3+,5+, …, superlattice should be constructed, one of which is shown in Fig. 1 drawn with VESTA [1]. This structure is called as double perovskite structured $BaBiO_3$. It was reported that this double perovskite structure can be stabilized with the doping of rare-earth ions. In the case of Ce doping, however, no double perovskite structure appeared. [2] Although it is essential to know substition site and charge state of doped rare-earth, such have not been clearly understood yet. In the current study, charge state of Eu ions in $BaBiO_3$ has been examined with Eu-M_5 X-ray absorption spectrum (XAS) measurements.

All the samples were fabricated with the solid-state reaction method. Reagent grade powders, $Ba(CO)_3$, Bi_2O3, Eu_2O_3 were ground and mixed in an agate mortar in air for 30 min. with ethanol, which were calcined at 1073 K for 6 hours in air. Resultant powders were ground and mixed again, which were pressed into a pellet form (10 mmϕ). These pellets were sintered in air at 1123 K for 12 hours.

Crystal structures of synthesized materials were examined by the conventional powder X-ray diffraction technique with Cu-Kα X-rays, which showed all the samples have double perovskite structure.

Eu-M_5 XAS were measured at BL2A in UVSOR with the total electron yield method. Samples powders were put on the carbon adhesive tape, which were attached on the first Cu-Be dinode of the electron mutiplier. Synchrotron beams were monochromatized with beryl (10-10)double- crystal monochrometar.

Observed Eu-M_5 XAS of Eu-doped $BaBiO_3$ are shown in Fig. 2 together with that of Eu_2O_3. All the Eu-M_5 XAS are almost identical and similar to that of Eu_2O_3. From the comparison with the standard oxide, in which Eu ions exist as trivalent, we can safely determine the charge state of the Eu ions in $BaBiO_3$ is trivalent.

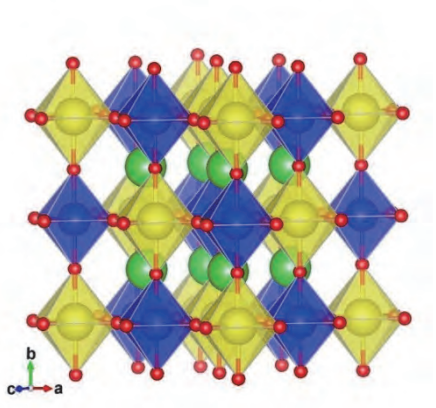

Fig. 1. Schematic illustration of double perovskite structured $BaBiO_3$. Green, blue, yellow and red balls denote Ba^{2+}, Bi^{3+}, Bi^{5+} and O^{2-} sites, respectively [1].

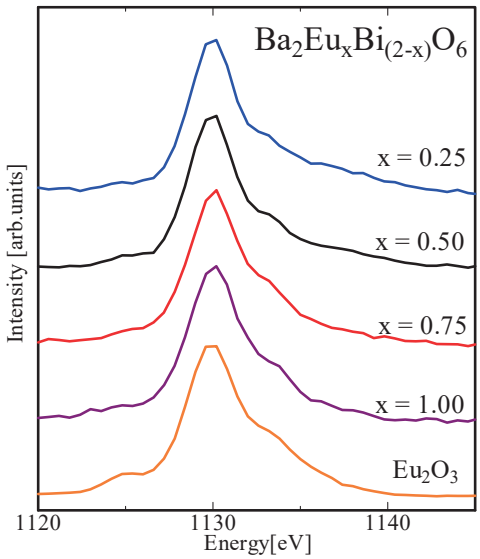

Fig. 2. Observed Eu-M_5 XAS spectra of $Ba_2Eu_xBi_{(2-x)}O_6$ and Eu_2O_3.

[1] K. Momma and F. Izumi, J. Appl. Crystallogr. **44** (2011) 1272.

[2] A. Matsushita *et al.*, Jpn. J. Appl. Phys. **51** (2012) 121802.

BL2A

Structural Evaluation of AlPO-5 with Si

A. Nakahira[1, 2], M. Togo[1], T. Takahashi[1], T. Minami[1], C. Takada[1], M. Matsumoto[1], M. Iida[1] and H. Aritani[3]

[1]*Faculty of Engineering, Osaka Prefecture University, Sakai 599-8531, Japan*
[2]*Trans-Regional Corporation Center for Industrial Materials Research (IMR), Tohoku University, Sakai 599-8531, Japan*
[3]*Saitama Institute of Technology, Fukaya 369-0293, Japan*

In recent years, the micro- and meso-porous inorganic materials attract much attention with growing concern about a lot of environmental problems. Although especially porous aluminophosphate (AlPO-n) is one of unique microporous materials, these materials have low catalytic ability. In order to achieve the catalytic activities of AlPO-n, various heterovalent elements have been incorporated into the framework of AlPO-n. These modified AlPO-n were generally found to incorporate negative charges in the framework, and extra-framework cations are present to balance the charges. For example, AlPO doped with Si, that is "SAPO-n", was synthesized to achieve the catalytic properties. In the so-called SAPO-n, a portion of P(V) is replaced by Si(IV). In special, SAPO-34 has attracted much attentions on the MTO (methanol to olefin) reaction because of high specific surface area, adsorptive capacities, and excellent catalytic activities.

The purpose in this study was to evaluate the local structure of SAPO-34 synthesized by the static hydrothermal process at 473 K using various starting materials and organic-structure-directing-agents (SDA) like tetraethylammonium hydroxide (TEAOH). The effect of synthetic condition parameters (starting materials, SDA, temperature, and time, etc) on the microstructure for various SAPO-34 samples was investigated.

All chemicals were analytical reagent-grade, and they used without further purification. The reagants used were γ-alumina, phosphoric acid, morpholine, and various silicon sources (TEOS, SiO_2, colloidal silica, and fumed silica etc). SAPO-34 were synthesized from starting gel with the composition of Al_2O_3 : P_2O_5 : TEAOH : SiO_2 : H_2O =1.0 : 1.6 : 4.0 : (0.3~0.6) : 140. γ-alumina was first mixed with TEAOH as a SDA and deionized water at room temperature. Various silica sources were then added into the mixture. Finally, phospholic acid was added dropwise to the resultant solution. The reaction mixture was further stirred for 1 h prior to being transferred into a stainless steel autoclave. The crystallization was conducted in an oven through the static hydrothermal process with preprogrammed heating profiles at 473 K for 24 h. In order to investigate the influence of hydrothermal synthetic conditions the samples were characterized. After all of the ground product powders were characterized by XRD method, FT-IR and TG-DTA. The microstructures of product powder were observed by SEM. The local structures around Si for the products of samples were characterized by measuring X-ray adsorption near edge structure (XANES) at BL02A in UVSOR.

The evaluation of XRD was carried out for various products synthesized by the static hydrothermal process. According to XRD results, products prepared by this hydrothermal process at 473K with the colloidal silica and fumed silica (0.3) as a silicon source and TEAOH as a SDA were identified to be SAPO-34. And similarly products with high contents of 0.6 for silica were composed of SAPO-34. Figure 1 shows the XANES spectra of various SAPO-34 samples with colloidal silica and fumed silica (0.6). As shown in Fig. 1, XANES spectra of sample obtained by hydrothermal process were quite similar. Furthermore, SAPO-34 with the high contents of colloidal silica and fumed silica as a silicon source were similar to SAPO-34 with low content of silica.

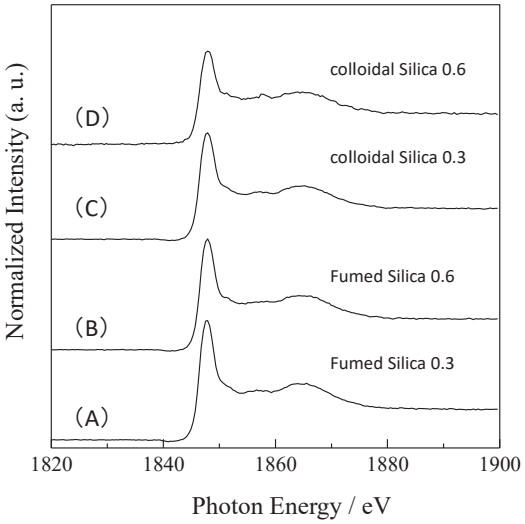

Fig. 1. Si-*K* XANES spectra of various products synthesized by the hydrothermal process at 473 K. (A) fumed silica of 0.3, (B) fumed silica of 0.6, (C) colloidal silica of 0.3, and (D) colloidal silica of 0.6.

BL2A

Soft X-ray Irradiation Effect on the Local Structural Deformation in a Molecular Conductor

T. Sasaki
Instutute for Materials Research, Tohoku University, Sendai 980-8577, Japan

It has been known that X-ray irradiation to the organic materials causes molecular defects and disorder. We have investigated the X-ray irradiation effect widely in the series of molecular materials κ-(BEDT-TTF)$_2$X showing superconductivity or Mott insulating state from the viewpoint of the relation between the correlated electronic states and randomness [1, 2]. Recently, we investigated the local structure deformation induced by X-ray irradiation in κ-(BEDT-TTF)$_2$Cu[N(CN)$_2$]Br using density functional theory based first-principles calculations [3]. The crystal structure is shown in Fig. 1. The calculations demonstrate that the structure change due to X-ray excitation can be predicted by introducing a core-hole at specific light atoms of anion molecules with infinite lifetime. Formation of the bond-shifted structure around dicyanamide group (NC-N-CN) in the anion layer was expected as a possible irreversible molecular defect leading to permanent irradiation damage.

In this study, soft X-ray irradiation experiments in organic conductor κ-(BEDT-TTF)$_2$Cu[N(CN)$_2$]Br was carried out in order to prove the calculation results. BL2A soft X-ray beamline was used for the irradiation. Beryl crystal was used for the monochromator at the soft X-ray photon energy of 1000 eV. The energy monochromatic soft X-ray was directory irradiated to the small single crystal surface in a vacuum chamber at room temperature. Total irradiation time was 52 hours. To determine the defect sites in the crystal, change of the molecular vibration modes was measured by means of the infrared optical reflectance experiments.

Figure 2 shows the mid-infrared reflectivity spectra ($E//a$ and $E//c$) of the crystal at 300 K before (black) and after 52 hours irradiation (red). Peak structures at approximately 1390 (Fig. 2(a)) and 2150 cm^{-1} (Fig. 2(b)) have been assigned to the vibration modes related to the dicyanamide group in the anion molecules, which have been significantly suppressed by white X-ray irradiation by using the tungsten tube with 40 kV in the lab experiments [1]. In the present SR soft X-ray irradiation, however, no detectable change was observed in the both vibration modes. Some possible reasons are expected such as short irradiation time, weak intensity, small penetration depth, and so on. We will check these points carefully for making next plans, including soft X-ray absorption experiments on the crystals irradiated by using the tungsten tube in advance to detect a defect structure consisting dicyanamide group.

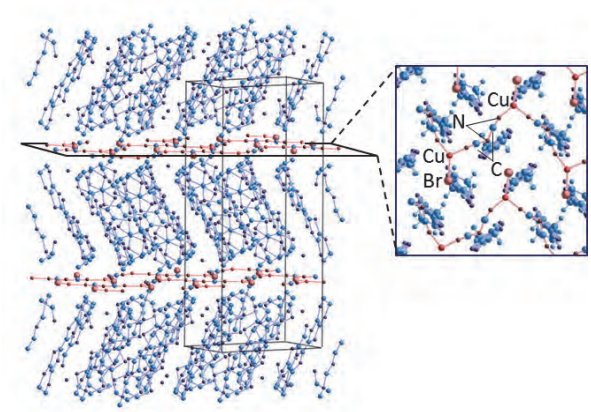

Fig. 1. Crystal structure of κ-(BEDT-TTF)$_2$Cu-[N(CN)$_2$]Br.

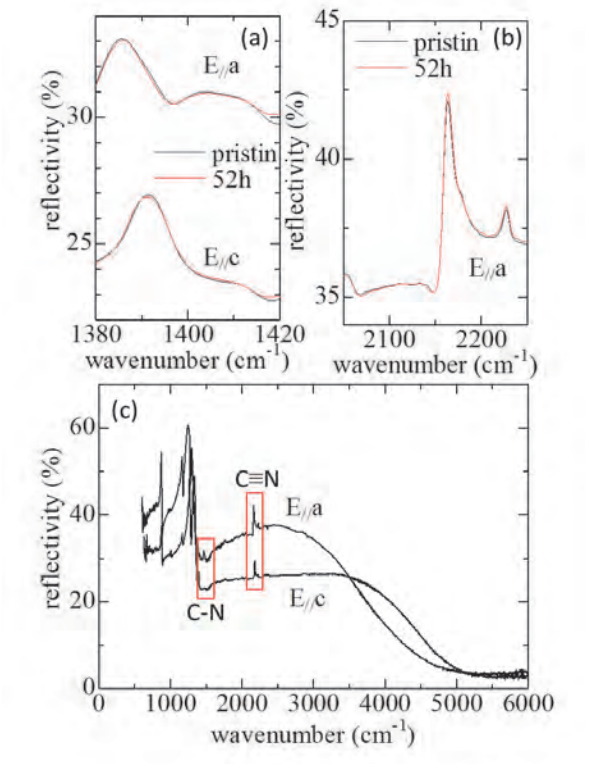

Fig. 2. IR optical reflectivity of κ-(BEDT-TTF)$_2$Cu-[N(CN)$_2$]Br before and after 52 hours soft X-ray irradiation.

[1] T. Sasaki, Crystals **2** (2012) 374.
[2] T. Furukawa *et al.,* Phys. Rev. Lett. **115** (2015) 077001.
[3] L. Kang, K. Akagi, K. Hayashi and T. Sasaki, submitted.

BL2A

Al *K*-edge XANES of AlN Films Doped with 3*d* Transition Metals

N. Tatemizo and S. Imada

Faculty of Electrical Engineering and Electronics, Kyoto Institute of Technology, Kyoto 606-8585, Japan

Recently, the doping of semiconductors with 3*d*-transition metals (3*d*-TMs) has been extensively investigated in order to realize semiconductors exhibiting additional electronic states and having improved properties. At high concentrations (~10%), the 3*d*-TMs' orbitals will start to overlap with one another, to form an impurity band. Such an impurity band well apart from the conduction band (CB) and the valence band (VB) can intermediate optical excitations of electrons from the VB to the CB when the impurity band is partially filled by electron. This is so called an intermediate band (IB) material proposed by Luque *et al.*, for use in absorption layers of solar cells to increase their conversion efficiency [1].

For wurtzite III-nitrides, such as AlN and GaN, the doped 3*d*-TMs can not only form impurity bands in the band gap but also reconstruct the intrinsic VB and CB when the 3*d*-TMs occupy III element sites due to non-centrosymmetry of the site. This can result in band gap narrowing of the semiconductors. In fact, it was reported that the band gap energy of GaN doped with 9% Cr, is 3.1 eV, whereas that of un-doped GaN is 3.4 eV [2].

Expecting both the band gap narrowing effect and sub-bandgap absorptions such as VB-IB and IB-CB, we chose AlN (*Eg* = 6.2 eV) as a base semiconductor for our study. In our previous study, it was shown that (i) the AlCrN films demonstrate distinctive optical absorption properties in the ultraviolet-visible-infrared region as shown in Fig. 1. and (ii) the top of valence band of wurtzite AlCrN (up to 17.1% Cr) contains considerable Cr *d* component via various photoemission spectroscopies and *ab initio* calculations [3].

In wurtzite AlN, main component of the bottom of the conduction band is Al *s* and *p* states, while that of the top of the valence band is N *p* [4]. To investigate effects of the 3*d*-TM doping on the conduction band of AlN, we carried out Al *K*-edge XANES measurements. Figure 2 shows Al *K*-edge XANES spectra and a differential spectrum of AlCrN with 10.46% Cr and un-doped AlN films. The electric field of the incident light was parallel to the *c*-plane of wurtzite structure. There are two features in the spectra: (i) the peak intensities of main edge (1558.5 and 1564.5 eV) in the AlCrN are lower than those of the AlN, and (ii) a small shoulder or tail is observed at around 1555eV. The former implies decrease of Al *p* local DOS in this energy region due to disorder associated with random distribution of Cr. The latter implies formation of unoccupied DOS under the bottom of the CB. Both the features in the Al *K*-edge XANES suggest that Cr atoms distribute homogeneously in the films. Further investigations such as incident angle and concentration dependences of the Al *K*-edge XANES measurements will reveal the effect of 3d-TM doping to the CB structure of the films.

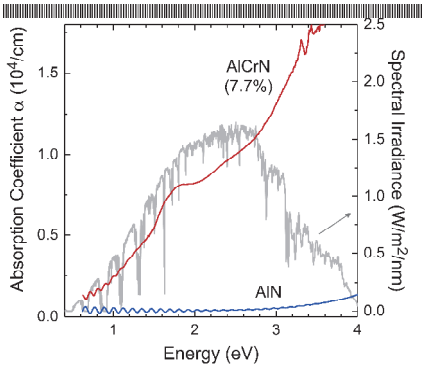

Fig. 1. Absorption coefficient α spectra of AlN and AlCrN films (7.7%) with the solar spectral irradiance for air mass of 1.5. The noise at high α region in the spectra is because of the high absorbance; transmitted light was too faint to detect.

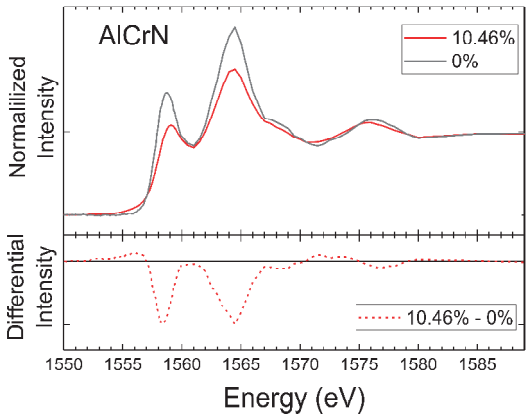

Fig. 2. Al *K*-edge XANES spectra of AlN and AlCrN (10.46%) films on SiO_2 substrates. The lower panel is differential spectra of AlCrN and AlN.

[1] A. Luque *et al.*, Phys. Rev. Lett. **78** (1997) 5014.
[2] S. Sonoda, Appl. Phys. Lett. **100** (2012) 202101.
[3] N. Tatemizo *et al.*, J. Phys.: Condens. Matter **29** (2016) 085502.
[4] E. Ruiz *et al.*, Phys. Rev. B **49** (1994) 7115.

BL2A

Evaluation of Local Structures of P for $CePO_4$

A. Nakahira[1, 2], M. Togo[1], T. Minami[1], C. Takada[1], M. Matsumoto[1], M. Iida[1] and H. Aritani [3]
[1]*Faculty of Engineering, Osaka Prefecture University, Sakai 599-8531, Japan*
[2]*Trans-Regional Corporation Center for Industrial Materials Research (IMR), Tohoku University, Sakai 599-8531, Japan*
[3]*Saitama Institute of Technology, Fukaya 369-0293, Japan*

In recent years, the research about rare earth phosphate materials with unique electronic transition are active for various application as magnetic materials, catalysts, and high performance luminescent devices etc. In special, much interest has been focused on the synthesis and luminescence of nano-sized rare earth orthophosphates for their potential application in optoelectronic devices and biological fluorescence labeling device. Among them, $CePO_4$ nanoparticles and nanowires have been expected to be used as luminescent probe for selective sensing. $CePO_4$ is one of quite unique rare earth phosphate material, hexagonal $CePO_4$ and monoclinic $CePO_4$ (natural monazite). In special, the development and research on nano-sized $CePO_4$ material (nanorods, nanowires, and nanofiber etc) with a variable size attract much attention. For example, monoclinic $CePO_4$ generally exists as natural monazite, bulk materials of which could be prepared via the solid state reaction and hydrothermal method at high temperature. In this study, the purpose was to evaluate the local structure of $CePO_4$ synthesized by hydrothermal process at 423 K and soft chemical process at room temperature. The effect of synthetic condition parameters (synthesis processing, temperature, time, aging etc) on the microstructure for various $CePO_4$ samples was investigated.

All chemicals were analytical reagent- grade, and they used without further purification. In a typical synthesis, $Ce(NO_3)_3$ solution with 0.05 mol/L concentrations were prepared. Into them, the cerium nitrate solution was added slowly to 6 mol/L of orthophosphoric acid solution while kept under stirring. The as-obtained solution with a different reactant PO_4/Ce molar ratio was transferred into a stainless steel autoclave with an inner teflon vessel (28 ml). And the hydrothermal treatment was carried out at 423 K for 24 h. Furthermore, the soft chemical process was done at 358 K and room temperature using the same chemical solutions as hydrothermal treatments. After hydrothermal process and soft chemical process, the as-synthesized precipitates were separated by filtration, washed with deionized water several times and ethanol, and dried at 343 K for 12 h. After drying, the products were ground with Al_2O_3 mortal. The final products appeared as light green solid powder. After all of the ground product powders were characterized by XRD method, FT-IR and TG-DTA. The microstructures of product powder were observed by SEM. The local structures around Si for the products of samples were characterized by measuring X-ray adsorption near edge structure (XANES) at BL02A in UV-SOR.

The evaluation of XRD done for various products. According to XRD results, products prepared by hydrothermal process at 423K was mainly composed of hexagonal $CePO_4$, although ones by soft chemical process at 358 K and room temperature were composed of monoclinic $CePO_4$. Figure 1 shows the XANES spectra of various $CePO_4$ samples. As shown in Fig. 1, XANES spectra of sample obtained by hydrothermal process and soft chemical process were quite different. Furthermore, there was slight difference for $CePO_4$ samples by soft chemical process at between 358 K and room temperature. In addition, the effect of synthetic condition parameters (processing, temperature, and PO_4/Ce on the microstructure for various $CePO_4$ samples was confirmed.

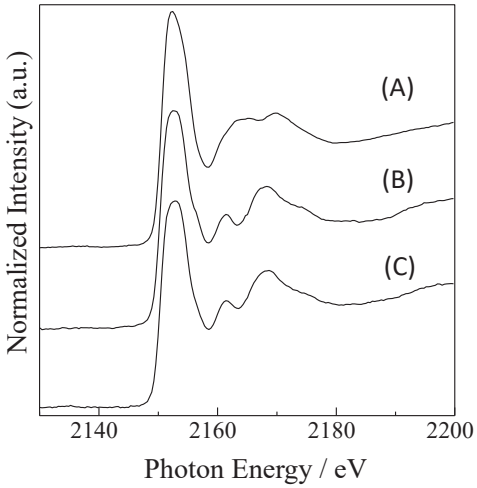

Fig. 1. P-*K* XANES spectra of various $CePO_4$ samples. (a) hydrothermal process at 423 K, (b) soft chemical process at 358 K and (c) soft chemical process at room temperature.

BL2B

Ultraviolet Photoelectron Spectra of $Lu_2@C_{90}$

T. Miyazaki[1], K. R. Koswattage[2], H. Shinohara[3] and S. Hino[4]

[1]*Faculty of Science, Research Laboratory for Surface Science, Okayama University, Okayama 701-8530, Japan*

[2]*Institutes for Molecular Science, Okazaki 444-858, Japan*

[3]*Graduate School of Science, Nagoya University, Nagoya 464-8602, Japan*

[4]*Graduate School of Science and Engineering, Ehime University, Matsuyama 790-8577, Japan*

The synthesis and separation of higher fullerenes and endohedral fullerenes are remarkable results brought by the investigation of the structure and the electronic structure. Until now, there have been a lot of attempts to synthesize and isolate endohedral fullerenes contains mono-metal atom, di-metal atoms, metal nitrides and metal–carbon clusters. This encapsulation modifies the electronic structure of the fullerene cage by changing the encapsulated atom(s). We have succeeded to measure ultraviolet photoelectron spectra (UPS) of Lu encapsulated C_{82} fullerenes: $Lu@C_{82}$, $Lu_2@C_{82}$, $Lu_2C_2@C_{82}$ [1]. In the current report, the UPS of $Lu_2@C_{90}$ will be presented.

The UPS of the endohedral fullerene were measured using a photoelectron spectrometer at BL2B of UVSOR. Energy calibration of the spectra was carried out using the Fermi edge of a gold-deposited sample disk before the UPS measurements of $Lu_2@C_{90}$. All spectra were normalized by the peak height of the structure α.

Figure 1 shows the UPS of $Lu_2@C_{90}$ obtained with hν = 25–55 eV. The spectral onset of $Lu_2@C_{90}$ was 0.99 eV below the Fermi level, which was much smaller than that of empty C_{90} (1.23 eV), which means encapsulation of metal atom inside the cage contribute to narrow the band gap of fullerene, but $Lu_2@C_{90}$ is still semi-conductive. There are 10 structures labeled A–D, α–δ, X and Y in the UPS of $Lu_2@C_{90}$. The intensity of these structures changed, when the incident photon energy was tuned, which was a typical behavior of fullerenes. From the UPS comparison of the other endohedral fullerenes, their structures α–δ appeared in the deeper binding energy region (E_b > 5 eV) of the UPS of $Lu_2@C_{82}$ is due to σ-electrons that constitute the C_{90} skeletal C–C bonds. Structures labeled A–D appeared in the upper binding energy region (E_b < 5 eV) of the UPS are derived from π-electrons. On the other hand, there are two structures X and Y in the 9–11 eV region. They are not observed when the incident photon energy is less than 35 eV, but they are distinct and their intensity becomes stronger in accordance with the increase of the incident photon energy. This behavior is quite different from that of other endohedral fullerenes and seems to be the characteristic ones to the entrapped Lu atom [1]. Possibly structures X and Y is due to $Lu4f_{7/2}$ and $Lu4f_{5/2}$. The ionization potentials of Lu $4f_{7/2}$ and $4f_{5/2}$ of Lu metal are 7.5 eV and 8.9 eV, respectively [2]. Structures X and Y of $Lu_2@C_{90}$ appear at 9.8 eV and 11.2 eV, respectively, which are higher than those of Lu metal by 2.3 eV. Lu atom is electron wanting state. Hence the ionization potential of entrapped Lu 4f levels moves to deeper level. Thus, the entrapped Lu atom donates electrons to the cage and the oxidation state of Lu atom might be +3.

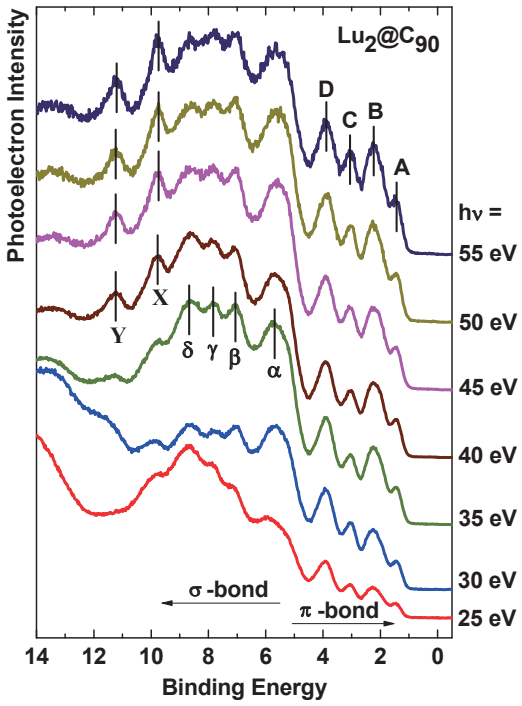

Fig. 1. The incident photon energy dependent UPS of $Lu_2@C_{90}$ at *hν* = 25–55 eV.

[1] T. Miyazaki, R. Sumii, H. Umemoto, H. Okimoto, T. Sugai, H. Shinohara and S. Hino, CPL **555** (2012) 222.

[2] M. Cardona and L. Ley (Eds.), Photoemission in Solids. I: General Principles, Springer-Verlag, Berlin, 1978.

BL3B

Radiative Decay of Intrinsic Luminescence from Self-Trapped Excitons in Orthoborates with Plural Nonequivalent BO_3^{3-} Groups upon VUV Excitation

N. Kodama, H. Kubota, M. Kudo and T. Takahashi
Graduate School of Engineering Science, Akita University, Akita 010-8502, Japan

The electronic structure of complex oxoanions, such as BO_3^{3-}, PO_4^{3-}, and SiO_4^{4-}, is expected to exhibit peculiar features. Until now, there has been very little work focusing on statistical fluctuations in the local structure of low-symmetry complex rare-earth oxides with plural nonequivalent oxoanions of the BO_3^{3-} group. We focused on three types of orthoborates with different numbers of nonequivalent BO_3^{3-} oxoanion groups. The first type includes $YSc(BO_3)_2$ (YSB) [1] and $Sr_6YSc(BO_3)_6$ (SYB) with one BO_3^{3-} group; these crystals are characterized by a statistical fluctuation in the local structure surrounding BO_3^{3-} groups caused by disorder of Y^{3+} and Sc^{3+} ions. The second type consists of rare-earth orthoborate crystals, such as $LaSc_3(BO_3)_4$ (LSB) [1] and $Ca_4LaO(BO_3)_3$ (CLOB), with two nonequivalent BO_3^{3-} groups. CLOB belongs to a class of double borates with oxygen as a foreign anion. The third type is $Ba_3Y(BO_3)_3$ (BYB) with three nonequivalent BO_3^{3-} groups.

We report on intrinsic luminescence spectra and decay characteristics of STEs in these crystals. In addition, we discuss the correlation between intrinsic luminescence bands associated with STEs and the number of nonequivalent BO_3^{3-} groups in YSB, SYB, LSB, CLOB, and BYB, from the viewpoint of the local structure, symmetry, and environment of BO_3^{3-} groups.

Luminescence and excitation spectra of STEs in YSB, SYB, LSB, CLOB, and YSB polycrystals were measured at twelve temperatures in the range of 8(11)-293 K using the undulator beamline BL3B at the UVSOR facility. The decay characteristics of the luminescence on the nanosecond scale were measured using a time corrected single photon counting method under excitation with single bunched pulses from UVSOR. The excitation spectral intensity for the orthoborates increased rapidly below about 200-210 nm. The broad excitation bands were assigned to bandgap excitations or molecular transitions of the BO_3^{3-} group. All samples were found to exhibit multiple STE luminescence bands in the UV region under VUV excitation at 70 and 160 nm.

The luminescence spectra of YSB and SYB at 11 and 8 K, respectively, consisted of two broad bands associated with STE(I) and (II) with peaks at 251 and 274 nm, and 288 and 337 nm. The spectra of LSB and CLOB at 11 K consisted of two broad bands with peaks at 245 and 303 nm, and 281 and 364 nm, respectively, again associated with STE(I) and STE(II) in two sets of nonequivalent BO_3^{3-} groups. On the other hand, as shown in Fig. 1(e), BYB exhibited three distinct broad bands at 8 K: an intense luminescence band with a peak at 306 nm, a short-wavelength shoulder with a peak at 246 nm, and a band with a long-wavelength tail and a peak at 389 nm. These three intrinsic bands are assigned to STE(I), STE(II), and STE(III) in three sets of nonequivalent BO_3^{3-} groups. In LSB, CLOB, and BYB, the number of intrinsic luminescence bands coincides with the number of nonequivalent BO_3^{3-} groups, whereas in YSB and SYB two bands appear, despite the presence of only one BO_3^{3-} group. The number of bands is inconsistent with the number of nonequivalent BO_3^{3-} groups. A possible interpretation for this discrepancy is that there are two types of BO_3^{3-} groups with different geometries, presumably caused by random disorder of Y^{3+} and Sc^{3+} ions.

Figures 1(a)-(f) show decay curves for the UV bands at 8 K for YSB, LSB, CLOB, and BYB, respectively. All samples exhibit a fast and a slow component due to high-spin and low-spin STEs associated with the two possible spin orientations for the exciton electron-hole pair of alkali halides [1]. For YSB, the decay times for STE(I) luminescence at 240 nm are 350 ps and 4.3 μs. For LSB, the decay times for STE(I) luminescence at 260 nm are 1.2 ns and 184 ns, and those for STE(II) at 330 nm are 1.8 ns and 180 ns. For CLOB, the decay times for STE(I) luminescence at 270 nm are 1.7 ns and 2.0 μs, and those at 400 nm for STE(II) are 2.0 ns and 2.0 μs. For BYB, the decay times for STE(I) luminescence at 400 nm are 1.7 ns and 2.0 μs.

The fast decay components for STE(I) in YSB and BYB originate from singlet STE states in BO_3^{3-} groups with D_3 and Cs symmetry, respectively. The fast decay components for STE(I) and STE(II) in LSB and CLOB may also originate from singlet STE states the BO_3^{3-} groups with C_1 and Cs symmetry, respectively. In contrast, the slow decay components for STE(I) in YSB, LSB, CLOB, and BYB, and those for STE(II) in LSB and CLOB are attributed to triplet STEs in BO_3^{3-} groups in which singlet STE states occur.

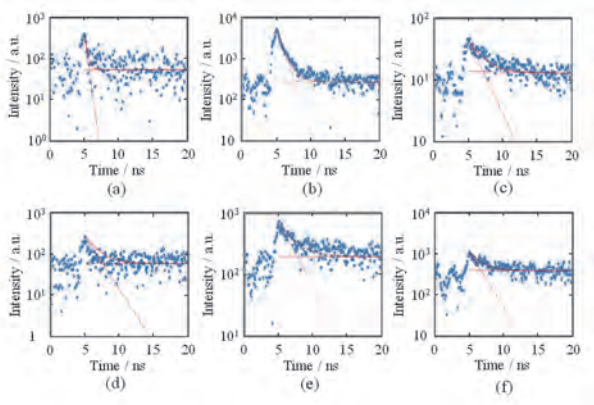

Fig. 1. Decay curves for STE luminescence at 8 K at (a) 240 nm for YSB, (b) 260 nm for LSB, (c) 330 nm for LSB, (e) 270 nm for CLOB, (e) 400 nm for CLOB, and (f) 400 nm for BYB.

[1] N. Kodama, K. Yanagidaira and T. Takahashi, UVSOR Activity Report **43** (2016) 53.
[2] T. T. Williama and K. S. Song, J. Phys. Chem. Solds. **51** (1990) 679.

BL3B

Excitation Process of Pr^{3+} Ions in $Lu_3Al_5O_{12}$ Crystals by VUV Photons

M. Kitaura[1], K. Kamada[2], S. Kurosawa[1, 2] and A. Ohnishi[1]
[1]*Faculty of Science, Yamagata University, Yamagara 990-8560, Japan*
[2]*New Industry Creation Hatchery Center, Tohoku University, Sendai 980-8579, Japan*

The impact excitation of hot photocarriers with impurity-localized electrons in crystalline solids has been studied with the use of synchrotron radiation (SR) [1]. Since a number of relaxation pathways compete under excitation with vacuum ultraviolet (VUV) photons from SR, the relaxation of hot photocarriers becomes complicated. The process of impurity-excitation by VUV photons still remains obscure, despite the basic subject concerning both sides of fundamental and applied physics.

The crystal of praseodymium-doped $Lu_3Al_5O_{12}$ (Pr:LuAG) has been utilized as the scintillator for the detection of X- or γ-rays. VUV excitation spectra for the Pr^{3+} 5*d*-4*f* luminescence in Pr:LuAG crystals have been reported [2, 3]. However, the process of Pr^{3+}-excitation by VUV photons has not been discussed in detail. The information on this process provides us hints to obtain high-quality Pr:LuAG scintillators.

The main aim of the present study is to clarify the processes of electron-hole (*e*-*h*) relaxation in undoped LuAG crystals and Pr^{3+}-excitation in Pr:LuAG crystals. The undoped LuAG and Pr:LuAG crystals were grown by the micro pulling down (μ–PD) method. The concentration of Pr^{3+} ions was set 0.8 mol%. In the present experiment, we measured excitation spectra for the excitonic luminescence peaking at 4.96 eV and the Pr^{3+} 5*d*-4*f* luminescence at 3.87 eV. The data were corrected for the distribution of excitation light source.

Figure 1 shows excitation spectra for the excitonic luminescence (blue line) and Pr^{3+} 5*d*-4*f* luminescence (red line). The fundamental absorption edge of undoped LuAG crystals was determined around 6.83 eV. The excitonic luminescence is excited in the region above the fundamental absorption edge. The intensity is almost kept constant in the 11-18 eV range, and it is gradually increased in the 18-26 eV range. The threshold energy is higher than the sum of the lowest exciton creation energy (6.83 eV) and the band-gap energy (7.93 eV [4]). In this case, hot photoelectrons have the kinetic energies enough to excite valence electrons into the conduction band minimum through inelastic scattering with them. Consequently, it is most likely that the multiplication of electronic excitations (MEEs) is realized above 18 eV. In order to obtain more detail information on the process of the MEEs, ultraviolet photoemission experiment are now in progress.

The Pr^{3+} 5*d*-4*f* luminescence is excited in the region below the fundamental absorption edge, in which the Pr^{3+} 4*f*-5*d* absorption occurs. In the region above the fundamental absorption edge, the excitation spectrum for the Pr^{3+} 5*d*-4*f* luminescence is similar to that for the excitonic luminescence mentioned above. This result indicates that no direct (elastic) excitation of Pr^{3+} ions by hot photoelectrons occurs in Pr:LuAG crystals. One may notice the spectral overlap between the excitonic luminescence and Pr^{3+} 4*f*-5*d* absorption, implying the energy transfer from the host to Pr^{3+} ions. However, the Pr^{3+} 5*d*-4*f* luminescence is observed under excitation above the fundamental absorption edge, even when the excitonic luminescence is completely quenched at 300 K. This fact excludes the possibility of the energy transfer from the host to Pr^{3+} ions. Thus, the following process is most suitable for the Pr^{3+}-excitation by VUV photons. The *e*-*h* pairs created under MEEs are captured by Pr^{3+} ions, and the excited states of Pr^{3+} ions are formed. The excited states relax into the ground states, giving rise to the Pr^{3+} 5*d*-4*f* luminescence.

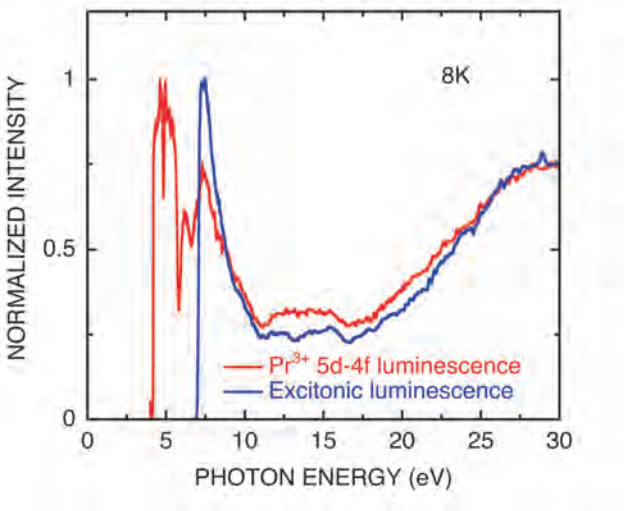

Fig. 1. Excitation spectra for the 4.96 eV (blue line) and 3.87 eV bands (red line). These data were obtained at 8 K. The former and latter correspond to the excitonic luminescence and Pr^{3+} 5*d*-4*f* luminescence, respectively.

[1] For example, M. Kitaura *et al*., J. Lumi. **172** (2016) 243.
[2] A. Yoshikawa *et al*., IEEE Tran. Nucl. Sci. **55** (2008) 1372.
[3] Y. Zorenko *et al.,* J. Lumi. **179** (2016) 496.
[4] P. Dorenbos, J. Lumi. **134** (2013) 310.

BL3B

Effects of Annealing and Mg-codoping on Luminescence Properties of Ce Doped Garnet-Based Scintillator Grown by Micro Pulling Down Method

H. Yamaguchi[1], K. Kamada[2, 3], S. Kurosawa[3], Y. Shoji[1, 2], Y. Yokota[3], Y. Ohashi[1], A. Yamaji[1] and A. Yoshikawa[1, 2, 3]

[1] *Tohoku University, Institute for Materials Research, Sendai 980-8577, Japan*
[2] *C&A Corporation, T-Biz, Sendai 980-8579, Japan*
[3] *Tohoku University, New Industry Creation Hatchery Center, Sendai 980-8579, Japan*

Recently, cations (B, Ca, Ba) codoping effects on scintillation mechanism and annealing effects on defect structures for Ce: $Gd_3Ga_3Al_2O_{12}$ (GGAG) has been reported [1], where further improvement of scintillation properties were also reported. In addition, Mg^{2+} codoping effects on shallow electron traps for Ce:GGAG by the UV-induced absorption spectroscopy against the thermoluminescence (TL) glow curve was reported [2]. In this study, we investigated the Mg codoping effect on the shallow traps of defect complexes related to oxygen vacancies for the multicomponent garnet-based scintillators by measuring the TL glow curves.

We prepared Mg codoped and non codoped Ce:$(Lu,Gd)_3Ga_3Al_2O_{12}$ single crystals grown by the micro-pulling-down method, and TL spectra for these samples were measured and evaluated within 7.5-300 K at BL3B of the UVSOR facility. The size and weight of each crystal were similar and the TL glow curves were normalized to the background intensity.

Figure 1 (a) - (b) show the TL glow curves for the Mg/non codoped Ce:$(Lu,Gd)_3Ga_3Al_2O_{12}$ single crystals under 210-190 nm excitation in the temperature range of 7.5-300K. Since absorption edge shifted from 210 nm to approximately 190 nm with increasing the Lu concentration, the 210-190 nm photons were selected as an exaction source accordingly.

2 or 3 glow peaks were observed in this temperature range of TL glow curves, which difference is most probably due to the difference of Ce concentration in the grown crystals. It was also found that the peak intensity around 300 K relatively strengthened with increasing the Lu concentration. Moreover, in case of high Lu concentrated crystals (x = 3), its intensity around 300 K significantly weakened by Mg codoping. Therefore, these results implies that Mg codoping affected the suppression of electron traps effectively in the higher Lu concentrated crystal.

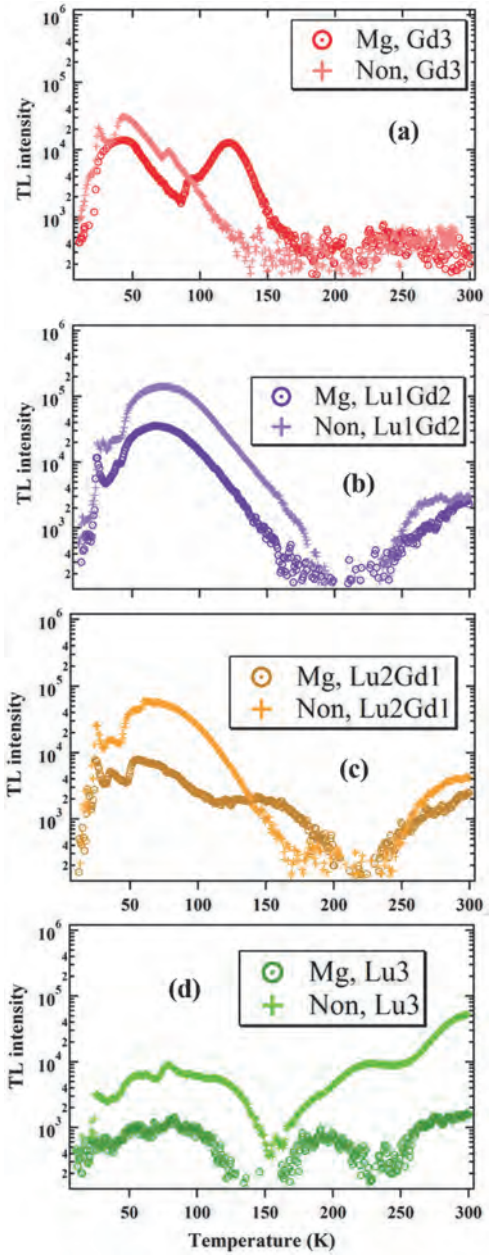

Fig. 1. The TL glow curves of Mg/non codoped Ce:$(Lu_xGd_{3-x})Ga_3Al_2O_{12}$ single crystals; (a) x = 0, (b) x = 1, (c) x = 2, (d) x = 3.

[1] M. Tyagi *et al.*, J. Phys. D; Appl. Phys. **46** (2013) 475302.
[2] M. Kitaura *et al.*, Applied Physics Express **9** (2016) 072602.

BL3B

Determination of the Bandgap Energy of Gd Admixed $Lu_2Si_2O_7$ Scintillator Crystals Using the UVSOR Facility

T. Horiai[1], S. Kurosawa[2, 3], A. Yamaji[1], H. Chiba[1], S. Kodama[1], Y. Shoji[1, 4], Y. Ohashi[1], K. Kamada[2, 4], Y. Yokota[2], A. Yoshikawa[1, 2, 4] and M. Kitaura[3]

[1]*Institute for Materials Research, Tohoku University, Sendai 980-8577, Japan*
[2]*New Industry Creation Hatchery Center, Tohoku University, Sendai 980-8579, Japan*
[3]*Department of Physics, Yamagata University, Yamagata 990-8560, Japan*
[4]*C&A Corporation, Sendai 980-8579, Japan*

Scintillator is a material that converts ionizing radiation such as alpha-rays, gamma-rays and X-ray to a visible/UV lights, and can be applied in oil well logging, high energy physics and nuclear medicine [1, 2]. Especially, pyrosilicate type scintillator, for example Ce-doped $Lu_2Si_2O_7$ (Ce:LPS), Ce-doped $Gd_2Si_2O_7$ (Ce:GPS) and Ce-doped (Gd, La)$_2Si_2O_7$ (Ce:La-GPS) were promising materials with high light output, fast scintillation decay and stable light output until high temperature (150ºC) [3-5]. These scintillation properties were good for application in oil well logging, where the scintillator is often exposed to high temperatures (~200ºC) under Earth surface.

Ce:GPS has been found to melt incongruantly, and therefore it could not be grown by conventional techniques from the melt [6]. On the other hand, the composition of Ce:LPS melts congruently and can be grown relatively easily [7]. Although Ce:LPS has large intrinsic gamma-rays background due to ^{176}Lu.

In this study, we focused on the Gd admixed Ce:LPS, because Gd is good constituents for the material without intrinsic background when compared to Lu, and estimated the bandgap energy of Gd admixed $Lu_2Si_2O_7$ scintillator crystals.

We prepared undoped $Lu_2Si_2O_7$ (LPS) and ($Lu_{0.95}$ $Gd_{0.05}$)$_2Si_2O_7$ (LPSGd5%)single crystals grown by the micro-pulling-down method, and UV absorption edge for these samples were evaluated with a photo diode (IRD, AXUV 100) at BL3B of UVSOR. The bandgap energies were calculated from the UV absorption edge.

We succeeded in growing the transparent samples by the μ-PD method (Fig. 1). From the result of the powder X-ray diffraction analysis, the crystal phase of these samples matched the previous result on LPS (JCPDS No. 35-0326). In addition, the crystalline structure of these crystals were determined to be monoclinic with space group of *C*2/*m*.

Figure 2 shows the UV absorption spectra, and the significant change due to Gd admixed was not observed. From this figure, the UV absorption edge wavelength were around 178 nm. The bandgap energy of LPS and LPSGd5% were calculated about 6.96 and 6.95 eV, respectively. Thus, the bandgap energy of LPSGd5% was remained high value, and this result suggested temperature dependence of light output was also good.

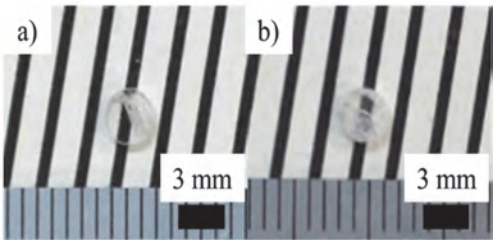

Fig. 1. Photograph of after polished samples, (a) $Lu_2Si_2O_7$, (b) ($Lu_{0.95}$ $Gd_{0.05}$)$_2Si_2O_7$.

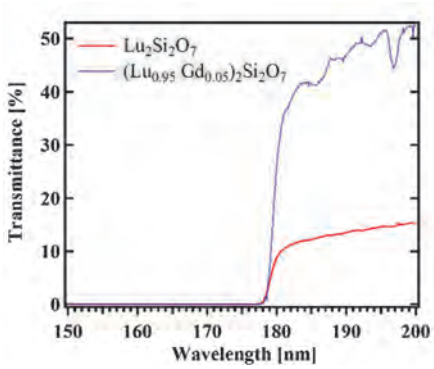

Fig. 2. UV absorption spectra.

[1] C.L. Melcher, J.S. Schweitzer, R.A. Manente and C.A. Peterson, J. Crystal Growth **109** (1991) 37.
[2] C.L. Melcher, J. Nuclear Medicine **41** (2000) 1051.
[3] L. Pidol, A. Kahn-Harari, B. Viana, E. Virey, B. Ferrand, P. Dorenbos, J.T.M. de Haas and C.W.E. van Eijk, IEEE Trans. Nucl. Sci. **51** (2004) 1084.
[4] S. Kawamura, J.H. Kaneko, M. Higuchi, T. Yamaguchi, J. Haruna, Y. Yagi, K.susa, F. Fujita, A. Homma, S. Nishiyama, K. Kurashige, H. Ishibashi and M. Furusaka, IEEE Trans. Nucl. Sci. **54** (2007) 1383.
[5] S. Kurosawa, T. Shishido, T. Sugawara, A. Nomura, K. Yubuta, A. Suzuki, R. Murakami, J. Pejchal, Y. Yokota, K. Kamada and A. Yoshikawa, Nucl. Instrum. Methods Phys. Res. A **772** (2015) 72.
[6] N.A. Toropov, F.Y. Galakhov and S.F. Konovalova Russ. Chem. Bull. **10** (1961) 497.
[7] A.N. Christensen, Zeitschrift fur Kristallographie **209** (1994) 7.

BL3B

Temperature Dependence of Luminescent Properties for Un-doped Cs_2HfCl_6

S. Kodama[1], S. Kurosawa[2, 3], A. Yamaji[1], J. Pejchal[4], R. Král[4], Y. Ohashi[1], K. Kamada[2, 5], Y. Yokota[2], M. Nikl[4] and A. Yoshikawa[1, 2, 5]

[1] *Institute for Materials Research (IMR), Tohoku University, Sendai 980-8577, Japan*
[2] *New Industry Creation Hatchery Center (NICHe), Tohoku University, Sendai 980-8579, Japan*
[3] *Faculty of Science, Yamagata University, Yamagata 990-8560, Japan*
[4] *Institute of Physics, CAS, Cukrovarnická 10, 162 00 Prague, Czech Republic*
[5] *C&A Corporation, Sendai 980-8577, Japan*

Halide scintillation materials are expected to have high light output due to smaller band gap energy than that for the oxide materials [1]. Indeed, Tl:NaI [2,3], Ce:$LaBr_3$ [4] and Eu:SrI_2 [5] have good light output. However, almost all halide materials have strong hygroscopic nature. Although these scintillators are packed in a hermetic sealing, aging degradation would be caused by remaining moisture in the package or damage of the package.

Recently, a non-hygroscopic halide material, Cs_2HfCl_6, was reported by Burger *et al.* [6], and this material has a high light output of 54,000 photons/MeV and good energy resolution of around 3 % (FWHM for 662 keV gamma-ray). Moreover, Cs_2HfCl_6 emits ~440 nm blue light under ~250 nm excitation [7]. This emission is considered to be of Zr-related defect origin while the other component of emission spectra located within 360-400 nm comes from self-trapped exciton (STE) luminescence on $[HfCl_6]^{2-}$ anion complex [8]. However, the details of its luminescence mechanism have not been investigated yet. Here, we investigated temperature dependence of photoluminescence spectra for undoped Cs_2HfCl_6.

Un-doped Cs_2HfCl_6 were synthesized from 99.9%-pure (Zr-free) $HfCl_4$ and 99.999%-pure CsCl. Then, the mixed powders were put into a quartz-glass ampoule and the crystal was grown by the vertical Bridgman growth method. The procedure is in detail described in [9].

The obtained single crystal was cut and polished to measure its photoluminescence spectra. We evaluated the temperature dependence in BL3B beamline at UVSOR. Cs_2HfCl_6 was excited by 250 nm UV light, and spectra were measured with a spectrometer (spectoropro-300i, Acton research). The chamber was cooled by liquid helium, and the spectra were measured from 8 to 300 K.

We succeeded in growing the undoped Cs_2HfCl_6 single crystal. Obtained photoluminescence spectra at 8, 100, and 300 K for Cs_2HfCl_6 are shown in Fig. 1. The intensity of luminescence decreased with decreasing temperature. We summarized the intensity versus temperature of undoped Cs_2HfCl_6 in Fig.2. In addition, emission peak shifted from 454 nm (at 300 K) to 441 nm (at 6 K). Given the fact that under 250 nm excitation rather Zr-impurity related defect emission peaking around 435 nm is excited at room temperature [7] the temperature dependence measured here is related to the same defect rather than to STE..

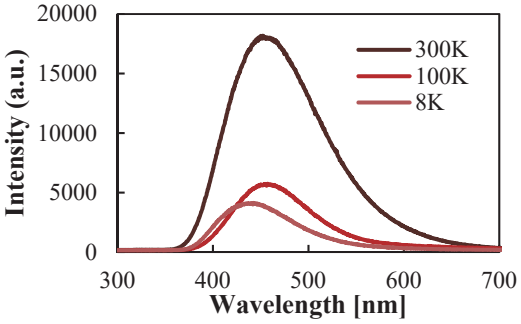

Fig. 1. Photoluminescence spectra of Cs_2HfCl_6 at 300, 100 and 6 K.

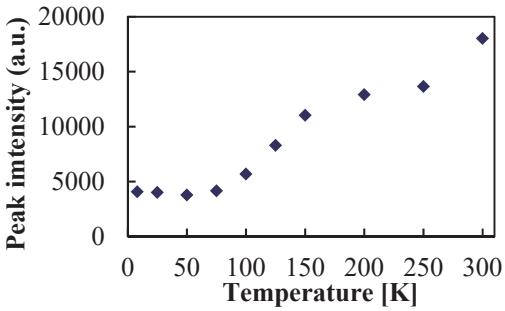

Fig. 2. Temperature dependence of emission intensity obtained as peak position at 454 nm From Fig. 1.

[1] P. Dorenbos, NIM**A486** (2002) 208.
[2] E. Sakai, IEEE TNS **1** (1987) 418.
[3] Bicron Co., physical properties of common inorganic scintillators (2001) 3101.
[4] E.V.D. van Loef *et. al.*, NIM**A486** (2002) 254.
[5] Y. Yokota *et. al.*, JCG **375** (2013) 49.
[6] A. Burger *et. al.*, App. Phys. Lett. **107** (2015) 143505.
[7] K. Saeki *et al.*, Appl. Phys. Ex. **9** (2016) 042602.
[8] B. Kang *et al.*, J. Phys. Chem. C **120** (2016) 12187.
[9] S. Kodama *et al.*, J. Lumin. in prep.

BL3B

Evaluation of Ce:$(Gd, La)_2Si_2O_7$ Scintillator Using an UVSOR Beam Line -FY2016-

S. Kurosawa[1, 2], A. Yamaji[3], T. Horiai[3], S. Kodama[3], T. Chiba[3], C. Tanaka[3], Y. Shoji[3, 4], Y. Ohashi[3], Y. Yokota[1], K. Kamada[1, 4], A. Yoshikawa[1, 3, 4] and M. Kitaura[2]

[1] *New Industry Creation Hatchery Center (NICHe), Tohoku University, Sendai 980-8579, Japan*
[2] *Faculty of Science, Yamagata University, Yamagata 990-8560, Japan*
[3] *Institute for Materials Research (IMR), Tohoku University, Sendai 980-8577, Japan*
[4] *C&A Corporation, Sendai 980-8577, Japan*

Scintillators are used in various fields such as medical imaging, astronomy, oil well ligging and so on. Recently, scintillation properties of $(Ce_{0.01}, Gd_{0.90}, La_{0.09})_2Si_2O_7$ (Ce:La-GPS) have been reported. The Ce:La-GPS crystal had a light output of approximately 35,000 photons/MeV, FWHM energy resolution of 5.0% at 662 keV [1, 2]. Moreover, the light output over 35,000 photons/MeV was found constant in the temperature range from 0 to 423 K. In addition, FWHM energy resolution of Ce:La-GPS (roughly 7–8%) at 662 keV remained constant up to 373 K [3]. Thus, this crystal can be applied to oil well logging or other radiation detection application at high temperature conditions.

Up to now, the bandgap energy of La-GPS has been not measured for La-GPS yet. In order to reveal the mechanism of the thermal quenching, the evaluation of the bandgap energy is required. Thus, in this paper, the bandgap energy was measured at low temperature (7K) using UVSOR beam line BL3B.

To evaluate the bandgap energy, pure La-GPS was prepared by the micro-pulling down method. Using this sample and the BL3B, we measured the transmittance spectrum as showin in Fig. 1. From this data, the band gap energy was estimated to be 7.13±0.01 eV. Compared with other oxide scintillators, La-GPS was found to have wider bandgap. On the other hand, the light output of Ce:La-GPS was larger than most of oxide scintillators with narrower bandgaps than La-GPS.

Light output (light yield Y) was related to bandgap energy (E_{gap}) in following equation:

$$Y = \frac{\eta E \gamma S Q}{\beta E_{gap}} \quad (0 < \eta, Q, S \leq 1),$$

where S, Q, E_γ and β are the transfer efficiency from the electron-hole pair into the luminescence center, the quantum yield of the final luminescence process in Ce^{3+} emission center, incident gamma-ray energy and the ratio between the energy needed to create one electron-hole pair and E_{gap} [4]. Usually β is used as constant (~2.5) , and η denotes generation coefficient for electron-hole pair. The value of $\eta \times S \times Q$ for Ce:La-GPS was found to be higher than for the other scintillators.

The quantum yield (Q) of Ce:-LaGPS was estimated to be around 0.8 using an integrating sphere and a spectrometer (Hamamatsu C9920-02G), and this is similar value to other oxide scintillator, where typical value of Q for oxide conventional scintillator is 0.6-0.8. Thus, it implies that Ce:La-GPS has good transfer efficiency or/and good electron-hole pair generation efficiency.

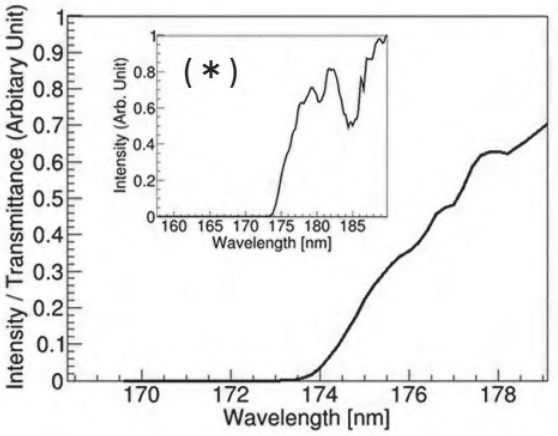

Fig. 1. Transmittance of pure La-GPS as function of wavelength. The small window marked (*) denotes enlarged view arond the absorption edge.

[1] A. Suzuki *et al.*, Applied Physics Express **5** (2012) 102601.
[2] S. Kurosawa *et al.*, Nucl. Inst. and Meth. in Phys. Res. **A774** (2014) 30.
[3] S. Kurosawa *et al.*, Nucl. Inst. and Meth. in Phys. Res. **A772** (2015) 72.
[4] R. H. Bartrama and A. Lempicki, 1996 Journal of Luminescence **68** (1996) 225.

BL3B, BL7B

Temperature Dependence of the PL Spectra of Laser Irradiated *a*-CN_x Thin Films

K. Nakamura[1], F. Sawa[1], K. Fukui[1] and K. Yamamoto[2]
[1]*Department of Electrical and Electronics Engineering, University of Fukui, Fukui 910-8507, Japan*
[2]*Far-infrared region Development Research Center, University of Fukui, Fukui 910-8507, Japan*

Amorphous carbon nitride (*a*-CN_x) is known to have interesting mechanical, electrical and optical properties. In the optical properties, *a*-CN_x shows a broad emission at visible region. Since *a*-CN_x is composed only of carbon and nitrogen, it is expected as an inexpensive white light emitting material. However, photoluminescence (PL) spectra of the samples evaporated under same conditions are, in some cases, different with each other, because the optical properties of *a*-CN_x are sensitive to the preparation conditions. Recently, it is found that laser irradiated *a*-CN_x thin films in the atmosphere after depositing show much higher PL intensity than those of as-deposited *a*-CN_x thin films, and their PL spectra have better reproducibility [1, 2]. In this report, we show temperature dependence of the PL spectra by using laser irradiated *a*-CN_x thin films.

All samples on Si substrates are deposited by the RF-sputtering method at Ryukoku University [1]. The sputtering conditions of the graphite target in each sample under low pressure nitrogen gas environment were kept constant, and the RF power was changed to 40 W, 60 W and 100 W. Beam diameter of laser-irradiation is about 1.2 mm, and irradiation time is 240 minutes by using He-Cd laser (325 nm) with 20 mW. All PL measurements have been performed at BL3B and BL7B from 10 to 320 K. The excitation energy of PL measurements is fixed at 4.6 eV, where excitation spectra of all samples have maximum intensities.

Figure 1 shows the PL spectra of RF power 60 W *a*-CN_x thin film at from 10 K to 320 K. It is found that a broad PL is observed from 1.6 to 4.0 eV, and broadness is independent on temperature. However, PL intensity gradually decreases with increasing temperature, and the peak energy of PL spectrum gradually shifts to the higher photon energy side with increasing temperature. These trends are also observed in both 40 W and 100 W *a*-CN_x thin films. They suggest that the relaxation mechanism of PL in *a*-CN_x thin films does not change at least below room temperature. However, both peak shift and intensity decreasing reveal that this broad PL peak consists of many emission bands, which are continuously distributed from 1.6 eV to 4.0 eV [2].

Figure 2 shows temperature dependence of the normalized PL intensity of 60 W *a*-CN_x at emission photon energy 2.43, 2.50, 2.55, 2.65, 2.76, 2.89, 2.97, 3.05 eV, respectively. Intensity normalization carried out to the intensity at 10 K. Temperature dependences show roughly similar with each other and relatively simple behavior, although it is difficult to explain this behavior as the resulting from single thermal quenching mechanism.

In summary, we measured temperature dependence of PL spectra of laser irradiated *a*-CN_x thin films. The *a*-CN_x thin films show a broad visible range emission band, which consist of various emission bands. However, their thermal quenching mechanisms are relatively simple.

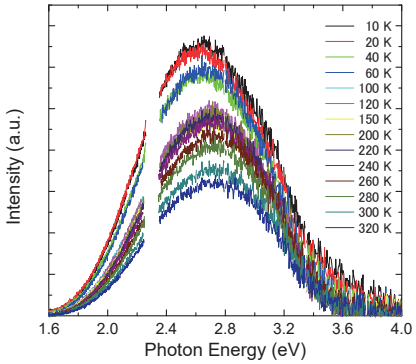

Fig. 1. Temperature dependence of the PL spectra of *a*-CN_x 60 W.

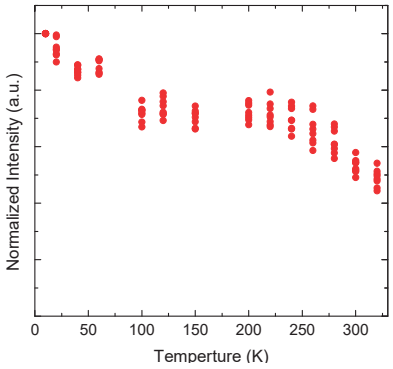

Fig. 2. Temperature dependence of the PL intensity at each emission photon energy.

[1] M. Satake *et al.*, 2013 JSAP Autumn Meeting 28p-PB3-11.
[2] K. Nakamura *et al.*, UVSOR Activity Reports **43** (2016) 61.

BL3B

Photoluminescence and Excitation Spectra of Ce^{3+}, Eu^{3+} Singly Doped $Lu_3Al_{4.75}Si_{0.25}O_{11.75}N_{0.25}$ Phosphors in VUV-Vis Region

K. Asami, K. Yasuda, J. Ueda and S. Tanabe
Graduated School of Human and Environmental Studies, Kyoto University, Kyoto 606-8501, Japan

The Ce^{3+} doped garnet phosphors are attracting much attention in the application for white light emitting diodes (LEDs) and scintillators [1]. Commercial white LED is composed of a blue LED and yellow phosphor such as $Y_3Al_5O_{12}:Ce^{3+}$ (YA*G*:Ce) [2]. YA*G*:Ce phosphor has strong absorption in the range of blue LED wavelength (λ:~ 450 nm) and shows broad yellow luminescence with high quantum yield (~90%). However, the generated whit light exhibits a low color rendering and high color temperature due to color deficiency in the red spectral region. In order to realize the redshift of emission, there are many reports to expand crystal field splitting of Ce^{3+} by substitution of the cation at each site [3]. Recently, it is reported that N^{3-} ligands which is lower electronegativity than O^{2-} ligands incorporate into YAG and $Lu_3Al_5O_{12}$ (LuA*G*) hosts to replace O^{2-} anions and Si^{4+} was used as a charge compensation [4]. Setlur et al. have proven that $Lu_3(Al,Si)_5(O,N)_{12}:Ce^{3+}$ phosphor shows a very broad and warmer emission spectrum and the lower thermal quenching [5]. To investigate the electronic structure of $Lu_3Al_{4.75}Si_{0.25}O_{11.75}N_{0.25}$ (LuASON*G*), we measured photoluminescence and excitation (PL & PLE) spectra of both Ce^{3+} and Eu^{3+}- singly doped phosphors at UVSOR BL3B. Ce^{3+}, Eu^{3+} singly doped LuASON*G* phosphors are prepared by solid state reaction method with N_2 atmosphere. Samples are identified as garnet structure by XRD.

Figure 1 shows the PLE and PL spectra of Ce^{3+}- doped LuASON*G* phosphor at 10 K. In PLE spectrum, the host exciton peaks are observed at around 170 nm and three bands derived from Ce^{3+} are observed at 220 nm (4f-$5d_{3,4,5}$), 350 nm (4f-$5d_2$) and 450 nm (4f-$5d_1$). From the host exciton peak, the bandgap energy is estimated to be 7.92 eV, which is almost the same as that of LuA*G* (7.94 eV) [5]. In PL spectrum, two emission bands are observed at around 500 and 560 nm, which are attributed to $5d_1$-$4f(^2F_{5/2})$ and $4f(^2F_{7/2})$, respectively. These emission bands are longer wavelength than that of LuA*G* slightly. From there results, the substitution of Si^{4+}-N^{3-} bonds for Al^{3+}-O^{2-} bonds increases crystal field strength and causes redshift of emission.

Figure 2 shows PLE and PL spectra of Eu^{3+}- doped LuASON*G* phosphor at 10 K. The strong broad band is located at around 230 nm, which is attributed to charge transfer transition (CTS) of Eu^{3+}. The sharp emission peaks ($^5D_0$-$^7F_{1,2,4}$ and $^5D_1$-$^7F_4$) due to the intra-4f transitions of Eu^{3+} are observed in the range of 580-720 nm. CTS energy of LuASON*G* (5.26 eV) is lower than that of LuA*G* (5.53~5.65 eV) [6,7]. CTS energy is equivalent to the bandgap between Eu^{2+} 4f ground state and valence band edge which *p* state of anion forms. By substitution of Si^{4+}-N^{3-}, p state of N^{3-} interacts with the top of VB. Therefore, CTS energy of oxynitride garnet is lower than that of oxide garnet.

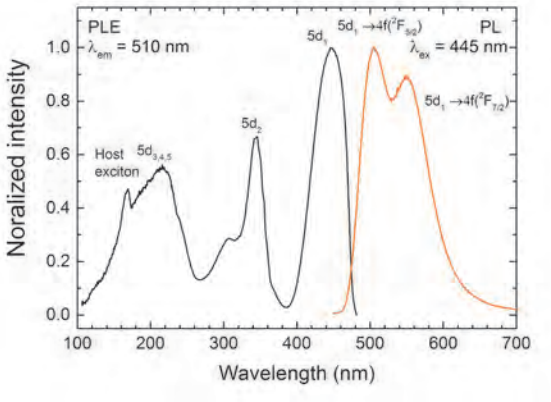

Fig. 1. PLE and PL spectra of LuASON*G* :Ce^{3+}.

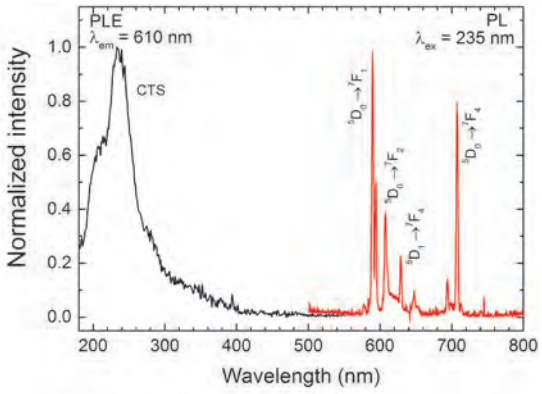

Fig. 2. PLE and PL spectra of LuASON*G* :Eu^{3+}.

[1] Z. Xia and A. Meijerink, Chem. Soc. Rev. **46** (2017) 275.
[2] G. Blasse and A. Bril, Appl. Phys. Lett. **11** (1967) 53.
[3] C. C. Chiang, M. S. Tsai and M. H. Hon, J. Electrochem. Soc. **155** (2008) B517.
[4] J. Liu, X. Wang, T. Xuan, C. Wang, H. Li and Z. Sun, J. Lumin. **158** (2015) 322.
[5] A. A. Setlur, W. J. Heward, M. E. Hannah and U. Happek, Chem. Mater. **20** (2008) 6277.
[6] P. Dorenbos, J. Lumin. **134** (2013) 310.
[7] L. Li and S. Zhang, J. Phys. Chem. B **110** (2006) 21438.

BL3B, BL7B

Total Photoelectron Yield Spectroscopy on 3*d* Transition Metal Doped AlN Films

N. Tatemizo[1], S. Imada[1], F. Sawa[2], S. Hirata[2] and K. Fukui[2]
[1]*Faculty of Electrical Engineering and Electronics, Kyoto Institute of Technology, Kyoto 606-8585, Japan*
[2] *Faculty of Electrical and Electronics Engineering, University of Fukui, Fukui 910-8507, Japan*

It is well known that 3*d*-transition metals (3*d*-TMs) can form impurity levels in the band gap of a semiconductor and these levels can accept and/or donate electrons when irradiated with light of appropriate energy. At high concentrations, the 3*d*-TMs' orbitals will start to overlap with one another, to form an impurity band. Such an impurity band well apart from the conduction band (CB) and the valence band (VB) in a heavily doped semiconductor can intermediate optical excitations of electrons from the VB to the CB. This is so called an intermediate band (IB) material proposed by Luque *et al*., for use in absorption layers of solar cells to increase their conversion efficiency [1].

Based on this hypothesis, we have synthesized and investigated 3*d*-TM-doped AlN films for artificial photochemical system. It is indispensable to reveal potential energies of VB, IB and CB with respect to the vacuum level if the potentials have ability for the water oxidation and hydrogen reduction potentials.

To investigate the potentials of the electron occupied states (VB and/or a part of IB), we carried out total photoelectron yield spectroscopy (TPYS) [2] for the 3*d*-TM doped AlN films deposited on Ti metal substrates. As show in Fig. 1. electrical contacts with the film were made both back (thorough the Ti substrate) and front (a Cu metal plate with hole). A photoelectron corrector was set in front of the film with around 1mm interspace. A negative bias was applied to the sample against the grounded photoelectron corrector. The number of photoelectrons was obtained by measuring the current needed to compensate for the photoexcited holes at the sample with an ammeter. The photoemission yield was measured as a function of incident photon energy.

Figure 2 shows TPY spectra of AlCrN with 17.3, 9.3 and 2.2% Cr and un-intentional doped AlN films. It is clear that the AlCrN films with high Cr concentrations have threshold at around 5.5 eV. This result agrees well with the level of $Cr^{4+/3+}$ [3, 4] and imply a partially filled IB is formed in the energy gap of AlN. We have obtained different thresholds for different 3d-TM elements, which means the potential of IB can be controlled via choice of 3*d*-TM elements, and adjust the band structure for the effective photoconversion. To reveal all potentials of the electron occupied band of the films, we will extend the energy region of the measurements to larger one.

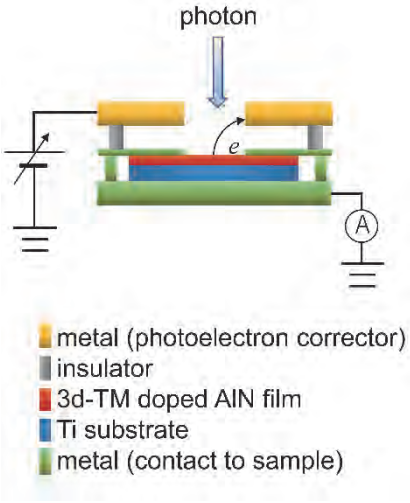

Fig. 1. Schematic of sample setting for the TPYS measurements.

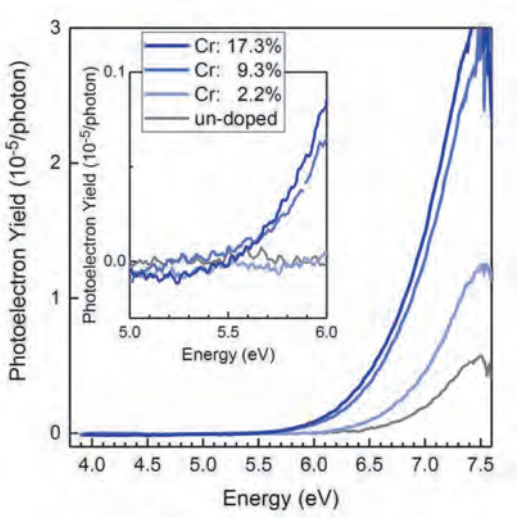

Fig. 2. Total photoelectron yield spectra of AlCrN (Cr: 17.3, 9.3 and 2.2 %) and un-intentional doped AlN films deposited on Ti metal substrates. The inset is magnified view of near thresholds of AlCrN films.

[1] A. Luque *et al*., Phys. Rev. Lett. **78** (1997) 5014.
[2] M. Honda *et al*., J. Appl. Phys. **102** (2007) 103704.
[3] U. Gerstmann *et al*., Phys. Rev. B **63** (2001) 1.
[4] N. Tatemizo *et al*., J. Phys.: Condens. Matter **29** (2017) 085502.

BL3B

Optical Properties of Ag^- Centers Doped in NaI Crystals

T. Kawai and S. Watanabe
Graduate School of Science, Osaka Prefecture University, Sakai 599-8531, Japan

Ag^- centers doped in alkali halide crystals belong to the family of the so-called Tl^+-type centers and exhibit the optical bands called A, B, and C, which are attributed to intra-ionic transitions from the $^1A_{1g}$ ground state to the $^3T_{1u}$, $^3T_{2u}$ +^3E_u, and $^1T_{1u}$ excited states, receptively [1-3]. Though optical studies on the Ag^- centers doped in various alkali halide crystals have been widely performed, no study on the Ag^- centers doped in NaI crystals has been reported until now. In this study, optical properties of the NaI:Ag^- crystals have been investigated at low temperature.

NaI:Ag^+ crystals were grown by the Bridgman method from NaI powders containing AgI powders. The conversion from the Ag^+ to Ag^- ions in the crystals was achieved by an electrolytic coloration technique. The optical measurements were performed at the BL-3B line of UVSOR.

Figure 1 shows the absorption and luminescence spectra of the NaI:Ag^- crystals at 6 K. A remarkable absorption band with a half-width of 0.15 eV is observed at 3.96 eV. The Ag^- centers doped in KI, RbI, and CsI crystals exhibit the C absorption bands at 3.985, 3.888, and 3.770 eV, respectively [1, 2]. As compared with these values, the band peaking at 3.96 eV in NaI:Ag^- is assigned to the C absorption band.

In the NaI:Ag^- crystals, the excitation on the C absorption band induces the two luminescence bands peaking at 2.50 and 3.48 eV at 6K. The excitation spectra for the 2.50 and 3.48 eV luminescence bands are shown in Fig. 2. Both luminescence bands are efficiently excited at the C absorption band. Therefore, the 2.50 and 3.48 eV luminescence bands are assigned to the A' and C' luminescence bands which are attribute to the radiative transitions from the relaxed excited states of $^3T_{1u}$ and $^1T_{1u}$, respectively. In addition to the C band, the excitation spectrum for the A' luminescence band has an excitation band around 2.92 eV. The excitation band would correspond to the A band due to the transition from the $^1A_{1g}$ to $^3T_{1u}$ states. The energy positions of the A, B, and C bands of the Ag^- centers doped in alkali iodide crystals are summarized in Table 1.

It should be noted that the band-shapes of the excitation spectra around the C absorption band are different between the A' and C' luminescence. The excitation band for the A' luminescence roughly reflect the C absorption band, while that for the C' luminescence is located on the slightly lower energy side of the C absorption band. The difference of the excitation band-shape would be concerned with the relaxation processes from the excited states of $^3T_{1u}$ and $^1T_{1u}$. Further studies will probably be necessary.

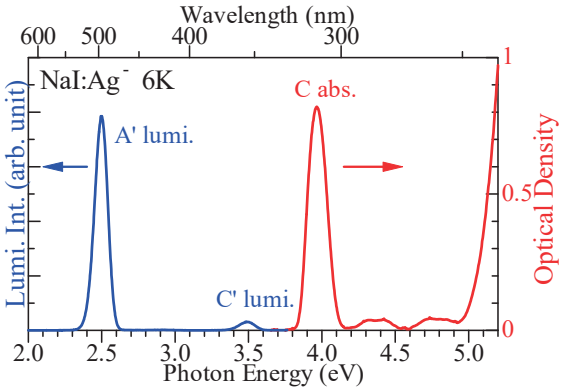

Fig. 1. Luminescence (blue) and absorption (red) spectra of NaI:Ag^- crystals at 6 K.

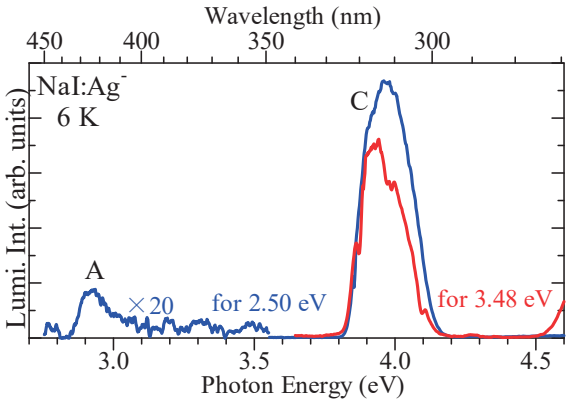

Fig. 2. Excitation spectra detected at 2.50 eV (blue) and 3.48 eV (red) of NaI:Ag^- crystals at 6 K.

Table 1. Energy positions (eV) of the bands of the Ag^- centers doped in alkali iodide crystals.

crystal	A	B	C	Ref.
NaI	2.92	–	3.96	this work
KI	2.878	2.981	3.985	[2]
RbI	–	–	3.888	[1]
CsI	2.776	2.865	3.770	[2]

[1] W. Kleemann, Z. Physik **214** (1968) 285.
[2] W. Kleemann, Z. Physik **248** (1970) 362.
[3] S. Shimanuki, J. Phys. Soc. Jpn. **35** (1973) 1680.

BL3B

Energy Transfer from I^- Centers to Eu^{2+} Centers in Co-Doped NaCl:I^-,Eu^{2+} Crystals

O. Yagi and T. Kawai

Graduate School of Science, Osaka Prefecture University, Sakai 599-8531, Japan

Alkali halide crystals have the wide band-gap up to the vacuum ultraviolet energy region and are suitable candidate hosts for doping of impurity ions. Though many experimental investigations have been performed on alkali halide crystals doped with impurity ions, energy transfer between two kind of impurity ions in co-doped alkali halide crystals is comparatively less studied [1, 2]. In this study, we have investigated the energy transfer from I^- centers to Eu^{2+} centers in NaCl crystals co-doped with I^- and Eu^{2+} ions.

Figure 1 shows the absorption spectrum of NaCl:Eu^{2+} and the luminescence spectrum of the NaCl:I^-. NaCl:Eu^{2+} produces two broad absorption bands in the uv-visible energy region, which are due to transitions from the $4f^7$ ground state to the t_{2g} and e_g components of the $4f^6 5d$ excited state [3]. The samples were annealed for 2h at 600ºC and quenched to disperse precipitations, because Eu^{2+} ions in the alkali halides are well-known to produce precipitations. NaCl:I^- shows the luminescence band appearing around 5.2 eV, which is called the NE luminescence band and comes from the one-center type exciton localized mainly on the central site of a substituted I^- impurity with small lattice relaxation [4]. The NE luminescence band in NaCl:I^- has a large overlap with the absorption band due to the e_g component in NaCl:Eu^{2+}. This fact indicates the potential of the energy transfer from the I^- centers to the Eu^{2+} centers in co-doped NaCl: I^-,Eu^{2+} crystals. According to the Förster model [5, 6], the critical distance between both centers for resonant energy transfer is estimated to be about 1.8 nm from the overlap with the luminescence and absorption bands.

Figure 2 shows the excitation spectra in NaCl:I^-, NaCl:Eu^{2+}, and co-doped NaCl:I^-,Eu^{2+} crystals. The NE luminescence band in NaCl:I^- is efficiently excited in the energy region around 6.7 eV, which corresponds to the absorption band of the I^- centers. In NaCl:Eu^{2+}, the luminescence band at 2.9 eV, which comes from the Eu^{2+} centers, is efficiently excited at the absorption bands of the Eu^{2+} centers.

In the co-doped NaCl:I^-,Eu^{2+} crystals, the excitation spectrum for the 2.9 eV luminescence band of the Eu^{2+} centers has the broad band around 6.7 eV in addition to the absorption bands of the Eu^{2+} centers. This result implies the existence of the energy transfer from the I^- centers to the Eu^{2+} centers in the co-doped NaCl:I^-,Eu^{2+} crystals. In order to clarify the energy transfer mechanism from the I^- centers to the Eu^{2+} centers in the co-doped NaCl:I^-,Eu^{2+} crystals, the measurements of the decay kinetics of the luminescence are needed.

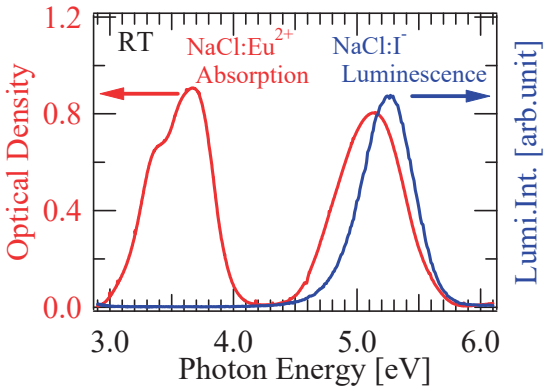

Fig. 1. Luminescence spectrum (blue) of NaCl: I^- and absorption spectrum (red) of NaCl: Eu^{2+} at RT.

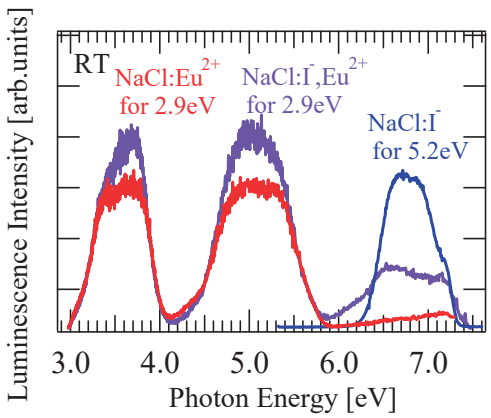

Fig. 2. Excitation spectra of NaCl: Eu^{2+} (red), NaCl: I^- (blue), and co-doped NaCl: I^-, Eu^{2+} (purple) at RT.

[1] A. F. Muñoz and J. O. Rubio, Phys. Rev. B **38** (1988) 9980.
[2] A. Méndez *et al*., J. Lumin. **79** (1998) 269.
[3] J. E. Muñoz-Sautiuste and J. Garcia-Sole, Phys. Rev. B **38** (1988) 10874.
[4] I. Akimoto *et al*., Phys. Status Solidi C **6** (2009) 342.
[5] T. Förster, Disc. Faraday Soc. **27** (1959) 7.
[6] D. L. Dexter, J. Chem. Phys. **21** (1953) 836.

BL3B

Luminescence and Photoexcitation Spectra of TlBr-TlI Mixed Crystals

N. Ohno[1] and K. Matsui[2]

[1]*Fundamental Electronics Research Institute, Osaka Electro-Communication University, Neyagawa 572-8530, Japan*

[2]*Graduate School of Engineering, Osaka Electro-Communication University, Neyagawa 572-8530, Japan*

Thallous halide crystals are compound semiconductors attractive for fabrication of γ ray detectors. They exhibit high stopping power due to high atomic number and high density [1]. TlCl and TlBr crystalize in cubic CsCl-type structure, while the stable form of TlI is orthorhombic structure below 170ºC [2] and is cubic CsCl-type one above it [3, 4]. Therefore, it is difficult to grow a large-sized single crystal of TlI under atmospheric conditions. In the present study, mixed crystals of TlBr-TlI in cubic CsCl-type structure have been grown and examined to reveal the optical properties such as absorption, reflection spectra, and photoluminescence, luminescence excita- tion spectra at low temperatures.

The crystals $TlBr_xI_{1-x}$ were grown by the Bridgeman method from appropriate amounts of TlBr and TlI after distillation and purification. A plate of the sample cut from as-grown crystals was polished with alumina abrasive plastic film, then etched in methyl alcohols containing dilute bromine. The optical measurements were made at 10 K at the BL3B station.

Figure 1 shows luminescence spectra (blue curves) of $TlBr_xI_{1-x}$ mixed crystals of different compositions at 10 K. On exciting $TlBr_xI_{1-x}$ with light at the energy above the indirect absorption edge [4, 6], a Stokes-shifted broad luminescence bands are observed for each crystal. Photoecitation spectra for the luminescence band are shown by black curves in the figure. The luminescence bands are found to be efficiently stimulated at the energy between the fundamental absorption edge transition and the direct exciton transition by indicated by arrows. As clearly seen in Fig.1, the excitation edge for the luminescence band moves to the lower energy with increasing iodine concentration x. In pure TlBr (x=1.0), the excitation edge at 2.64 eV is ascribed to the indirect-forbidden exciton transition [5]. At x=0.4, the absorption edge is located at around 2.0 eV. Below $x \leq 0.3$, no luminescence band was observed, which is caused by the phase transition of the crystal; in iodine-rich mixed crystal, the cubic phase is unstable below the room temperature [4].

In TlBr (x=1.0), the spectral shape of the broad luminescence band is almost Gaussian as previously observed in lightly doped TlBr [5]. The broad band has been identified as annihilation of relaxed excitons due to the impurity-induced self-trapping. It is worth noting that the amount of the Stokes shift and the width of the observed luminescence band in mixed crystals becomes small as the iodine concentration x is increased as clearly seen in the figure. Therefore, with adding iodine ions in TlBr, the lattice relaxation of the self-tapped excitons becomes small, which is ascribed to the weak exciton-phonon interaction.

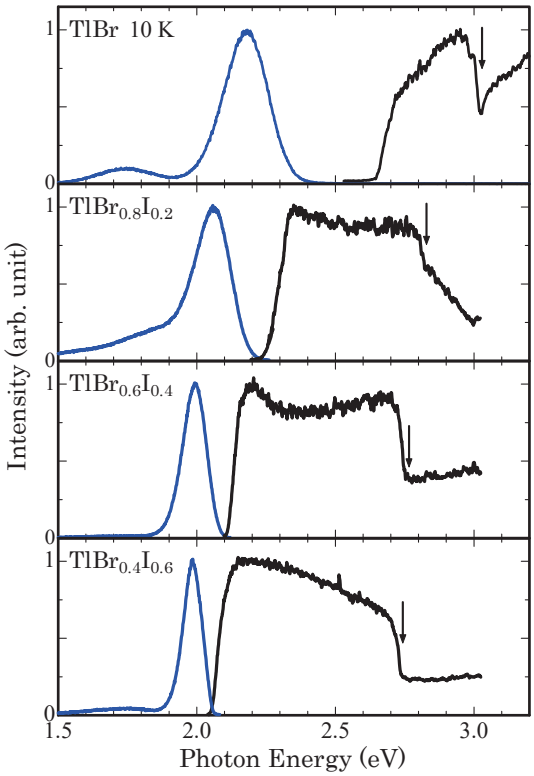

Fig. 1. Luminescence (blue) and photoexcitation (black) spectra of $TlBr_xI_{1-x}$ at 10 K.

[1] K. Hitomi, T. Shoji and K. Ishii, J. Crystal Growth **379** (2013) 93.
[2] N. Ohno and M. Itoh, J. Phys. Soc. Jpn. **62** (1993) 2966.
[3] K. Heidrich, W. Staude, J. Treusch and H. Overhof, Solid State Commun. **16** (1975) 1043.
[4] A. Fujii, J. Phys. Soc. Jpn. **58** (1989) 2173.
[5] K. Takahei and K. Kobayashi, J. Phys. Soc. Jpn. **44** (1978) 1850.
[6] N. Ohno and K. Matsui, UVSOR Activty Report **43** (2016) 65.

BL4U

Improved Photoelectrochemical Performance of Au@TiO_2-coated Fe_2O_3 Nanorods Studied by Scanning Transmission X-ray Microscopy

Y. R. Lu[1, 2], Y. F. Wang[1], Y. C. Huang[1, 2], J. W. Chiou[3], C. L. Dong[1], W. F. Pong[1], T. Ohigashi[4] and N. Kosugi[4]

[1]*Department of Physics, Tamkang University, Tamsui 251, Taiwan*
[2]*Department of Electrophysics, National Chiao Tung University, Hsinchu 300, Taiwan*
[3]*Department of Applied Physics, National University of Kaohsiung, Kaohsiung 811, Taiwan*
[4]*Institute for Molecular Science, Okazaki 444-8585, Japan*

Since Fujishima and Honda had found the photoelectrochemical (PEC) water splitting could be made directly by TiO_2 under UV irradiation thirty years ago, this direct solar fuel conversion is regarded as one of the most promising clean and renewable energy resource. The main drawback of TiO_2 is the bandgap is too large so it can only absorb the UV light. Hematite (α-Fe_2O_3) is a promising material for solar water splitting owing to its smaller band gap energy about 2.1-2.3 eV, which can capture 40% of incident sunlight. However, it is only suitable for oxygen evolution half reaction and electron-hole recombines very easily due to its intrinsic short hole diffusion length and poor electron conductivity. Doping is an effective way to adjust the band edge and overcome the charge transfer ability in hematite.[1-2] In addtion, by taking advantage of plasmonic effect caused by metal nanocrystals, the PEC performance could be further improved. In this work, the hematite nanorods coated with a thin layer of TiO_2 with/without Au nanoparticles embbeded in between have been studied by STXM to elucidate the correlation between the PEC properties and interfacial electonic structures.

Figures 1 present the O *K*-edge (left panel) and Fe *L*-edge (right panel) STXM stack mappings of selected single nanorod of bare-, TiO_2 coated and Au embedded TiO_2-coated Fe_2O_3. The stack mappings display yellow, red and green areas, corresponding to the different regions that are associated with different regions and chemical properties of the nanorods. Figures 1 also present the XANES spectra, which correspond to their stack mappings. While there is no significant difference of XANES of Ti L-edge (not shown here) could be revealed, the variation of both O K-edge and Fe L-edge are observed. Spectroscopic results indicate the surface region contains more defects compared with core region, which enhance the density of states both in O and Fe sites. However, the TiO_2 layer and embedded Au nanoparticles may inhibit the charge recombination.

The enhanced PEC performance of TiO_2-coated Fe_2O_3 with Au nanoparticles embedded is likely to be not only the plasmonic effect caused by Au nanoparticles, but also the intrinsic improvement of charge transfer ability that is attributable to embedded Au nanoparticles.

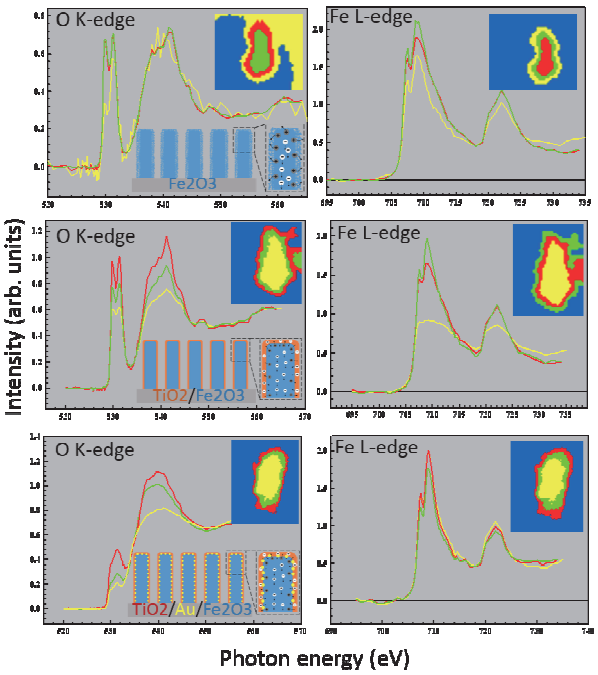

Fig. 1. O *K*-edge (left panel) and Fe *L*-edge (right panel) scanning transmission X-ray microscopy image and its corresponding stack mappings of selected single (top) bare-, (middle) TiO_2-coated, and (bottom) TiO_2/Au- coated Fe_2O_3 nanorod.

[1] Y. Fu *et al.*, Chem Nano Mat **2** (2016) 704.
[2] Y. Fu *et al.*, Phys. Chem. Chem. Phys. **18** (2016) 5203.
[3] Y. R. Lu *et al.*, to be submitted.

BL4U

Structural Identification of Cellulose Nanocrystal/Nanofibril Hybrids and Composites Using Soft X-ray Techniques

M. Y. Ismail[1], M. Huttula[2], M. Patanen[2], H. Liimatainen[1], T. Ohigashi[3] and N. Kosugi[3]
[1]*Fibre and Particle engineering unit, University of Oulu, P.O. Box 3000, 90014 University of Oulu, Finland*
[2]*Nano and Molecular Systems unit, University of Oulu, P.O. Box 3000, 90014 University of Oulu, Finland*
[3]*UVSOR Synchrotron, Institute for Molecular Science, Okazaki 444-8585, Japan*

Nanocellulose hybrids are high strength materials consisting of cellulose nanofibrils or nanocrystals embedded in a continuous biopolymeric matrix with additives such as mineral nanoparticles. In the present work, the structure of the hybrid formed of nanosilica, nanocellulose (cellulose nanofibrils) and chitosan matrix is studied. The critical factors affecting the mechanical performance of these materials are the interaction between the constituents and their spatial distribution. So far, these properties have mainly been analysed using electron microscopy techniques (TEM and SEM), but they possess limited ability to localize nanocellulose and biopolymers within the hybrid structure (e.g. to determine interactions between minerals and nanocelluloses). Therefore, novel methods are desired to better address the structural details of the hybrids. Previously, soft X-ray spectroscopy has shown to be able to identify the localized distribution of biopolymers, but based on our best knowledge this methodology has not been used for nanocellulose hybrids. This report shows significant new outcomes on structural characteristics of nano-scale hybrids based on nanocelluloses.

Chitin is one of the most abundant natural biopolymers and it is used for the production of chitosan by deacetylation [1]. Chitosan is antibacterial, non-toxic, and biodegradable; thus, it can be used for the production of biodegradable films which are potential green alternatives for commercially available synthetic counterparts. However, poor mechanical and thermal properties of chitosan restrict its wide spread applications. Consequently, hybrids fabricated from chitosan matrix reinforced by nanofibers are attractive materials to develop sustainable products [2].

The aim of the present work was to obtain a nano-scale spatial distribution of constituents within the hybrid. The hybrids had constant nanocelluloses: chitosan ratio of 50:50, and variable nanosilica content (5-30%). The samples (thickness of 100 nm) were prepared from solution casted hybrid films using an ultramicrotome. Pure nanocellulose, nanosilica and chitosan samples were used as references.

The samples were exposed to soft X-ray radiation at BL4U beamline at UVSOR synchrotron. The absorption at carbon 1s-edge was recorded for investigation of the nanocellulose and the matrix distribution, with photon energies between 280 and 300 eV. The Si 2p absorption edge around 100 to 130 eV was utilized for the same spatial parts of the sample for observing the distribution of nanosilica on the hybrid.

Figure 1 presents examples of the image data of the 30% nanosilica sample. In the first preliminary interpretation the nanosilica (Si2p on leftmost) appears to be concentrated on the fiber bundles of the sample. The nanocellulose fibers were found to provide somewhat characteristic absorption structure (Fig.2.), matching the intense absorption patterns on the Fig.1. Similarly the appearance of smaller “dots” of nanosilica on the fibers were also found in the sample containing only 5% of the nanosilica.

The obtained data seem to provide a strong evidence of the agglomeration of the nanosilica at the nanofibers. Indications on the spectral changes in the Si rich regions suggest also possible chemical binding mechanism of the nanoselluloce and nanosilica. The present data will give valuable information of behavior of the additive mineral which will affect the mechanical properties of composite hybrid materials.

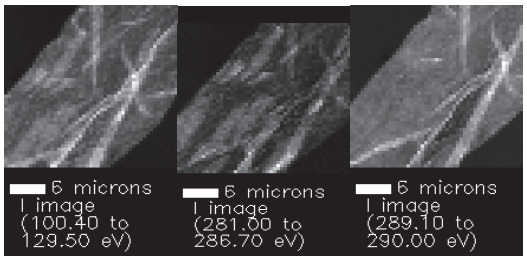

Fig. 1. STXM images for 30% nanosilica sample.

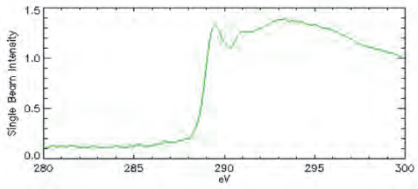

Fig. 2. The C1s absorption reference for nanocellulose fibers.

[1] Abdul Khalil H.P.S. Chaturbhuj K. Saurabha, Adnan A.S., *et al*., Carbohydrate Polymers **150** (2016) 216.
[2] R. J. Moon, A. Martini, J. Nairn, J. Simonsen and J. Youngblood, Chemical Society Reviews **40** (2011) 3941.

BL4U

Dopant Effect of Lead(II) Thiocyanate ($Pb(SCN)_2$) for $FA_{0.9}Cs_{0.1}PbI_3$ Perovskite Solar Cells

M. W. Lin[1], M. H. Li[2], H. W. Shiu[1], Y. L. Lai[1], T. Ohigashi[3], N. Kosugi[3], P. Chen[2] and Y. J. Hsu[1, 2]

[1]*National Synchrotron Radiation Research Center, Hsinchu 300, Taiwan*
[2]*Department of Photonics, National Cheng Kung University 701, Tainan, Taiwan*
[3]*Institute for Molecular Science, Okazaki 444-8585, Japan*

Thiocyante ($Pb(SCN)_2$), as a dopant in perovskite $FA_{0.9}Cs_{0.1}PbI_3$ (FA: $HC(NH)_2$), and mesoscopic titania (mp-TiO_2) as scaffold/electron-transport layer show high power conversion efficiencies (PCEs) up to 15.1%. Herein we studied the origin of such high PCEs in terms of morphology and chemical structure of mp-TiO_2/$Pb(SCN)_2$ doped- $FA_{0.9}Cs_{0.1}PbI_3$ heterojunction by scanning electron microscopy (SEM) and scanning transmission X-ray microscopy (STXM).

In SEM studies (Fig. 1), the $Pb(SCN)_2$ doped-$FA_{0.9}Cs_{0.1}PbI_3$ displays much larger perovskite crystalline than $FA_{0.9}Cs_{0.1}PbI_3$. More than 70% of the larger crystals in 5% $Pb(SCN)_2$ doped- $FA_{0.9}Cs_{0.1}PbI_3$ crystals exhibit a size distribution in the range of 0.8-1 μm size. Increasing $Pb(SCN)_2$ dopant to 10% in $FA_{0.9}Cs_{0.1}PbI_3$, the size of perovskite crystals decrease to the 0.5 μm and display homogeneous distribution. The large crystals in the perovskite bulk film are beneficial for charge transport in the perovskite,[1] that is possible to explain 5% $Pb(SCN)_2$ doped- $FA_{0.9}Cs_{0.1}PbI_3$ has best PECs than the others.

To further examine the effects of adding $Pb(SCN)_2$ on the crystalline morphology, chemical maps of N *K*-edge and Ti *L*-edge were acquired to obtain the distributions of micro-aggregates of SiN/mp-TiO_2/5% and 10% $Pb(SCN)_2$ doped- $FA_{0.9}Cs_{0.1}PbI_3$ by STXM. Figure 2 displays the STXM images of SiN/mp-TiO_2/5% $Pb(SCN)_2$ doped- $FA_{0.9}Cs_{0.1}PbI_3$ (Fig. 2(a)), and SiN/mp-TiO_2/10% $Pb(SCN)_2$ doped-$FA_{0.9}Cs_{0.1}PbI_3$ (Fig. 2(b)) which are optical density (OD) maps obtained at 403.5 eV for N *K*-edge and 457 eV for Ti *L*-edge, the characteristic absorption peaks of $FA_{0.9}Cs_{0.1}PbI_3$ and mp-TiO_2, respectively. The N mapping on above samples show similar distribution in morphology and size to SEM results. The 5% $Pb(SCN)_2$ doped- $FA_{0.9}Cs_{0.1}PbI_3$ shows grain size of ~1 μm, and decrease to 0.5 μm when 10% $Pb(SCN)_2$ doped. However, we notice some additional line shape and large aggregation as shown in red color in the composite images, that is determined as TiO_2 nanoparticles which are in a uniform diameter of 2–5 μm and appear to be more uniformly dispersed in the sample of 5% $Pb(SCN)_2$ doped- $FA_{0.9}Cs_{0.1}PbI_3$. It suggests 5% $Pb(SCN)_2$ dopant has effective charge transfer between perovskite and TiO_2. Fig. 2(c) and (d) show the micro-scpectra of N *K*-edge and Ti *L*-edge extracted from 5% and 10% $Pb(SCN)_2$ doped-$FA_{0.9}Cs_{0.1}PbI_3$ film. We notice that both N and Ti spectra exhibit dissimilar in peak ratio and shape between 5% and 10% $Pb(SCN)_2$ doped sample. It implies that the interaction between mp-TiO_2 and perovskite may be play a key role in determining the PCEs performance.

In conclusion, STXM results clear show that morphology variation attributed by TiO_2 and $Pb(SCN)_2$, and also illustrate that an important chemical interaction between mp-TiO_2 and perovskite.

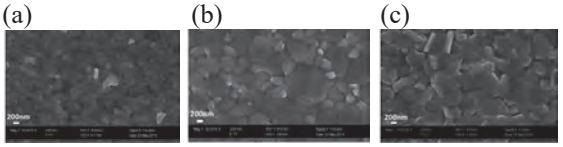

Fig. 1. The SEM image of (a) $FA_{0.9}Cs_{0.1}PbI_3$, (b) 5% $Pb(SCN)_2$ doped- $FA_{0.9}Cs_{0.1}PbI_3$, and (c) 10% $Pb(SCN)_2$ doped- $FA_{0.9}Cs_{0.1}PbI_3$.

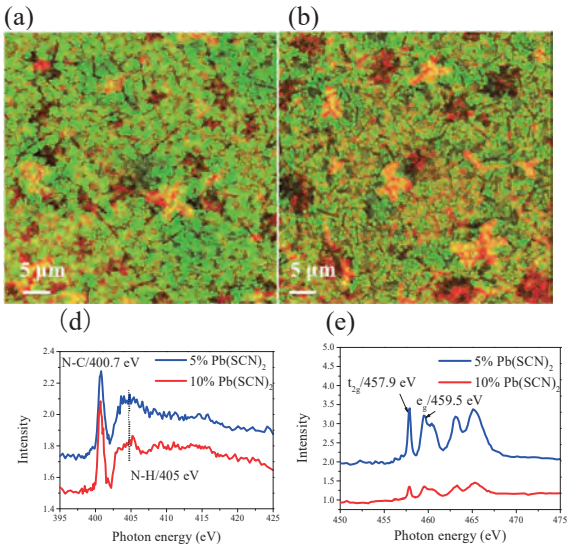

Fig. 2. OD mapping of Ti *L*-edge (red) and N *K*-edge (green) of (a) SiN/mp-TiO_2/5% $Pb(SCN)_2$ doped-$FA_{0.9}Cs_{0.1}PbI_3$, and (b) SiN/mp-TiO_2/10% $Pb(SCN)_2$ doped- $FA_{0.9}Cs_{0.1}PbI_3$. (c) and (d) micro-spectra of N *K*-edge and Ti *L*-edge extracted from (a) and (b), respectively.

[1] Z. Xiao, *et al.*, Adv. Mater. **26** (2014) 6503.
[2] M.-W. Lin, *et al.*, Adv. Mater. Interfaces **3** (2016) 1600135.

BL4B

Valence State Analysis of Fe Ions in $LaGaO_3$

Y. Osada[1] and T. Yamamoto[1, 2]
[1]*Faculty of Science and Engineering, Waseda University, Tokyo 169-8555, Japan*
[2]*Institute of Condensed-Matter Science, Waseda University, Tokyo 169-8555, Japan*

Solid Oxide Fuel Cell (SOFC) has been widely studied because of its importance as one of the energy sources. Among the SOFCs, $LaGaO_3$ has been extensively investigated because of its high oxygen ion conductivity. In order to increase its ionic conductivity, incorporation of Sr^{2+} and Mg^{2+} ions in $LaGaO_3$ were proposed, so-called LSGM, which can produce oxygen vacancies in the material to keep the charge neutrality. It was reported that additional incorporation of Co ions in LSGM increase ionic conductivity. [1] Although it is quite important to know the charge state of such transition elements in LSGM for the understanding of increase of ionic conductivity owing to the additional ion incorporation, such investigations have not yet been carried out. In the current study, valence state of the Fe ions in $LaGaO_3$ was examined as a proto-type experiment by measuring the Fe-L_3 X-ray absorption spectrum (XAS).

All the samples were synthesized with the conventional solid-state reaction method changing the concentration of Fe ions, i.e., x = 0, 0.05, 0.1 and 0.15 in LaGa1-xFexO3. High purity powders of La2O3, Ga2O3 and Fe2O3 were used as starting materials. For precise weighing, La2O3 were dried at 773 K for 30 min. in air prior to weighing. These powders were mixed in an agate mortar for 30 min., which were calcined in air at 1273 K for 6 hours. Resultant powders were ground again in an agate mortar, which were pressed into a pellet form (10 mmϕ). Finally, these pellets were sintered in air at 1773 K for 6 hours.

The synthesized specimens were characterized by the powder X-ray diffraction with Cu-Kα X-ray irradiation, which showed all the samples were crystallized in a single-phased orthorhombic perovskite structure.

Cell volumes were obtained from the observed XRD patterns, which are shown in Fig. 1. As shown in this figure, cell volumes increase as increment of Fe concentration, which suggests that Fe ions substitute at Ga^{3+} site as divalent or trivalent ions from a viewpoint of ionic radius. [2]

Fe-L_3 XAS were recorded at BL-4B with the total electron yield method. Incident beam was monochromatized with the varied-space grating (800 lines/mm), which was irradiated onto the sample. Sample powders were put on the carbon adhesive tape, which was attached on the first dinode of the electron multiplier.

Observed Fe-L3 XAS of Fe ions incorporated in LaGaO3 were shown in Fig. 2 together with those of Fe oxides. Fe-L3 profile of Fe ions in LaGaO3 are quite similar, which suggests that local environment and valence state of the Fe ions are almost identical. In addition, the profile is close to that of α-Fe_2O_3, which can confirm the valence state of Fe ions in $LaGaO_3$ is trivalent.

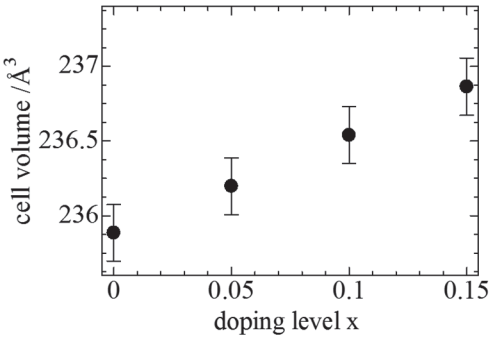

Fig. 1. Cell volumes of Fe incorporated $LaGaO_3$, $LaGa_{1-x}Fe_xO_3$.

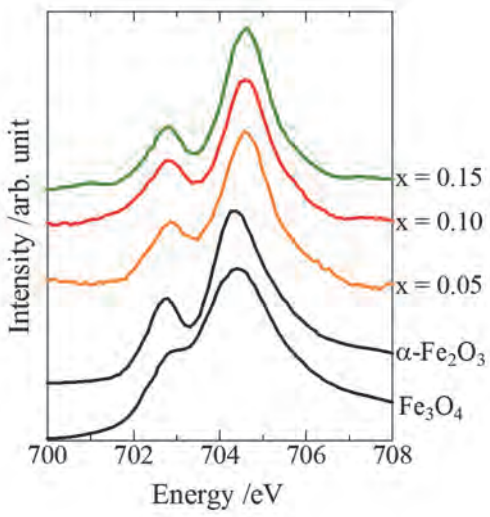

Fig. 2. Observed Fe-L_3 XAS spectra of Fe doped $LaGaO_3$ and Fe oxides.

[1] T. Ishihara *et al.*, Chem. Mater. **11** (1999) 2081.
[2] R.D. Shanon, Acta Crystallogr. **A32** (1976) 751.

BL4B

Thickness Dependence of Spin and Orbital Magnetic Moment of Ultrathin Magnetic Films: Au/Fe/Au and MgO/Fe/Au

S. Yamamoto[1], K. Yamamoto[1], Y. Hirata[1], K. Fukuta[2], D. Oshima[3], T. Kato[2], S. Iwata[3], H. Wadati[1] and I. Matsuda[1]

[1] *Institute for Solid State Physics, The University of Tokyo, Kashiwa 277-8581, Japan*
[2]*Department of Electrical Engineering and Computer Science, Nagoya University, Nagoya 464-8603, Japan*
[3]*Nagoya University, IMaSS, Nagoya 464-8603, Japan*

Interface magnetism has been one of the central topics for investigating fundamental magnetic properties. They range from the relation between the dimensionality and the magnetic structure to the control of magnetism by the electric field rather than by electric current or magnetic field. Thinner magnetic film systems have a larger contribution from the interface to the magnetism. Furthermore, it is expected that an interfacial spin-orbit interaction enhances the perpendicular magnetic anisotropy (PMA) of magnetic layers. However the effect of spin-orbit interaction on interface magnetism has not been investigated systematically so far [1].

In our previous study, we have investigated interfacial perpendicular magnetic anisotropy (PMA) energy of an ultrathin magnetic system, Au/Fe/Au, comparing with a reference system, MgO/Fe/Au [2]. By utilizing a torque magnetometer, it was revealed that PMA energy in the Au/Fe/Au system had a smaller interfacial PMA energy (455 μJ/cm^2) than that in the MgO/Fe/Au system (696 μJ/cm^2). In order to reveal the origin of the interfacial PMA for both systems, we measured thickness dependence of Fe 2*p* X-ray absorption spectroscopy (XAS) and X-ray magnetic circular dichroism (XMCD) at BL4B in UVSOR.

Samples were fabricated using a molecular beam epitaxy method before the beamtime. All of the layers were evaporated at room temperature using electron beam evaporator in an ultrahigh vacuum (7.0E-8 Pa). The epitaxial growth was confirmed by observing RHEED pattern during evaporation for both magnetic systems. The sample structure is Au(2 nm)/Fe(0.29 – 1.4 nm)/Au(25 nm)/Cr(5 nm)/MgO(001) (substrate, 0.5 mm) for Au/Fe/Au system. The top Au layer avoids oxidation of magnetic layer. The MgO/Fe/Au system has a similar structure except for being MgO layer with a thickness of 2 nm inserted between top Au and Fe layer. We confirmed that the Fe layer had not oxidized in the measurement by Fe 2*p* XAS measurements.

Measurements were conducted with a total-electron yield mode at 10 K. The samples were cooled down with a liquid He. External magnetic field, ± 2 T was applied parallel to the incident light. The sample surface was perpendicular to the incident light. The XAS (XMCD) was extracted from the sum (difference) of absorption spectra measured under applying positive and negative external field. By applying magneto-optical sum-rule for 2*p* edge XMCD, the spin and orbital magnetic moment were extracted. The Fe thickness dependence of the magnetic moment is shown in Fig. 1. In the figure, magnetic moment is expressed in the unit of μ_B/hole. We adopted this notation because in the ultrathin magnetic films, the hole number is not trivial. Furthermore, spin magnetic moment (m_{spin}^{eff}) includes magnetic dipole moment. It indicates that in both systems, larger orbital moments were observed with reducing Fe film thickness with respect to the value of bulk bcc Fe. On the other hand, the spin magnetic moment does not depend on the Fe film compared to the orbital moment. It was shown that the PMA originates from the orbital moment in both systems. The variation of orbital magnetic moment of Au/Fe/Au was smaller than that of MgO/Fe/Au system, which was consistent with our previous measurements of interfacial PMA energy.

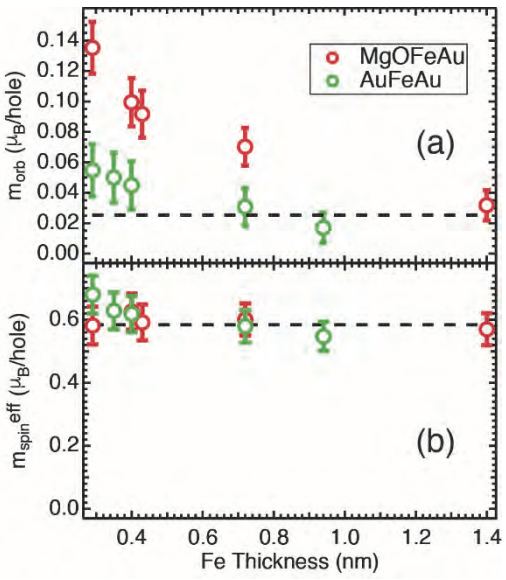

Fig. 1. Fe thickness dependence of (a) orbital (m_{orb}) and (b) spin (m_{spin}^{eff}) magnetic moment. The dashed line shows correspondent value for bulk bcc Fe.

[1] C. A. F. Vaz *et al.*, Rep. Prog. Phys. **71** (2008) 056501.
[2] J. Okabayashi *et al.*, Appl. Phys. Lett. **105** (2014) 122408.

BL5U

Electronic Structure of $Ba_{0.75}K_{0.25}Fe_2As_2$ Observed by ARPES

S. Ideta[1], M. Nakajima[2] and K. Tanaka[1]

[1]*National Institutes of Natural Science, Institute for Molecular Science, Okazaki, 444-8585, Japan*

[2]*Department of Physics, Graduate School of Science, Osaka University, Toyonaka 560-0043, Japan*

Iron-based superconductors have a complex phase diagram with the antiferromagnetic (AFM) transition and the structural phase transition. Recently, nematicity, defined as broken rotational symmetry [a trigonal(C_4)-to-orthorhombic (C_2) structural transition], has shed light on the understanding of the mechanism on the iron-based superconductivity [1-4]. In hole-doped $BaFe_2As_2$ (Ba122) system, inelastic neutron diffraction experiments of $Ba_{1-x}Na_xFe_2As_2$ and $Ba_{1-x}K_xFe_2As_2$ (K-Ba122) have shown the magnetic order without C_4 symmetry breaking [5, 6]. This indicates that the magnetism can survive even in the absence of orbital order. Besides, the superconductivity is suppressed between the superconductivity and the C_4-magnetic phase. The electronic structure at the C_4 magnetic phase has been unclear yet, and it would give us a great interest to elucidate the mechanism of the hole-doped Ba122.

Here, we have investigated the electronic structure of detwinned $Ba_{0.75}K_{0.25}Fe_2As_2$ to elucidate the occupied d_{xz} and d_{yz} states, reflecting the nematic ordering [3, 4]. As a first step, we demonstrated an angle-resolved photoemission spectroscopy (ARPES) experiment to confirm the electronic structure of the twinned K-Ba122 ($x \sim 0.25$) with the C_4-magnetic phase as shown in Fig. 1(a).

High-quality single crystals of $Ba_{0.75}K_{0.25}Fe_2As_2$ ($T_c \sim 25$ K) were grown by self-flux technique. ARPES experiments were carried out at BL 5U of UVSOR using the linearly polarized light of $h\nu$ = 32 eV-60 eV photons. Temperature was set at T = 5 and 45 K and clean sample surfaces were obtained for the ARPES measurements by cleaving single crystals *in-situ* in an ultrahigh vacuum better than 1×10^{-8} Pa.

In order to confirm the electronic structure of K-Ba122 ($x \sim 0.25$) in the k_z direction, we have performed FS mapping as shown in Fig. 1(b). From the three-dimensional shape of the FS, we found that the inner potential is $V_0 \sim 15.6$ eV which is similar to the previous ARPES study [7].

Figure 1(c) shows the ARPES intensity mapping in the two-dimensional k_x-k_y plane taken at $h\nu$ = 60 eV corresponding to the Z point. The electronic structure does not show clearly the band folding due to the spin-density-wave formation. We consider that we would need to study the temperature dependence and understand the band folding in detail.

In summary, we have performed an ARPES study of K-Ba122 ($x \sim 0.25$) and measured in- and out-of-plane ARPES intensity maps. We found that the inner potential is V_0 = 15.6 eV which is similar to the previous ARPES study and the electronic structure shows almost the same. We will demonstrate an ARPES study in detail using detwinned K-Ba122 and the temperature dependence in future work.

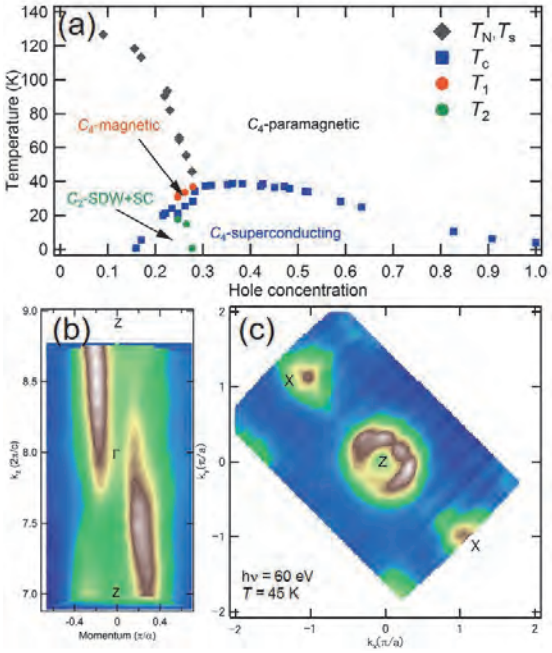

Fig. 1.(a) Phase diagram of hole-doped $Ba_{1-x}K_xFe_2As_2$ taken from Ref. [6]. T_N, T_s, and T_c denote the temperature of the magnetic, structural, and superconducting phase transition, respectively. T_1 and T_2 show the C_4-magnetic phase and superconductivity-induced reentrance of the C_2-SDW phase, respectively. (b) ARPES intensity map taken at $h\nu$ = 60 eV (T = 45 K), corresponding to the Z point (left) and FS mapping in the $k_{\parallel}$-k_z mapping taken from $h\nu$ = 32 eV–56 eV (right) (T = 5 K).

[1] R. M. Fernandes *et al.*, Nat. Phys. **10** (2014) 97.
[2] R. M. Fernandes *et al.*, Phys. Rev. Lett. **111** (2013) 127001.
[3] T. Shimojima *et al.*, Phys. Rev. B **90** (2014) 12111 (R).
[4] Y. Ming *et al.*, PNAS **108** (2011) 6878.
[5] L. Wang *et al.*, Phys. Rev. B **93** (2016) 014514.
[6] A. E. Böhmer *et al.*, Nat. Commun. **6** (2015) 7911.
[7] Y. Zhang *et al.*, Phys. Rev. Lett. **105** (2010) 117003.

BL5U

Electronic Structure of MAX Phase Compound Cr_2AlC Studied by Angle-resolved Photoemission Spectroscopy

T. Ito[1, 2], T. Fujita[2], D. Pinek[3], M. Nakatake[4], S. Ideta[5], K. Tanaka[5] and T. Ouisse[3]

[1]*Synchrotron Radiation Research Center, Nagoya University, Nagoya 464-8603, Japan*
[2]*Graduate School of Engineering, Nagoya University, Nagoya 464-8603, Japan*
[3]*Université Grenoble-Alpes, CNRS, LMGP, F-38000 Grenoble, France*
[4]*Aichi Synchrotron Research Center, Seto, 489-0965, Japan*
[5]*Institute for Molecular Science, Okazaki 444-8585, Japan*

MAX phase compounds, i.e., $M_{n+1}AX_n$ where M is a transition metal, A belongs to groups 13-16 and X is the C or N element, have recently attracted much attention due to their possible application to the production of a new class of two-dimensional systems called MXenes, obtained by removing the A atom planes [1]. On the other hand, the bulk electronic structure of MAX phase has been studied mostly through *ab initio*, density functional theory (DFT) calculations, mainly due to a lack of single crystalline samples. In this study, we have for the first time performed angle-resolved photoemission spectroscopy (ARPES) on single crystals of the MAX phase compound Cr_2AlC [2] in order to directly investigate the bulk electronic structure of this system.

ARPES measurements were performed at the beamline BL5U of UVSOR-III. Clean surfaces were obtained by *in situ* cleaving.

Figure 1 shows the Fermi surface of Cr_2AlC along ΓMK plane obtained by using hν = 65 eV photons. The photon energies corresponding to high-symmetry k_z points were obtained by using normal-emission ARPES, where the inner potential has been estimated to be 15.5 eV. The band structure along the ΓK cut (orange line in Fig. 1) is shown in Fig. 2(a) together with the band calculation (Fig. 2(b) [3]). From the present ARPES study, it has been found that the electronic structure near the Fermi level (E_F) of Cr_2AlC consists of a few closed electron-like Fermi surfaces (FS's) around the Γ point (e, e') as well as hole-like FS around the M point (h). From the comparison with the band structure calculations [3], we have found that the observed Fermi surface topology seems to be consistent with the calculation. On the other hand, we have found the qualitative difference of the band width of the electron pockets, possibly due to some mass enhancement ($m^*/m_{cal.} \sim 2$) of the carriers.

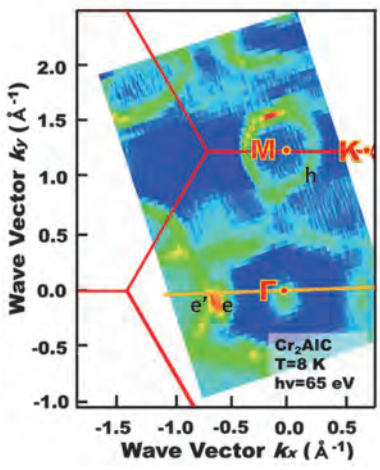

Fig. 1. Fermi surface image of Cr_2AlC along ΓMK plane. Orange line corresponds to ARPES cut shown in Fig. 2 (a).

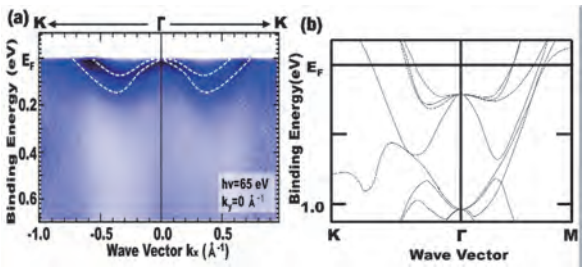

Fig. 2. (a) Band structure of Cr_2AlC along ΓK line. Dashed lines are guide for the eye. (b) Band structure calculations of Cr_2AlC [3].

[1] M. Barsoum, *MAX phases* (Wiley, Weinheim, 2013).
[2] T. Ouisse *et al.*, J. Cryst. Growth **384** (2013) 88.
[3] S. Cui *et al.*, J. Solid State Chem. **191** (2012) 147.

BL5U

Search for a Nematic State in the Cuprate Superconductor Bi2212 by Angle-resolved Photoemission Spectroscopy

S. Nakata[1], M. Horio[1], K. Koshiishi[1], K. Hagiwara[1], C. Lin[1], S. Ideta[2], K. Tanaka[2], D. Song[3], Y. Yoshida[3], H. Eisaki[3] and A. Fujimori[1]

[1]*Department of Physics, University of Tokyo, Tokyo 113-0033, Japan*
[2]*UVSOR Facility, Institute for Molecular Science, Okazaki 444-8585, Japan*
[3]*National Institute of Advanced Industrial Science and Technology (AIST), Tsukuba 305-8568, Japan*

In cuprate superconductors, to understand the origin of the pseudogap region in the phase diagram remains a most significant issue. Recently, experimental evidence for several kinds of order (e.g. charge density wave, spin density wave, electronic nematic order) has been reported in the pseudogap region [1]. Electronic nematicity, which does not break the translational symmetry but breaks the fourfold rotational symmetry of the lattice, has been reported below the pseudogap temperature and may play an important role in the pseudogap region [2]. For instance, evidence for electronic nematicity appeared in $YBa_2Cu_3O_{6+x}$ from transport [3, 4], neutron scattering [5] and magnetic susceptibility [6] measurements and in $Bi_2SrCaCu_2O_{8+\delta}$ from resistivity measurement [7].

Electronic nematicity has been discussed also in Fe-based superconductors [8] and studied by angle-resolved photoemission spectroscopy (ARPES) [9], which is the most direct way to reveal the electronic structure. However, at the moment, there has been no report that reveals the electronic nematicity in cuprates by ARPES. We performed ARPES measurements in order to study the electronic nematicity in cuprates. Furthermore, by ARPES one can investigate whether the electronic nematicity is specific to the pseudogap state or remains in the superconducting state.

$Bi_{1.7}Pb_{0.5}Sr_{0.9}CaCu_2O_{8+\delta}$ (Pb-Bi2212) single crystal samples were grown by the floating-zone method. It was nearly optimally doped sample and T_c was 91 K. ARPES measurements were carried out at UVSOR BL5U. We used linearly polarized light with $h\nu$ = 60 eV. The total energy resolution was set at 10 meV. The samples were cleaved *in-situ* under the pressure of ~ 2 × 10^{-8} Pa. In order to obtain big signals of electronic nematicity, mechanical strain was applied in the direction of the Cu-O bond.

Figure 1 shows Fermi surface plots determined from momentum distribution curves at the Fermi level taken at 200 K, 100 K, 50 K and 5 K. In order to detect the possible anisotropy of the Fermi surface, we used tight-binding fitting function with x and y axis anisotropy ($\varepsilon(k_x,k_y)$ = $-2t[(1+\delta)\cos k_x+(1-\delta)\cos k_y]$ – $4t'\cos k_x\cos k_y$ $-2t''(\cos 2k_x+\cos 2k_y)$ + E_0). Figure 2 shows the temperature dependence of the anisotropy parameter δ, representing anisotropy in the tight-binding parameter. So far, we have not been able to identify definitive evidence for electronic nematicity due to the lack of accuracy. Further measurements with improved accuracy are necessary.

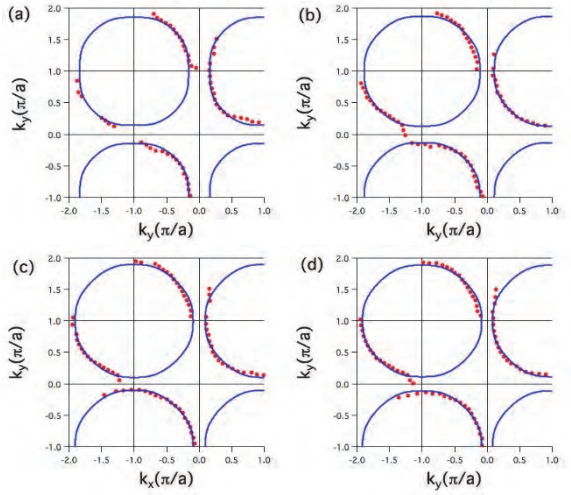

Fig. 1. Fermi surface plots (red points) and fitting curves (blue line) at (a) 200 K, (b) 100 K, (c) 50 K and (d) 5 K, respectively.

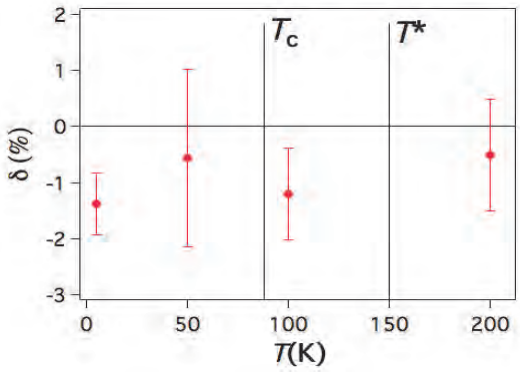

Fig. 2. Temperature dependence of δ representing the anisotropy of the nearest-neighbor tight-binding parameter *t*.

[1] B. Keimer *et al.*, Nature **518** (2015) 179.
[2] S. A. Kivelson *et al.*, Nature **393** (1998) 550.
[3] Y. Ando *et al.*, Phys. Rev. Lett. **88** (2002) 137005.
[4] R. Daou *et al.*, Nature **463** (2010) 519.
[5] V. Hinkov *et al.*, Science **319** (2008) 597.
[6] Y. Sato *et al.*, JPS fall meeting (2016) 14pJC-5.
[7] K. Ishida *et al.*, JPS fall meeting (2016) 14pJC-12.
[8] S. Kasahara *et al.*, Nature **486** (2012) 382.
[9] M. Yi *et al.*, PNAS **108** (2011) 6878.

BL5U

Preparation of Au(111) Reconstructed Surfaces Toward the Understanding of Fe/Au Spin-orbit Coupled Interfaces

J. Okabayashi[1*], S. Ideta[2] and K. Tanaka[2]
[1]*Research Center for Spectrochemistry, University of Tokyo, Tokyo 113-0033, Japan*
[2]*UVSOR, Institute of Molecular Science, Okazaki 444-8585, Japan*

The gold Au(111) surfaces are investigated extensively by means of scanning tunneling microscopy and angle-resolved photoemission spectroscopy (ARPES) because this surface exhibits the large Rashba-type spin-orbit splitting. Large spin-orbit interaction in the heavy element of gold brings the wide varieties for the topological physics and spin-orbit coupled sciences not only in the bulk but also in the surface and interfaces. The Rashba splitting of 110 meV in Au(111) surface was reported firstly by LaShell *et al.* [1]. Recently, the interfaces between Au(111) and other heavy elements such as Bi or Ag have been researched extensively [2, 3]. On the other hand, the interfaces between Au(111) and functional molecules are also investigated [4]. Here, we focus on the interfaces between ferromagnetic materials and Au(111) interfaces because the thin Fe layers on the heavy elements exhibit the perpendicular magnetic anisotropy (PMA) through the spin-orbit interaction.

In the research fields of *spintronics*, the spin-orbit coupling between the ferromagnetic 3*d* transition metal Fe or Co and 5*d* heavy elements of non-ferromagnetic materials such as Pt and Au has been utilized for the PMA through the proximity at the interfaces. It is believed that the future researches concerning not only spins but also orbitals are recognized as the *orbitornics*. Therefore, to clarify the origin of the PMA at these interfaces is a crucial role for future *spin-orbitronics*. The relationship between Au(111) Rashba-type spin-orbit interaction and PMA in 3*d* TMs has not been clarified explicitly. In order to investigate the orbital-resolved states in the Fe films showing the PMA, ARPES at the interfaces becomes the powerful techniques through the photon-energy and polarization dependences in each 3*d* orbital. By using ARPES, we aim to understand the orbital-resolved electronic structures at the magnetic interfaces on Au(111) Rashba-type surfaces in order to develop the researches of novel PMA using spin-orbit coupled interfaces.

In the project proposed in 2016, we planned to prepare the clean Au(111) surface for the deposition of Fe. The single-crystalline 200-nm-thick Au(111) films grown on mica (Phasis, Switzerland) were used as substrates. At the beamline 5U in UVSOR, we performed the Ar-ion sputtering at 1 kV accelerating voltage and subsequent annealing at 500 °C under the high vacuum conditions with repeated cycles. After the preparation, the samples were transferred to the ARPES chamber. We performed ARPES at 160 K using the photon energy of 45 eV because of the large cross-section of Au(111) surface states.

We successfully detected the band dispersions in the Au(111) surface states are shown in Fig. 1. The parabolic dispersions derived from the surface states are observed. Clear Rashba splitting in the mapping of surface states can be observed.

Considering this experiment, we plan to detect more precise band dispersions and the modulation of these bands by the ultra-thin Fe deposition. In order to achieve the purpose, we will perform the following tasks;

(i) the preparation of clear Au(111) surface and the observation of low-energy diffraction patterns
(ii) the determination of precise Fe deposition rates
(iii) Au deposition onto the Fe layers.

After performing above tasks, the spin and electronic states in the Rashba-type spin-orbit coupled interfaces combining both ARPES and X-ray magnetic circular dichroism are clarified.

We acknowledge the fruitful comments and discussion with Assistant Professor H. Yamane in IMS.

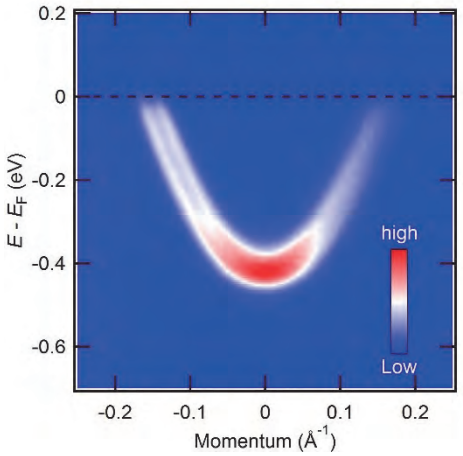

Fig. 1. ARPES of Au (111) surface states near the Fermi level.

[1] S. LaShell *et al.*, Phys. Rev. Lett. **77** (1996) 3419.
[2] C. Tusche *et al.*, Ultramicroscopy **159** (2015) 620.
[3] B. Yan *et al.*, Nature Commun. **6** (2015) 10167.
[4] H. Yamane, Molecular Science **9** (2015) A0078.

*e-mail: jun@chem.s.u-tokyo.ac.jp

BL5U

Photoemission Study on Sm-oxide Thin Films Prepared by Molecular Beam Epitaxy

H. Miyazaki[1], Y. Sakai[1], K. Yoshikawa[2] and N. Nishino[1]

[1]*Department of Physical Science and Engineering, Nagoya Institute of Technology, Nagoya 466-8555, Japan*

[2]*Department of Environmental and Materials Engineering, Nagoya Institute of Technology, Nagoya 466-8555, Japan*

Topological insulators are materials which exhibit a fundamentally new physical phenomena that were first predicted by theorists [1]. Recently, SmO is predicted to have a topological nontrivial ground state at ambient pressure [2], and we succeeded to fabricate SmO thin films by molecular beam epitaxy method controlled precisely adjusting the substrate temperature and oxygen partial pressure. However, the valence state of Sm is important for whether it is a topological insulator. In this report, we have performed *in-situ* photoemission spectroscopy (PES) on SmO thin films.

Sm-metal and Sm-oxide thin films have been grown by molecular beam epitaxy (MBE) method. We evaporated Sm-metal and Sm-oxide thin films onto Y-stabilized ZrO_2 (100) substrates at 800 °C without oxygen gas and under the oxygen pressure of 1.0 x 10^{-5} Pa, respectively. The PES measurements were performed at the beamline 5U of UVSOR-III, the Institute for Molecular Science, combined with the molecular beam epitaxy system, as shown in Fig. 1.

Figure 2 shows the PES spectra of Sm-metal and Sm-oxide thin films recorded at $h\nu$ = 60 eV and 180 eV. The experimental spectra are normalized with respect to their integrated intensity on the whole valence band up to E_B = 15 eV. The peaks and shoulder observed around 7.5, 10, and 12 eV at $h\nu$ = 180 eV are steeper than those at $h\nu$ = 60 eV. If the photon energy is increased from 60 to 180 eV, the atomic cross-sections of the O 2*p* and Sm 4*f* states change by 0.07 and 0.5 times, respectively [3]. As a result, the partial DOS originated from the Sm 4*f* state is expected to be enhanced compared with that from the O 2*p* state and the peaks and shoulder observed around 7.5, 10, and 12 eV are attributed to the Sm 4*f* state and the peak around 6.0 eV is attributed to the O 2*p* state. This hypothesis is consistent with the past PES results of Sm_2O_3 and the valence state of Sm 4*f* state is the $4f^{3+}$ state.

Sm $4f^{3+}$ valence state originates from Sm_2O_3 have been observed in PES, despite Sm $4f^{2+}$ valence state from SmO expected from the results of X-ray diffraction measurement. There is a contradiction between the results of PES and XRD measurements. Considering that the surface of the Sm-metal thin film is oxidized, one possibility is that the surface of the thin films has been oxidized during the transfer of the sample from MBE chamber to PES system. In order to discuss the essential surface electronic structure of thin films, further MBE system improvements are needed.

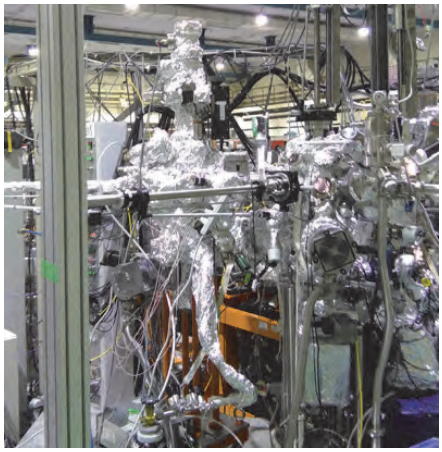

Fig. 1. Photo of the *in-situ* MBE system combined to UVSOR-III BL5U beamline.

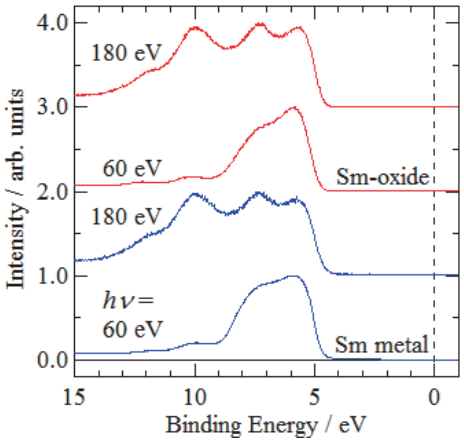

Fig. 2. Photon-energy dependence of the photoemission spectra of Sm-metal and Sm-oxide thin films.

[1] C. L. Kane and E. J. Mele, Phys. Rev. Lett. **95** (2005) 146802.
[2] D. Kasinathan *et al.*, Phys. Rev. B. **91** (2015) 195127.
[3] J. J. Yeh and I. Lindau, At. Data Nucl. Data Tables **32** (1985) 1.
[4] G. Dufour *et al.*, Chem. Phys. Lett. **42** (1976) 433.

BL5U

Angle Resolved Photoemission Spectroscopy Study of Fermi Surface and Superconducting Gap in NdFeAs(O,F)

Z. H. Tin[1], T. Adachi[1], A.Takemori[1], S. Ideta[2, 3], K. Tanaka[2, 3], S. Miyasaka[1] and S. Tajima[1]

[1]*Department of Physics, Graduate School of Science, Osaka University, Toyonaka 560-0043, Japan*

[2]*UVSOR Facility, Institute for Molecular Science, Okazaki 444-8585, Japan*

[3]*School of Physical Sciences, The Graduate University for Advanced Studies (SOKENDAI), Okazaki 444-8585, Japan*

Since the discovery of iron-based superconductors in 2008, intensive research has been going on in order to find out the origin of superconductivity. Among various families of Fe-based superconductors, 1111 system such as *R*FeAs(O,F) (*R*=rare-earth elements) achieves the highest T_c~ 55K [1]. In spite of highest T_c, 1111 system is not the popular research target among iron-based superconductors. The main reason is that it is very difficult to synthesize the single crystal of 1111 system. In our previous study, we have been able to grow the single crystal of NdFe(P,As)(O,F) and observe the evolution of Fermi surfaces with the isovalent doping of As site to P. In order to clarify the pairing mechanism, we have measured the superconducting gap of NdFeAs(O,F) single crystal by using angle resolved photoemission spectroscopy (ARPES) method.

The single crystals of NdFeAs(O,F) were grown by self-flux method under high pressure [2]. T_c of the single crystal was 41K. The ARPES were measured at BL5U in UVSOR facility.

Figure 1 shows the mapping of the Fermi surfaces (FSs) around Γ point, in horizontal (*P*) and vertical (*S*) polarized photon configurations. In these mapping, two hole FSs (inner and outer) were clearly observed around Γ point. Figure 2 shows k_z dependence of both FSs. Both of the FSs showed less dispersive feature along the k_z direction, which is consistent with the band calculation [3].

Superconducting gap was measured in k_x-k_y momentum space around Γ point. Figure 3 shows the angle dependence of superconducting gap values on the inner and outer FSs around Γ point. Both two hole FSs have a nodeless superconducting gap of ~17.0meV - 27.7meV on the outer FS and ~16.1meV - 23.3meV on the inner FS. These correspond to large gap ration, $2\Delta/kT_c$ = 8-12 and 9-15, respectively.

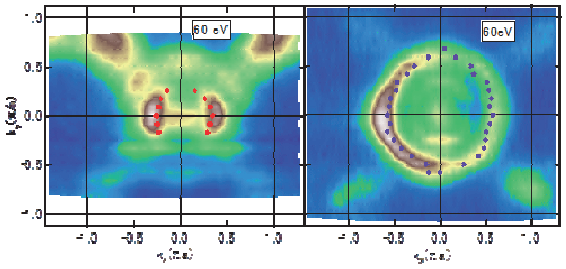

Fig. 1. Fermi surface mapping around Γ point in NdFeAs(O,F) single crystal in *S* (left panel) and *P* (right panel) polarization configurations, respectively.

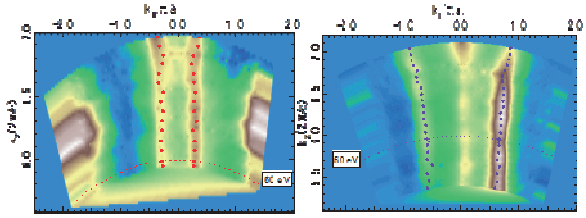

Fig. 2. The k_z dependence of Fermi surfaces in NdFeAs(O,F) single crystal in *S* (left panel) and *P* (right panel) polarization configurations, respectively.

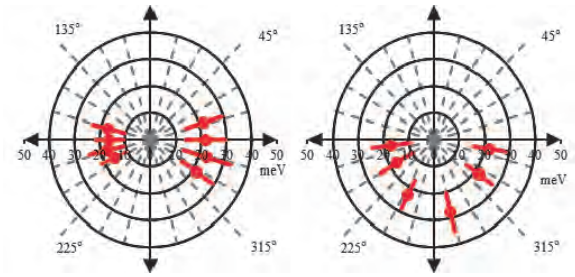

Fig. 3. The angle dependence of superconducting gap values on the inner (left panel) and outer Fermi surfaces (right panel) around Γ point, respectively.

[1] Ren Zhi-An *et al*., Chinese Phys. Lett. **25** (2008) 2215.
[2] A. Takemori *et al*., JPS Conf. Proc. **1** (2014) 012111.
[3] H. Usui *et al*., Supercond. Sci. Tech. **25** (2012) 084004.

BL6B

UV-Induced Absorption Spectra for Cerium-doped $Gd_3Al_{5-x}Ga_xO_{12}$ Crystals

M. Kitaura[1], K. Kamada[2], S. Kurosawa[1, 2], A. Ohnishi[1] and K. Hara[3]
[1]*Faculty of Science, Yamagata University, Yamagata 990-8560, Japan*
[2]*New Industry Creation Hatchery Center, Tohoku University, Sendai 980-8579, Japan*
[3]*Research Institute of Electronics, Shizuoka University, Hamamatsu 432-8011, Japan*

The cerimu-doped $Gd_3Al_2Ga_3O_{12}$ (Ce:GAGG) crystal is known one of high performance scintillators [1]. This material is characterized by high light yield and good energy resolution, and the scintillation properties are superior to other inorganic scintillators. However, there is a serious problem for Ce:GAGG that Ce^{3+} emission accompanies not only phosphorescence but also afterglow [2]. Since these components impede scintillation application requiring high-speed response, they must be suppressed as small as possible.

Most of scintillator crystals necessarily include lattice imperfections, which are unavoidably introduced in the process of the crystal growth. Such imperfections create donor- and acceptor-like levels near valence and conduction bands, and they act as traps for photocarriers. The traps are responsible for the occurrence of phosphorescence and afterglow. It is therefore necessary to clarify the origin of the traps degrading the scintillation response.

Recently, we have demonstrated that the defect complexes including oxygen vacancies form trapped electron centers in Ce:GAGG crystals [3]. We also explained that the trapped electron centers are introduced as charge compensators for cation deficiency. However, the origin of the trapped electrons center remains unsolved.

We show absorption spectra of cerium-doped $Gd_3Al_{5-x}Ga_xO_{12}$ mixed crystals induced under irradiation with UV-light at 375 nm for 10 min. The data allow us to see the effect of x on the electronic structure of trapped electron centers, and they are available to identify the origin of trapped electron centers. In the present experiment, we used the single crystals of $Ce:Gd_3Al_{5-x}Ga_xO_{12}$ grown by the micro-puling down (μ-PD) method. The concentration of cerium ions was set 1.0 mol%. The single crystals of $x < 2.5$ could not be obtained, because they contain the secondary phase with perovskite structure. The absorption spectra were measured under UV-irradiation and non-UV-irradiation. Here, the difference between the two is called as UV-induced absorption spectrum.

The UV-induced absorption spectra for x=3.0, 3.5, 4.0, and 5.0 are shown in Fig. 1. The data were obtained at 12 K. The absorption spectra cannot be obtained in the range below 1500 cm^{-1}, because of strong Reststrahlen reflection. The UV-induced absorption spectrum for x=3 exhibits a prominent band at around 12000 cm^{-1}. This feature is good agreement with our previous data in Ref. 3, in which the prominent band was assigned to trapped electron centers associated with oxygen vacancies. This band is weakened for x=3.5. Another band also appears in the range below 4000 cm^{-1}, together with the 12000 cm^{-1} band. This band is gradually increased with x.

The present results reveal that two kinds of absorption bands are replaced with increasing x. This fact suggests that gallium and aluminum ions are also essential for the formation of trapped electron centers, together with oxygen vacancies. The disappearance of the 12000 cm^{-1} band may occur also by the lowering of the conduction band minimum with increasing x [4]. Further investigations are needed to clarify the origin of the trapped electron centers responsible for the UV-induced absorption bands.

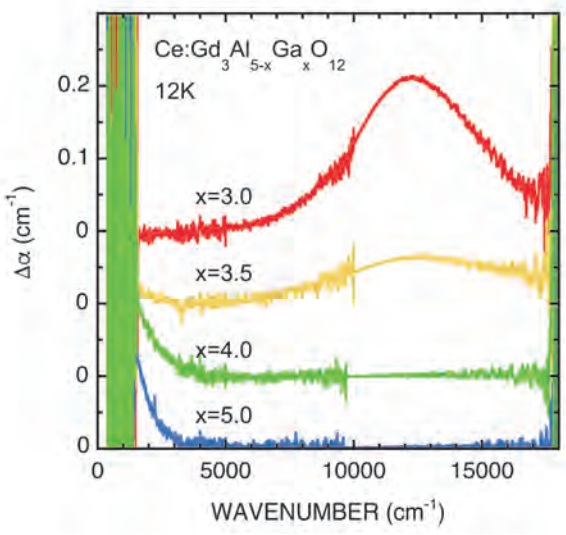

Fig. 1. UV-induced absorption spectra of $Ce:Gd_3Al_{5-x}Ga_xO_{12}$ crystals (x=3.0, 3.5, 4.0, and 5.0) measured at 12 K. The longitudinal axis represents the difference in absorption coefficient between the absorption spectra measured under UV-irradiation and non-UV-irradiation.

[1] K. Kamada *et al*., J. Cryst. Growth **352** (2012) 88.
[2] M. Kitaura *et al*., J. Appl. Phys. **115** (2014) 083517.
[3] M. Kitaura *et al*., Appl. Phys. Express **9** (2016) 072602.
[4] P. Dorenbos, J. Lumi. **134** (2013) 310.

BL6B

Ground-State Splitting of Ultrashallow Thermal Donors in Silicon

A. Hara and T. Awano
Department of Electronic Engineering, Tohoku Gakuin University, Tagajo 985-8537, Japan

We had found ultrashallow thermal donors (USTDs) in carbon-doped and hydrogen-doped Czochralski silicon (CZ Si) crystals.[1] To the best of our knowledge, these are the shallowest energy levels among previously reported donors in Si crystals. We found new peaks with increasing measurement temperature.

To evaluate the relationship between the absorption coefficient of the new peaks and the measurement temperature, we analyzed the temperature dependence of the absorption coefficient. We assumed that absorption coefficient at 15 K to be zero to simplify the analysis, and that absorption coefficient is proportional to $N_0 \times \exp(-\Delta E/k_B T)$, where ΔE, N_0, and k_B are the activation energy for occupying the new peak state, the total population, and the Boltzmann constant, respectively. Figure 1(a) plots ln[Trans.(T)/Trans.(15 K)] at various measurement temperatures T (in units of kelvin), where Trans.(T) represents the transparent coefficient at T K. Figure 1(b) shows a magnification around spectral peaks A and B. Because we assumed the absorption coefficient of the new peaks at 15 K to be zero, the vertical values are correlated with their absorption coefficient at T K. Figure 2 plots the variation of the intensity of peak B in Fig. 1(b) as a function of 1/T. The vertical axis expresses ln{-ln[Trans.(T)/Trans.(15 K)]}. The gradient of this curve is $-\Delta E/k_B$, implying ΔE = 6 meV. This magnitude is reasonable because we observed the new peaks with a thermal energy of $k_B T$ (T = 20–40 K), of 2–4 meV. The reduction of the absorption coefficient above 40 K is attributed to the excitation of electrons to the conduction band.

We propose the following model to explain the origin of the new peaks (A and B). These lines are associated with the excitation of electrons from the upper level of the ground state to the original $2p_0$, $2p_{+-}$, and $3p_{+-}$ states of the USTDs, arising from the level splitting of the ground-state. This model is consistent with the thermal excitation energy of 6 meV required to generate new peaks because the optical energy-level splitting between the upper level of the ground state and the ground state is approximately 4 meV.

Ground-state splitting indicates that the wave functions of the ground state of the USTDs are composed of linear combinations of the wave functions of the conduction-band minimum.

In summary, the ground-state splitting of the USTDs was observed. This is the direct evidence that the ground state of the USTDs is composed of linear combinations of wave functions of the conduction band minimum.

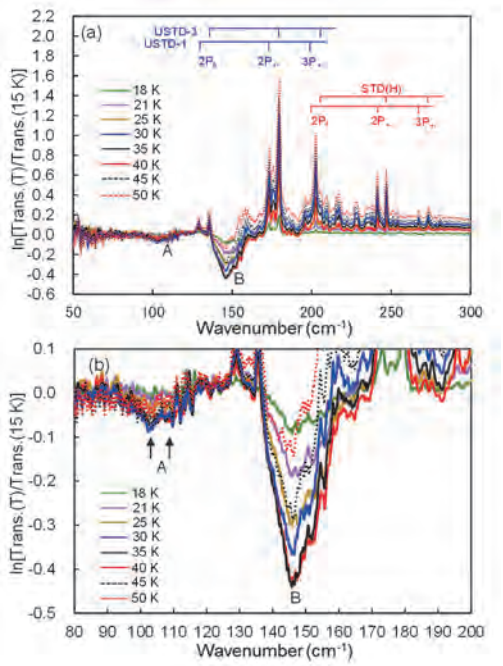

Fig. 1. Temperature dependence of the absorption coefficient. The vertical axis is ln[Trans.(T)/Trans.(15 K)], where Trans.(T) represents the transmittance at temperature T K. (b) Magnified image of spectra A and B.

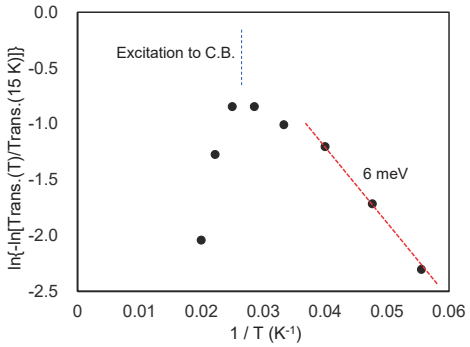

Fig. 2. Temperature dependence of the absorption coefficient of the new shallow donor. The vertical axis is ln{-ln[Trans.(T)/Trans.(15 K)]}. The gradient reflects the thermal activation energy.

[1] A. Hara, T. Awano, Y. Ohno and I. Yonenaga, Jpn. J. Appl. Phys. **49** (2010) 050203.

BL6B

Far-Infrared Reflective Analysis for Unipolar Fatigued Alkali Niobate Piezoceramics

H. Nishiyama, N. Matsubara, K. Yoshida, D. Ando, T. Fuchigami and K. Kakimoto
Graduate School of Engineering, Nagoya Institute of Technology, Nagoya 466-8555, Japan

Electromechanical property of piezoceramics changes due to a long-term and repeated exposure to high unipolar electric fields. Although some fatigue mechanisms of the electromechanical property have been discussed based on a change of domain structure [1], an experimental fact has not been showed directly. Previously, we have reported that it is possible to clarify the difference in permittivity ε' of piezoceramics by analyzing IR reflectivity spectra [2]. In this study, we thought it was possible to clarify the change of domain structure before/after fatigue experiment by investigating the difference of the permittivity in alkali niobate piezoceramics with far-infrared (FIR) reflectivity analysis. Especially, we focused on ionic polarization in perovskites because FIR analysis has been used to explain soft-mode theory for displacive type of ferroelectric perovskites [3].

Alkali niobate piezoceramic, $Li_{0.06}Na_{0.52}K_{0.42}NbO_3$ with additives (Li_2CO_3, SiO_2, $MnCO_3$, and $SrZrO_3$) (NKN-additive), was polarized in silicon oil under DC field up to 4 kV/mm. Fatigue tests was carried out for specimens under unipolar triangle waves up to 10^6 cycles by applying electric field of 0 - 3 kV/mm with a frequency of 50 Hz. FIR measurement was conducted by a FT-IR spectrometer (Bruker, VERTEX 70v). A beam splitter and detector were used a Mylar 6 μm and Si bolometer, respectively. The spectra were fitted to obtain complex permittivity according to Drude-Lorentz equation:

$$\varepsilon(\omega) = \varepsilon_\infty + \sum_j \frac{\omega_{jp}^2}{\omega_{jTO}^2 - \omega^2 - n\gamma_j\omega} \quad (1)$$

where, ε_∞ is the high-frequency dielectric constant, ω_p and ω_{TO} are the plasma and transverse optic frequencies, and γ is the damping constant. The complex dielectric function $\varepsilon^*(\omega) = \varepsilon'(\omega) - i\varepsilon''(\omega)$ is related to the reflectivity R by Fresnel equation:

$$R(\omega) = \left|\frac{\sqrt{\varepsilon^*(\omega)} - 1}{\sqrt{\varepsilon^*(\omega)} + 1}\right|^2 \quad (2)$$

Figure 1 shows FIR reflectivity spectra for NKN-additive. Peak shifts and a change of waveforms were observed in all wavenumber range after polarization (As-poled) and fatigue treatment (Fatigued). Figure 2 shows real part (ε') and imaginary part (ε'') of permittivity calculated from the FIR reflectivity spectra shown in Fig.1. The ε'' peak shifted from 88.2 cm^{-1} to 53.8 cm^{-1} with increasing intensity from 54.9 to 450.5 after polarization treatment. After the fatigue treatment, the peak shifted to 65.4 cm^{-1} with decreasing intensity to 109.3. A similar tendency was observed in the ε'. On the assumption that the ε'' peak relates to the Slater mode (Nb-O vibrations), these results imply reduction of Nb-O ionic polarization getting back to the virgin state. Thus, we believe that FIR analysis is useful as an experimental method to reveal the fatigue mechanisms of the electromechanical property.

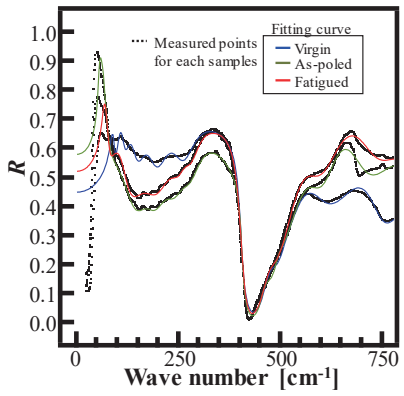

Fig. 1. FIR reflectivity spectra for NKN-additive. Dot lines indicate measured points. Colored lines indicate fitting curves for each measured points.

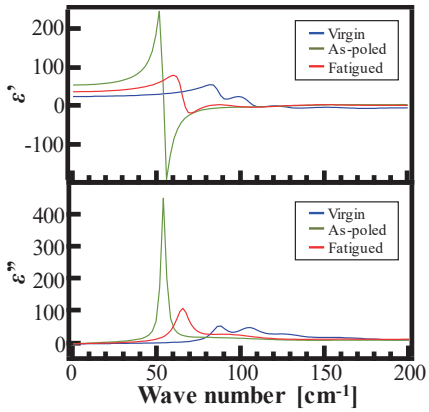

Fig. 2. Real and imaginary part of permittivity for NKN-additive calculated from FIR reflectivity spectra.

[1] F-Z. Yao *et al.*, Appl. Phys. Lett. **103** (2013) 192907.
[2] Y. Taniguchi and K. Kakimoto, Jpn. J. Appl. Phys. **54** (2015) 10ND09.
[3] J. L. Servoin and F. Gervais, Phys. Rev. B **21** 5 (1980) 2038.

BL7U

ARPES Study of Possible Topological Superconductor $Tl_{0.5}Bi_2Te_3$

C. X. Trang[1], Z. Wang[2], D. Takane[1], K. Nakayama[1], S. Souma[3, 4], T. Sato[1, 4], A. A. Taskin[2], Y. Ando[2] and T. Takahashi[1, 3, 4]

[1]*Department of Physics, Tohoku University, Sendai 980-8578, Japan*
[2]*Institute of Physics II, University of Cologne, Köln 50937, Germany*
[3]*WPI Research Center, Advanced Institute for Materials Research, Tohoku University, Sendai 980-8577, Japan*
[4]*Center for Spintronics Research Network, Tohoku University, Sendai 980-8577, Japan*

The discovery of topological insulators (TIs), in which a gapless topological surface state (SS) with a Dirac-cone energy dispersion appears at the edge or surface, has stimulated intensive investigations into an even more exotic state of matter, a topological superconductor (TSC). TSCs generically possess a gapless Andreev bound state at the edge or surface which consists of Majorana fermions [1]. Owing to the peculiar characteristics of Majorana fermions and the potential application to a fault-tolerant quantum computer, TSC is one of the emergent topics in current condensed-matter physics. It has been suggested that a superconductor derived from a TI is a promising candidate for a TSC because of the strong spin-orbit coupling that would lead to unconventional electron pairing. However, only a limited number of candidate materials, such as $Cu_xBi_2Se_3$, $Cu_x(PbSe)_5(Bi_2Se_3)_6$, and $Sr_xBi_2Se_3$, have been discovered and their topological properties are still under intensive debate. It is thus of great importance to explore new platforms of TSCs and establish the electronic structure to investigate the possible topological superconductivity.

In this study, we report high-resolution angle-resolved photoemission spectroscopy (ARPES) on a new TSC candidate, $Tl_{0.5}Bi_2Te_3$ (T_c = 2.28 K) [2], which is derived from thallium (Tl) doping into a prototypical TI, Bi_2Te_3. By utilizing energy-tunable photons from synchrotron radiation, we determined the bulk and surface electronic states and found that $Tl_{0.5}Bi_2Te_3$ provides an excellent platform to realize topological superconductivity [3].

Figure 1(a) shows the experimental Fermi surface (FS) measured with $h\nu$ = 21 eV whose k cut nearly crosses the Z point of the bulk Brillouin zone. The FS consists of three large and three small pockets slightly away from the Z point. These FSs commonly have a hole-like character as recognized from the Fermi level (E_F) crossing of the valence band (VB) in Fig. 1(b). This demonstrates that Tl doping leads to a direct hole doping into the VB top. Besides the M-shaped VB feature, we found a V-shaped electron-like band in the vicinity of E_F inside the valley of the VB. This tiny feature is assigned to a topological SS. This indicates that the band-inverted nature is conserved even upon Tl doping. As shown in Fig. 1(c), we were able to trace the dispersion of the SS up to ~0.2 eV above the VB top simply by keeping the samples in a vacuum of 2 × 10^{-10} Torr for 12 h, which resulted in a significant downward surface band bending. Since the surface chemical potential can be systematically controlled by the surface-aging technique, it is possible to well isolate the topological SS from the bulk bands in both the k space and the energy axis by controlling the strength of the surface band bending. This is in favor of the realization of 2D topological superconductivity in the topological SS through the proximity effect from the SC bulk. In this regard, the $Tl_xBi_2Te_3$ system provides an excellent platform to realize the 2D topological superconductivity.

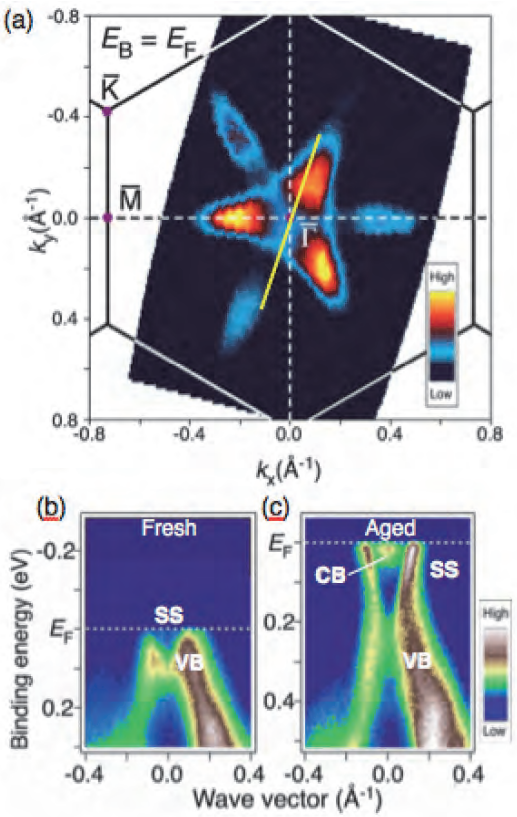

Fig. 1. (a) APRES intensity at E_F in $Tl_{0.5}Bi_2Te_3$ plotted as a function of 2D wave vector. (b) and (c) Experimental band dispersion along yellow line in (a) measured just after cleaving (fresh) and 12 h after cleaving (aged), respectively.

[1] Y. Ando, J. Phys. Soc. Jpn. **82** (2013) 102001.
[2] Z. Wang *et al.*, Chem. Mater. **28** (2016) 779.
[3] C. X. Trang *et al.*, Phys. Rev. B **93** (2016) 241103(R).

BL7U

Slater to Mott Crossover in the Metal to Insulator Transition of $Nd_2Ir_2O_7$

M. Nakayama[1], T. Kondo[1], Z. Tian[1], J. J. Ishikawa[1], M. Halim[1], C. Bareille[1], K. Kuroda[1], T. Tomita[1], S. Ideta[2], K. Tanaka[2], M. Matsunami[3], S. Kimura[4], L. Balents[5], S. Nakatsuji[1] and S. Shin[1]

[1]*ISSP, University of Tokyo, Kashiwa 277-8581, Japan*
[2]*UVSOR Facility, Institute for Molecular Science, Okazaki 444-8585, Japan*
[3]*Toyota Technological Institute, Nagoya 468-8511, Japan*
[4]*Graduate School of Frontier Biosciences, Osaka University, Suita 565-0871, Japan*
[5]*Kavli Institute for Theoretical Physics, Santa Barbara, California 93106, USA*

The 5*d* iridium oxides (iridates), having comparable scales for their kinetic energy, Coulomb interaction, and spin-orbit coupling, provide an excellent platform for studying new types of strongly correlated phenomena. Amongst them, the pyrochlore iridates ($Ln_2Ir_2O_7$, where *Ln* is a lanthanide), endowed with frustrated geometry and cubic symmetry, have a particularly fascinating phase diagram. $Pr_2Ir_2O_7$, with the largest *Ln* ion, is a metallic spin liquid and exhibits an anomalous Hall effect. For *Ln* ions with a smaller ionic radius, an antiferromagnetically ordered insulating phase appears at low temperature.

Theoretically, topological band structures have been ascribed to the $Ln_2Ir_2O_7$ series. The metallic phase is predicted to exhibit quadratically, dispersing conduction and valence bands touching at the Γ point close to the Fermi level (E_F). We have recently identified this structure by angle-resolved photoemission spectroscopy (ARPES) in $Pr_2Ir_2O_7$ [1]. Theory predicts that such a quadratic Fermi node state may be converted into various topological states such as a topological insulator or a Weyl semimetal by appropriate symmetry breaking.

Antiferromagnetism in these materials is of the Ising type, consisting of an "all-in–all-out" (AIAO) configuration of Ir moments on alternating tetrahedra. This can be considered an "octupolar" spin order which breaks time-reversal but preserves cubic symmetry, and does not enlarge the unit cell. Early density functional studies predicted the magnetic state to be a Weyl semimetal, and general arguments imply that, if a quasiparticle picture applies at low energy in the antiferromagnetic phase, and the magnetic ordering is weak, it must exhibit Weyl points and cannot have a true gap. Nevertheless, optical and transport measurements indicate a gapped insulating ground state for $Nd_2Ir_2O_7$, despite its low antiferromagnetic–metal-insulator (MI) transition temperature $T_{MI} \approx 30$ K and proximity to metallic $Pr_2Ir_2O_7$. This begs the question of whether the weakness of the order, the quasiparticle assumption, or both, break down in this system. More generally, we seek to understand the influence of the MI transition on the conduction electrons.

We use ARPES to investigate the evolution of the electronic structure through the MI transition in $Nd_2Ir_2O_7$, which is the most suitable member of the series for such study because its low T_{MI} minimizes thermal broadening. Although the layered iridates have been extensively studied by photoemission, ours is the first study across a MI transition in any iridate, since the latter occurs only in the pyrochlores. Using high-quality single crystals, we are able to directly measure both the single particle excitations of the metallic and insulating phases. Our data in Fig. 1 indicate that $Nd_2Ir_2O_7$ displays a dramatic Slater to Mott crossover with reducing temperature [2]. This implies that Weyl fermions, if they exist, may do so only in a narrow region of temperature slightly below T_{MI}, in which the order is, indeed, weak and quasiparticles can survive.

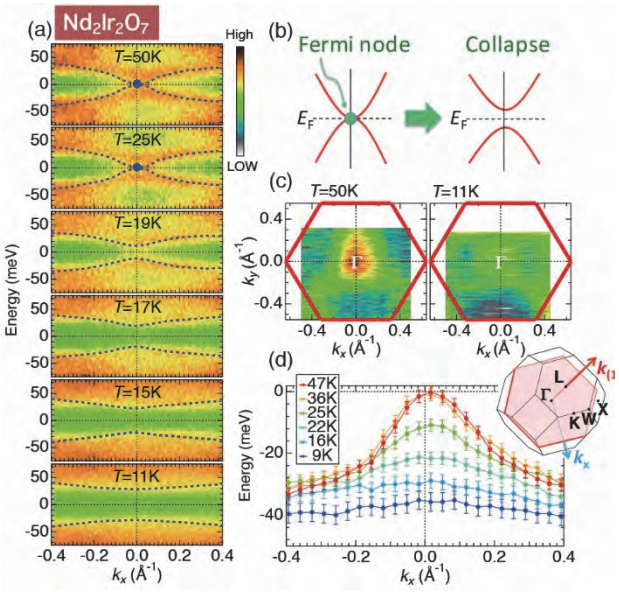

Fig. 1. Temperature evolution of ARPES dispersion map across Γ showing a quadratic Fermi node state in the metallic phase of $Nd_2Ir_2O_7$, and its destruction upon cooling below T_{AF}.

[1] T. Kondo *et al.*, Nat. Commun. **6** (2015) 10042.
[2] M. Nakayama *et al.*, Phys. Rev. Lett. **117** (2016) 056403.

BL7U

d-wave Superconducting Gap Observed in the Protect-annealed Electron-doped Cuprate Superconductor $Pr_{1.3-x}La_{0.7}Ce_xCuO_4$

M. Horio[1], K. Koshiishi[1], S. Nakata[1], K. Hagiwara[1], S. Ideta[2], K. Tanaka[2], A. Takahashi[3], T. Konno[3], T. Ohgi[3], T. Adachi[4], Y. Koike[3] and A. Fujimori[1]

[1]*Department of Physics, University of Tokyo, Tokyo 113-0033, Japan*
[2]*UVSOR Facility, Institute for Molecular Science, Okazaki 444-8585, Japan*
[3]*Department of Applied Physics, Tohoku University, Sendai 980-8579, Japan*
[4]*Department of Engineering and Applied Sciences, Sophia University, Tokyo 102-8554, Japan*

The symmetry of the superconducting (SC) gap provides a strong clue for the origin of unconventional superconductivity. As for the electron-doped cuprate superconductors, most of the previous studies have supported *d*-wave symmetry [1, 2], and large contribution of antiferromagnetic (AF) spin fluctuations to the superconductivity has been proposed.

Recently, a new annealing method, which is called protect-annealing, has enabled superconductivity in electron-doped cuprates with lower Ce concentration than that in previous studies [3]. This is probably because the impurity apical oxygen atoms which stabilize short-range antiferromagnetic (AF) order have been efficiently removed by the improved annealing. Our recent ARPES study on protect-annealed $Pr_{1.3-x}La_{0.7}Ce_xCuO_4$ (PLCCO, x = 0.10) has revealed strong suppression of the AF pseudogap, suggesting a dramatic reduction of the AF spin correlation length and/or the magnitude of the fluctuating magnetic moments [4]. In order to investigate the nature of the SC state with a high T_c and suppressed antiferromagnetism, we have performed ARPES measurements on protect-annealed PLCCO (x = 0.10, 0.15) single crystals and directly observed a momentum-dependent SC gap.

Single crystals of PLCCO with x = 0.10 (samples #1-#3) and 0.15 (samples #4 and #5) were synthesized by the traveling-solvent floating-zone method and were protect annealed for 24 hours at 800 °C. After the annealing, samples with x = 0.10 and x = 0.15 showed T_c's of 27 K and 22 K, respectively. ARPES measurements were performed at beamline 7U of UVSOR facility. Linearly polarized light with $h\nu$ = 16.5 eV was used for the measurements. The total energy resolution was set at 8 meV. Considering the relatively quick surface degradation which is typical for electron-doped cuprates, ARPES spectra were recorded within 4 hours after cleavage at only one momentum position at two temperatures below and above T_c for each sample.

Figure 1(a) shows energy distribution curves (EDCs) of PLCCO (x = 0.10) at the Fermi wave vector (k_F) near (π/2, π/2) and (0.3π, π), which are in the nodal and antinodal regions, respectively, in the case of d_{x2-y2}-wave paring. We compared the spectra taken above and below T_c and estimated the magnitude of the leading-edge shift Δ_{shift} caused by the opening of SC gap. EDCs near (π/2, π/2) taken above and below T_c cross almost at E_F and Δ_{shift} is as small as 0.3 meV. On the other hand, those near (0.3π, π) cross appreciably below E_F and a leading-edge shift of 1.3 meV was observed, which is also confirmed in the measurements on another x = 0.10 sample as shown in Fig. 1(b). The same tendency also applies to the x = 0.15 samples (Fig. 1(c)).

The present result suggests that d_{x2-y2}-paring, which is associated with strong electron correlation and AF spin fluctuations, persists after the strong reduction of AF correlation length and/or magnitude of the fluctuating magnetic moment by protect annealing. The short-range AF order induced around the apical oxygen atoms is harmful for superconductivity, but it is still possible that electron correlation itself drive the d_{x2-y2}-wave SC state in the electron-doped cuprates.

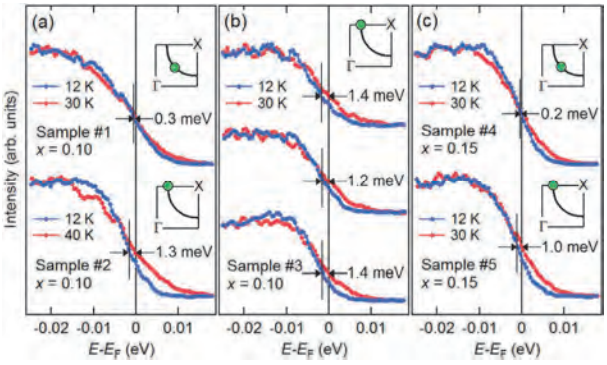

Fig. 1. Leading-edge shift observed in PLCCO samples. EDCs of (a) samples #1 and #2 with x = 0.10, (b) sample #3 with x = 0.10, and (c) samples #4 and #5 with x = 0.15 measured at temperatures above (red curves) and below (blue curves) T_c. Insets indicate the k_F positions where the EDCs were taken.

[1] G. Blumberg *et al.*, Phys. Rev. Lett. **88** (2002) 107002.
[2] H. Matsui *et al.*, Phys. Rev. Lett. **95** (2005) 017003.
[3] T. Adachi *et al.*, J. Phys. Soc. Jpn. **82** (2013) 063713.
[4] M. Horio *et al.*, Nat. Commun. **7** (2016) 10567.

BL7U

Electronic Structure of FeS

J. Miao[1], X. H. Niu[1], D. F. Xu[1], Q. Yao[1], Q. Y. Chen[1], T. P. Ying[1], S. Y. Li[1,2], Y. F. Fang[3], J. C. Zhang[3], S. Ideta[4], K. Tanaka[4], D. L. Feng[1,2] and F. Chen[3]

[1]*State Key Laboratory of Surface Physics, Department of Physics, and Laboratory of Advanced Materials, Fudan University, Shanghai 200433, People's Republic of China*

[2]*Collaborative Innovation Center of Advanced Microstructures, Nanjing, 210093, China*

[3]*Materials Genome Institute, Shanghai University, Shanghai 200444, People's Republic of China*

[4]*UVSOR Synchrotron Facility, Institute for Molecular Science, Okazaki 444-8585, Japan*

Among all the iron-based superconductors, the iron-chalcogenide FeSe has the simplest layered structure yet extraordinarily rich physics [1]. The most remarkable one is the interfacial superconductivity as high as 65 K in FeSe monolayer thin film grown on $SrTiO_3$ (001) substrate, which has attracted great attention of the community [2].

As a counterpart, the bulk FeSe processes a superconducting transition temperature of about 8K. It will be further enhanced by hydrostatic pressure, surface dosing or liquid gating to around 40K [3-5]. Element substitution in the bulk is another effective way to explore the properties of FeSe. Recently, it was found that by dilute S doping, the transition temperature of $FeSe_{1-x}S_x$ is first enhanced, then decreases upon further substitution. The end member of this series, FeS, is still superconducting with a T_c of 4.5 K[6-7]. The presence of superconductivity in FeS is quite surprising, since S substitution is expected to significantly reduce the electron correlations which are crucial for the unconventional superconductivity. To address this surprise, we performed angle-resolved photoemission spectroscopy (ARPES) at BL7U to examine the electronic structure of FeS.

Here we report the electronic structure of FeS. Our high-resolution ARPES studies show two hole-like (α and β) and two electron-like (η and δ) Fermi pockets around the Brillouin zone center and corner, respectively, all of which exhibit moderate dispersion along k_z. However, a third hole-like band (γ) is not observed, which is expected around the zone center from band calculations and is common in iron-based superconductors. Since this band has the highest renormalization factor and is known to be the most vulnerable to impurities, its absence in our data is likely due to impurity scattering and yet superconductivity can exist without coherent quasiparticles in the γ band. This may help resolve the current controversy on the superconducting gap structure of FeS. Moreover, by comparing the β bandwidths of various iron chalcogenides, including FeS, $FeSe_{1-x}S_x$, FeSe, and $FeSe_{1-x}Te_x$, we find that the β bandwidth of FeS is the broadest. However, the band renormalization factor of FeS is still quite large, when compared with the band calculations, which indicates sizable electron correlations. This explains why the unconventional superconductivity can persist over such a broad range of isovalent substitution in $FeSe_{1-x}Te_x$ and $FeSe_{1-x}S_x$.

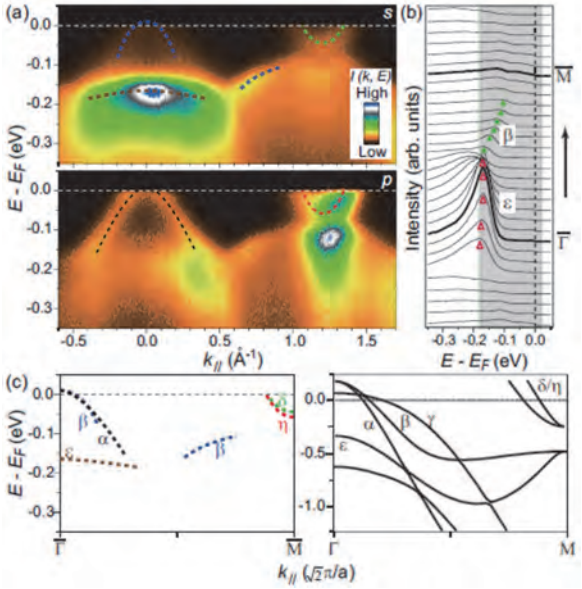

Fig. 1. (a) Photoemission intensity distributions along the Γ-M direction taken with *s*- and *p*-polarized photons, respectively. (b) Corresponding energy distribution curves of data in panel (a) taken with s-polarized photons. (c) Left panel: the band structure of FeS measured by ARPES. Right panel: the calculated FeS band structure along Γ-M reproduced from Ref. [8]. All the ARPES data were taken with 30 eV photons.

[1] F. C. Hsu, J. Y. Luo, K. W. Yeh, *et al.*, Proc. Natl. Acad. Sci. U.S.A. **105** (2008) 14262.
[2] Q. Y. Wang, Z. Li, W. H. Zhang, *et al.*, Chin. Phys. Lett. **29** (2012) 037402.
[3] S. Medvedev, T. M. McQueen, I. A. Troyan, *et al.*, Nature Mater. **8** (2009) 630.
[4] B. Lei, J. H. Cui, Z. J. Xiang, *et al.*, Phys. Rev. Lett. **116** (2016) 077002.
[5] C. H. P. Wen, H. C. Xu, C. Chen, *et al.*, Nat. Commu. **7** (2016) 10840.
[6] X. F. Lai, H. Zhang, Y. Q. Wang, *et al.*, J. Am. Chem. Soc. **137** (2015) 10148.
[7] U. Pachmayr, N. Fehn, and D. Johrendt, Chem. Commun. **52** (2016) 194.
[8] A. Subedi, *et al.*, Phys.Rev. B **78** (2008) 134514.

BL7U

High-Resolution ARPES Study of Topological Line-Node Semimetal HfSiS

D. Takane[1], Z. Wang[2], S. Souma[3, 4], K. Nakayama[1], C. X. Trang[1], T. Sato[1, 4], Y. Ando[2] and T. Takahashi[1, 3, 4]

[1]*Department of Physics, Tohoku University, Sendai 980-8578, Japan*
[2]*Institute of Physics II, University of Cologne, Köln 50937, Germany*
[3]*WPI Research Center, Advanced Institute for Materials Research, Tohoku University, Sendai 980-8577, Japan*
[4]*Center for Spintronics Research Network, Tohoku University, Sendai 980-8577, Japan*

Topological semimetals are recently attracting a great deal of attention. In contrast to conventional semimetals with a finite band overlap between valence band (VB) and conduction band (CB), topological semimetals are categorized by the band- contacting nature between the VB and CB in the Brillouin zone (BZ); point-contact (Dirac/Weyl semimetals) or line-contact (line-node semimetals; LNSMs). The existence of three-dimensional Dirac semimetals was first confirmed in Cd_3As_2 and Na_3Bi, where the VB and CB contact each other at the point (Dirac point) protected by rotational symmetry of the crystal. Recent studies on noncentrosymmetric transition-metal monopnictides (TaAs family) have clarified pairs of bulk Dirac-cone bands and Fermi-arc surface states, supporting their Weyl-semimetallic nature. While the existence of Dirac/Weyl semimetals with point nodes has been confirmed experimentally, the experimental studies of LNSMs with line nodes are relatively scarce despite many theoretical calculations.

Recently, it was theoretically proposed that ZrSiO with PbFCl-type crystal structure (space group *P*4/*nmm*) and its isostructural family *WHM* [*W* = Zr, Hf, or La; *H* = Si, Ge, Sn, or Sb; *M* = O, S, Se and Te; see Fig.1 (a) for crystal structure] may host the LNSM phase protected by a glide-mirror symmetry of the crystal [1]. In this study, we performed high-resolution angle-resolved photoemission spectroscopy (ARPES) on HfSiS. By utilizing energy-tunable photons from synchrotron radiation, we determined the overall VB structure and revealed the LNSM nature of HfSiS.

HfSiS crystal consists of a stack of S-Hf-Si-Hf-S five square nets along *c* axis. A natural cleaving plane is indicated by an orange square in Fig. 1(a). The low-energy electron diffraction (LEED) measurement on the cleaved surface shows a clear 1×1 pattern [see Fig. 1(b)], demonstrating high-quality nature of the cleaved surface. Figures 1(c) and 1(d) show the ARPES-intensity plot and the corresponding second-derivative-intensity plot, respectively, in the VB region as a function of wave vector and binding energy (E_B) measured along the ΓM cut at $h\nu = 21$ eV with linear polarization. One can notice several dispersive bands; hole-like bands (α) at the Γ point with the top of dispersion at 3 eV, an undulating band (β) with the top of dispersion at 1.6 eV midway between Γ and M, and linearly dispersive bands (γ, δ) within 1.6 eV of the Fermi level (E_F). These bands are well reproduced in the band calculation [1]. According to the band calculation, the γ and δ bands are attributed to the electron-like Hf 5*d* and the hole-like Si 3*p* bands at Γ, respectively. These bands intersect each other near E_F to form line nodes in the case of negligible spin-orbit coupling (SOC) [1]. In fact, through the band-structure mapping over entire BZ, we have observed the diamond-shaped quasi-two-dimensional Fermi surface hosting line nodes. Therefore the present observation supports the LNSM nature of HfSiS.

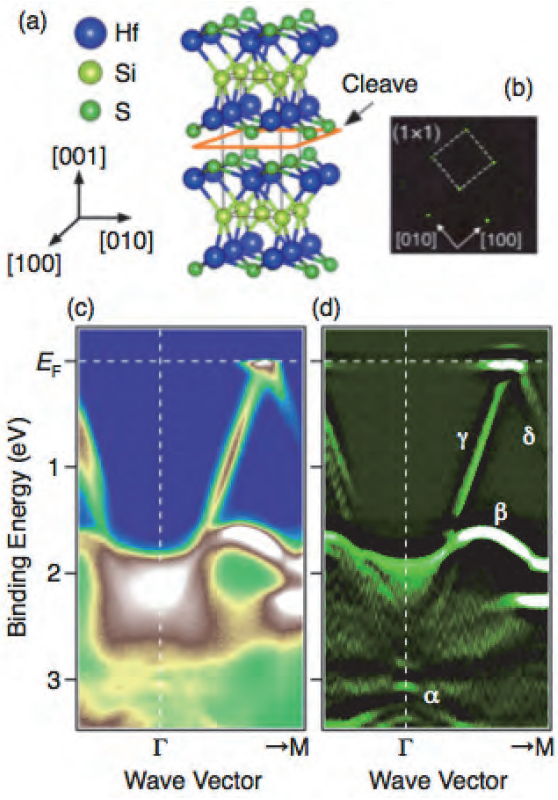

Fig. 1. (a) Crystal structure of HfSiS. (b) LEED pattern on a cleaved surface measured with a primary electron energy of 90.5 eV. (c) and (d) Plots of ARPES intensity and corresponding second- derivative intensity, respectively, in the VB region measured at T = 40 K along the ΓM line with linearly polarized 21-eV photons.

[1] Q. Xu *et al.*, Phys. Rev. B **92** (2015) 205310.

BL7U

Electronic Structure of Triple-layer Cuprate Superconductor $Bi_2Sr_2Ca_2Cu_3O_{10+\delta}$ Observed by ARPES

S. Ideta[1], T. Yoshida[2], S. Ishida[3], K. Takashima[4], S. Uchida[3, 4], A. Fujimori[4] and K. Tanaka[1]

[1]*National Institutes of Natural Science, Institute for Molecular Science, Okazaki, 444-8585, Japan*
[2]*Graduate School of Human and Environmental Studies, Kyoto University, Kyoto 606-8501, Japan*
[3]*National Institute of Advanced Industrial Science and Technology (AIST), Tsukuba 305-8568, Japan*
[4]*Department of Physics, University of Tokyo, Tokyo 113-0033, Japan*

Effects of interlayer interaction between CuO_2 planes which may contribute the enhancement of critical temperature (T_c) in the multi-layer high-T_c cuprate superconductors (HTSCs) have been investigated to elucidate the mechanism of superconductivity [1]. While it has been well known that the number of doped carriers and the number of CuO_2 planes are one of the essential factors to control the T_c of cuprates, unexpectedly T_c does not decrease in the overdoped $Bi_2Sr_2Ca_2Cu_3O_{10+\delta}$ (Bi2223) [2]. In spite of extensive studies both experimentally and theoretically [3-7], the microscopic origin of the high-T_c superconductivity in the triple-layer HTSCs still remains unclear.

We reported that the electronic structure of Bi2223 by ARPES showed two bands originating from the outer and inner CuO_2 planes [8-10], and recently we also observed the third band caused by the triple-layer splitting [11]. Here, we report an ARPES study on overdoped Bi2223 using low-energy photons and the linearly polarized synchrotron light. In this study, we found that each band shows a superconducting (SC) gap with different magnitude.

Single crystals of Bi2223 (T_c ~ 110 K) were grown by the travelling solvent floating zone method. ARPES experiments were carried out at BL 7U of UVSOR using $h\nu$ = 7 eV - 8.5 eV photons. The total energy resolution was set at 7 - 8 meV. Temperature was set at T = 12 K and clean sample surfaces were obtained by cleaving single crystals *in-situ* in an ultrahigh vacuum better than 7×10^{-9} Pa. The samples were aligned by Laue diffraction and set so that the direction of Cu-O [(π, 0)-(π, π)] was perpendicular to the electric field direction of the incident light.

In order to estimate the SC gap of overdoped Bi2223, symmetrized energy-momentum (*E*-*k*) plots in the offnodal region taken at different photon energies are presented in Fig. 1. Black bars show the peak position of the energy-distribution curve (EDC) indicating the SC gap size. The SC gap estimated along the Fermi surface (FS) is plotted as a function of the *d*-wave order parameter in Fig. 1(c). The SC gaps of the inner-plane band (IP) and outer-plane-antibonding band (OP-AB) show almost the same magnitudes (Δ_{IP} ~ 50 meV and $\Delta_{OP\text{-}AB}$ ~ 40 meV) as the previous ARPES study [8]; however, that of the outer-plane-bonding band (OP-BB) shows a smaller gap size at the antinode ($\Delta_{OP\text{-}BB}$ ~ 20 meV). This result indicates that the large SC gap of OP-AB may contribute to the higher T_c in the overdoped Bi2223.

As future work, we need to investigate the Fermi arc length in order to determine how much these three bands contribute to the superconductivity. Also, theoretical work to interpret the different SC gap magnitude of the three bands should be done.

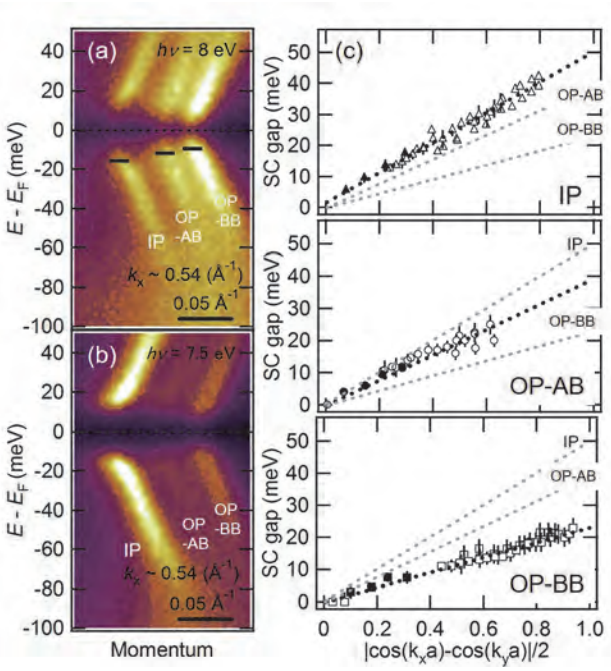

Fig. 1. Symmetrized *E*-*k* plots in the Cu-O bond direction taken at $h\nu$ = 8 and 7.5 eV (T = 12 K) and SC gap anisotropy. IP, OP-AB, and OP-BB indicate the inner, middle, and outer bands, respectively.

[1] J. M. Wheatley *et al*., Nature **333** (1988) 121.
[2] T. Fujii *et al.,* Phys. Rev. B **66** (2002) 024507.
[3] E. Pavarini *et al*., Phys. Rev. Lett. **87** (2001) 047003.
[4] S. Chakravarty *et al*., Nature **428** (2004) 53.
[5] S. Okamoto *et al*., Phys. Rev. Lett. **101** (2008) 156401.
[6] D. L. Feng *et al*., Phys. Rev. Lett. **88** (2002) 107001.
[7] T. Sato *et al*., Phys. Rev. Lett. **91** (2003) 157003.
[8] S. Ideta *et al*., Phys. Rev. Lett. **104** (2010) 227001.
[9] S. Ideta *et al*., Phys. Rev. B **85** (2012) 104515.
[10] S. Ideta *et al*., Physica C **470** (2010) S14-S16.
[11] S. Ideta *et al.*, Activity repot **43** (2015) 45.

BL7U

Self-Energy in the Superconducting States of the High-T_c Cuprates $Bi_2Sr_2CaCu_2O_{8+\delta}$

D. Ootsuki[1], K. Yamawaki[1], D. Shimonaka[1], D. Shibata[1], H. Eisaki[2], T. Sasagawa[3], A. Fujimori[4], S. Ideta[5], K. Tanaka[5] and T. Yoshida[1]

[1]*Graduate School of Human and Environmental Studies, Kyoto University, Kyoto 606-8501, Japan*
[2] *National Institute of Advanced Industrial Science and Technology (AIST), Tsukuba 305-8562, Japan*
[3]*Materials and Structures Laboratory, Tokyo institute of Technology, Yokohama 226-8503, Japan*
[4]*Department of Physics, University of Tokyo, Tokyo 113-0033, Japan*
[5]*UVSOR Facility, Institute for Molecular Science, Okazaki 444-8585, Japan*

Angle-resolved photoemission spectroscopy (ARPES) can directly detect the spectral function $A(\boldsymbol{k},\omega)$ and, hence, one can determine the self-energy $\Sigma(\boldsymbol{k},\omega)$. From the discovery of the kink structure in the high T_c-cuprate superconductors, a considerable number of studies have been conducted on the self-energy in the nodal region where the superconducting gap closes [1, 2]. On the other hand, the self-energy in the anti-nodal region in the superconducting states also has many information of the formation of Cooper paring. Several studies have reported the self-energy in the anti-nodal region in the superconducting state and pointed out that there is a bosonic structure [3, 4]. However, the origin of the bosonic mode has not been clarified yet.

In the present study, we have performed an ARPES study of the over-doped $Bi_{2-x}Pb_xSr_2CaCu_2O_{8+\delta}$ (Pb-Bi2212) in order to determine the self-energy in the superconducting state. Here, we have applied Kramars-Kronig relation to $A(\boldsymbol{k},\omega)$ for deducing the self-energy $\Sigma(\boldsymbol{k},\omega)$ in a wide energy range [3, 5]. ARPES experiment was carried out at BL7U of UVSOR. All the data were taken with the photon energy $h\nu$ = 22.7 eV. The total energy resolution was ~10 meV. The single crystal Pb-Bi2212 was cleaved in the pressure better than 1.6×10^{-8} Pa. The measurement temperature were T = 16 K and 110 K.

Figure 1 shows the spectral function $A(\boldsymbol{k},\omega)$, the real part $\mathrm{Re}\Sigma(\boldsymbol{k},\omega)$ and the imaginary part $\mathrm{Im}\Sigma(\boldsymbol{k},\omega)$ of the self-energy deduced from ARPES spectra using the Kramers-Kronig transformation. A sharp quasiparticle peak appears corresponding to the gap opening in the superconducting state in Fig.1 (a). In the imaginary part of the self-energy $\mathrm{Im}\Sigma(\boldsymbol{k},\omega)$, the peak at E_F increases from the nodal to anti-nodal regions, which indicates the d-wave superconducting gap. In the anti-nodal region, the dip structure around 50 meV are observed in the spectral function, compared with that in the normal state. This dip structure in $A(\boldsymbol{k},\omega)$ corresponds to the drop in the imaginary part $\mathrm{Im}\Sigma(\boldsymbol{k},\omega)$ and is suppressed in going from the anti-nodal region to the nodal region. Also, the same energy scale ~50 meV appears in the $\mathrm{Re}\Sigma(\boldsymbol{k},\omega)$ below T_c, particularly in the anti-nodal direction.

In summary, we have deduced the self-energy in the superconducting states and found a characteristic energy scale ~50 meV, corresponding to the peak-dip hump structure of the spectral function. Since the characteristic structure evolves in the anti-nodal region, the observed energy scale may be relevant to the signal of the Cooper paring.

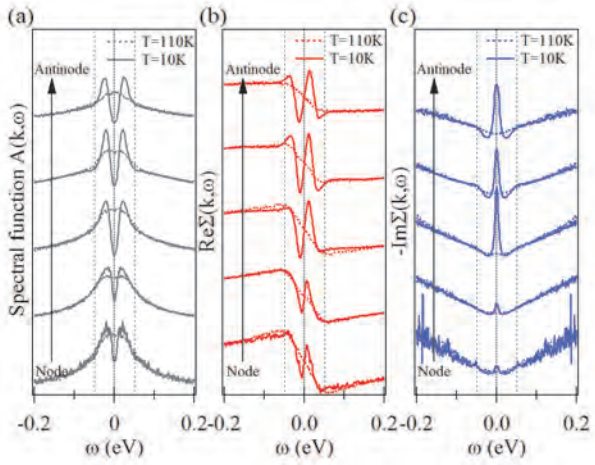

Fig. 1. (a) Spectral function $A(\boldsymbol{k},\omega)$ for the over-doped Pb-Bi2212. (b),(c) The real part $\mathrm{Re}\Sigma(\boldsymbol{k},\omega)$ and imaginary part $\mathrm{Im}\Sigma(\boldsymbol{k},\omega)$ of the self-energy deduced from the ARPES spectra using the Kramers-Kronig transformation.

[1] P. D. Johnson *et al.*, Phys. Rev. Lett. **87** (2001) 177007.
[2] A. Lanzara *et al.*, Nature **412** (2001) 510-514.
[3] M. R. Norman *et al.*, Phys. Rev. B **60** (1999) 7585.
[4] J. M. Bok *et al.*, Sci. Adv. **2** (2016) e1501329.
[5] S. Aizaki *et al.*, Phys. Rev. Lett. **109** (2012) 056401.

BL7U

Superconducting Gap of $Sr_{1-x}Ca_xFe_2(As_{1-y}P_y)_2$ (x = 0.08, y = 0.25) Revealed by Angle Resolved Photoemission Spectroscopy

T. Adachi[1], S. Ideta[2, 3], K. Tanaka[2, 3], Z. H. Tin[1], S. Miyasaka[1] and S. Tajima[1]

[1]*Graduate School of Science, Department of Physics, Osaka University, Toyonaka 560-0043, Japan*

[2]*UVSOR Facility, Institute for Molecular Science, Okazaki 444-8585, Japan*

[3]*School of Physical Sciences, The Graduate University for Advanced Studies (SOKENDAI), Okazaki 444-8585, Japan*

It is essential for elucidating the superconducting mechanism to evaluate the anisotropy of superconducting gap sizes in k-space. In our measurement performed last year, the topology of Fermi surfaces and the superconducting gap sizes on some points of Fermi surfaces in $Sr_{1-x}Ca_xFe_2(As_{1-y}P_y)_2$ (x = 0.08, y = 0.25) have been clarified. In this material, we have detected the gap minimum, which is possibly a node, in the outer electron Fermi surface around X point [1]. On the other hand, according to tight binding model + RPA calculation [2], it has been pointed out that there are superconducting gap nodes in the outermost hole Fermi surface among three hole Fermi surfaces around Z point in phosphorus doped 122 systems.

In this measurement, we observed the electronic structure, particularly the superconducting gap structure of hole Fermi surfaces near Z point of $Sr_{1-x}Ca_xFe_2(As_{1-y}P_y)_2$ (x = 0.08, y = 0.25, T_{cmax}=32K). Figure 1(a) shows Fermi surface mapping around Z point. We observed three hole Fermi surfaces around Z point, indicated by broken lines in Fig. 1(a). The superconducting gap values have been estimated at the points on these Fermi surfaces, which are indicated by dots in Fig. 1(a).

Figure 1(b) shows the superconducting gap value around Z point as a function of Fermi surface angle θ_{FS}. Here, θ_{FS} is restricted between 0 and 90 degrees reflecting the C_4 rotational symmetry of the crystal structure. The superconducting gaps on hole Fermi surface show small anisotropy but any node like behavior has not been detected. Considering the present and previous our results, only spin fluctuation due to Fermi surface nesting is not sufficient to explain the superconducting gap structures of phosphorus doped 122 systems. Our experimental results indicate that it is needed to take into account of the hybridization between the two electron pockets which makes the interlayer hopping finite, or the multiorbital effects such as orbital fluctuation due to interorbital quadrupole interaction [3, 4].

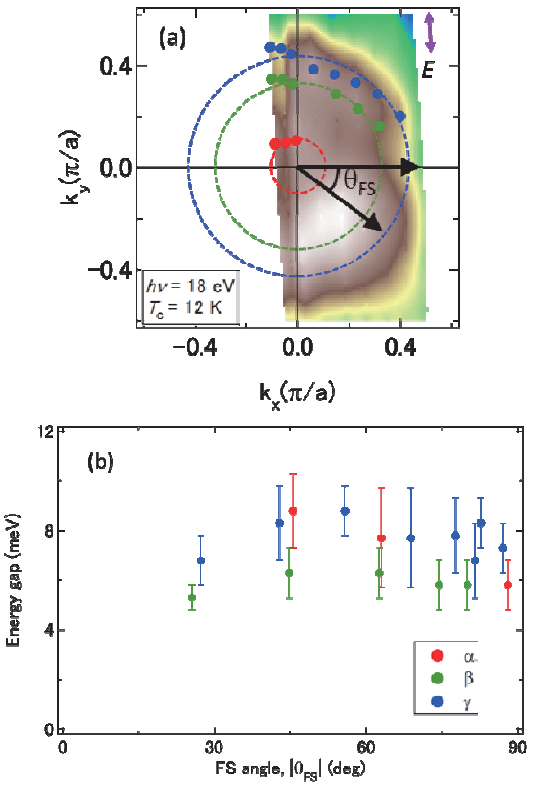

Fig. 1. (a) Fermi surface mapping around Z point in $Sr_{1-x}Ca_xFe_2(As_{1-y}P_y)_2$ (x = 0.08, y = 0.25). Three hole Fermi surfaces are indicated by the broken lines. The dots indicate the point, where the superconducting gap is estimated. θ_{FS} is Fermi surface angle. (b) Superconducting gaps around the Z point as a function of θ_{FS}.

[1] T. Adachi *et al.*, UVSOR activity report **43** (2016).
[2] K. Suzuki *et al.*, J. Phys. Soc. Jpn. **80** (2011) 013710.
[3] M. Khodas *et al.*, Phys. Rev. B **86** (2012) 144519.
[4] T. Saito *et al.*, Phys. Rev. B **88** (2013) 045115.

BL7B

Luminescence Properties of Ce- or Nd-doped $SrAl_2O_4$ Crystals with Vacuum Ultraviolet Excitation

D. Nakauchi[1], M. Koshimizu[2], T. Yanagida[1], G. Okada[1], Y. Fujimoto[2] and K. Asai[2]
[1]*Nara Institute of Science and Technology, Ikoma 630-0101, Japan*
[2]*Graduate School of Engineering, Tohoku University, Sendai 9808579, Japan*

Luminescence materials based on $SrAl_2O_4$ have extensively studied from a viewpoint of long-term persistent phosphors. In such usage, trap sites for electron-hole pairs are introduced by co-doping strategy. On the other hand, we recently reported excellent scintillation properties of Ce-, Eu-, or Nd-doped $SrAl_2O_4$ [1–3]. The band gap energy of $SrAl_2O_4$ is reported to be 6.5 eV, which corresponds to the energy of a photon with wavelength of 190 nm [4]. Therefore, vacuum ultraviolet (VUV) light is a suitable tool for analyzing the luminescence properties in the case of host excitation. In this report, we present the luminescence properties of Ce- or Nd-doped $SrAl_2O_4$ crystals with an emphasis on those with VUV excitation.

Undoped, Ce-doped, and Nd-doped crystals were grown in a floating zone method. Luminescence spectra with VUV excitation were measured at the Beamline 7B at UVSOR. X-ray-induced radioluminescence (RL) spectra were obtained using a CCD detector equipped with a monochromator.

Figure 1 shows the X-ray-induced RL spectrum of 1.0% Ce-doped $SrAl_2O_4$ crystal. A broad emission band at 380 nm is attributed to 5d-4f transition of Ce^{3+} ions. Figure 2 shows the excitation spectrum of a 1.0% Ce-doped $SrAl_2O_4$ crystal. The monitored wavelengths correspond to the 5d-4f transition of Ce^{3+} ions. 4f-5d transitions are clearly observed at 120 and 150 nm, in addition to a band-edge at 180 nm.

Figure 3 shows the photoluminescence spectra of undoped and Nd-doped $SrAl_2O_4$ crystals with excitation at 160–180 nm. The observed bands for the Nd-doped samples can be attributed to self-trapped excitons perturbed by Nd^{3+} ions.

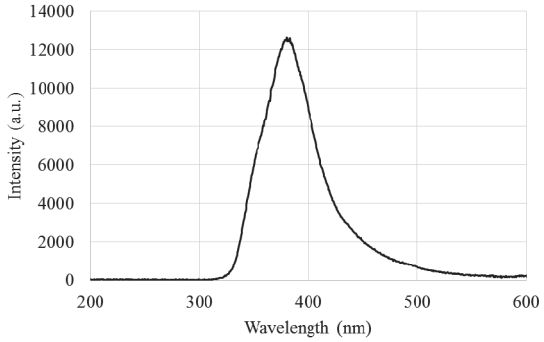

Fig. 1. X-ray-induced RL spectra of 1.0% Ce-doped $SrAl_2O_4$ crystal.

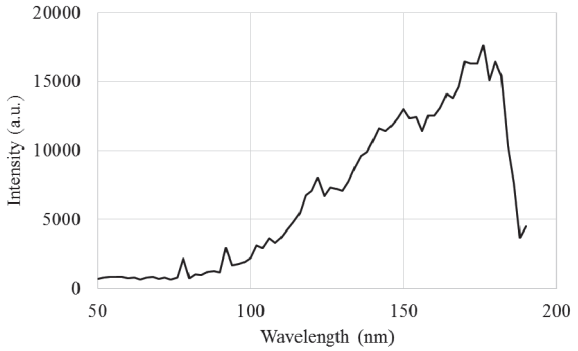

Fig. 2. Excitation spectra of 1.0% Ce-doped $SrAl_2O_4$ crystal. The monitored wavelengths correspond to the 5d-4f emission of Ce^{3+} ions.

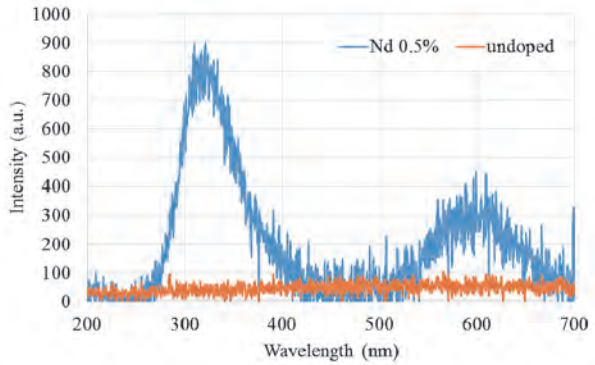

Fig. 3. Photoluminescence spectra of undoped and Nd-doped $SrAl_2O_4$ crystals with excitation at 160–180 nm.

[1] D. Nakauchi, G. Okada, M. Koshimizu and T. Yanagida, Nucl. Instrum. Methods Phys. Res. B **377** (2016) 89.
[2] D. Nakauchi, G. Okada, M. Koshimizu and T. Yanagida, J. Lumin. **176** (2016) 342.
[3] D. Nakauchi, G. Okada, M. Koshimizu and T. Yanagida, J. Rare Earths **34** (2016) 757.
[4] D. Jia, X.-J. Wang, W. Jiad and W. M. Yen, J. Lumin. **122–123** (2007) 311.

BL7B

Optical Properties of Pr^{3+} and Ce^{3+} Co-doped APLF Glass as a Fast Neutron Scintillator

T. Shimizu[1], Y. Minami[1], M. J. F. Empizo[1], M. V. Luoug[1], T. Taniguchi[1], A. Shiro[1], J. Watanabe[1], K. Yamanoi[1], N. Sarukura[1] and T. Murata[2]

[1] *Institute of Laser Engineering, Osaka University, Suita 565-0871, Japan*

[2] *Faculty of Education, Kumamoto University, Kumamoto 860-8555, Japan*

Neutron detection plays an important role in our society. Several characteristic parameters can be obtained by measuring neutrons which are generated by the fusion reaction and then elastically scattered in the high-density fusion plasma. On the other hand, neutron detection is considered as one of the non-destructive methods to inspect forms of infrastructure. Scintillator materials which are able to detect and discriminate neutrons should then be developed to be able to satisfy the demand.

The complex fluoro-oxide glass, $20Al(PO_3)_3$-80LiF (APLF) has been investigated as a candidate neutron scintillator material due to its high ^6Li content and fast decay times [1]. APLF glasses doped with Pr and Ce ions exhibit less than 30-ns decay times with optical, x-ray, and radioactive excitation. With broadband energy neutron excitation from ^{252}Cf, Pr-doped and Ce-doped APLF glasses have fast decay times of 5.3 and 28.9 ns, respectively, which are faster than a conventional scintillator, GS2 [2]. But like most scintillator materials, the fast lifetimes come at the expense of the emission intensities. To achieve fast decay times and high conversion efficiencies, we then devise a way to co-dope APLF glass with Pr and Ce. In this study, we investigate the optical properties of Pr/Ce-doped APLF glasses with different concentrations using the BL7B of UVSOR.

The optical properties of the Pr/Ce-doped APLF glasses were characterized using room-temperature photoluminescence (PL) and photoluminescence excitation (PLE) spectroscopies. Three samples were prepared, namely: (1) APLF glass doped with 1.0 mol% Pr and 2.0 mol% Ce (APLF+1.0Pr/2.0Ce); (2) APLF glass doped with 1.5 mol% Pr and 1.5 mol% Ce or (APLF+1.5Pr/1.5Ce); and, (3) APLF glass doped with 2.0 mol% Pr and 1.0 mol% Ce or (APLF+2.0Pr/1.0Ce). All samples were cut into 20-mm diameter cylinders with 8-mm thickness and were polished on both sides to an optical finish.

Figure 1 shows the PL spectra of the Pr/Ce-doped APLF glasses with 200-nm excitation. The emission peaks, which shift to lower wavelengths with decreasing Ce concentration, correspond to the inter-configurational 5d-4f transition of Ce^{3+}. In addition, all samples exhibit small emission peaks, which correspond to the 4f5d → $^3H_4$, $^1S_0$ → $^3F_4$, and $^1S_0$ → $^1G_4$ transitions of Pr^{3+}. The intensity of these emission peaks increases with increasing Pr concentration.

Figure 2 shows the PLE spectra of the Pr/Ce-doped APLF glasses monitored at their dominant peak emissions (~ 340 nm). This glasses exhibits a broad excitation channel and a peak at 270 nm regardless of the Pr and Ce concentration. These results suggest that the ~ 340-nm emission (5d-4f Ce^{3+} transition) has efficient excitation with 270 nm as evidenced by the PL spectra of the Pr/Ce-doped APLF glasses with 270-nm excitation in Fig. 2. On the other hand, the PLE spectra monitored at around the emissions corresponding to the Pr^{3+} transitions are not recorded because of their weak intensities.

The effect of co-doping on the optical properties of APLF will be elucidated in the future.

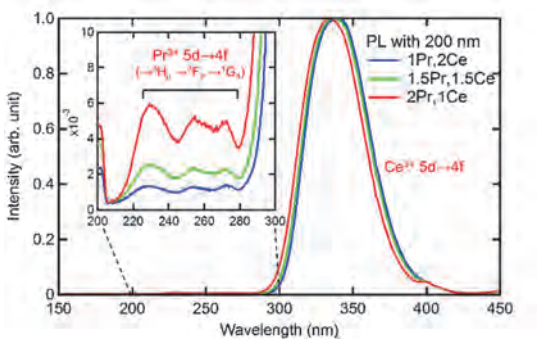

Fig. 1. PL spectra of Pr/Ce-doped APLF glasses with 200-nm excitation.

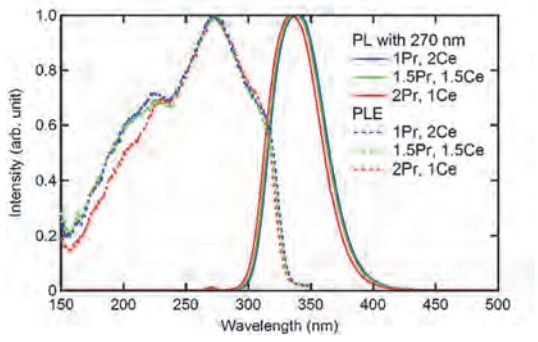

Fig. 2. PLE monitored at ~ 340 nm and PL spectra with 270-nm excitation of Pr/Ce-doped APLF glasses.

[1] Y. Arikawa *et al.*, Rev. Sci. Instrum. **80** (2009) 113504.

[2] Y. Arikawa *et al.*, Rev. Sci. Instrum. **81** (2010) 106105.

BL7B

Excitation and Emission Spectra of Pr-doped SrY_2O_4

M. Yoshino, S. Nishiki and S. Watanabe
Graduate School of Engineering, Nagoya University, Nagoya 464-8603, Japan

The trivalent lanthanide ions (e.g., Ce^{3+}, Nd^{3+}, Er^{3+}) in oxide crystals have drawn attentions due to their application for luminescent materials in NIR to UV regions such as solid-state lasers, phosphors or scintillators. The trivalent praseodymium ion, Pr^{3+}, has also attracted attentions as luminescence centers. In this work, the excitation spectra and emission spectra for Pr^{3+} in SrY_2O_4 crystal have been measured. The Pr-doped SrY_2O_4 samples are synthesized by solid state reactions. The samples are annealed in N_2-H_2 atmosphere in order to reduce Pr^{4+} to Pr^{3+}. The concentration of Pr in the samples are 0.2, 1.0 and 5.0 mol%.

The excitation spectrum monitored at 518 nm emission is shown in Fig. 1. The peak near 200 nm relates the absorption from the optical transition around the band edge in SrY_2O_4. This corresponds to the peak in the spectrum monitored at 423 nm in pure SrY_2O_4 [1]. The absorption around 315 nm and 273 nm originate the 4*f*-5*d* transitions of Pr^{3+}. The emission spectra at 315 and 273 nm excitation in 300 K are shown in Fig. 2 and Fig. 3, respectively. Peaks A, B, C exist in the each spectra. On the other hand, peak D appears only in 273 nm excitation and has different dependency to Pr concentration compared with the other peaks. The intensity of D decrease with Pr concentration while it decreases after the increase in A, B and C. The emission spectra at 273 nm excitation in different temperatures are shown in Fig. 4. It is found that the peak D has also different dependency to temperature compared with the peaks A, B and C.

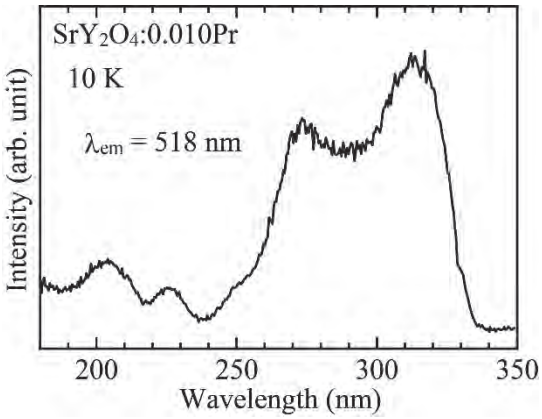

Fig. 1. Excitation spectrum of SrY_2O_4:0.010Pr.

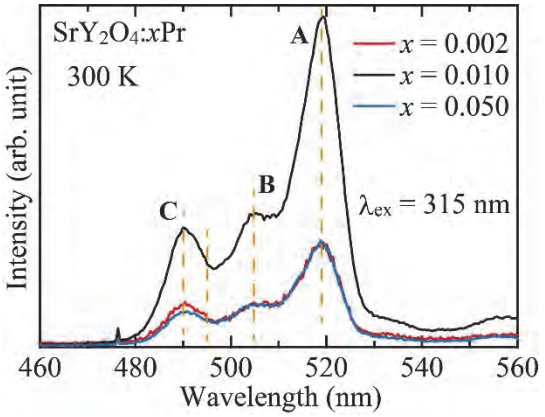

Fig. 2. Emission spectra of SrY_2O_4:*x*Pr. (λ_{ex}= 315 nm, 300 K)

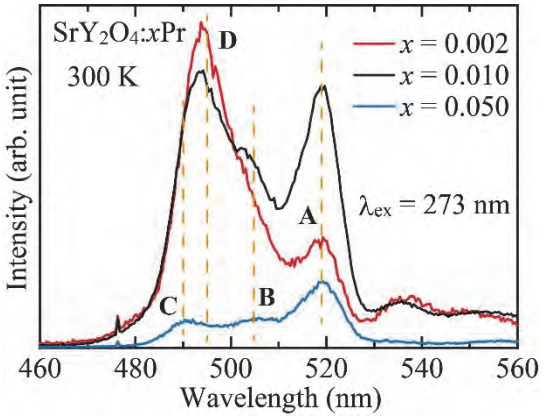

Fig. 3. Emission spectra of SrY_2O_4:*x*Pr. (λ_{ex}= 273 nm, 300 K)

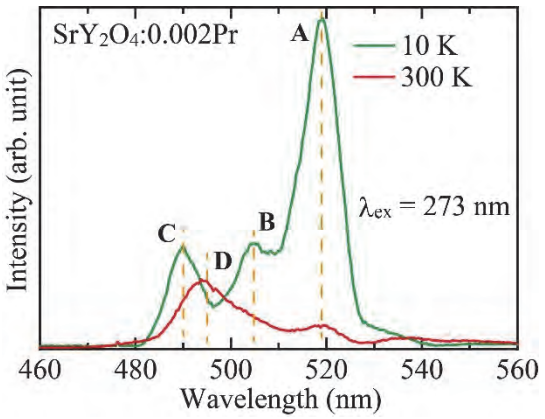

Fig. 4. Emission spectra of SrY_2O_4:0.002Pr. (λ_{ex}= 273 nm)

[1] M. Yoshino, S. Watanabe and Y. Ichikawa, UVSOR Activity Report **36** (2009) 122.

BL7B

Optical Conductivity of Zn-Ag-Sc Quasicrystal and Approximant Crystal

K. Imura[1], M. Hayashi[1], S. Kimura[2, 3] and N. K. Sato[1]

[1]*Department of physics, Graduate School of Science, Nagoya University, Nagoya 464-8602, Japan*

[2]*Graduate School of Frontier Biosciences, Osaka University, Suita 565-0871, Japan*

[3] *Department of Physics, Osaka University, Toyonaka 566-0043, Japan*

Quasicrystal (QC) is a solid in which constituent atoms are arranged according to a special rule "quasi-periodicity". QCs show a sharp x-ray diffraction pattern as shown in usual crystals, however, peculiar five or ten folded rotation symmetry is observed which is forbidden to normal crystals [1]. Therefore, the electronic state of the QC is considered to be different from the normal one; however, it has not been clarified experimentally yet. Zn-Ag-Sc QC which has an isostructural to a typical binary icosahedral Cd-Yb QC [2], and Zn-Ag-Sc approximant crystal (AC), which has locally the same structure as QC are target materials of this study.

Polycrystalline Zn-Ag-Sc QC and AC were obtained by annealing method using an evacuated quartz tube. The reflectivity measurement in the visible, ultraviolet, and vacuum-ultraviolet region i.e., the photon energy region of 1.2-30 eV, was performed at the BL7B which consists of a 3-m normal incidence monochrometer at room temperature. Low-energy reflectivity (0.01-1.5 eV) has been carried out by using a Michelson-type rapid-scan Fourier spectrometer at selected temperatures from 10 to 300 K. The optical conductivity spectra σ(ω) were obtained from the Kramers-Kronig analysis (KKA) of the reflectivity spectra extrapolating to zero-energy (DC) limit assuming Hagen-Rubens relation.

Figure 1 shows an incident energy dependence of the reflectivity $R(\omega)$ at several temperature. Comparing between QC and AC, $R(\omega)$ of QC is higher than AC in a wide energy region and some broad structures are observed at around 0.09, 1 and 3 eV.

Figure 2 shows optical conductivity spectra σ(ω) of AC at several temperatures from 10 to 300 K obtained by KKA. σ(ω) slightly increases as decreasing temperature which is consistent with the DC conductivity as shown in the inset of Fig. 2. It does not seem to reach the DC value even if it is extrapolated smoothly.

σ(ω) decreases as increasing photon energy at whole temperatures. This energy dependence is qualitatively different from icosahedral-QC Al-Cu-Fe: the σ(ω) increases linearly from DC limit to near-IR region [3]. An understanding of this difference may give important information to elucidate the electronic state of the QC. In order to clarify the low-energy electronic state, further experiments are needed.

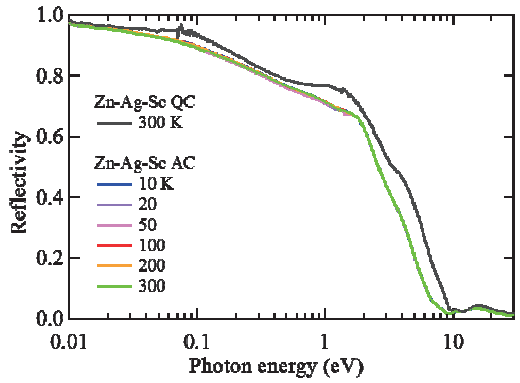

Fig. 1. Incident photon energy dependence of the reflectivity of Zn-Ag-Sc quasicrystal (T = 300 K) and 1/1 approximant crystal (T = 10, 20, 50, 100, 200, 300 K).

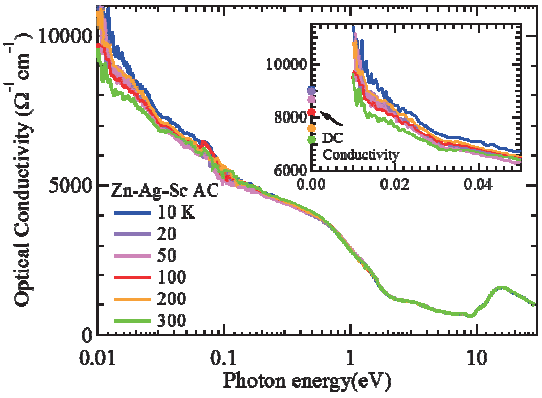

Fig. 2. Incident photon energy dependence of the optical conductivity of Zn-Ag-Sc 1/1 approximant crystal. Closed circles show DC conductivity measured by conventional four terminal method.

[1] D. Shechtman, I. Blech, D. Gratias and J. W. Cahn, Phys. Rev. Lett. **53** (1984) 1951.

[2] H. Takakura, C. P. Gomez, A. Yamamoto, M. Boissieu and A. P. Sai. Nature Matter. **6** (2007) 58.

[3] C. C. Homes, T. Timusk, X. Wu, Z. Altounian, A. Sahnoune and J. O. Strom-Olsen, Phys. Rev. Lett. **67** (1991) 2694.

BL7B

Effects of Fluorine Substitution on the Bi 6s-6p Transition of Zinc Bismuth Phosphate Glass

N. Kitamura
National Institute of Advanced Industrial Science and Technology, Ikeda 563-8577, Japan

Bismuth phosphate glasses, which have high refractive index and low deformation temperature, are candidate materials for producing high performance optical components such as compact lenses and diffractive optics. It is of interest that a zinc bismuth phosphate glass system has two distinct glass-forming regions; orthophosphate and isolated phosphate structures are dominant in the region that the atomic ratio O/P is higher than 3.5 and metaphosphate and pyrophosphate structures are dominant in the region of O/P < 3.5 [1, 2]. We have reported the glass structure and local structure around bismuth ions in a previous work [2, 3]. Recently, we found that the absorption edge of the glasses in the region O/P<3.5 shifts higher energy side by substituting ZnF_2 for ZnO [4], as shown in fig. 1. In the present study, reflectivity of the fluorine substituted bismuth phosphate glasses has been measured to make clear the band structure in the vacuum ultraviolet region.

Ternary $55ZnO\text{-}20Bi_2O_3\text{-}25P_2O_5$ glass was used a base glass. Fluorine doping was performed by substituting ZnF_2 for ZnO in the mixture of starting materials (ZnO, Bi_2O_3, and $Zn(PO_3)_2$). Fluorine content was determined by the electron probe micro analysis (EPMA). Two samples, 8%ZnF_2 (x=10 in fig.1) and 12%ZnF_2 (x=20 in fig. 1) substituted glasses, were used for reflection measurement. Reflectivity of optically polished samples was measured in the photon energy region of 3.6-25 eV with an incident angle of 10˚ at the BL7B.

Figure 2 shows reflection spectra of the un-substituted $55ZnO\text{-}20Bi_2O_3\text{-}25P_2O_5$ glass, and 8% and 12% ZnF_2 substituted glasses. Spectra for polycrystalline samples of BiF_3, ZnF_2 and ZnO were also shown in the figure. Distinct reflection peak and broad contour were respectively observed at around 4.5 eV and 5-10 eV. The peak and contour are assigned to the $6s^2 \rightarrow 6s^1 6p^1$ transition in the Bi^{3+} ion [2, 4-6]. We know that transitions from the ground state ($^1S_0$) to excited states $^3P_0$ and $^3P_2$ are spin-forbidden, but transition to $^3P_2$ level would be allowed by spin-orbit coupling [6]. Therefore, the lower distinct peak is expected to the $^1S_0 \rightarrow {}^3P_1$ transition and the next contour could be due to the $^1S_0 \rightarrow {}^3P_2$ and $^1S_0 \rightarrow {}^1P_1$ transition at least. The peak of BiF_3 was located at about 5.0 eV. The lowest peak at 4.5eV for the glass sample shifted toward higher energy side by the substitution, and the magnitude of the peak shift was about 0.3 eV by the 12%ZnF_2 substitution. It was very consistent with the absorption edge shift (~0.3eV). It was deduced that some of substituted fluorine ions would terminated to bismuth ions directly for oxygen ions.

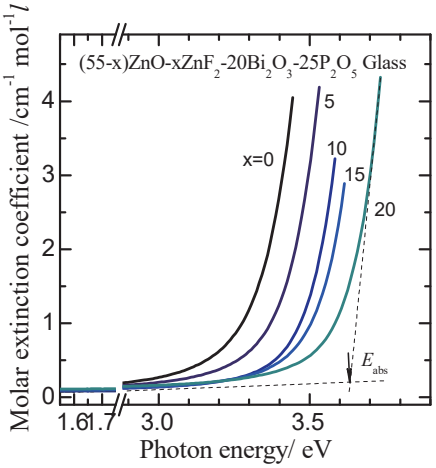

Fig. 1. Absorption spectra of (55-x)ZnO-xZnF_2-20Bi_2O_3-25P_2O_5 glasses.[4]

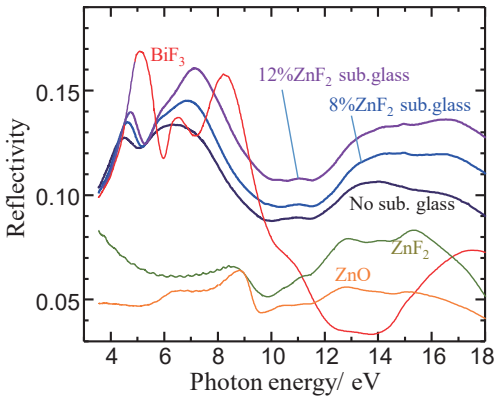

Fig. 2. Reflection spectra of 8% and 12% fluorine (ZnF_2) substituted $55ZnO\text{-}20Bi_2O_3\text{-}25P_2O_5$ glass. Spectra of un-substituted glass, polycrystalline BiF_3, ZnO and ZnF_2 also shown.

[1] B. Elouadi *et al.*, Phase Trans. **13** (1988) 219.
[2] N. Kitamura *et al.*, Mater. Sci. Eng. B **161** (2009) 91.
[3] N. Kitamura and K. Fukumi, J. Ceram. Soc. Jpn. **121** (2013) 355.
[4] N. Kitamura *et al.*, J. Non-Crysta. Solids **357** (2011) 1188.
[5] G. Blasse and A. Bril, J. Chem. Phys. **48** (1968) 217.
[6] R. H. P. Awater and P. Dorenbos, J. Lumin. **184** (2017) 221.

UVSOR User 5

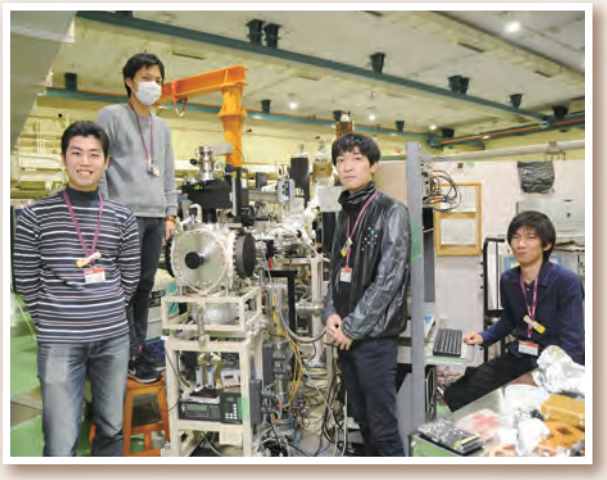

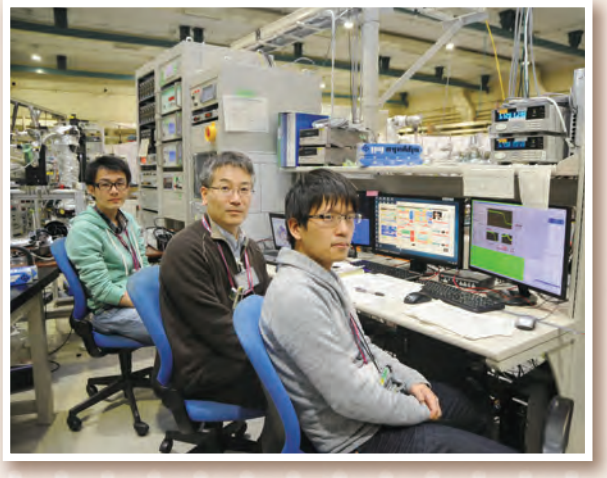

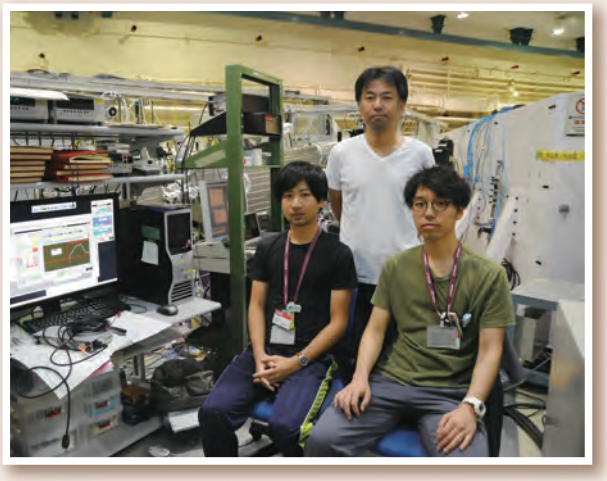

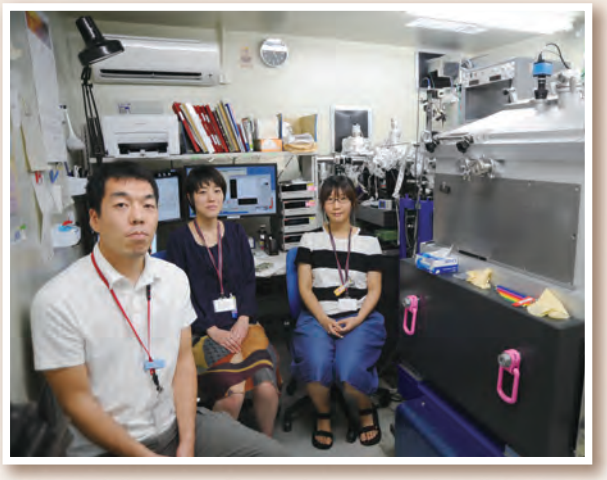

Ⅲ-3

Chemistry

Highlight

BL1U

Limitations in Photoionization of Helium by an Extreme Ultraviolet Vortex

T. Kaneyasu[1], Y. Hikosaka[2], M. Fujimoto[3], M. Katoh[3], H. Iwayama[3] and E. Shigemasa[3]

[1]*SAGA Light Source, Tosu 841-0005, Japan*

[2]*Graduate School of Medicine and Pharmaceutical Sciences, University of Toyama, Toyama 930-0194, Japan*

[3]*UVSOR Facility, Institute for Molecular Science, Okazaki 444-8585, Japan*

We report the experimental investigation on the photoionization of helium atoms irradiated with a circularly polarized extreme ultraviolet (XUV) vortex beam produced by a helical undulator [1]. The XUV vortex has a helical wavefront and carries orbital angular momentum (OAM) as well as spin angular momentum associated with it circular polarization. In recent years, several theoretical works have been reported on the photoionization and photoexcitation of atoms by OAM-carrying photons [2]. Differing from plane-wave photons, a violation of the standard electric dipole selection rules is predicted for vortex, as a consequence of the transference of the OAM to the internal degrees of freedom of the atom. In contrast to these advances in theory, to our knowledge, there has been no experimental work on vortex-matter interactions in the short wavelength regime, owing to the technical difficulty of producing brilliant and energy-tunable vortex beams.

The experiment was carried out at the undulator beamline BL1U. The experimental setup is shown in Fig. 1. The XUV vortex beams at about 30 eV photon energy were produced by a helical undulator as the higher harmonics of its radiation because the *n*th harmonic off-axis radiation from a helical undulator carries OAM of $(n-1)\hbar$ per photon [3, 4], as a result of the spiral motion of electron which naturally emits electromagnetic wave with a helical wavefront [5]. To avoid possible distortions of the helical wave front characterizing the XUV vortex, we did not use any optical elements in the experiment. The interaction point was placed at about 11 m downstream from the undulator, where the sample gas was admitted from an aperture. The central part of the undulator radiation was cut out by a 1-mm-diameter pinhole. Photoelectron angular distributions of helium atoms were measured by using a velocity map imaging (VMI) spectrometer.

Figure 2 shows the angular distributions measured for the first, second and third harmonics, corresponding to plane-wave photons (l=0), and XUV vortices of l=1 and 2, respectively. While the violation of the electric dipole transition rules has been predicted for interactions between vortices and atoms, the photoelectron angular distributions are well reproduced by the dipole components alone, and non-dipole contributions are not detected within the experimental uncertainty. This observation can be explained by considering the localized nature of the helical phase effect of the vortex on the interaction with atoms, and demonstrates that non-dipole interactions induced by vortex are hardly observable in conventional gas-phase experiments.

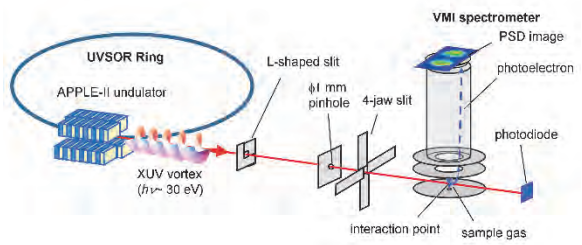

Fig. 1. Experimental setup used for photoionization experiment of helium atoms by the XUV vortex. The XUV vortex produced by the APPLE-II undulator is introduced into the interaction point without any optical elements.

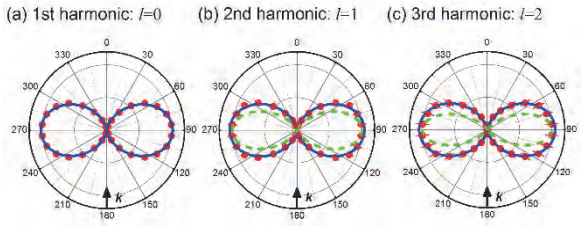

Fig. 2. Photoelectron angular distributions of helium atoms measured for the (a) first, (b) second and (c) third harmonics from helical undulator. The solid blue curves represent fits assuming electric dipole transition. The dotted green curves in (b) and (c) show the angular dependence of the photoelectron expected for non-dipole transitions induced by the OAM carried by the XUV vortex.

[1] T. Kaneyasu *et al*., Phys. Rev. A **95** (2017) 023413.
[2] A. Picón *et al*., New J. Phys. **12** (2010) 083053.
[3] S. Sasaki and I. McNulty, Phys. Rev. Lett. **100** (2008) 124801.
[4] J. Bahrdt *et al*., Phys. Rev. Lett. **111** (2013) 034801.
[5] M. Katoh *et al*., Phys. Rev. Lett. **118** (2017) 094801.

BL1U

Optical Vortex or Polarized UV Light Induced Supramolecular Chiral Orientation of an Achiral Metal Complex in a Soft Polymer Matrix

M. Takase[1], T. Akitsu[1] and M. Katoh[2]

[1]*Department of Chemistry, Faculty of Science, Tokyo University of Science, Tokyo 162-8601, Japan*

[2]*UVSOR Facility, Institute for Molecular Science, Okazaki 444-8585, Japan*

It is well known that a lot of organic polymers of liquid crystals containing azo-groups exhibit optical anisotropy after polarized UV light irradiation (Weigert effect). In recent years, we have systematically investigated organic/inorganic hybrid materials composed of chiral Schiff base metal complexes and azo-compounds in PMMA polymer films [1], chiral Schiff base metal complexes without azo-groups in protein matrix [2], and achiral Schiff base metal complex without azo-group in PVA polymer film [3] to discuss induced optical anisotropy after linearly polarized UV light irradiation or induced chiral supramolecular arrangement after circularly UV light irradiation.

In this time, we prepared organic/inorganic hybrid materials composed of water soluble binuclear Zn(II) Schiff base complex (Zn2L) without azo-compound in a PVA film to investigate not only linearly or circularly polarized UV light induced molecular orientation but also optical vortex UV light induced molecular orientation or changes by means of UVSOR BL1U.

As shown in Fig. 1, we have synthesized and characterized new Schiff base dinuclear Zn(II) complex involving chroride axial ligands and also prepared PVA polymer cast films. Without photochrmoic additives, optical dichroism at charge transfer bands could be observed after linearly polarized UV light irradiation with electric field vector of polarization due to increasing anisotropy of molecular orientation of the complexes directly. For example, the related Ni(II) complex most clearly exhibited anisotropy after linearly polarized UV light irradiation for 10 min. Fig. 2 exhibits angular dependence of polarized UV-vis spectra (absorbance at 367 nm) of Ni(II) complex. The Zn(II) complex also indicated similar behavior to Ni(II) one.

Comparing with several CD data of control experiments (only PVA film or hybrid materials, solutions or film, wavelengths or orbital angular moment dependence of UV light), we could derive preliminary results that optical vortex or polarized UV light (Fig. 3) induced molecular orientation of the Zn(II) complex in hybrid materials.

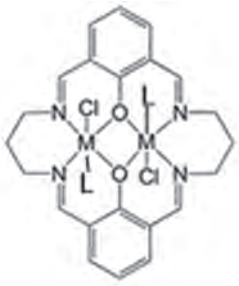

Fig. 1. Molecular structure of Zn(II) complex.

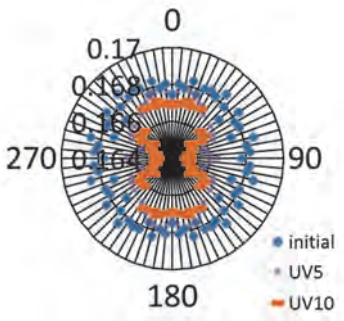

Fig. 2. Angular dependence of polarized UV-vis spectra (367 nm) of Ni(II) complex in PVA film after linearly polarized UV light irradiation (< 350 nm).

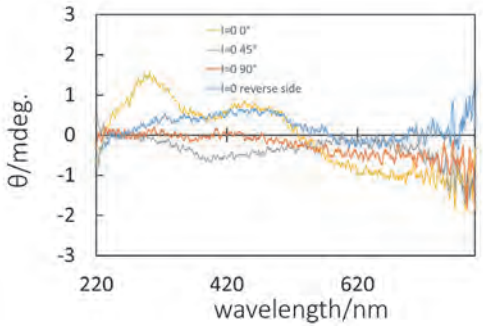

Fig. 3. CD spectra of of Zn(II) complex in PVA film after optical vortex (l=0) UV light irradiation (380 nm).

[1] N. Sunaga, C. Kominato, N. Ishida, M. Ito, T. Akitsu, T. Konomi and M. Katoh, *Azobenzene: Aspects, Applications and Reserach* (Nova Science Publishers, Inc., New York, 2017).

[2] E. Tsuda, Y. Mitsumoto, K. Takakura, N. Sunaga, T. Akitsu, T. Konomi and M. Katoh, J. Chem. Chem. Eng. **2** (2016) 53.

[3] M. Takase and T. Akitsu, *Polymers Book Series #1: Polymer science: research advances, practical applications and educational aspects* (Formatex Research Center, Badajoz (Spain), 2016).

BL3U

Local Structure of Crown Ether Inclusion Complex in Water by Soft X-ray Absorption Spectroscopy I. Interaction between Crown Ether and Ca^{2+}

H. Yuzawa, M. Nagasaka and N. Kosugi
Institute for Molecular Science, Okazaki 444-8585, Japan

Since the interaction in inclusion complexes shows a crucial role for life phenomena etc. but is not investigated in detail with conventional spectroscopic analysis [1], new methodologies are still required for detailed analysis of the interaction. Our research group has developed a liquid cell for the soft X-ray XAS in the transmission mode and has applied it to measurements of various aqueous solutions [2]. In the present study, we have extended this method to the measurement for the inclusion complex system of crown ethers in water to observe the interaction. Especially, we paid attention to the influence of the pore diameter of crown ether on the interaction in inclusion complexes by using three different crown ethers. In this part, we report Ca L-edge XAS of aqueous $Ca(SCN)_2$ crown ether solutions.

The experiments were carried out at BL3U. Aqueous solution samples (molar ratio, $Ca(SCN)_2 : H_2O = 1 : 59$, $Ca(SCN)_2 : H_2O$: 18-crown-6 = 1 : 59 : 1, $Ca(SCN)_2 : H_2O$: 15-crown-5 = 1 : 59 : 1 and $Ca(SCN)_2 : H_2O$: 12-crown-4 = 1 : 195 : 1) were prepared by using the commercial reagents without further purification. After the liquid cell which is composed of two Si_3N_4 membranes was filled with the liquid sample, the thickness (absorbance) of liquid samples was optimized by controlling the He pressure around the cell and then the Ca L-edge XAS was measured. The photon energy was calibrated by using the C K-edge XAS spectrum of the proline thin layer.

Figure 1 shows the obtained Ca L-edge XAS spectra. Two intense absorption peaks are assigned to Ca $2p_{3/2}$ → 3d excitation around 349.3 eV and Ca $2p_{1/2}$ → 3d one around 352.6 eV. These peak energies are slightly shifted to the lower energy (orange, green and blue lines in inset figures) compared with that in the simple aqueous $Ca(SCN)_2$ solution (red line). On the other hand, in the case of aqueous $Ca(SCN)_2$-EtOH solution (molar ratio, $Ca(SCN)_2 : H_2O$: EtOH = 1 : 59 : 3), the energy shift is not observed (data not shown). This result indicates that the observed energy shift arises from the formation of crown ether-Ca^{2+} inclusion complex.

In the lower energy regions for the intense peaks, fine absorption structures in weak intensity are observed (Fig. 1, upper figure) mainly because the crystal field splitting of 3d states [3]. In the 18-crown-6 contained solution (orange line), the shapes of peaks around 348.4 and 351.4 eV is clearly different from the other samples. Compared with the previous report for the Ca L-edge spectra of solid CaF_2, the obtained difference is similar to the change for the coordinative unsaturation (disordered coordination symmetry) [4]. In addition, the pore diameter of 18-crown-6 is larger than the ionic diameter of Ca^{2+} (1.98 Å), whose size is fitted for that of 15-crown-5. Thus, Ca^{2+} would be coordinated by 18-crown-6 more unsymmetrically than the other samples with its molecular frame folding. In the 15-crown-5 contained sample (green line), the peak shape around 351.6 eV is more symmetrical than the other samples. This may be because the coordination symmetry is the highest in the samples [4].

Therefore, Ca L-edge XAS can be used as an effective indication of the coordination symmetry of crown ether complexes.

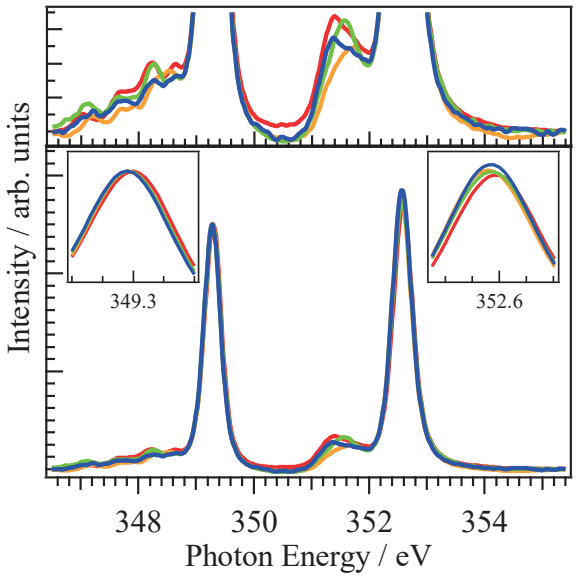

Fig. 1. Ca L-edge soft x-ray absorption spectra of aqueous $Ca(SCN)_2$ solution (red line), that containing 18-crown-6 (orange line), that containing 15-crown-5 (green line) and that containing 12-crown-4 (blue line). Upper figure is magnified view of small peaks and two inset figures are magnified views of two intense absorption (Ca-L_3 and L_2) peaks.

[1] G.W. Gokel, W.M. Leevy and M.E. Weber, Chem. Rev. **104** (2004) 2723.
[2] M. Nagasaka, H. Yuzawa and N. Kosugi, J. Spectrosc. Relat. Phenom. **200** (2015) 293.
[3] M.F.M. de Groot *et al*., Phys. Rev. B **41** (1990) 928.
[4] M.F.M. de Groot *et al*., Phys. Rev. B **43** (1991) 6899.

BL3U

Local Structure of Crown Ether Inclusion Complex in Water by Soft X-ray Absorption Spectroscopy II. Interaction between Crown Ether-Ca^{2+} Complex and SCN^- Anion

H. Yuzawa, M. Nagasaka and N. Kosugi
Institute for Molecular Science, Okazaki 444-8585, Japan

It is shown in Part I that the Ca L-edge XAS spectra of $Ca(SCN)_2$-crown ether solutions can give the information about the coordination symmetry of crown ether-Ca^{2+} inclusion complexes [1]. In this Part II, we show C K-edge and N K-edge XAS spectra for SCN^- anion to investigate the interaction between crown ether-Ca^{2+} inclusion complex and SCN^- anion.

The experiments were carried out at BL3U. The procedure of the XAS measurement is the same as that in Part I [1]. Another aqueous solution ($Ca(SCN)_2$: H_2O : EtOH = 1 : 59 : 3) was also prepared. In N K-edge XAS, a liquid cell composed of two SiC membranes instead of Si_3N_4 was used. The photon energy was calibrated by using C K-edge and N K-edge XAS spectra of the proline thin layer.

Figure 1 (a) shows the obtained N K-edge XAS spectra. The absorption peak around 399.5 eV is assigned to the 1s → π* excitation of SCN^- anion, whose peak top energy is constant regardless of the addition of the crown ethers. In the previous report of KSCN aggregate structure in aqueous solution, the N atom in SCN^- interacts with K^+ and the N K-edge peak top energy is shifted to the lower energy than that of hydrated SCN^- [2]. Thus, the constant absorption peak energy for the Ca(SCN)-crown ether solutions would be because N atom in SCN^- is apart from crown ether-Ca^{2+} complex.

Figures 1 (b) and (c) show C K-edge XAS spectra. The obtained peak around 287.3 eV is assigned to the 1s → π* excitation of SCN^- anion. The peak energy is shifted to the lower energy (Fig. 1 (b), orange, green and blue lines) compared with that in the simple aqueous $Ca(SCN)_2$ solution (red line), while in the case of aqueous $Ca(SCN)_2$-EtOH solution, the energy shift is not observed (Fig. 1 (c), gray line). This indicates that crown ether-Ca^{2+} inclusion complex and SCN^- anion are not completely dissociated and are interacted with each other. However, in the case of KSCN aqueous solution, the peak energy of C K-edge XAS in SCN^- is constant without relation to the formation of aggregate structures, which means that the C atom in SCN^- hardly interacts with cations [2]. Furthermore, peak energy shift is not induced by EtOH without the coordination to Ca^{2+} (Fig. 1 (c), grey line). Thus, the obtained energy shift would arise from the interaction between the C atom in SCN^- and crown ether ligand.

Therefore, the interaction between crown ether-Ca^{2+} inclusion complex and SCN^- is expected as follows. The coordination of crown ether to Ca^{2+} induces the interaction between Ca^{2+} and SCN^- from the S atom direction. In this structure, the C atom is close to (interacted with) the crown ether ligand to induce the energy shift of C K-edge XAS.

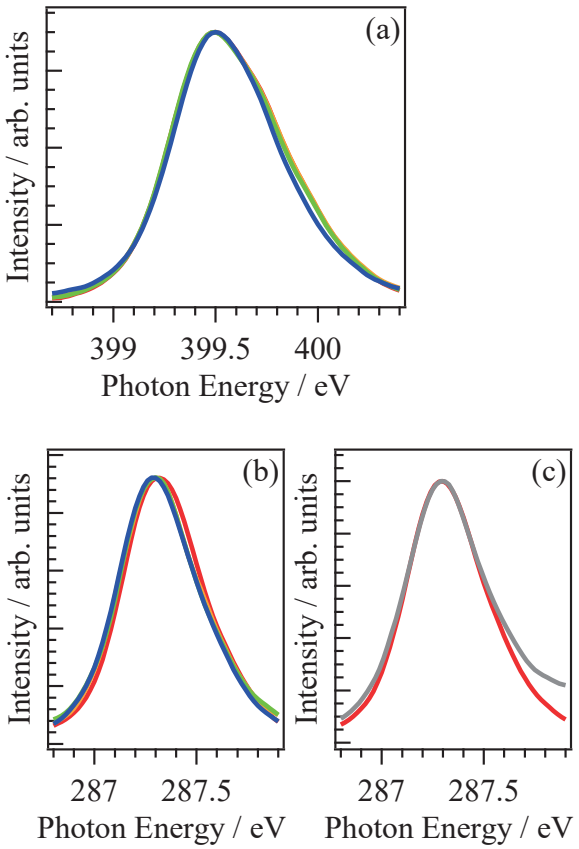

Fig. 1. (a) N K-edge XAS spectra of aqueous $Ca(SCN)_2$ solution (red line), that containing 18-crown-6 (orange line), that containing 15-crown-5 (green line) and that containing 12-crown-4 (blue line), (b) C K-edge XAS spectra for the same solutions as those of (a) and (c) C K-edge XAS of aqueous $Ca(SCN)_2$ solution (red line) and that containing EtOH (gray line). The deviation in higher energy region (> 287.5 eV) between red line and gray line is derived from the absorption of EtOH.

[1] H. Yuzawa, M. Nagasaka and N. Kosugi, UVSOR Activity Report in this volume.
[2] H. Yuzawa, M. Nagasaka and N. Kosugi, UVSOR Activity Report **42** (2015) 97.

BL3U

Study of Salting Effects in Compounds with Atmospheric Relevance by Using Soft X-ray Absorption Spectroscopy

G. Michailoudi[1], M. Patanen[1], N. Prisle[1], M. Huttula[1], H. Yuzawa[2], M. Nagasaka[2] and N. Kosugi[2]
[1]*Nano and Molecular Systems research unit, University of Oulu, P.O. Box 3000, 90014 University of Oulu, Finland*
[2]*UVSOR Synchrotron, Institute for Molecular Science, Okazaki 444-8585, Japan*

The aerosol particles in the atmosphere have an important effect on climate. Previous studies revealed the great impact of interactions between organic and inorganic compounds on atmospheric chemistry [1, 2]. In order to study salting effects on atmospheric organics, soft X-ray absorption spectroscopy was applied. This method has the advantage of high sensitivity to the chemical environment of the absorbing atom and together with molecular dynamics / quantum mechanics modelling our aim is to learn i) what are the structures of the formed hydrates of these organics ii) what are the relative concentrations of hydrated forms iii) how addition of salts changes the relative abundance of the hydrates and does e.g. ion-pairing or complex formation occur.

Aqueous solutions of organic compounds glyoxal ($C_2H_2O_2$), methylglyoxal ($C_3H_4O_2$), and glycerol ($C_3H_8O_3$) were prepared in the chemistry laboratory right before the experiments, in different concentrations, ranging from 0.1 to 2 M. These compounds were also mixed with sodium chloride (NaCl) or sodium sulfate (Na_2SO_4), with different mixing ratios, while the concentrations of salts were 1 and 2 M. The samples were placed to a liquid flow cell [3] and exposed to soft X-ray radiation at BL3U beamline at UVSOR synchrotron. In order to investigate the carbon K-edge absorption spectra, the photon energy was scanned between 280 and 305 eV, and for the oxygen K-edge absorption spectra, the chosen photon energy range was from 525 to 550 eV.

Figure 1 presents examples of the preliminary analysed data at the C 1s absorption edge of binary glyoxal - water and methyl glyoxal – water solutions (black and red circles, respectively) together with Na_2SO_4 addition. A background spectrum containing absorption from water and liquid cell membranes has been subtracted. The addition of salt does not introduce shifts to the observed absorption features and it can be concluded that in case of glyoxal, the bihydrated form is dominating. Methyl glyoxal shows three distinct absorption features which can be associated with its three inequivalent carbons.

Figure 2 shows a comparison of 2 M glyoxal solution (purple), 2 M Na_2SO_4 solution (green) and their mixture (red), together with a water spectrum (dashed blue line). The spectra have been normalized to the background preceding the water pre-peak. The pre-peak shifts upon addition of Na_2SO_4, which is evident from pure Na_2SO_4 aqueous solution. Modelling is needed to further conclude about the aqueous forms of the studied organics.

The obtained data will give valuable information of bulk properties of these solutions, as in larger framework we are interested in the interactions occurring in clusters and aerosols containing these compounds, their physical and chemical properties and their reactivity. Our goal is to access the missing molecular scale information of aerosol particles and to better understand their impact on climate.

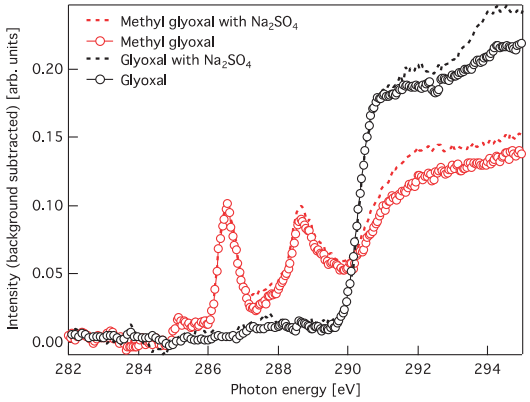

Fig. 1. C K-edge spectra of glyoxal – water (2 M) and methyl glyoxal - water (1 M) binary solutions and 1 : 1 mixtures with Na_2SO_4.

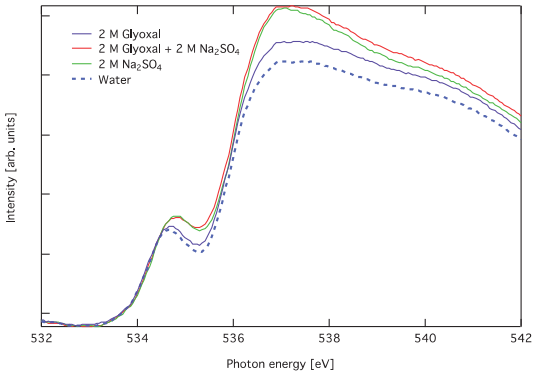

Fig. 2. A comparison of 2 M aqueous solution of glyoxal, 2 M Na_2SO_4 solution and their mixture, together with a water spectrum.

[1] T. Kurtén *et al.*, J. Phys. Chem. A **119** (2015) 4509.
[2] A.M.K. Hansen *et al.*, Atmos. Chem. Phys. **15** (2015) 14071.
[3] M. Nagasaka, T. Hatsui, T. Horigome, Y. Hamamura and N. Kosugi, J. Electr. Spectrosc. Rel. Phen. **177** (2010) 130.

BL3U

Development of a Microfluidic Cell for Soft X-ray Absorption Spectroscopy

M. Nagasaka[1], H. Fischer[2], H. Yuzawa[1], M. Nakano[1], N. Takada[1], M. Aoyama[1], E. Rühl[2] and N. Kosugi[1]

[1]*Institute for Molecular Science, Okazaki 444-8585, Japan*
[2]*Physikalische Chemie, Freie Universität Berlin, Takustr. 3, D-14195 Berlin, Germany*

Microfluidics is a chemical technique to realize highly efficient chemical reactions in liquids and solutions [1]. Recently, X-ray diffraction in the hard X-ray region has been used for a variety of systems by using microfluidics [2]. However, it is difficult to apply spectroscopic techniques in the soft X-ray region since soft X-rays cannot penetrate a microfluidic cell. In this study, we have successfully measured fluorescence excitation spectra resembling soft X-ray absorption spectroscopy (XAS) of structured liquids by developing a microfluidic cell with a 100 nm thick SiC membrane window.

The experiments were performed at BL3U connected to a developed microfluidic cell. A T-shape microfluidics setup with the width of 50 μm is made from PDMS resin which is covered by a 100 nm thick SiC membrane. The adhesion of PDMS to the SiC membrane is realized by pressing a Si frame of the membrane with O-rings. Pyridine and water are mixed in the T-shape microfluidics cell with flow rate of 10 μL/min by using syringe pumps. The microfluidic cell is placed in a helium in atmosphere. The ultrahigh vacuum of the soft X-ray beamline is separated from the microfluidic cell by a 100 nm thick SiC membrane with a window size of 36 × 23 μm^2, which determines the soft X-ray beam size. Spatially resolved XAS spectra of microfluidic cell are measured in the fluorescence mode by using a silicon drift detector.

Figure 1 shows a soft X-ray fluorescence image of the T-shape microfluidic cell excited by soft X-rays at 550 eV. The fluorescence image shows high intensity due to water, since the excitation energy of 550 eV is above the O K-edge. Water flows from the upper side, and pyridine from the lower side. The water-pyridine mixture flows to the right hand part after the junction of the liquids. Figure 2 shows N K-edge XAS spectra of microfluidic cell at different positions. The N 1s → π* peak of pyridine in the mixed position (X=350, Y=200) shows a shift to higher photon energy than is observed for pure pyridine at X=200, Y=100. The energy shift of the pyridine-water mixture is consistent with our previous XAS studies [3], in which the formation of a hydrogen bond of the N atom in pyridine with water causes a shift to higher photon energy of the π* peak.

We have successfully measured spatially resolved XAS of microfluidics in the soft X-ray regime with a spatial resolution of 36 × 23 μm^2. In the future, we will investigate several chemical reactions occurring in microfluidic cell by spatially resolved XAS using our T-shape microfluidics setup.

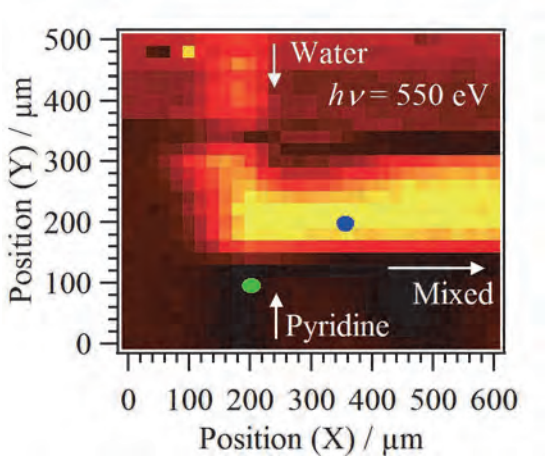

Fig. 1. Soft X-ray fluorescence image of a T-shape microfluidic cell excited by soft X-rays at 550 eV. The flows of pyridine and water are mixed in this device. It also shows two spots to measure N K-edge XAS spectra, as shown in Fig. 2.

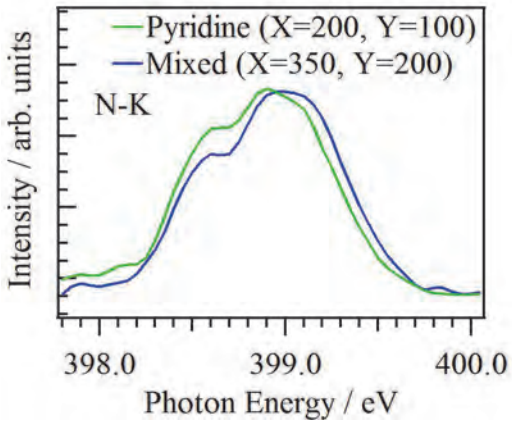

Fig. 2. N K-edge XAS spectra at different positions in the T-shaped microfluidic cell at positions indicated in Fig. 1.

[1] T. Kitamori *et al.*, Anal. Chem. **76** (2004) 53.
[2] B. Weinhausen and S. Köster, Lab Chip **13** (2013) 212.
[3] M. Nagasaka *et al.*, J. Electron Spectrosc. Relat. Phenom. **200** (2015) 293.

BL4U

Characterization of Macroporous Monolithic Polymers Containing Amphiphilic Macro-RAFT Agent by Scanning Transmission X-Ray Microscopy (STXM)

D. Arrua[1], A. Khodabandeh[2], T. Ohigashi[3], N. Kosugi[3] and E. Hilder[1]

[1]*Future Industries Institute, University of South Australia, Building X, Mawson Lakes Campus, GPO Box 2471 Adelaide SA 5001, Australia*

[2]*Australian Centre for Research on Separation Science (ACROSS), School of Chemistry, University of Tasmania, Private Bag 75, Hobart 7001, Australia*

[3]*UVSOR Facility, Institute for Molecular Science, Okazaki 444-8585, Japan*

Macroporous polymer materials with interconnected structures represent a useful class of polymers used in different fields including separation science in the last decades [1]. An increasingly exploited method for the preparation of highly porous scaffolds is based on the solidification of the continuous phase of a high internal phase emulsion (HIPE) through polymerization. A cellular monolithic structure, commonly with interconnected pores and hence an open cellular network is produced, referred to as a poly(HIPE). Our aim here is to develop a surfactant-assisted functionalization strategy for preparation of styrene-based porous polymers by HIPE polymerization, whereby the obtained porous polymers have a specific application [2]. An accurate characterization of such polyHIPE material is needed to better understand the polymer morphology as well as surface chemistry [3].

The characterization by STXM of polyHIPE materials was performed at the BL4U beamline of the UVSOR synchrotron radiation facility. STXM imaging was conducted by focusing on the C 1s core-line signal in NEXAFS. Fig. 1 shows the C 1s NEXAFS spectra obtained for both polyHIPEs (A1 with macro-RAFT agent and A2 with End-group removed macro-RAFT agent) cross-linked styrene network.

The components found by STXM were the poly(Sty-co-DVB) polyHIPE, the macro-RAFT agent, and the embedding resin. The spectrum for the crosslinked styrene-based scaffold has a strong peak at 284.6 eV, which is characteristic of C 1s → π*C=C transition in a phenyl ring. The macro-RAFT agent spectrum shows two peaks: a strong peak at 284.9 eV, which corresponds to the C 1s → π*C=C transition of the phenyl ring (styrene of macro-RAFT agent) and a peak at 288.9 eV, which is characteristic of C 1s → π*C=O transition in esters. Using a sequence of highly resolved X-ray photon energies covering the C 1s spectral region (280 to 320 eV), successive image was obtained for polyHIPE A2. STXM composite component map on polyHIPE respect to the corresponding X-ray spectra of references, the macro-RAFT agent, Styrene-DVB crosslinked polymer network and epoxy components are shown in blue, green, and red, respectively in Fig. 2.

As a conclusion, soft X-ray microscopy images recorded at multiple wavelengths have been used to qualify the chemical composition in polyHIPE. The results shown in this work clearly demonstrate how STXM analysis can reveal chemical information for these materials.

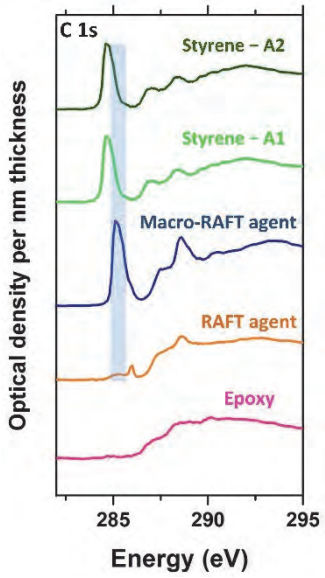

Fig. 1. NEXAFS reference spectra of the epoxy (embedding matrix), RAFT agent, macro-RAFT agent, and polystyrene cross-linked polyHIPEs that correspond to 1 nm thickness of each component.

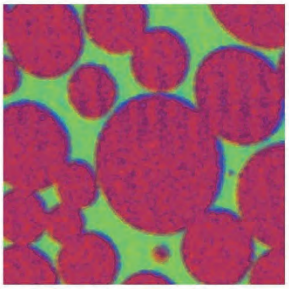

Fig. 2. STXM color coded composite map (red=epoxy, green=PSty, blue=macro-RAFT agent).

[1] D. Wu *et al.*, Chem. Rev. **112** (2012) 3959.
[2] A. Khodabandeh *et al.*, Poly Chem **7** (2016) 1803.
[3] D. Arrua *et al.*, UVSOR Activity Reports **42** (2014) 76.

BL4U

Liquid-Liquid Interface between Triethylamine and Water Phases Studied by Spatially-Resolved Soft X-ray Absorption Spectroscopy

M. Nagasaka, T. Ohigashi, H. Yuzawa, Y. Inagaki and N. Kosugi
Institute for Molecular Science, Okazaki 444-8585, Japan

Aqueous triethylamine (TEA) solution shows a lower critical solution temperature (LCST) behavior [1], in which two liquids are mixed at the lower temperature and splits into two phases with the temperature increase. Because the phase transition is contrary to normal, the mechanism of LCST has not yet been fully understood. In this study, we have investigated local structures of liquid-liquid interfaces between TEA and water phases by spatially-resolved soft X-ray absorption spectroscopy (XAS).

The experiments were performed using a liquid flow cell in STXM (scanning transmission X-ray microscope) on BL4U [2]. The liquid layer is sandwiched between 100 nm-thick Si_3N_4 membranes. The liquid-liquid interface between TEA and water phases is formed from aqueous TEA solutions with the molar fraction of 0.4 at the temperature of 29.9 ºC, which is above the LCST.

Figure 1 shows O K-edge XAS of water at different positions of the liquid-liquid interfaces. The inset shows the soft X-ray transmission image at 530 eV, in which the center part is a water phase and is surrounded by a TEA phase. We have measured O and C K-edge XAS in the region indicated by the red arrow. Figure 2 shows molar concentrations of water and TEA at different positions, which is determined from the edge-jumps of XAS in O and C K-edges, respectively. In the TEA phase, the molar fraction of TEA is increased to 0.6 because water molecules are gathered to the water phase. It is consistent with the phase diagram of TEA-water mixtures [1], where the LCST is increased at the higher fraction of TEA. In the liquid-liquid interface, on the other hand, the amount of TEA is reduced to one third, and that of water is drastically increased. In the water phase, the most part is water molecules due to the formation of hydrogen bonding (HB) network of water.

Figure 3 shows the energy shifts of the pre-edge peaks (535 eV) in the O K-edge XAS at different positions. It is already known that the pre-edge peak is shifted to the lower photon energy when HB between water molecules is elongated. From the water to the TEA phase, the pre-edge peaks show lower energy shifts. Because the amount of water is decreased with the direction of the TEA phase, the hydrophobic interaction of ethyl group in TEA is stronger than the HB interaction of water, which leads to the elongation of the HB network. Water and TEA molecules are coexisted in the TEA phase because the HB network of water is weakened. The liquid-liquid interface between water and TEA phases is formed with the balance of the hydrophobic interaction of TEA and HB interaction of water, which is changed by gathering water molecules to the water phase.

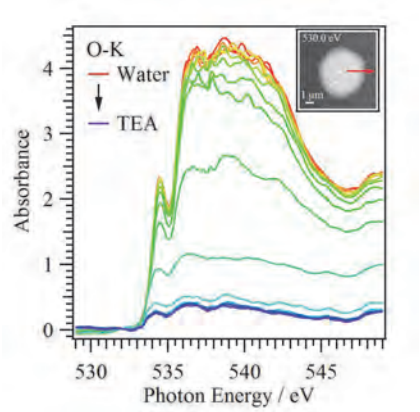

Fig. 1. O K-edge XAS of water at different positions. The inset shows the image at 530 eV, in which the red arrows indicate the measurement region.

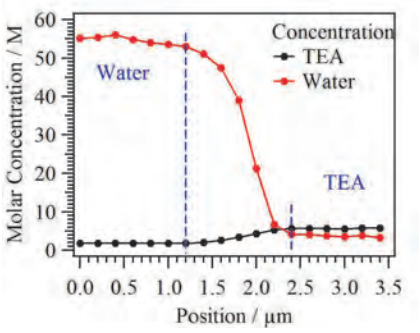

Fig. 2. Molar concentration of liquid-liquid interface determined from the edge-jump of XAS.

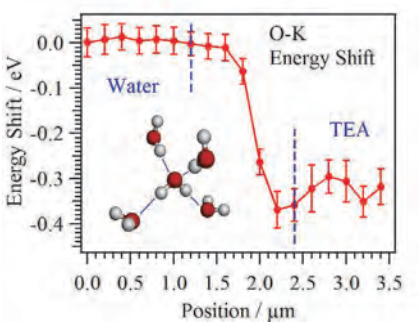

Fig. 3. Peak shift of the pre-edge peak in O K-edge XAS as a function of positions in the liquid-liquid interface.

[1] F. Kohler and O. K. Rice, J. Chem. Phys. **26** (1957) 1614.
[2] T. Ohigashi *et al.*, AIP Conf. Proc. **1741** (2016) 050002.

BL4B

Photoelectron-Auger Electron Coincidence Study of the Electron Emission from Condensed Water Molecules

R. Mashiko[1], K. Soejima[1], E. Shigemasa[2] and Y. Hikosaka[3]

[1]*Department of Environmental Science, Niigata University, Niigata 950-2181, Japan*

[2]*UVSOR Facility, Institute for Molecular Science, Okazaki 444-8585, Japan*

[3]*Graduate School of Medicine and Pharmaceutical Science, University of Toyama, Toyama 930-0194, Japan*

Electron coincidence spectroscopy enables one to clarify energy correlations between electrons emitted after a single photon. Extremely-efficient electron coincidence measurements can be achieved by a use of the magnetic bottle technique [1]. In the present study, photoelectron-Auger electron coincidence spectroscopy using a magnetic bottle electron spectrometer is applied to the study of inner-shell photoionization of water molecules condensed on solid surface [2].

The experiment was performed at the beamline BL4B under the single bunch operation of the storage ring. Water molecules were adsorbed on the surface of a copper wire, by continuously cooling the wire down to the liquid nitrogen temperature, under the base pressure of ~1.8×10^{-8} Torr. Coincidence datasets were accumulated with a magnetic bottle electron spectrometer [3], for electrons emitted from the condensed water on irradiation of 738.2 eV photons.

The two-dimensional map in Fig. 1 displays the energy correlation of the coincident electrons included in the coincidence datasets. A clear structure running vertically is associated with the coincidences between the O1s photoelectrons and the Auger electrons from condensed water. To display the O1s photoelectron structure closely, the coincidence counts on the map are projected onto x-axis and are presented in the top panel. The projection curve shows an O1s photoelectron peak displaying a continuous structure on the lower kinetic energy side. The long tail is attributed mainly to the photoelectrons with reduced energies due to inelastic scatterings on the escape from the inside of the water condensation.

Figure 2 presents Auger electron spectra observed in coincidence with O1s photoelectrons (region (a) in Fig. 1) and energy-loss photoelectrons due to inelastic scatterings (region (b) in Fig. 1). The coincidence Auger spectrum in Fig. 2 (a) shows a considerable intensity below 420 eV, which is ascribable to an energy loss of the Auger electrons due to the inelastic scattering. In Fig. 2 (b), the contribution from the inelastic scattering is enhanced. This observation can be understood as follows: the selection of photoelectrons with energy loss picks out the photoemission events for H_2O molecules distant from the outermost surface and thus the Auger electrons ejected from these molecules are also subject to remarkable inelastic scattering.

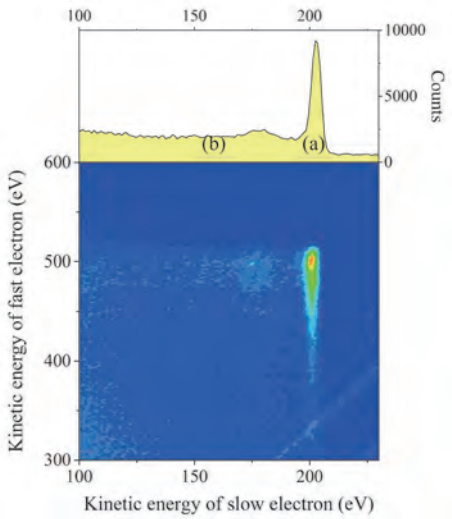

Fig. 1. Two-dimensional map showing the energy correlation of the coincident electrons emitted from condensed water molecules on irradiation of 738.2 eV photons.

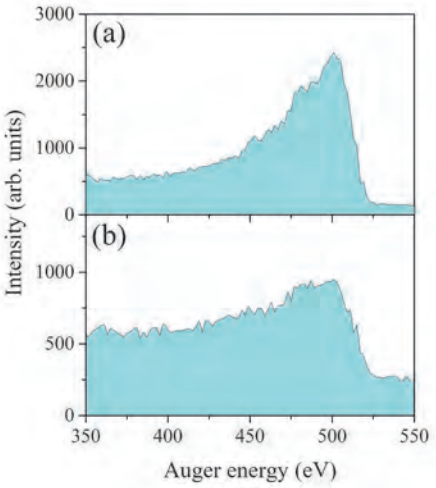

Fig. 2. Auger electron spectra observed in coincidence with O1s photoelectrons (region (a) in Fig. 1) and energy-loss photoelectrons due to inelastic scatterings (region (b) in Fig. 1).

[1] J. H. D. Eland *et al*., Phys. Rev. Lett. **90** (2003) 053003.
[2] Y. Hikosaka *et al*., J. Electron Spectrosc. Rel. Phenom. **213** (2016) 17.
[3] Y. Hikosaka *et al*., J. Electron Spectrosc. Rel. Phenom. **192** (2014) 69.

BL6U

Producing Mechanism of Metastable OCS^{3+} Studied by Photo-Electron-Ion Coincidence Method

F. Kumaki[1], H. Iwayama[2], E. Shigemasa[2] and K. Soejima[1]

[1]*Department of Environmental science, Niigata University Niigata 950-2181, Japan*

[2]*UVSOR Facility, Institute for Molecular Science, Okazaki 444-8585, Japan*

We have studied that dissociation processes and stabilities of molecules absorbed a soft X-ray which are photo-ionized and subsequently lead to Auger decay. While most multicharged molecular ions produced after photo-ionization immediately dissociate due to the Coulomb repulsion, the existence of metastable multicharged molecular ions depending on the electronic states is known. As a few exceptions, producing processes of the metastable multicharged molecular ions are almost not clarified. The OCS molecule is known to produce a doubly-ionized molecular ion. In the past work, we studied the processes of the producing metastable OCS^{2+} by an Auger electron-photo ion coincidence technique. The observation was done for Auger decay from C1s, O1s and S2p inner shell photoionization. The valence electronic configuration of the OCS is described as $(6\sigma)^2(7\sigma)^2(8\sigma)^2(9\sigma)^2(2\pi)^2(3\pi)^2$. This measurement revealed that metastable OCS^{2+} can be produced when its Auger final states with the $(3\pi)^{-2}$ configuration. Also it was revealed that metastable OCS^{2+} produced following S2p photoionization is populated with much higher possibility compared with that arising from C1s and O1s photoionizations. It is understood that the origin of this site-specificity in the production of metastable OCS^{2+} arises from the spacial distribution of 3π valence orbital involved [1, 2]. It is also known that the metastable triply-ionized OCS molecule exists. Does theproduction mechanism of the metastable OCS^{3+} have characters like that of metastable OCS^{2+}? In this work, we have studied metastable OCS^{3+} by the photoelectron-photoion coincidence measuremens.

The experiment was performed at the beamline 6U of the UVSOR facility. We used the electron-ion coincidence spectrometer consisting of a double toroidal electron analyzer and an ion time-of-flight (TOF) analyzer [2]. We measured photoelectronphotoion coincidence signals following C1s, O1s and S2p photoionization.

Figure 1 shows TOF spectra of photoions arising from Auger decay following C1s, O1s and S2p photoionization respectively in coincidence with the photo-electrons. The peaks of OCS^{3+} are commonly observed around 2500 ns though these are weak. The ratio of the coincidence counts of C1s, O1s and S2p photoionization is C1s:O1s:S2p = 2.8:1:1.9. The ratio in metastable OCS^{2+} is S2p > O1s > C1s in the past experiment. The result of OCS^{3+} is different from that. This indicates the existence of site-specificity in the production metastable OCS^{3+} different from that in the production of metastable OCS^{2+}. In the future experiment, we will observe using an Auger electron - photoion coincidence method.

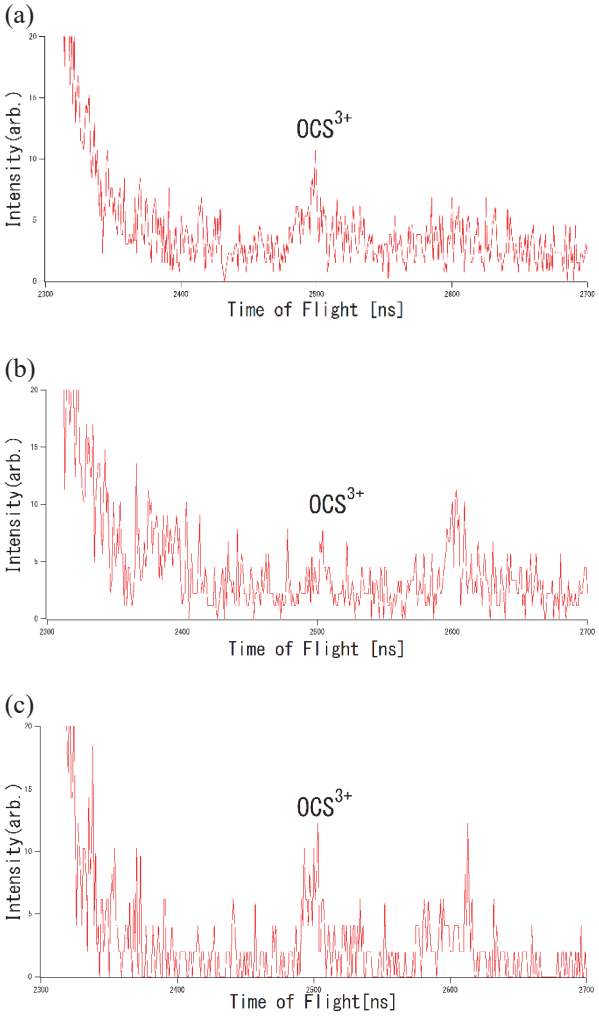

Fig. 1. TOF spectra of ions produced by Auger decay following C1s, O1s and S2p ionization in coincidence with photo-electron. (a) C1s ionization (b) O1s ionization (c) S2p ionization.

[1] T. Kaneyasu *et al*., J. Korean Phys. **54** (2009) 371.
[2] T. Kaneyasu *et al*., J. Phys. B: At. Mol.Opt. Phys. **48** (2015) 125101.

BL6U

F KVV and Xe $M_{45}N_{45}N_{45}$ Auger Spectra of Xenon Difluoride across the Xe 3d and F 1s Thresholds

F. Yamashita[1], M. Kono[2, 3, 4], H. Iwayama[5, 6], K. Okada[1] and E. Shigemasa[5, 6]

[1]*Department of Chemistry, Hiroshima University, Higashi-Hiroshima 739-8526, Japan*
[2]*Senri International School of Kwansei Gakuin, Minoh 562-0032, Japan*
[3]*School of Science and Technology, Kwansei Gakuin University, Sanda 669-1337, Japan*
[4]*RSPE, Australian National University, Canberra, ACT 2601, Australia*
[5]*UVSOR Facility, Institute for Molecular Science, Okazaki 444-8585, Japan*
[6]*School of Physical Sciences, The Graduate University for Advanced Studies (SOKENDAI), Okazaki 444-8585, Japan*

Xenon difluoride has been of great interest as a noble gas compound. The molecule intrigues X-ray spectroscopists because it has similar binding energies among Xe $3d_{5/2}$, Xe $3d_{3/2}$ and F 1s subshells [1]. Southworth *et al.* recently measured the partial ion yield curves of XeF_2 and found that the charge state distribution of Xe^{q+} shifts down compared to the Xe atom case [2]. This report focuses on the Auger spectroscopy in order to get more insight into the molecular electronic states leading to the production of Xe^{q+}. Resonant and normal Auger spectra are acquired as a function of photon energy in this study.

The experiments were performed on the soft X-ray beamline, BL6U. A main chamber was equipped with a gas cell and a high-resolution hemispherical electron analyzer (MBS A-1). Sublimated XeF_2 sample was introduced into the cell so as to keep the pressure in the main chamber at 7.5×10^{-4} Pa during the measurements. The electron spectra were acquired over the photon energy range of 668.9–709.9 eV. The energy resolutions of incident photons and detected electrons were set at 0.7 and 0.48 eV, respectively.

Figure 1 shows typical resonant and normal Auger spectra plotted on the electron kinetic energy scale. The peaks labeled A–E can be assigned to the Auger transitions of F KV_oV_o, F KV_iV_o, F KV_iV_i, Xe $M_4N_{45}N_{45}$ and Xe $M_5N_{45}N_{45}$, respectively, referring to the Auger spectra of Xe [3] and F_2 [4]. Here the symbols V_o and V_i represent outer- and inner-valence orbitals, respectively. The photon energy of 682.9 eV corresponds to the resonance transition from Xe $3d_{3/2}$ and/or F 1s to the σ^* orbital. Figure 1 reveals that the Auger band A is most intense at this resonance, indicating that the F 1s excitation is dominant and thereby suggesting that the Auger final states have two holes in the V_o orbital(s) plus an electron in the σ^* orbital. This is consistent with the study by Southworth *et al.*, reporting the specific increase in the Xe^+ and F^+ ion yields at the σ^* resonance [2]. At the photon energy of 686.7 eV, on the other hand, which is assigned to the shape resonance, Xe $3d_{5/2}^{-1}\epsilon f$, the Auger band E (Xe $M_5N_{45}N_{45}$) is predominantly observed. This transition is followed by the cascade Auger processes where ionization repeats until the holes are left in the valence orbitals. The occurrence of these processes is consistent with the fact that the branching ratios of multi-charged Xe^{2+}, Xe^{3+} and Xe^{4+} ions increase [2]. Our results illustrate that a strong correlation exists between the Auger transitions and fragmentation channels. We have a plan to carry out the Auger-electron–photoion coincidence (AEPICO) measurements to justify this directly and the results will be published in the near future.

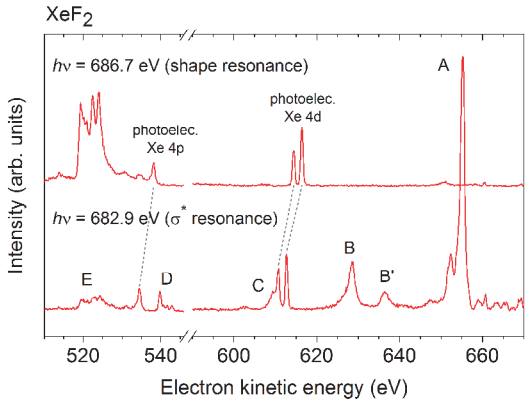

Fig. 1. Resonant and normal Auger spectra of xenon difluoride. A, F KV_oV_o; B and B′, F KV_iV_o; C, F KV_iV_i; D, Xe $M_4N_{45}N_{45}$; and E, Xe $M_5N_{45}N_{45}$. The dotted lines show the peak correspondence for the Xe 4p and 4d photoelectrons.

[1] T. X. Carroll, R. W. Shaw Jr., T. D. Thomas, C. Kindle and N. Bartlett, J. Am. Chem. Soc. **96** (1974) 1989.
[2] S. H. Southworth, R. Wehlitz, A. Picón, C. S. Lehmann, L. Cheng and J. F. Stanton, J. Chem. Phys. **142** (2015) 224302.
[3] L. O. Werme, T. Bergmark and K. Siegbahn, Phys. Scr. **6** (1972) 141.
[4] P. Weightman, T. D. Thomas and D. R. Jennison, J. Chem. Phys. **78** (1983) 1652.

BL6U

Formation of H_2^+ Fragments in Dissociation of Methanol Dication

M. Higuchi[1], K. Soejima[1], H. Iwayama[2], E. Shigemasa[2] and Y. Hikosaka[3]

[1]*Department of Environmental Science, Niigata University, Niigata 950-2181, Japan*
[2]*UVSOR Facility, Institute for Molecular Science, Okazaki 444-8585, Japan*
[3]*Graduate School of Medicine and Pharmaceutical Sciences, University of Toyama, Toyama 930-0194, Japan*

When a molecule absorbs a soft x-ray photon, inner-shell photoionization emitting a photoelectron are induced and then Auger decay emitting an Auger electron follows. Because two electrons are emitted through this process, the molecule with two positive charges, or molecular dication, is produced. The dication dissociates into ion pairs due to the Coulomb repulsion between the two positive charges. In this study, we have investigated the dissociation fragments from dication states formed after the inner-shell photoionization and the Auger decay process of methanol molecules.

The experiment was performed in the undulator beamline BL6U at the UVSOR facility. We used an electron-ion coincidence spectrometer composed of a toroidal electron analyzer and an ion momentum imaging analyzer.

In this report, we focus on the formation of molecular hydrogen ion from dication states in methanol molecule. Fig. 1 shows time-of-flight spectra of light fragment ions produced after the C1s inner-shell ionization of CH_3OH (black), CD_3OD (green), CH_3OD (red) and CD_3OH (blue). In the three panels, the spectra for the individual deuterated methanol molecules are compared with the one for CH_3OH. The formation of H_2^+ fragments is observed in the CH_3OH spectrum, where the fragments can be produced from two hydrogen atoms originally bonded to the C atom, or from one hydrogen atom at the C side and the hydrogen atom at the O side. The intensity of D_2^+ in the CD_3OD spectrum is about the half of H_2^+ in the CH_3OH spectrum, which manifests that deuteration reduces the formation of molecular hydrogen ion from the dication states.

When only the hydrogen atom at the O side is deuterated (i.e., for CH_3OD), the HD^+ formation, as well as the intense H_2^+ peak, is weakly observed. This observation implies that, while the molecular hydrogen ions are mainly from the hydrogen atoms at the C side, a fraction of the molecular hydrogen ions is produced from one hydrogen atom at the C side and the hydrogen atom at the O side. On the other hand, formation of HD^+ is hardly identified in the CD_3OH spectrum; the HD^+ formation using the hydrogen atoms at both sides is reduced by the deuteration at the C side. This finding suggests that the hydrogen migration forming HD^+ is mainly from the C side to the O side, and the migration is discouraged by the deuterium of hydrogen atoms at the C side.

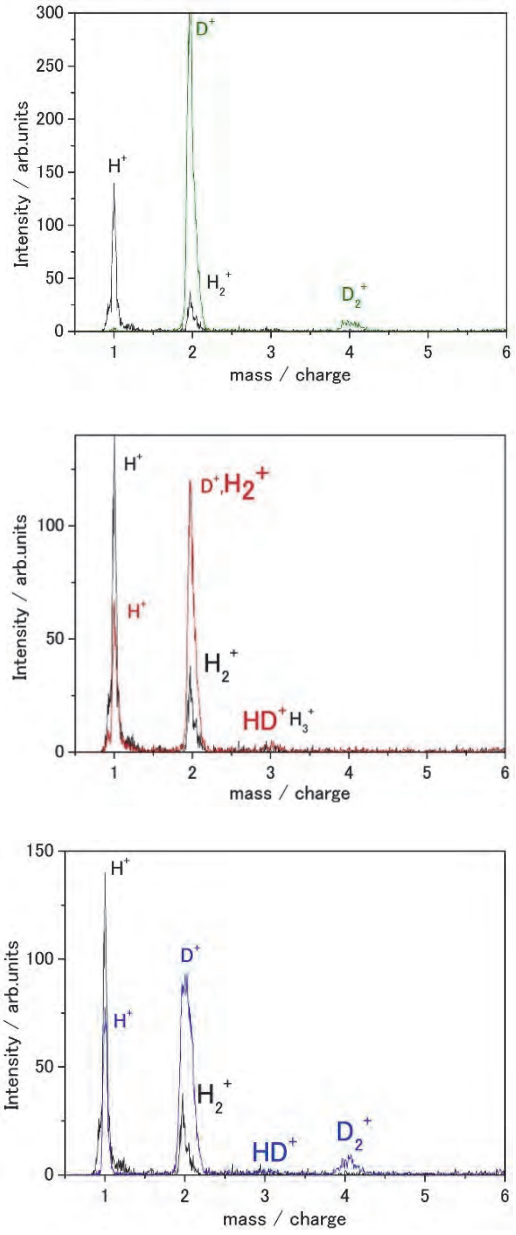

Fig. 1. Time-of-flight spectra for CD_3OD (green), CH_3OD (red) and CD_3OH (blue), compared with the time-of-flight spectrum for CH_3OH (black).

BL6U

Dissociation Dynamics of Dication States in Water Molecules

F. Kumaki[1], K. Soejima[1], H. Iwayama[2], E. Shigemasa[2] and Y. Hikosaka[3]

[1]*Department of Environmental science, Niigata University Niigata 950-2181, Japan*

[2]*UVSOR Facility, Institute for Molecular Science, Okazaki 444-8585, Japan*

[3]*Graduate School of Medicine and Pharmaceutical Sciences, University of Toyama, Toyama 930-0194, Japan*

A molecule absorbed a soft X-ray photon may lead to inner shell ionization and subsequently to Auger decay. Emission of two electrons through this sequential process results in the production of a doubly-ionized molecule. The doubly-ionized molecule called dication is unstable because of the Coulomb repulsion of two plus charge in the molecule, and often becomes fragmentation into ion pairs. In this work, we have studied the dissociation processes of dication states in water molecules by an electron-ion coincidence method.

The experiment was performed at the beamline 6U of the UVSOR facility. We used the electron-ion coincidence spectrometer consisting of a double toroidal electron analyzer and an ion time-of-flight (TOF) analyzer [1]. We measured Auger electron-ion coincidences for the gas-phase H_2O, D_2O and HDO to understand the deuteration effect in the dissociations of the dication states.

The black curves in Fig. 1 are the Auger spectra of H_2O and D_2O, which show band structures. The coincidence Auger spectra filtered for the two-body fragmentations into H^++OH^+ or D^++OD^+ are represented in red, and those filtered for the three-body fragmentations into H^++O^++H or D^++O^++D are in blue. The peaks of the two-body fragmentations and three-body fragmentations are commonly observed around 41eV and 45eV, respectively. In both H_2O and D_2O, the two-body dissociation is preferred to the three-body dissociation. The ratios of the coincidence counts for the two-body and the three-body dissociations are 1.9:1 for H_2O and 3.1:1 for D_2O; the contribution from the three-body dissociation is higher in H_2O than in D_2O [2].

Figure 2 shows the two-dimensional TOF map of ion pairs formed after the Auger decay in HDO, observed in coincidence with Auger electrons in the whole energy range. Two structures indicated by circles correspond to two-body dissociations of $HDO^{2+}\rightarrow H^+$-OD^+ and $HDO^{2+}\rightarrow D^+$-OH^+. The intensity ratio of the two dissociations is estimated, from the coincidence counts in the map, to be H^+-OD^+ : D^+-OH^+ = 2.3:1. The elongation of the D-O bond takes longer in time than that of the H-O bond because of the heavier hydrogen atom, which may results in the favorable dissociation of the H-O bond.

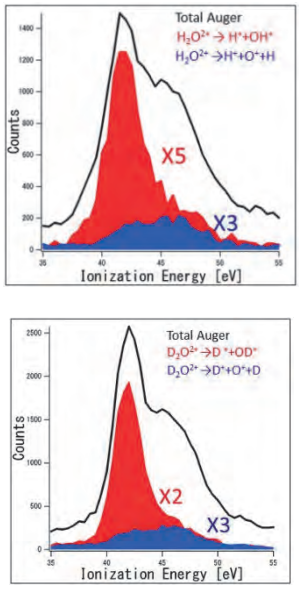

Fig. 1. Total Auger spectra (black) and coincidence Auger spectra filtered for the two-body dissociation (red) and for the three-body dissociation (blue) in (a) H_2O and (b) D_2O [2].

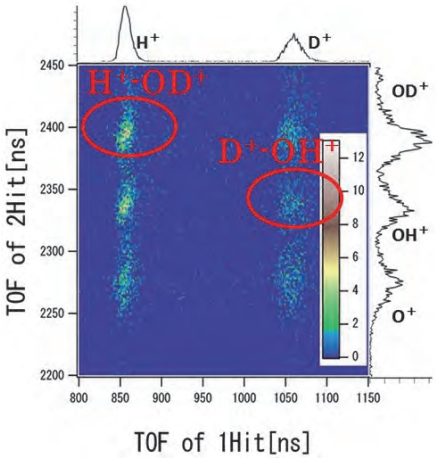

Fig. 2. Two-dimensional TOF map of ion pairs following HDO Auger decay observed in coincidence with Auger electrons in the whole energy range.

[1] T. Kaneyasu *et al*., J. Phys. B: At. Mol. Opt. Phys. **48** (2015) 125101.

[2] M. Kikuchi *et al*., UVSOR Act. Rep. **43** (2016) 106.

BL6U

Chemical Shift of Inner-Shell Binding Energies in Primary Bromoalkanes

H. Fujise[1, 2], H. Iwayama[1, 2] and E. Shigemasa[1, 2]

[1]*Institute for Molecular Science, Okazaki 444-8585, Japan,*

[2]*School of Physical Sciences, The Graduate University for Advanced Studies (SOKENDAI), Okazaki 444-8585, Japan*

Molecular inner-shell electrons do not play significant roles in forming chemical bonds, however, studies suggest that there are differences in the inner-shell binding energy for an atom of certain elements, depending on the chemical environments of the probed atom. This is called a "chemical shift". Remarkable chemical shifts of inner-shell binding energies of the carbon 1s electron in four different bonding environments of ethyl trifluoroacetate have been successfully demonstrated by Siegbahn [1]. To elucidate the molecular size effects of these chemical shifts on inner-shell ionization energies and binding energies of Auger final states, we have measured the Br 3d photoelectrons and MVV (V = valence level) Auger electrons produced after inner-shell photoionization in primary bromoalkanes.

The experiment was conducted on the soft X-ray beamline BL6U at UVSOR. The radiation from the undulator was monochromatized by a variable included angle varied line-spacing plane grating monochromator. The monochromatized light was introduced into a gas call with the sample gas mixture ($CH_3(CH_2)_nBr$ (n = 0 - 6): 90%, Kr: 10%). The photon energies for 3*d* photoelectron and Auger electron measurements were set to 200 eV, and 88 eV, respectively. The kinetic energies of the emitted electrons were measured by a hemispherical electron energy analyzer (MBS-A1), at a magic angle of 54.7° from the polarization vector. The resolution of the kinetic energy depends on the pass energy of the electrons in the hemisphere, and the width of the entrance slit of the analyzer, which were set to ~30 meV and ~6 meV, at pass energies 50 and 10 eV, respectively, at a slit width of 0.2 mm. The kinetic energy scales were calibrated with the 3*d* and 4*s* photoelectrons of Kr atoms in the sample gas mixture, for 3*d* photoelectron and Auger electron measurements, respectively.

The Br 3*d* photoelectron spectra of $CH_3(CH_2)_nBr$ (n = 0 - 6) are shown in Fig. 1. Two broad structures observed for all n, are assignable to the Br $3d_{3/2}$ and $3d_{5/2}$ components. In practice, it is known that the broad structures are attributed to the total of five ligand field splitting peaks [2], furthermore, there were no differences observed between the position of the ligand-field splitting components and molecular size. The broad structures shift to the lower binding energy side, as the molecular size increases. These chemical shifts imply that the charge distribution of bromoalkanes are different in size, and may be attributed to factors such as the different electronegativities of larger ligands. The Auger spectra for CH_3Br and $C_7H_{15}Br$ are shown in Fig. 2. The peak profile of the spectra become more complex as the number of carbon atoms increase in the alkane chain, and the kinetic energies shifts to the higher energy side. This is attributed to the more complex molecular orbitals and electronic structures involved in the MVV Auger process observed.

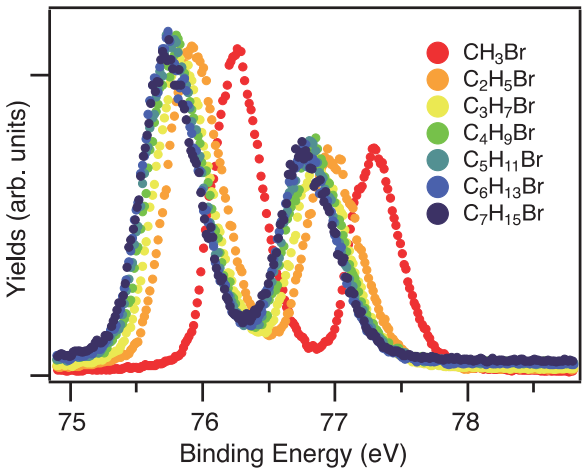

Fig. 1. Photoelectron spectra of $CH_3(CH_2)_nBr$ (n = 0 - 6) measured at photon energies 200 eV.

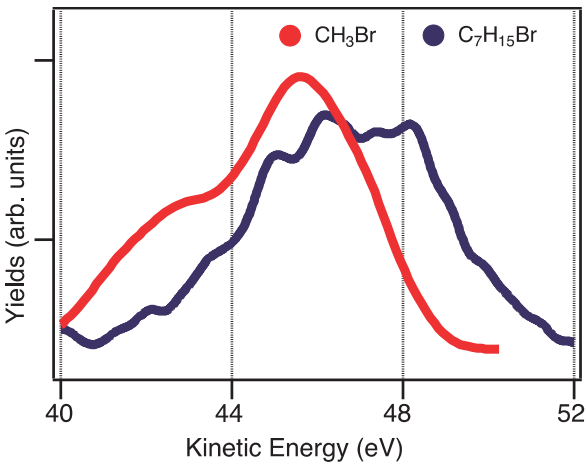

Fig. 2. Auger spectra of $CH_3(CH_2)_nBr$ (n = 0 ~ 6) measured at photon energies 88 eV.

[1] K. Siegbahn, Pure & Appl. Chem. **48** (1976) 77.
[2] J. Johnson *et al.*, J. Phys. B: At. Mol. Opt. Phys. **30** (1997) 4899.

BL6U

Intermolecular Vibrational Relaxations of Core Excited Nitrogen Clusters

H. Iwayama[1, 2] and E. Shigemasa[1,2]

[1]*UVSOR Facility, Institute for Molecular Science, Okazaki 444-8585, Japan*
[2]*School of Physical Sciences, The Graduate University for Advanced Studies (SOKENDAI), Okazaki 444-8585, Japan*

The photoreaction of isolated molecules in the gas phase is one of the most studied chemical reactions. However, since most chemical reaction in nature take place in condensed matter such as solids and liquids, it is important to understand intermolecular processes. Photodissociation of molecules in condensed matter would be quite different from that of isolated molecules, since energy and charge transfers into neighboring molecules may suppress molecular dissociation. Mass measurements of fragment ions in condensed matter are desirable, but it is difficult to extract them from solids or liquids. On the other hand, molecules in clusters have a similar environment to condensed matter, and their fragments can be easily measured as well as isolated molecules. In this work, we performed Auger-electron-ion coincidence measurements for isolated nitrogen and clustered nitrogen and investigated intermolecular processes of core excited nitrogen clusters.

The Auger-electron-ion coincidence measurements were performed on the undulator beamline BL6U at UVSOR. The Auger electrons and product ions were measured in coincidence by a double toroidal electron analyzer (DTA) and an ion momentum spectrometer, respectively. The pass energy of DTA was set to 400 eV. All signals from the ion and electron delay-line detectors were recorded with an 8ch TDC board. The photon energy was tuned to 401.1 eV, which corresponds to the resonance energy of the N 1s $\rightarrow\pi^*$ excitation for isolated and clustered nitrogen[1]. Nitrogen clusters were produced by supersonic expansion through a 100-μm nozzle at 110 K. The average cluster size was estimated to be ~300 molecules per cluster.

Figure 1 shows time-of-flight mass spectra for (a) molecular nitrogen and (b)clustered nitrogen. For molecular nitrogen, we observed parent molecular ions of N_2^+ and fragment ions of N^+. For clustered nitrogen, we observed $(N_2)_n^+$ ($n \geqq 1$) and $(N_2)_nN^+$ ($n \geqq 0$). In the present condition, the abundance of N^+ ions from core excited nitrogen clusters was negligibly small.

Figure 2 shows the coincidence Auger spectra for (a)isolated and (b)clustered nitrogen. Most N_2 molecules dissociate into N^+ fragment ions above 23.4 eV, which is corresponds to the lowest dissociation limit of N_2^+. This is because isolated molecules can release the excess energy only by radiative decays, whose time scales are nanoseconds, much slower than that of the dissociation process. On the other hand, for clustered nitrogen, we observed significant amount of N_2^+ ions well above the N_2^+ dissociation limit. This may suggest that intermolecular process, such as, vibrational relaxations suppress molecular dissociation. Analysis in more detail is in progress.

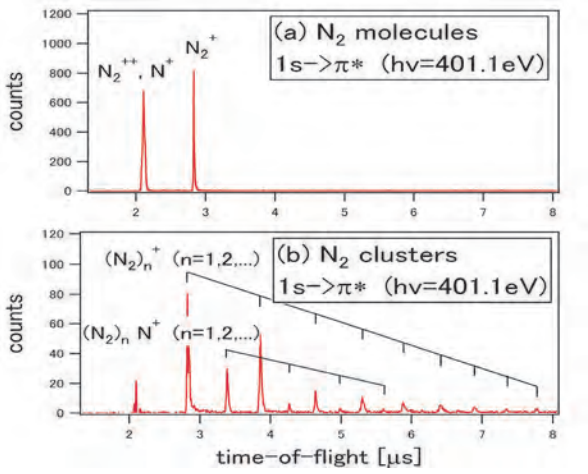

Fig. 1. Time-of-flight mass spectra for (a) N_2 molecules and (b) clusters. For nitrogen clusters, we subtracted contributions of molecular nitrogen in the cluster beam.

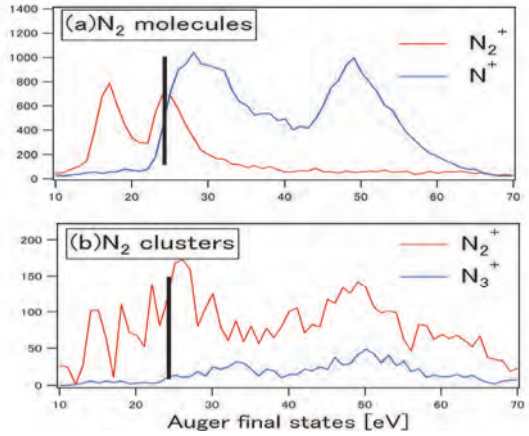

Fig. 2. Coincidence Auger spectra for (a)N_2 molecules and. (b)clusters. For nitrogen clusters, we subtracted contributions of molecular nitrogen in the cluster beam. Black bars represents the lowest dissociation limit of N_2^+.

[1] R. Flesch *et al.*, Phys. Rev. Lett. **86** (2001) 3767.

BL6B

Infrared Microscopy of Pyridine-Water Mixtures in T-Shape Microfluidics

M. Nagasaka[1], H. Fischer[2], H. Yuzawa[1], M. Nakano[1], N. Takada[1], M. Aoyama[1], E. Rühl[2] and N. Kosugi[1]

[1]*Institute for Molecular Science, Myodaiji, Okazaki 444-8585, Japan*
[2]*Physikalische Chemie, Freie Universität Berlin, Takustr. 3, D-14195 Berlin, Germany*

Microfluidics is a chemical technique to realize highly efficient chemical reactions in liquids and solutions [1]. Recently, X-ray diffraction in the hard X-ray region has been used for a variety of systems by using microfluidics [2]. On the other hand, we have developed a microfluidic system for soft X-ray absorption spectroscopy (XAS) [3]. In this study, we have used it for infrared (IR) microscopy.

The experiments were performed by using the IR microscopy setup IRT-7000 at UVSOR BL6B. A T-shape microfluidics setup with the width of 50 μm is made from PDMS resin which is covered by a 100 nm thick Si_3N_4 membrane. Pyridine and water are mixed in the T-shape microfluidic cell with a flow rate of 20 μL/min by using syringe pumps. The spatial resolution of 30 × 30 μm^2 is reached by using a ×16 Cassegrain mirror. IR spectra are taken by detecting the reflected infrared light with an MCT detector.

Figure 1(a) shows an optical microscopic image of the T-shape microfluidic cell. Water and pyridine are flowed in the left and right hand parts, respectively. We have found a laminar flow, in which pyridine and water are separately flowed at the center of the mixing region behind the junction of the liquids. Figure 1(b) shows IR spectra of pyridine and water taken from the microfluidic system. The IR spectra show the OH stretching vibration of water at 3507 cm^{-1} and the CH stretching vibration of the pyridine ring around 3100 cm^{-1}, respectively. We have measured IR spectra with a spatial resolution of 30 × 30 μm^2 in the same region of the optical image shown in Fig. 1(a). The absorbance of pyridine and water at different positions is obtained by fitting the IR spectra to the mentioned vibrational peaks of pyridine and water.

Figure 1(c) shows the 2D image of the absorbance of pyridine. The right hand part and the mixed region of the T-shape microfluidic cell show high intensity of pyridine. The left hand part of the laminar flow in the mixed region, which is mainly filled with water, also shows high intensity of pyridine. Because the spatial resolution of the IR microscope (30 × 30 μm^2) is larger than the width of the pyridine part in the laminar flow (25 μm), the water part in the laminar flow also shows some intensity of pyridine. Figure 1(d) shows a 2D image of the absorbance of water. Unlike the pyridine case, water shows high intensity outside the microfluidic channel. This means that the adhesion of the Si_3N_4 membrane to PDMS was insufficient in the water part, which is unlike the pyridine part. Recently, we have measured XAS of pyridine-water mixtures in our T-shape microfluidic system, and confirmed the adhesion of SiC is sufficient even in the water part [3]. Note that the microfluidic cell is kept in a helium atmosphere, where the pressure is several percent higher than the ambient pressure. The adhesion of SiC to PDMS is then strong enough because the SiC membrane is pressed by the helium gas. In the future, we will include this helium pressing system to the microfluidic cell in order to take more reliable IR microscopy images of T-shape microfluidics.

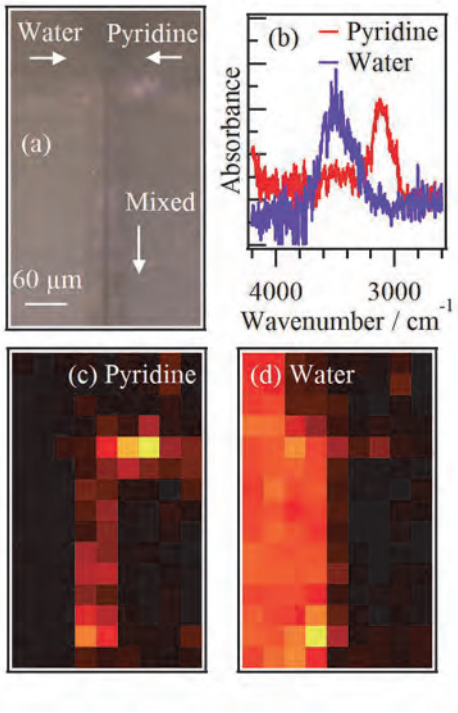

Fig. 1. (a) An optical microscopy image of the T-shape microfluidic cell. A laminar flow is formed after mixing the flows of pyridine and water. (b) IR spectroscopy of pyridine and water taken from the positions of pyridine and water in T-shape microfluidic cell. The 2D images of the absorbance of (c) pyridine and (d) water in the T-shape microfluidic cell are also shown.

[1] T. Kitamori *et al.*, Anal. Chem. **76** (2004) 53.
[2] B. Weinhausen and S. Köster, Lab Chip **13** (2013) 212.
[3] M. Nagasaka *et al.*, in this volume.

UVSOR User 6

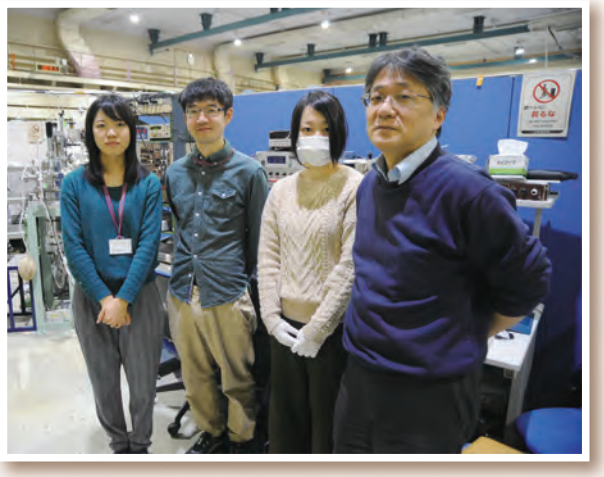

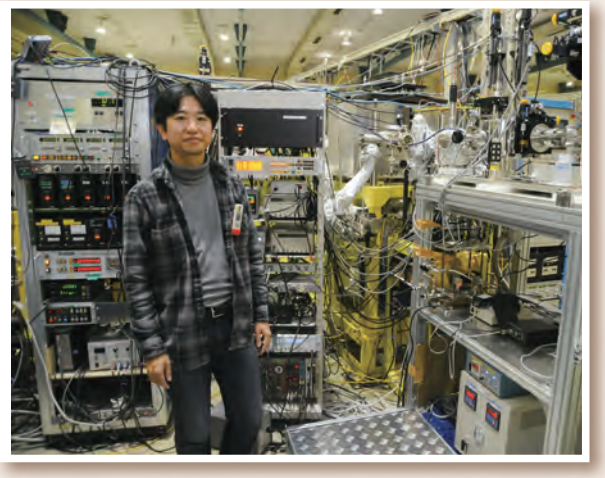

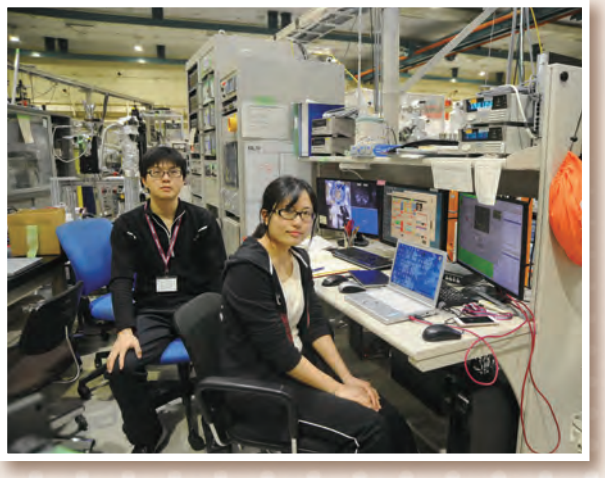

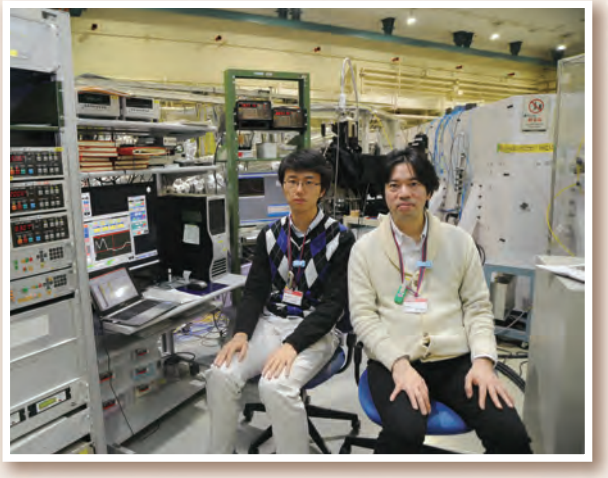

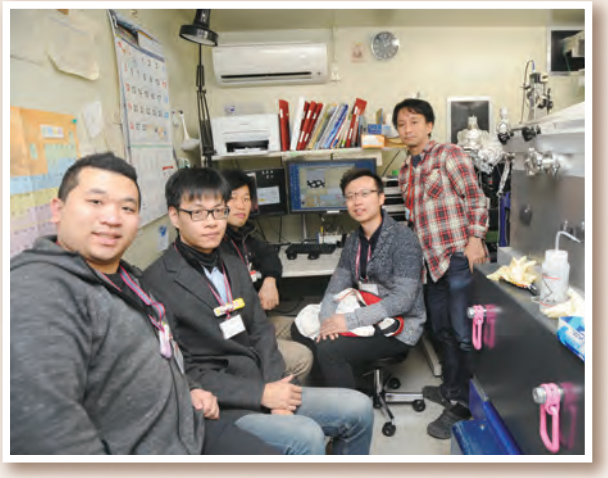

UVSOR User 7

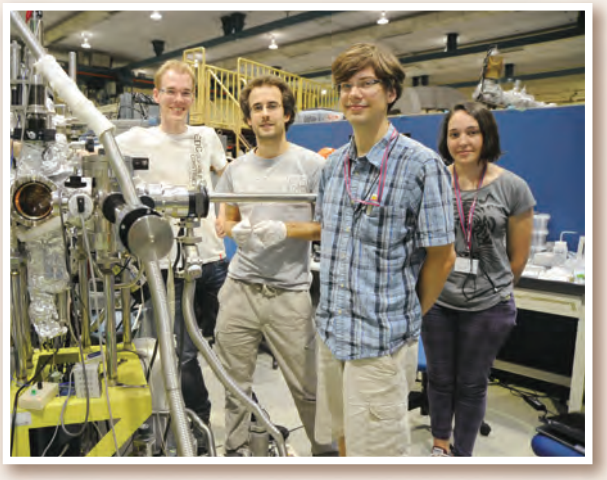

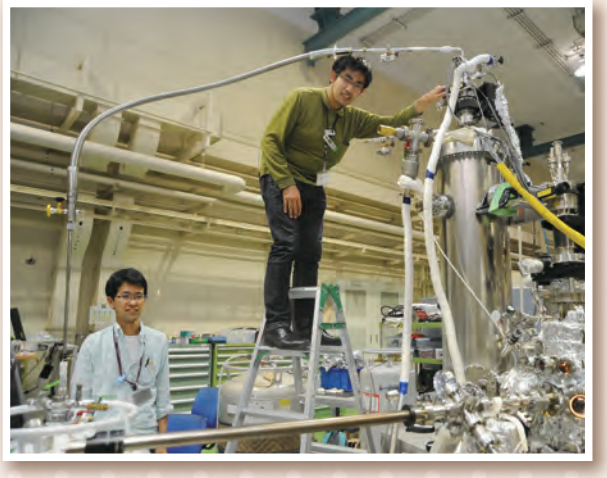

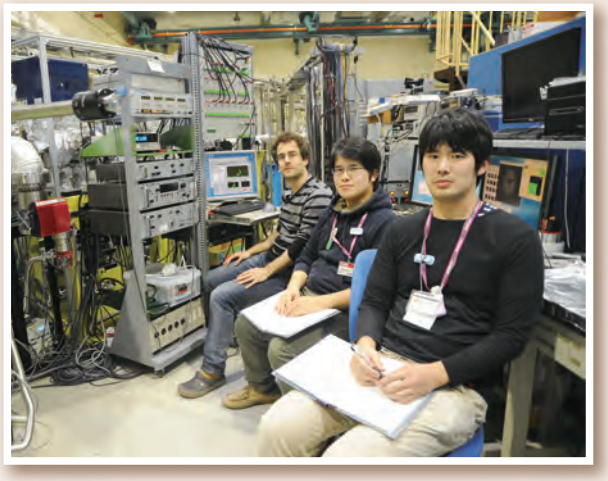

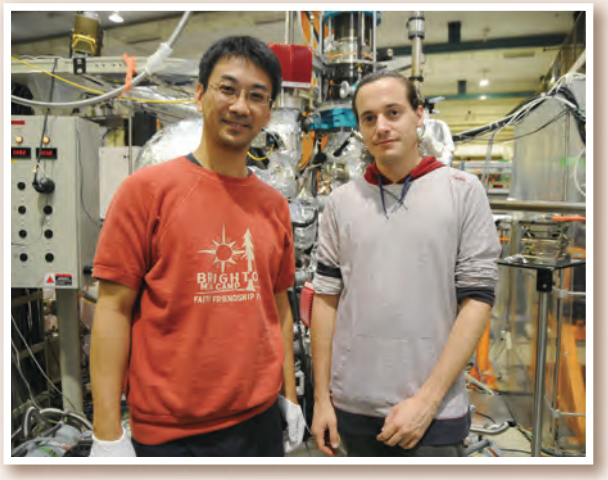

Ⅲ-4

Surface, Interface and Thin Films

Highlight

BL3U

In-situ O K-edge XAFS Measurements of MnO_x Oxygen Evolution Catalysts Containing Alkali Metal Cations

M. Yoshida[1, 2], F. Yamamoto[1], M. Nagasaka[3], H. Yuzawa[3], N. Kosugi[3] and H. Kondoh[1]

[1]*Department of Chemistry, Keio University, Yokohama 223-8522, Japan*

[2]*Cooperative Research Fellow, Institute for Catalysis, Hokkaido University, Sapporo 001-0021, Japan*

[3]*Institute for Molecular Science, Okazaki 444-8585, Japan*

Electrochemical hydrogen production from water using renewable energy attracts attention to construct a sustainable society. For this purpose, electrocatalysts for hydrogen and oxygen evolution reactions (HER and OER, respectively) are used to decompose water ($2H_2O \rightarrow 2H_2+O_2$). However, the efficiency of OER is insufficient compared with that of HER. Thus, the development of efficient OER catalysts has been required to improve the activity for overall water splitting. In this situation, the layered manganese oxide containing K^+ cation (K:MnO_x) was reported to function as an efficient catalyst for OER over a wide pH range [1]. Meanwhile, we found that the OER activity of the layered Mn oxide is enhanced when Cs^+ cation is contained in the catalysts (Cs:MnO_x). Therefore, in this study, we investigated the reaction mechanism of M:MnO_x (M = Na, K, Cs) catalysts by in-situ O K-edge X-ray absorption fine structure (XAFS) measurements under potential control conditions and discussed the effect of cations in the catalysts.

Electrochemical O K-edge XAFS measurements with transmission mode using soft X-rays were performed at BL3U in the UVSOR Synchrotron, according to the previous works [2]. A home-made electrochemical cell was used with Au/Cr/SiC thin film substrates as working electrodes, a Pt counter electrode, and a Ag/AgCl reference electrode. The Na:MnO_x, K:MnO_x, and Cs:MnO_x catalysts were electrodeposited on the Au/Cr/SiC working electrode at 0.6 V in methylphosphonate electrolyte containing $MnCl_2$ and XOH (X = Na, K, and Cs, respectively).

Prior to the O K-edge XAFS, in-situ Mn K-edge XAFS measurements were tested for the Na:MnO_x, K:MnO_x, and Cs:MnO_x. The results exhibited that the manganese species in the catalysts were present as Mn^{3+} with δ-MnO_2 structure at lower electrode potential and as Mn^{4+} with δ-MnO_2 structure at higher electrode potential. In addition, the estimation of manganese valence suggested that the fraction of Mn^{3+} species in the Cs:MnO_x under OER condition was higher than those in the Na:MnO_x and K:MnO_x.

Next, the in-situ O K-edge XAFS spectra for Na:MnO_x, K:MnO_x, and Cs:MnO_x were taken under electrode potential control in a phosphate buffered electrolyte, as shown in Figure 1. An absorption peak was observed around 529 eV at 0.0 and 1.0 V for all catalysts. From the comparison with reference samples, it was found that the absorption peak was attributed to the δ-MnO_2, consistent with the results of Mn K-edge XAFS. However, even if the electrode potential was changed from 0.0 to 1.0 V, the O K-edge XAFS spectra did not change so much, meaning that the electronic states of oxygen species in the δ-MnO_2 structure were almost the same between lower and higher electrode potentials. On the other hand, a peak of higher energy around 531.8 eV was slightly disordered for Cs:MnO_x compared with Na:MnO_x and K:MnO_x, indicating that the larger amount of hydroxide or hydroxyl group may be generated for Cs:MnO_x, in response to the presence of Mn^{3+} species.

In conclusion, we measured in-situ O K-edge XAFS for M:MnO_x catalysts and revealed that the chemical state of M:MnO_x was δ-MnO_2 under OER condition. The presence of Mn^{3+} species in the Cs:MnO_x is likely to be the key of OER activity.

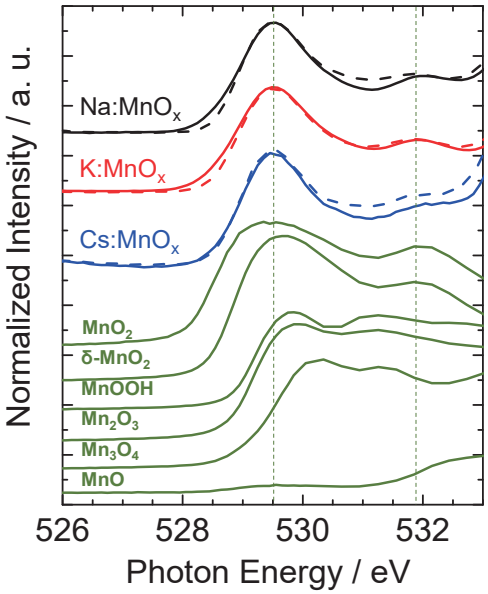

Fig. 1. In-situ O K-edge XAFS spectra of Na:MnO_x, K:MnO_x, Cs:MnO_x electrocatalysts at 1.0 V (solid line) and 0.0 V (dotted line) in phosphate buffered electrolyte.

[1] (a) D. G. Nocera *et al.*, J. Am. Chem. Soc. **136** (2014) 6002. (b) J. Am. Chem. Soc. **137** (2015) 14887.
[2] (a) M. Nagasaka *et al.*, J. Phys. Chem. C **117** (2013) 16343. (b) M. Yoshida *et al.*, J. Phys. Chem. C **119** (2015) 19279.

BL2A

Studies on Interface of Thin Film by Near-edge X-ray Absorption Fine Structure

E. Kobayashi[1], K. K. Bando[2], O. Takahashi[3], K. K. Okudaira[4] and T. Okajima[1]

[1]*Kyushu Synchrotron Light Research Center, Tosu 841-0005, Japan*

[2]*National Institute of Advanced Industrial Science and Technology, Tsukuba 305-8565, Japan*

[3]*Institute for Sustainable Science and Development, Hiroshima University, Higashi-Hiroshima 739-8526, Japan*

[4] *Chiba University, Chiba 263-8522, Japan*

Resistive random access memory (ReRAM) is expected as a new next generation memories. The memory operates by applying a voltage to a structure in which an oxide film is sandwiched between electrodes. However, the mechanism of action and degradation mechanism have not been clarified yet. It is important to investigate the metal/oxide interface to elucidate them. Near-edge X-ray absorption fine structure (NEXAFS) is effective as one of methods to investigate the change in chemical state and depth profiling of the film. In this paper, we investigated the interface of Al/SiO_2/Si(111) by NEXAFS.

The silicon oxide thin films (~3ML) prepared on Si(111) using molecular beam epitaxy (MBE). Si *K*-edge NEXAFS spectra of thin film were measured at the beamline 2A of the UVSOR. The experimental setup for NEXAFS measurement is shown in Fig. 1. The soft x-ray was passed through a metal mesh and was irradiated to the sample. In the total electron yield (TEY), the drain current of the sample was measured. The fluorescence from sample was detected by silicon drift detectors. Potential of the sample was applied between the metal mesh and metal plate. All experiments were performed at room temperature.

Figure 2 shows the Si *K*-edge NEXAFS spectra of Al/SiO_2/Si(111) obtained from partial fluorescence yield (PFY) and TEY mode.

The spectra of TEY mode show a strong peak at around 1847 eV. The spectral features are similar to that of bulk SiO_2. Although the overall structure of the spectrum has hardly changed before and after discharging, the peak intensity of spectrum after discharging became weak. This indicates that interaction occurs at the interface between Al and SiO_2 by voltage application.

The peak of the spectrum in the PFY mode was observed on the lower energy side than in the TEY mode. The spectrum peak of bulk Si is observed at about 1840 eV. Therefore the origin of the observed peak is near the SiO_2/Si interface. The intensity changed when a potential was applied. This indicates that the silicon oxide changed due to voltage application.

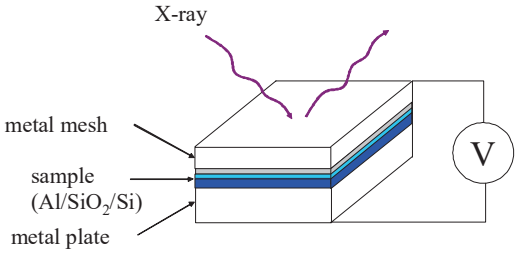

Fig. 1. experimental setup.

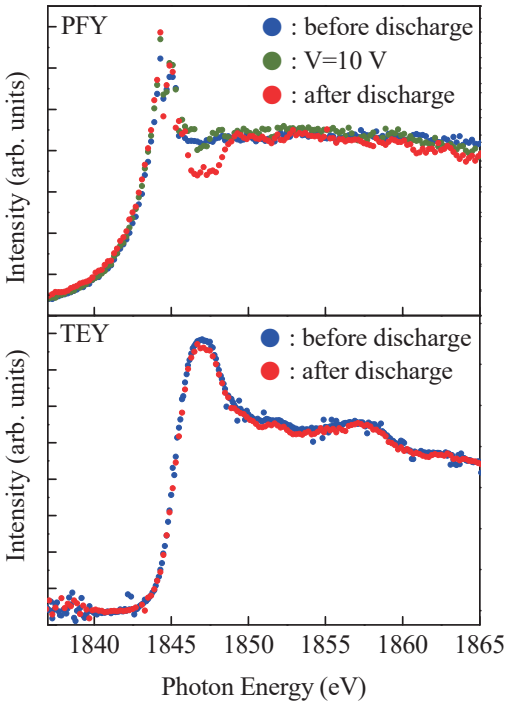

Fig. 2. Si *K*-edge NEXAFS spectra of Al/SiO_2/Si(111) obtained from PFY and TEY mode.

BL2A

Studies on Chemical State of Oxide Film under Applied Voltage by Near-edge X-ray Absorption Fine Structure

K. K. Okudaira[1], O. Takahashi[2], K. K. Bando[3] and E. Kobayashi[4]

[1] *Chiba University, Chiba 263-8522, Japan*

[2]*Institute for Sustainable Science and Development, Hiroshima University, Higashi-Hiroshima 739-8526, Japan*

[3]*National Institute of Advanced Industrial Science and Technology, Tsukuba 305-8565, Japan*

[4]*Kyushu Synchrotron Light Research Center, Tosu 841-0005, Japan*

High-k aluminum oxide (Al_2O_3) is considered a potential alternative gate dielectric material on Si substrates for application to not only conventional inorganic transistor but also organic filed-effect transistors (OTFT). In particular, OTFT have been the focus of considerable research activity during the past 10 years [1]. The performance of OTFT depends critically on the use of high-performance dielectrics that form active interfaces with low defect densities. In principle, for a given thickness of dielectric, a high-*k* dielectric is preferable to a low-k dielectric for an FET application that requires the FET to exhibit a high drive current at low drive voltage. Various solution-processible high-*k* dielectrics for low-voltage OFET have been used such as anodized aluminum oxide (dielectric constant = 8–10) [2]. The charge injection efficiency depends on energy level alignment of the interface between the dielectrics surface and the organic semiconductor layer. The surface Al_2O_3 is strongly influenced by the degree of surface hydroxylation [3].

In this paper, we investigated the chemical state of an Al_2O_3 under applied voltage by NEXAFS.

An alumina film was made on a polished stainless steel plate by dip-coating with a diluted alumina sol (Kawaken Fine Chemicals, F1000). The coated plate was dried at 333 K, 6 hours and calcined at 473 K, 3 hours in an oven.

Al *K*-edge NEXAFS spectra of aluminum oxide thin film were measured at the beamline 2A of the UVSOR. The soft x-ray was passed through a metal mesh and was irradiated to the sample. The fluorescence from sample was detected by silicon drift detectors. Potential of the sample was applied between the metal mesh and metal plate. All experiments were performed at room temperature.

Figure 1 shows the Al *K*-edge NEXAFS spectra of aluminum oxide obtained from PFY mode at various applied voltage. The spectra were measured while applying a voltage. This sample caused breakdown at ~ 0.8 V. After breakdown, the potential to the sample could not be applied. The spectra show a strong peak at around ~1568 eV, attributed to Al bonded to OH group in the Al_2O_3 film. Although the overall structure of the spectrum has hardly changed, the intensity of the main peak decreases as applied voltage becomes higher. Furthermore, after discharge the intensity of the main peak does not turn back to that at V = 0 V This indicates that the application of voltage affect the structure of the Al-OH moiety in the film.

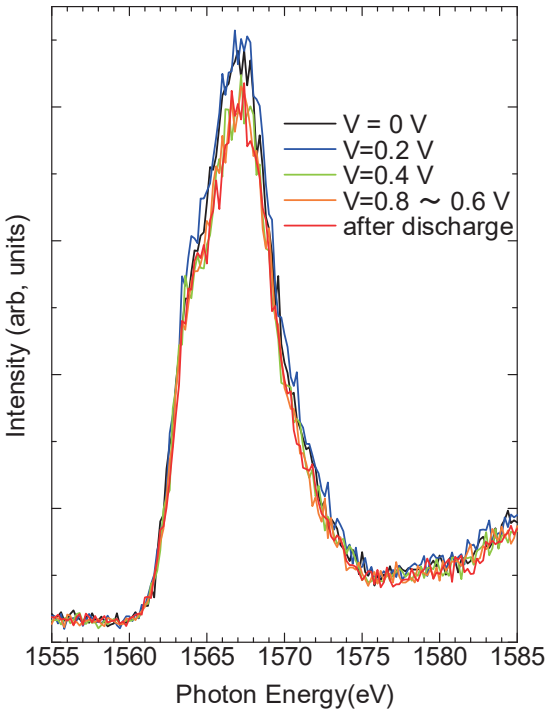

Fig. 1. Al *K*-edge NEXAFS spectra of aluminum oxide thin film obtained from PFY mode at various applied voltage.

[1] H. Sirringhaus, Adv. Mater. **17** (2005) 2411.
[2] L. A. Majewski, M. Grell, S. D. Ogier and J. Veres, Org. Electron. **4** (2003) 27.
[3] P. J. Eng, T. P. Trainor, G. E. Brown Jr., G. A. Waychunas, M. Newville, S. R. Sutton and M. L. Rivers, Science **288** (2000) 1029.

BL2B

Modification of the Overlapping of the Frontier Orbitals

Y. Yamada[1], Y. Hasegawa[1], T. Maeda[1], T. Hosokai[2] and K. R. Koswattage[3]
[1]*Institute of Applied Physics, University of Tsukuba, Tsukuba 305-8573, Japan*
[2]*National Institute of Advanced Industrial Science and Technology, Tsukuba 305-8568, Japan*
[3]*Institute for Molecular Science, Department of Photo-Molecular Science, Okazaki 444-8585, Japan*

Organic semiconductors with enhanced intermolecular interaction have attracted attentions since they may exhibit an enhanced intermolecular overlapping of the frontier orbitals and thus the band-like transport. By tailoring unique ordering of these molecules on the well defined substrate, we are able to modify the intermolecular overlapping of the frontier orbitals, resulting in significant alteration of the electronic states from that of the bulk. In this study, we focused on simple examples of these molecules such as DNTT and sumanene.

In order to realize the control of molecular packing and electronic structure of these molecules in a realistic environment, all the experiments were done at room temperature. ARPES measurements are done in BL2B of UVSOR with the incident light of 28 eV.

[1. DNTT on Ag(110)]

We have shown that, there exist two types of ordering of the monolayer of DNTT, i.e, the dense phase and the loose phase, and that the dense packing induces a considerable splitting of HOMO due to overlapping [1]. Recently, we found that the one-dimensional structure of the "loose" DNTT monolayer can be formed on the anisotropic Ag(110) substrate (Fig. 1 (a)). The monolayer consists of apparent molecular rows; the long axis of molecules in the row is parallel to the direction of the rows.

In the ARPES spectra obtained along the direction of the molecular rows, i.e, parallel to the molecular axis (Fig. 1 (b)), the intra-molecule dispersion-like feature was observed, similarly to the case of well-ordered pentacene [2] or 6P [3]. The intramolecule dispersion apparently exhibits a backfolding due to the periodicity of half-length of the molecule, possibly reflecting the characteristic molecular shape. On the other hand, in the perpendicular to the row, i.e, perpendicular to the molecular axis, each orbitals show almost negligible band dispersion, suggesting that the intermolecule overlapping is small because of the loose packing in this structure, in contrast to our previous observation in the dense monolayer of DNTT [1]. Therefore, we note that the band dispersion in this type of system does not necessarily reflect the band dispersion of the bulk system.

[2. Sumanene/Cu(111)]

Sumanene on Au(111) and Ag(111) are found to take a flat-lying geometry with the bowl-up and bowl-down molecules [4]. On the other hand, Sumanene monolayer on Cu(111) exhibit one-dimensional stacking of slightly-tilted sumanene molecules (Fig. 2 (a)). The monolayer consists of the five different rows of sumanene.

The ARPES spectrum along the molecular rows is shown in Fig. 2 (b). The molecular orbitals are broad because of the presence of five bands. Although enhanced π-stacking in the molecular row is expected, we found almost no apparent dispersion in the upper frontier orbitals such as HOMO and HOMO-1. On the other hand, weak dispersing feature is seen in the lower-lying orbitals which is not seen in the ARPES spectrum taken perpendicular to the row. The detailed calculation is ongoing in order to determine the orbitals responsible to the observed dispersion.

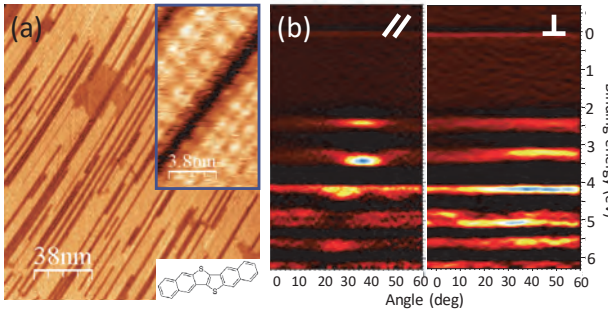

Fig. 1. (a) STM image of several layer of DNTT/Ag (110). (b) ARUPS along and perpendicular to the molecular axis.

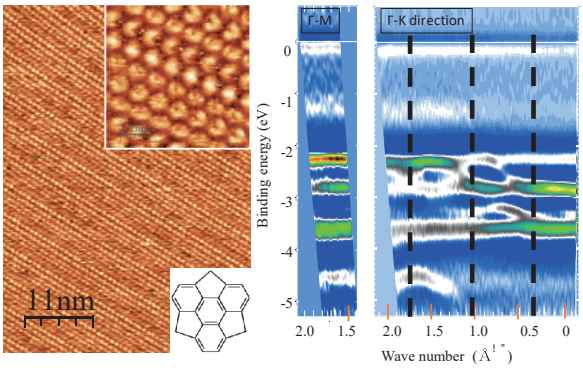

Fig. 2. (a) STM image of monolayer of sumanene/cu (111). (b) ARUPS along and perpendicular to the molecular row.

[1] Y. Hasegawa *et al.*, J. Phys. Chem. C, **120** (2016) 21536.
[2] S.Berkebile, *et al.*, Phys. Rev. B **77** (2008) 115312.
[3] G. Koller, *et al.*, Science **317** (2007) 351.
[4] Y. Yamada, (in preperation).

BL2B

ARUPS of Pentacene on a-TES Film Prepared on SiO_2

Y. Urabe[1], Y.Aoki[2] and K. K. Okudaira[1]
[1]*Association of Graduate Schools of Science and Technology, Chiba University,Chiba 263-8522, Japan*
[2]*Faculty of Engineeringy, Chiba University, Chiba 263-8522, Japan*

An organic thin-film transistor (OTFT) has been actively studied in recent years. To achieve high mobility it is important to improve the charge injection efficiency at the interface between the substrate and the organic semiconductor layer and charge transfer probability. Self-assembled monolayers (SAMs) has been introduced on metal electrode and insulator layer in order to arrange the molecular orientation of organic semiconductor film and energy level alignment of the interface [1].

For the case of a bottom-contact type OTFT, it is necessary to introduce two kinds of SAM chemically bonded to not only metal electrode but also insulator layer. A triazine-based molecular adhesion agent (a-TES : 6-triethoxysilyl propylamino-1,3,5- triazine-2,4-dithiol(TES)) was used for preparing thin film like self-assembly monolayers on Cu surface as well as SiO_2 insulator layer

In this work we used a-TES modified SiO_2 substrate and examined the molecular orientation of pentacene thin films thermally deposited on the surface by angle-resolved ultraviolet photoelectron spectroscopy (ARUPS) measurements. To obtain the quantitative analysis on the molecular orientation; we compare observed take-off angle dependence of π band and calculated ones by the independent-atomic-center (IAC)/MO approximation [2].

ARUPS measurements were performed at the beam line BL2B of the UVSOR. The take-off angle (θ) dependencies of photoelectron spectra were measured with the photon energy (hν) of 28 eV. We use a-TES modified SiO_2 and SiO_2 as substrate. SiO_2 substrate was subjected to ultrasonic cleaning for 10 minutes in acetone, isopropanol, and then ozone cleaning for 30 minutes. a-TES modified SiO_2 substrate was obtained by dipped in 0.1% solution at 20°C for 30 minutes. Pentacene was deposited on 1.4 nm on both substrates.

We observed take-off angle (θ) dependence of HOMO peak in UPS of pentacene deposited on a-TES/SiO_2 and SiO_2 (thickness of 1.4 nm).

The HOMO peaks of pentacene on a-TES/SiO_2 and on SiO_2 appear at binding energy of about 1 eV and 2eV, respectively. The HOMO peaks of pentacene both on a-TES/SiO_2 and on SiO_2 show intense peaks at higher take-off angle (θ = 60°), and at lower θ these intensities become small. For a-TES/SiO_2, HOMO intensity at θ = 20° is smaller than that at θ = 0°. On the other hand, for SiO_2 substrate, HOMO intensity at θ = 20° is almost same as that at θ = 0°. Due to the difference of θ dependence of HOMO peak on a-TES/SiO_2 and on SiO_2, it is found that the molecular orientation of pentacene on a-TES/SiO_2 is different from that on SiO_2. The difference of surface energy of a-TES and SiO_2 indicates that the surface modification by a-TES affects the molecular orientation of organic semiconductor layer, which would have an effect on the characteristics of OTFT such as mobility.

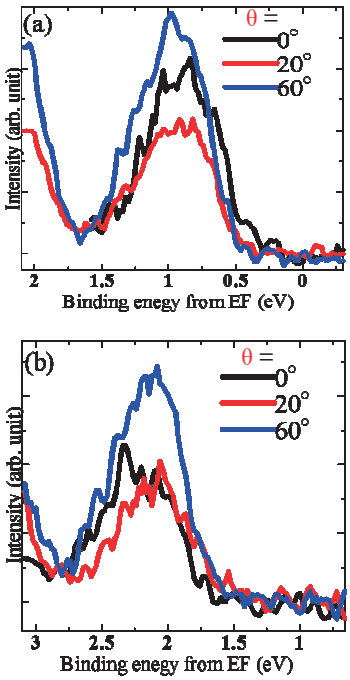

Fig. 1. ARUPS of pentacene(1.4nm)/SiO_2 (a) and pentacen(1.4nm)/a-TES/SiO_2 (b).

[1] F. Wang *et al*., Nanoscale Res. Lett. **6** (2011) 483.
J. –P. Hong *et al*., Appl. Phys. Lett. **92** (2008) 143311.
[2] N. Ueno *et al*., J. Chem. Phys. **99** (1993) 7169.

BL2B

Electronic States of Self-assembled Peptide Films on the Graphite Surface

Y. Nakayama[1], T. Narimatsu[2] and Y. Hayamizu[2, 3]

[1]*Faculty of Science and Technology, Tokyo University of Science, Noda 278-8510, Japan*
[2]*Department of Materials Science and Engineering, Tokyo Institute of Technology, Tokyo 152-8550, Japan*
[3]*PRESTO, Japan Science and Technology Agency (JST), Kawaguchi 332-0012, Japan*

One promising route for bioelectronics and biosensing is functionalization of electrodes by proteins such as enzymes and antibodies. Therefore, attachment of the protein molecules onto the electrode surfaces is a crucial problem. Thiol groups of the cysteine residues can be utilized as "anchors" for binding the protein molecule covalently onto the noble metal electrodes, whose interface properties our group has already reported so far [1]. Besides these conventional electrode materials, graphene is attracting growing interests due to its biocompatibility. On the graphene or graphite, benzene rings of some amino residues (such as tyrosine) preferentially adsorb on the surface through the π-π interaction.

Recently, peptides, fragments of proteins, of certain sequences are discovered to build regular networked structures spontaneously on the graphite surface [2]. Some of these peptide molecules dope the graphene electric devices to switch the transport properties [3], yet the electronic origins of such functionalities are still unsolved. In the present study, we examined the interface electronic structures between a functional peptide GrBP5-WT [2] and the graphite surface.

Self-assembled peptide film samples were prepared by procedures described elsewhere [2, 3]. Ultraviolet photoelectron spectroscopy (UPS) measurements were conducted at BL2B of UVSOR.

Figure 1 (a) shows UPS spectra of submonolayer and multilayer films of the peptide. The profile of the latter is fairly consistent to simulated density-of-states (DOS) curve based on quantum-chemical calculation results for the whole GrBP5-WT molecule, while that of the former rather resembles the DOS of the left-half fragment of this peptide molecule. Taking into consideration that the anchoring groups on graphite are tyrosine (Y) residues in the right-half of this peptide, this changing tendency of the UPS profiles implies disordering in the molecular orientation from the first adsorbed layer to the multilayers. The UPS spectra of the highest-occupied molecular orbital (HOMO) and secondary-electron cutoff (SECO) regions are shown in Figs. 1 (b) and (c), respectively. From the low-energy onset position of the HOMO and work function value derived from the SECO spectra, the ionization energy of this peptide is determined to be 7.6 eV. A rise in the work function by formation of the GrBP5-WT film indicates electron transfer from graphite to the overlayer, which rationalizes the reported functionality of this peptide as an acceptor for the graphene devices [3].

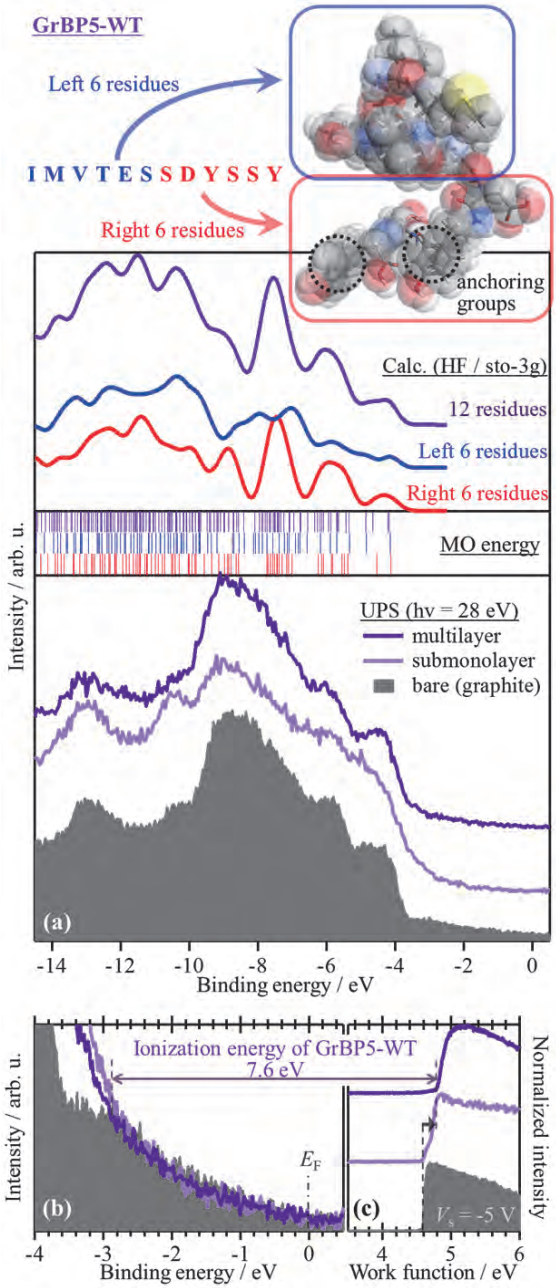

Fig. 1. (a-c) UPS spectra of self-assembled peptide GrBP5-WT (upper inset) films on graphite substrates. Simulated DOS distributions and molecular orbital (MO) energies are also displayed in (a).

[1] K. R. Koswattage *et al*., e-J. Surf. Sci. Nanotechnol. **13** (2015) 373; *idem*, UVSOR Activity Reports **40** (2013) 90.
[2] C. R. So *et al*., ACS Nano **6** (2012) 1648.
[3] Y. Hayamizu *et al*., Sci. Rep. **6** (2016) 33778.

BL2B

Electronic Structures of Organic-Metal Interface Measuring by UPS: bis(l,2,5-thiadiazolo)-p-quinobis(l,3-dithiole) and Tris-(8-hydroxyquinoline)aluminum Alq3

N. Ohashi[1], S. Kobayashi[1], M. Hikasa[2], Y. Nakayama[2] and Y. Watanabe[1]

[1]*Department of Electrical and Electronic Engineering, Faculty of Engineering, Tokyo University of Science, Chino 391-0292, Japan*

[2]*Department of Pure and Applied Chemistry, Faculty of Science and Technology, Tokyo University of Science, Noda 278-8510, Japan*

In this report, we were investigated two types of metal-organic interface. First one is bis (l, 2, 5-thiadiazolo)-p-quinobis (l, 3-dithiole) (BTQBT)-aluminum interface. BTQBT was known as high performance organic semiconductor which shows maximum mobility of 4 cm^2/Vs. [1] A vertical type transistors with BTQBT shows current density of 1 A/cm^2 and on/off current ratio of over 10^5. [2] These reports prove a superiority of BTQBT, however, device operation mechanism of the vertical-type transistor is still unclear. So we investigate BTQBT and aluminum interface by ultraviolet photoelectron spectroscopy (UPS) at the first of the research.

The UPS measurement was performed at BL2B of UVSOR. Photon energy was 38 eV. We have prepared Si substrate covered with gold film. Aluminum and BTQBT were fabricated on the substrates by vacuum deposition. All experiments were carried out in vacuo.

Figure 1 shows UPS spectra of BTQBT on aluminum electrode. BTQBT thickness dependence with UPS spectra was examined for the purpose of estimating the energy level diagram of BTQBT-aluminum interface. The UPS results of SECO position indicates that the vacuum level varies with thickness of BTQBT. The vacuum level shift of the bulk region correspond to the HOMO edge of BTQBT shown in Fig. 1 (b). It is attributed band bending of BTQBT. We summarized vacuum level shift of BTQBT film in Fig. 2. The Vacuum level is abruptly changed at the very interface of BTQBT and aluminum. The vacuum level is stable near the interface, then varies with thickness at the bulk region. The charge injection barrier of BTQBT-aluminum interface was estimated 0.78 eV.

Next then, we briefly explained second topic, Alq3-PEI-ITO interface. (Alq3 and PEI stand for Tris-(8-hydroxyquinoline)aluminum and poly ethylene imine, respectively.) Recently, it was reported that ITO covered with ultrathin PEI performed excellent electron injection layer. [3] We investigated electronic structure of Alq3-PEI-ITO interface by UPS. Figure 3 shows UPS spectra of Alq3. Energy level of the Alq3 spectrum was shifted to low kinetic energy side, and there was no interface state. It suggest that vacuum level shift (0.5 eV) by PEI partly diminished electron injection barrier (1.5 eV). The electron injection mechanism of PEI is still under investigation.

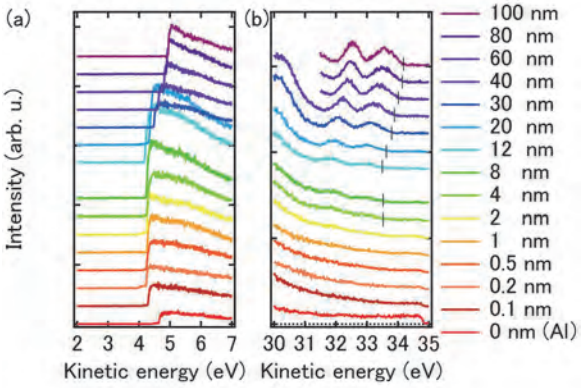

Fig. 1. Photo emission spectra of BTQBT on Al interface. (a) the secondary electron cut-off (SECO) position (b) the Fermi edge position. Black solid lines indicates HOMO edge of BTQBT.

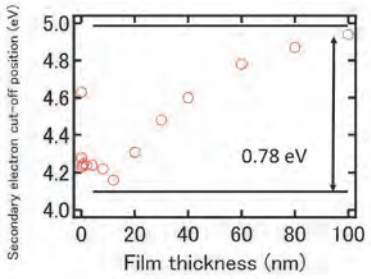

Fig. 2. SECO vs film thickness of BTQBT.

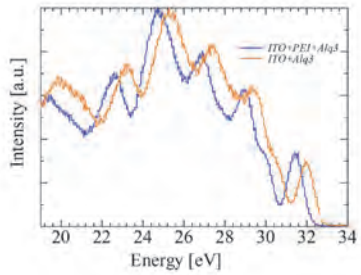

Fig. 3. UPS spectra of Alq3 on ITO interface, with and without PEI ultrathin layer.

[1] S. Hasegawa, *et al*., J. Chem. Phys. **100** (1994) 6969.
[2] H. Fukagawa, Y. Watanabe, *et al.*, AIP Advance **6** (2016) 045010.
[3] H. Fukagawa *et al*., APEX **7** (2014) 082104.

BL3B

Oxygen Vacancy in Solution-processed IGZO Thin-Film Transistors and Its Effect on Transistor Characteristics

Y. Ochiai[1], T. Morimoto[1], N. Fukuda[3] and Y. Ohki[1,2]

[1]*Waseda University, Tokyo 169-8555, Japan*

[2]*Research Institute for Materials Science and Technology, Waseda University, Tokyo 169-8555, Japan*

[3]*Flexible Electronics Research Center (FLEC), National Institute of Advanced Industrial Science and Technology (AIST), Tsukuba 305-8565, Japan*

Using a solution process, by which films can be produced at low cost, we have successfully made IGZO thin-film transistors (TFTs) with a mobility of 5.1 cm^2/Vs, which is higher than that of amorphous Si TFTs [1]. In this paper, the transfer characteristics of these TFTs are studied, focusing on the effects of oxygen vacancy, Ga content, and sintering temperature.

Six precursor solutions of IGZO were prepared by dissolving each nitrate of In, Ga, or Zn with a molar ratio of 1:*x*:1 (*x*: 0 to 8) in 2-methoxyethanol. The solution was spin-coated on a 300-nm thick thermally oxidized SiO_2 on a p-type silicon substrate and sintered at 300 or 800 °C for 1 hour in air. Then, Al was vacuum-evaporated on the film to form a drain electrode and a source electrode, by which we obtained a TFT with a gate length of 50 μm and a width of 500 μm. Next, its transfer characteristics were measured by raising the gate voltage applied to the substrate from -40 to +80 V, while the source electrode was earthed and the drain electrode was biased to +40 V dc.

The inset in Fig. 1 shows the drain current as a function of gate voltage, while Fig. 1 shows the relation between the on-current (I_D at V_G = 80 V) obtained from the transfer characteristics and the Ga content. For the films sintered at 300°C, the on-current decreases monotonically with the increase in Ga content, whereas it becomes maximum at the Ga content of 40% in the films sintered at 800°C.

The inset in Fig. 2 shows an XPS spectrum of O1s electrons observed in an IGZO film with a Ga content of 0% sintered at 300°C and its three components at 530 eV due to oxygen bonding with metal, at 531 eV due to oxygen adjacent to oxygen vacancies (V_O), and at 532 eV due to hydroxide [2]. As shown in Fig. 2, the intensity of V_O peak increases with the increase in Ga content in the films sintered at 300°C, whereas it becomes minimum at Ga contents of 20 and 40 % in the films sintered at 800°C.

The inset in Fig. 3 shows PL spectra observed in IGZO films with Ga contents of 0 and 80 % sintered at 300°C, while Fig. 3 shows the intensities of the PL at 2.5 eV as a function of Ga content. The 2.5-eV PL has a similar Ga-content dependence to the O1s intensity due to oxygen vacancy shown in Fig. 2. A similar PL appearing in ZnO at 2.36 eV has been attributed to oxygen vacancy [3]. Thus, the present 2.5-eV PL should be due to oxygen vacancy. This indicates that PL can detect the presence of oxygen vacancies in IGZO films.

It has also become clear that the on-current becomes maximum when the density of oxygen vacancies is minimized, namely, at Ga content of 0% for the films sintered at 300°C or at 40% for the films sintered at 800°C. These results indicate that oxygen vacancies act as electron scattering centers.

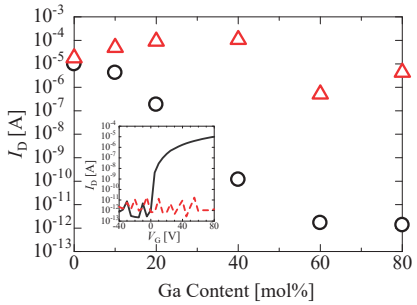

Fig. 1. I_D as a function of Ga content measured at V_G = 80 V for IGZO films sintered at 300 (○) and 800 °C (Δ). (Inset) Transfer characteristics measured at V_D = 40 V for IGZO films with Ga contents of 0 (—) and 80% (---) sintered at 300°C.

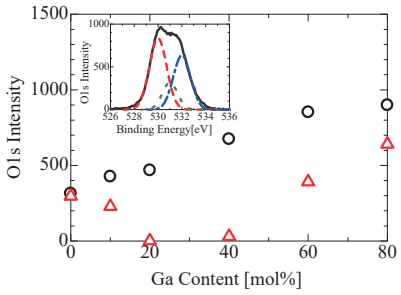

Fig. 2. Intensities of O1s XPS component due to oxygen adjacent to oxygen vacancy (V_O) in IGZO films sintered at 300 (○) and 800 °C (Δ), as a function of Ga content. (Inset) O1s spectrum of IGZO film with Ga content of 0% sintered at 300°C (—) and its components due to oxygen bonding with metal (---), V_O (···), and hydroxide (-•-).

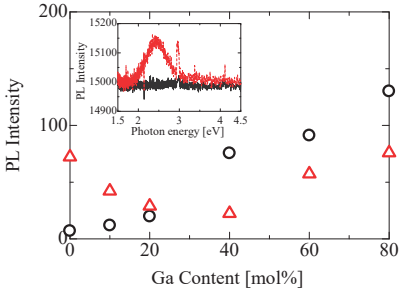

Fig. 3. PL intensities due to oxygen vacancy in IGZO films sintered at 300 (○) and 800 °C (Δ). (Inset) PL spectra of IGZO films with Ga contents of 0 (—) and 80% (---), sintered at 300°C.

[1] S. Ogura *et al.*, Flex. Print. Electron. **1** (2016) 045001.
[2] K. K. Banger *et al.*, Nature Mat. **10** (2011) 45.
[3] K. Vanheusden *et al.*, J. Appl. Phys. **79** (1996) 7983.

BL4U

STXM Analysis of Adsorbent for Effective Recovery of Radioactive Elements

Y. Sano[1], S. Watanabe[1], Y. Miyazaki[1], S. Kibe[1], H. Matsuura[2], T. Uchiyama[2] and Y. Katai[2]
[1]*Japan Atomic Energy Agency (JAEA), Tokai 319-1194, Japan*
[2]*Tokyo City University, Tokyo 158-8557, Japan*

Spent nuclear fuels generated from nuclear power plants contain U and Pu which can be reused, and several long-lived radioactive elements. It will be quite important for effective utilization of energy and environmental loading reduction to process the spent fuel adequately. JAEA has been developing the selective recovery process of radioactive elements, which uses adsorbents of SiO_2 supports coated with styrene-divinylbenzene (SDB) copolymer (SiO_2-P) and extractants on its surface. Scanning transmission X-ray microscopy (STXM) is one of useful techniques to obtain the information about such an adsorbent surface. Our previous study using STXM analysis showed that the SDB polymer and extractants were distributed within several hundred nanometers from the pore surface in SiO_2 supports, and their distributions were spread by the increase of crosslinking degree of polymer (CDP) [1]. In this study, the change of adsorbent surface, such as thickness of polymer and uniformity of extractants, after adsorbing metal ions was investigated by STXM analysis.

The adsorbents in which Di-(2-ethylhexyl) phosphoric acid (HDEHP) was impregnated as an extractant were synthesized by the flowsheet reported by Wei et al. [2]. The average diameter and pore size of the SiO_2 supports were 50 μm and 600 nm, respectively. Some adsorbents were mixed with Zr/HNO_3 solution and filtered for preparing the adsorbents adsorbing Zr. These adsorbents were sliced to 300 nm in thickness by focused ion beam (FIB), and were supplied to STXM analysis.

The O-NEXAFS spectra observed on the adsorbents before and after adsorbing Zr were shown in Fig. 1. The intensity of pre-edge peak at 532 eV increased after Eu adsorption at any position in the adsorbent. Figure 2 shows the colorized composition maps on the cross section of sliced adsorbents before and after adsorbing Zr, which were calculated by fitting C-NEXAFS spectra with those of SDB polymer and HDEHP. The SDB polymer and HDEHP were distributed within several hundred nanometers from the pore surface, and their distributions, especially SDB polymer, were spread uniformly in the adsorbent adsorbing Zr.

The increase of pre-edge peak at 532 eV in O-NEXAFS spectra after Zr adsorption indicates the adsorption of some kinds of molecules contained in Zr/HNO_3 solution, such as H_2O. The adsorption of Zr and these molecules will bring the swelling of SDB polymer in the pore of SiO_2 support, which was observed in Fig. 2. The excessive swelling of SDB polymer is undesirable for the recovery process of radioactive elements. It will be important to select the appropriate pore size in SiO_2 support and coating condition (thickness and CDP) of SDB.

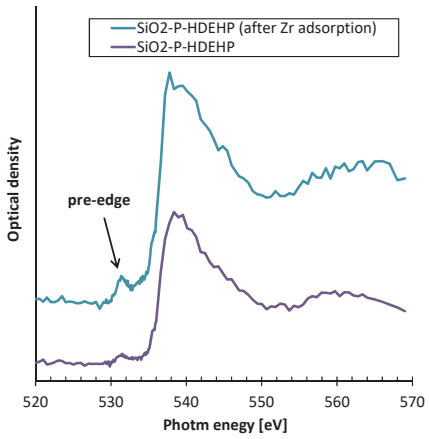

Fig. 1. Change of O-NEXAFS spectra (O-K edge).

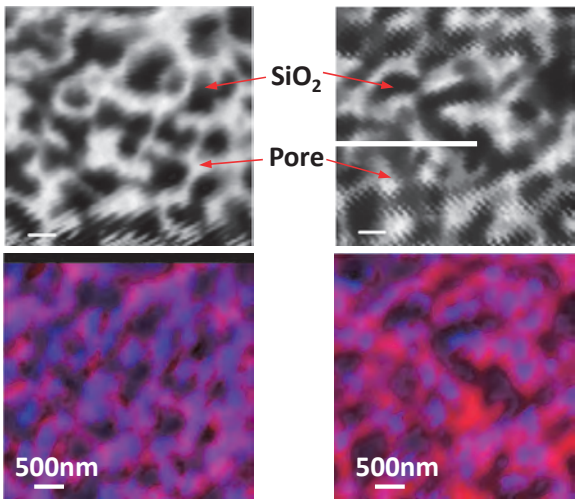

(a) before Zr adsorption (b) after Zr adsorption

Fig. 2. Colorized composition maps (black; SiO_2, white; pore, red; SDB, blue; HDEHP (purple; mixture of red and blue)).

[1] Y. Sano, S. Watanabe and S. Kibe, UVSOR Activity Report **43** (2016) 120.
[2] Y. Wei, M. Kumagai and Y. Takashima, Nucl. Technol. **132** (2000) 413.

BL4B

Nanoscale Magnetic Coupling at the Interface of Mn/Fe Thin Film Heterostructures

T. Miyamachi[1], S. Nakashima[1], Y. Takahashi[1], T. Hattori[1], Y. Takagi[2, 3], M. Uozumi[2, 3], T. Yokoyama[2, 3] and F. Komori[1]

[1]*Institute for Solid State Physics, University of Tokyo, Kashiwa 277-8581, Japan*
[2]*Department of Materials Molecular Science, Institute for Molecular Science, Okazaki 444-8585, Japan*
[3]*Department of Structural Molecular Science, The Graduate University for Advanced Studies (SOKENDAI), Okazaki 444-8585, Japan*

Electronic and magnetic properties of a multilayer system strongly rely on its interfacial conditions. In the case of a magnetic heterostructure composed of antiferromagnetic (AFM) and ferromagnetic (FM) thin films, the strength of the magnetic coupling at the AFM/FM interface, e.g., the exchange energy, is considerably lower for experimental values compared to theoretical ones with the ideal interface. This difference is mainly attributed to the interface roughness caused by intermixing or alloying between AFM and FM layers. Thus, detailed information on the AFM/FM interface structure is essential to understand its intrinsic magnetic coupling. In this study, we performed a complementary study for structural, electronic and magnetic properties of the AFM/FM Mn/Fe thin film heterostructures in combination with scanning tunneling microscopy (STM) and x-ray absorption spectroscopy/x-ray magnetic circular dichroism (XAS/XMCD) [1].

7 monolayer (ML) Fe thin films on Cu(001) in the fcc phase were chosen as a FM layer. AFM Mn layers with a thickness ranging from 0 to 5 ML were subsequently grown at room temperature in ultrahigh vacuum. The electronic and magnetic properties of fcc Fe thin films are sensitive to the structural variation on the surface [2], which is advantageous to investigate the impact of the interface roughness on the magnetic coupling of the AFM/FM thin film heterostructure. The growth and structural properties of the heterostructures were checked by STM before XAS/XMCD measurements.

The XAS/XMCD measurements were performed at BL4B in UVSOR at B = 0, ± 5 T and T = 80 K. The spectra were recorded in the total electron yield mode in the normal (NI :θ = 0°) and the grazing (GI: θ = 55°) and incidences. Note that θ is the angle between the sample normal and the incident x-ray. The XMCD is defined as $\mu_+ - \mu_-$, where μ_+ and μ_- denote XAS at the Fe $L_{2,3}$ adsorption edge with the photon helicity parallel and antiparallel to the sample magnetization.

Figure 1 (a) displays XAS and remanent (± 5 → 0 T) XMCD spectra of bare 7 ML Fe/Cu(001). As previously reported by surface magneto-optic Kerr effect measurements [3], the XMCD signal arising from ferromagnetically-coupled top two Fe layers is slightly larger in NI than GI geometry, indicating the magnetic easy axis towards out-of-plane direction.

In contrast, we find that adding Mn layers induces the spin reorientation transition (SRT) to Fe layers. Figure 1 (b) displays XAS and remanent (± 5 → 0 T) XMCD spectra of 5 ML Mn/ 7ML Fe/Cu(001). The absence of the XMCD signal in GI geometry is observed, while the XMCD signal in NI geometry is nearly unchanged. The result demonstrates the SRT from out-of-plane to in-plane directions. In addition, the enhanced magnetic anisotropy is expected from the larger difference in the XMCD signal between NI and GI geometries. An Mn-thickness dependence of the XMCD signal combined with atomically-resolved STM observations on the surfaces with thin Mn thickness ranges (0-3 ML) reveal that the SRT is driven by the alloy formation in the vicinity of the Mn/Fe interface.

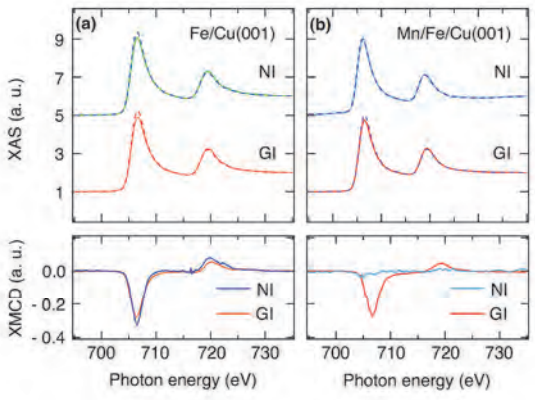

Fig. 1. Fe $L_{2,3}$ edge XAS and remanent XMCD spectra of (a) bare 7 ML Fe/Cu(001) and 5ML Mn/7ML Fe/Cu(001) at NI and GI geometries. Solid and dashed lines for XAS spectra represent μ_+ and μ_-, respectively.

[1] S. Nakashima *et al.*, submitted.
[2] T. Miyamachi *et al.*, Phys. Rev. B **94** (2016) 045439.
[3] J. Thomassen *et al.*, Phys. Rev. Lett. **69** (1992) 3831.

BL4B

XMCD Measurements on a Ferromagnet/Topological Insulator Heterostructure

R. Nakanishi[1], R. Akiyama[1], Y. Okuyama[2], Y. Takagi[3], T. Yokoyama[3], S. Hasegawa[1] and T. Hirahara[2]

[1]*Department of Physics, University of Tokyo, Tokyo 113-0033, Japan*
[2]*Department of Physics, Tokyo Institute of Technology, Tokyo 152-8551, Japan*
[3]*Department of Materials Molecular Science, Institute for Molecular Science, Okazaki 444-8585, Japan*

Topological insulators (TI) are extensively studied recently due to its peculiar properties [1]. The Dirac-cone surface states of TI are protected by time-reversal symmetry (TRS) and backscattering among these surface states is prohibited. But when TRS is broken by application of a magnetic field or incorporating magnetic materials, a gap opening in the Dirac cone is expected and an intriguing phase called the quantum anomalous Hall state can be realized [2]. This phase is expected to show even more exotic phenomena such as the topological magnetoelectic effect. To realize such state, two types of sample fabrication techniques have been employed up to now: (1) magnetic doping while growing the single crystal or thin film of TI [3], and (2) magnetic impurity deposition on the surface of TI [4]. While method (1) was successful and showed evidence of the TRS violation, no one has succeeded using method (2), which should be a more direct way to examine the interaction between the topological surface states and magnetism.

Previously, we have found that when we make a heterostructure of Bi_2Se_3 (TI) and a magnetic insulator $MnBi_2Se_4$, it is possible to observed a massive Dirac cone with a gap of ~ 80 meV. This is a novel method to incorporate magnetism into topological insulators. The calculated band structure reproduced the experimental observation nicely, and the gap opening was reasonably explained as due to the time-reversal symmetry breaking of the Dirac cone due to the ferromagnetic $MnBi_2Se_4$. In the present work, we have performed XMCD measurements at BL4B to experimentally prove that the $MnBi_2Se_4/Bi_2Se_3$ is ferromagnetic. Figure 1 shows the X-ray absorption (XAS) spectra and the corresponding XMCD spectra at 5T. One can find clear XMCD peaks at the Mn L_3 and L_2 edges. The measurements were also performed at remanence, and the result is shown in Fig. 2. Although very weak, one can find a dip structure at the L_3 edge and this shows that the heterostructure is ferromagnetic, consistent with the prediction of the ab initio calculations.

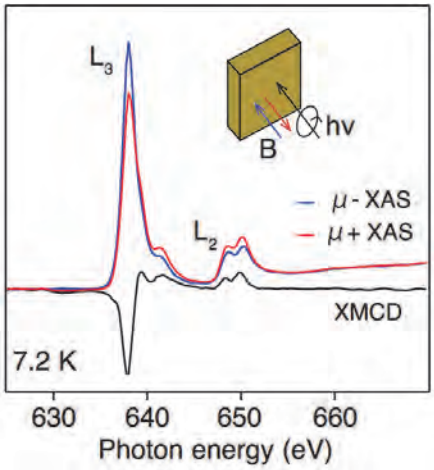

Fig. 1. XAS and XMCD spectra at 5T.

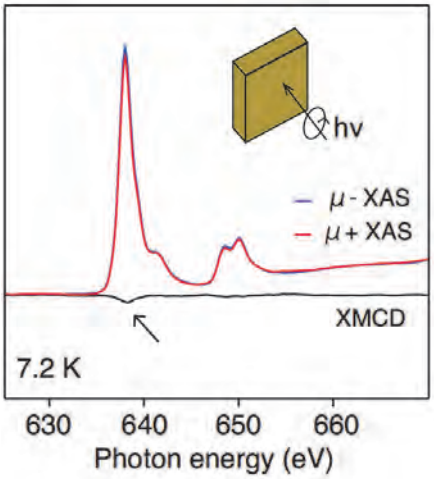

Fig. 2. XAS and XMCD spectra at remanence.

[1] M. Hasan and C. Kane, Rev. Mod. Phys. **82** (2010) 3045.
[2] X.-L. Qi and S.-C. Zhang, Rev. Mod. Phys. **83** (2011) 1057.
[3] For example, C. Z. Chang *et al.,* Science **340** (2013) 167.
[4] For example, M. Ye *et al.,* Phys. Rev. B **85** (2012) 205317.

BL4B

XMCD Study of Ferro Orbital Ordered System: FeV_2O_4

J. Okabayashi[1*] and S. Miyasaka[2]

[1]*Research Center for Spectrochemistry, University of Tokyo, Tokyo 113-0033, Japan*

[2]*Department of Physics, Osaka University, Toyonaka 560-0043, Japan*

The orbital degree of freedom has attracted interest in the condensed-matter physics because of adding of new functional functionalities. Couplings between orbital and spin degrees of freedom in transition metal (TM) oxides exhibit a wide variety of interesting physical phenomena studied in strongly correlated electron systems. The orbital degeneracy of t_{2g} or e_g orbitals, split by the crystal field in TM oxides, gives rise to the orbital ordering phenomena in perovskite-type Fe or V oxides accompanied by Jahn-Teller distortion. Spinel-type FeV_2O_4 is a candidate to study orbital ordering since orbital magnetic moments of Fe^{2+} (d^6) are strongly affected by the Jahn-Teller distortion in the Fe sites, which brings the ferro orbital ordering in V sites through the spin-orbit interaction. An unresolved issue related to orbital ordering of spinel-type vanadium oxides is the relationship between the orbital magnetic moments in vanadium sites and orbital ordering [1]. In case of FeV_2O_4, the V orbital states consist of complex wave functions of degenerated *yz* and *zx* states, which expect the ferro-orbital ordering with the large orbital moments of almost 1 μ_B. On the other hand, in the case of MnV_2O_4, real wave functions in the V sites which are described as d_{yz} and d_{zx} are ordered alternatively, resulting in an antiferro orbital ordering with quenching orbital moments. Therefore, the investigation of orbital moments in V sites enables to discuss the types of orbital ordering. X-ray absorption spectroscopy (XAS) and X-ray magnetic circular dichroism (XMCD) with the sum-rule analysis enables to estimate the orbital moments. In this study, we investigated the element specific electronic and magnetic properties of FeV_2O_4 using XAS and XMCD, and examined the relationship between orbital magnetic moments and orbital ordering.

Single crystals were grown by the floating-zone method. The magnetic and orbital ordering temperatures of FeV_2O_4 were estimated to be 110 K and 70 K, respectively, accompanying the lattice distortions from tetragonal to orthorhombic structures with decreasing temperature. The XAS and XMCD measurements were performed at BL4B, UVSOR, Institute of Molecular Science. Total photoelectron yield mode by directly detecting the sample current was adopted. A magnetic field of ±5 T was applied along the direction of the incident polarized soft x-ray.

Figure 1 shows XAS, XMCD spectra of Fe and V $L_{2,3}$-edge regions taken at 5 K, which is sufficiently lower than the orbital ordered transition temperature. The resulting residuals from the XMCD integrals for both L_2 and L_3 edges suggest that the finite values of orbital magnetic moments remain in the V^{3+} states, which is consistent with the ferro orbital ordering. Using the integrals over XAS spectra and assuming that the V 3*d* electron number to be 2, we deduced the orbital magnetic moments (m_l) to be less than 0.1 μ_B/(V atoms) from the orbital sum rule. This value is small but finite. This result indicates that unquenched orbital magnetic moments contribute to the formation of the complex wave functions in V sites that the d_{yz}+id_{zx} type wave functions consist of the ground states. Although the Fe *L*-edge XAS includes the oxidized states, the finite orbital moments also remain in the Fe sites through the Jahn-Teller distortion.

The t_{2g} states in V 3*d* states are split into two levels by the tetragonal distortion and the lowest *xy* states are occupied by one of the electrons. The other electron occupies the *yz* or *zx* states. The existence of the small but finite orbital magnetic moments in the V sites can be explained by the (i) complex orbital ordering as discussed in the case of FeV_2O_4, (ii) domain formation, and (iii) mixing of the real and complex orbital orderings due to the trigonal distortion around the V sites [2].

We acknowledge to Prof. T. Yokoyama, Dr. Y. Takagi, and Dr. K. Uemura for the technical supports at BL4B.

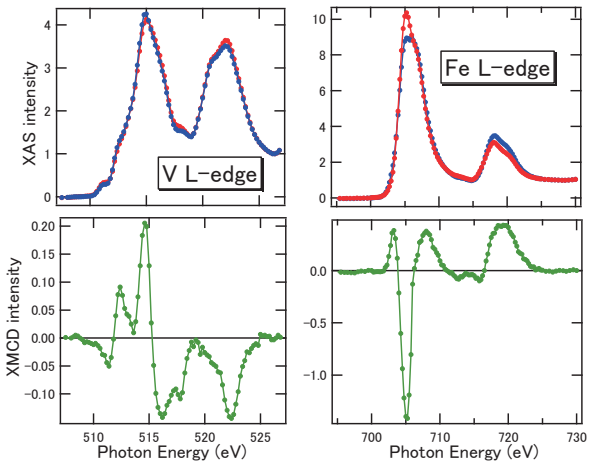

Fig. 1. V and Fe *L*-edge XAS and XMCD spectra in FeV_2O_4.

[1] Y. Nii *et al.*, Phys. Rev. B **86** (2012) 125142.
[2] J. Okabayashi *et al.*, J. Phys. Soc. Jpn. **84** (2015) 104703.

*e-mail: jun@chem.s.u-tokyo.ac.jp

BL4B

Oxygen Adsorption on Single and Double Fe Ultrathin Films

T. Nakagawa[1], T. Nomitsu[1], M. T. Kibria[1], S. Mizuno[1], Y. Takagi[2] and T. Yokoyama[2]
[1] *Department of Molecular and Material Sciences, Kyushu University, Kasuga 816-0955, Japan*
[2] *Institute for Molecular Science, Okazaki 444-8585, Japan*

Iron oxides have been widely studied both due to fundamental research interests and its application for catalysis and solid devices. However, the magnetism of its thinnest unit, a single layer Fe oxide, and the Fe thin films with oxygen adsorption have not been well studied [1]. The magnetic order at the surface of oxide has not been well understood yet [2, 3].

Experiments were done in the x-ray magnetic circular dichroism (XMCD) endstation with the base pressures of 2×10^{-8} Pa for sample preparation and better than 1×10^{-8} Pa for XMCD measurement. Single and double Fe layers were grown on W(110). Oxygen was dosed via a variable leak valve at 2×10^{-7} Pa with the sample kept at the room temperature, and the Fe films exposed up to 150 L(1 L = 1.3×10^{-4} Pa s) of oxygen were examined by XMCD. XMCD spectra were taken with a circularly polarized light (circularly polarization ~ 0.6) at $H = \pm5$ T at a sample temperature of 8 K.

Figure 1 shows x-ray absorption spectra (XAS) and XMCD spectra for single and double Fe layers with increasing the oxygen exposure. At 150 L, XAS for the single layer (SL) and double layer (DL) show splitting at the L_2 edges, which indicates a transition from metallic to oxide states. XMCD signals both for the SL and DL are almost zero. On the contrary, at least up to 5 L, the L_2 edges does not show splitting, which indicates that the Fe films are in metallic states.

On the SL, at 0.2 L, corresponding to ~1/4 monolayer oxygen adsorption, the magnetic moment that is a sum of spin and orbital magnetic moments drastically decreases to 0.4 μ_B, which is much smaller than that of the clean SL, 2.1 μ_B. After 5 L, the magnetic moment is restored to 1.1 μ_B. At 150 L exposure of oxygen, the XMCD single is almost zero.

On the DL, at 0.2 L, XMCD does not change much as compared with that for the clean DL. The magnetic moment at 0.2 L is 2.0 μ_B. With increasing the oxygen exposure, the magnetic moment slowly decreases and it is 1.6 μ_B at 5 L.

With increasing the oxygen adsorption, the SL rapidly loses its ferromagnetic order, resulting in reduced magnetic moments. On the other hand, the DL maintains its magnetic moment until it is oxidized, although the magnetic moment for the DL monotonically and slowly decreases with increasing the oxygen adsorption. This different is attributed to ferromagnetic coupling. On the SD, the oxygen adsorption strongly weakens its ferromagnetic order. However, on the DL, the second layer Fe in the proximity of the W substrate, which is not directly affected by oxygen adsorption, ferromagnetically couples with the topmost Fe layer.

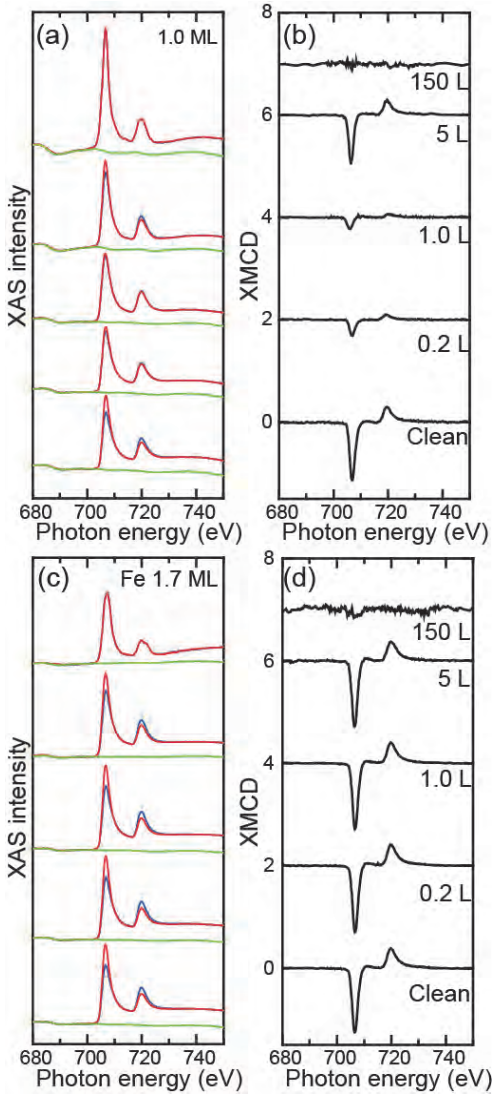

Fig. 1. XAS and XMCD spectra for single (1.0 ML) and double (1.7 ML) Fe layers with increasing oxygen exposure (0 ~ 150 L). (a) XAS spectra taken at ±5 T for the single iron layer (SL). (b) XMCD spectra for SL. (c) the same as (a), but for the double layer (DL). (d) the same as (b), but for DL.

[1] K. Feindl *et al*., Surf. Sci. **617** (2013) 183.
[2] K. Mori *et al*., Phys. Rev. B **72** (2005) 014418.
[3] E. Vescovo, Phys. Rev. B**74** (2006) 026406.

BL4B

XMCD Study of Fe Nanoparticles Synthesized on h-BN Nanomesh

S. Sakai[1, 2], T. Watanabe[1, 2], Y. Yamada[2], S. Entani[1], A. Koide[3], Y. Takagi[3] and T. Yokoyama[3]

[1]*Quantum Beam Science Research Directorate / QST Future laboratory, National Institutes for Quantum and Radiological Science and Technology QST, Tokai 319-1106, Japan*

[2]*Japan Institute of Applied Physics, University of Tsukuba, Tsukuba 305-8577, Japan*

[3]*Department of Materials Molecular Science, Division of Electronic Structure, Institute for Molecular Science, Okazaki 444-8585, Japan*

Tailoring magnetic properties of nanomagnets is the central research issue in developing magnetic and spintronic memory devices. Recent studies have demonstrated graphene-induced perpendicular magnetic anisotropy in a ultra-thin cobalt film on graphene [1, 2] and at the interface region of graphene/Ni(111) [3]. It was also shown that in Co atoms on graphene/metal substrate the magnetization easy axis of the Co atoms changes by the choice of the metal substrate [4]. In addition, single layer graphene and hexagonal boron nitride on Rh(111) and Ru(0001) (so-called graphene and h-BN nanomesh) were shown to be useful as a template for fabricating regularly-arranged nanoparticles of magnetic metals [4-6] relevant to the nanoscale periodicity of the Moiré pattern. The above results in the previous studies make the magnetic metal/atomic layer material structures promising for the magnetic and spintronic memory device applications.

In this study, we investigated the magnetic property of Fe nanoparticles synthesized on h-BN nanomesh (h-BN/ Ru(0001)) with X-ray magnetic dichroism (XMCD) spectroscopy. Total electron yield X-ray absorption (XAS) and XMCD measurements were performed at BL-4B of UVSOR III using an ultra-high-vacuum XMCD apparatus with a base pressure of 10^{-8} Pa. The sample was prepared *in-situ* by depositing Fe on the surface of h-BN/Ru(0001) at ambient temperature. The Fe $L_{2,3}$ edge XAS and XMCD were measured at low temperatures (6.8 K and 140 K) under the magnetic field up to 5 T.

Figure 1 shows the atomic force microscopy (AFM) image of the Fe/h-BN/Ru(0001) sample after the deposition of Fe with a nominal thickness of 1.4 nm. The AFM image and the height cross section profile indicate planar Fe nanoparticles with a mean diameter of ~10 nm and the thickness less than 2 nm.

Figure 2 shows (a) the Fe $L_{2,3}$ edge XAS spectra of the same sample at 6.8 K measured under the grazing incidence (30º) and by applying the magnetic fields of ±5 T (the red and blue lines represent the spectra under the conditions of the circular x-ray vector parallel and antiparallel to the magnetic field) and the magnetic hysteresis loops at 6.8 K and 140 K under the (b) normal and (c) grazing incidence as a function of the magnetic field, which were measured for the L_3 edge absorption intensity. A clear XMCD signal from the Fe nanoparticles was detected as shown in Fig. 2 (a). The Fe nanoparticles are found to be ferromagnetic and have an in-plane easy axis of magnetization as can be judged from the good coincidence between the hysteresis at 6.8 K and 140 K and the change of the curve shape by the incidence direction in Figs. 2 (b) and 2 (c). The magnetic anisotropy field is roughly estimated to be 0.6 T from the intercept of the normal and grazing incidence curve, which is reasonably attributed to the shape anisotropy of the planer Fe nanoparticles (Fig. 1).

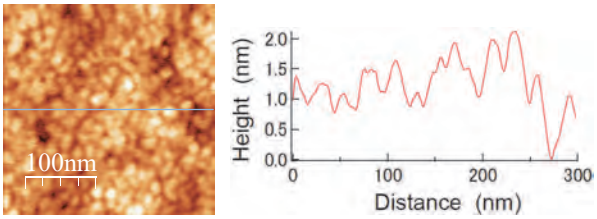

Fig. 1. (left) AFM image and (right) the height cross section profile of 1.4 nm Fe/h-BN/Pt(111)

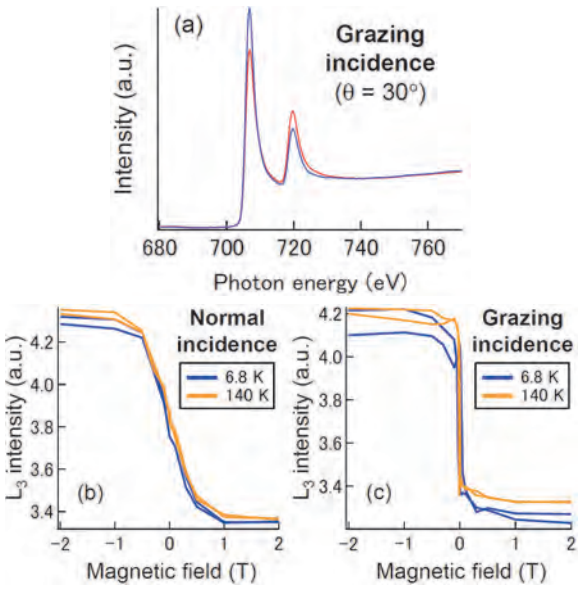

Fig. 2. (a) Fe $L_{2,3}$ edge XAS spectra of 1.4 nm Fe/h-BN/Pr(111) at 6.8 K under the grazing incidence and the hysteresis at 6.8 K and 140 K of the Fe L_3 intensity under the (b) normal and (c) grazing incidence

[1] C. Vo-Van *et al.*, New J. Phys. **12** (2010) 103040.
[2] J. Coraux *et al.*, J. Phys. Chem. Lett. **3** (2012) 2059.
[3] Y. Matsumoto *et al.*, J. Mater. Chem. C **1** (2013) 5533.
[4] F. Donati *et al.*, Phys. Rev. Lett. **113** (2014) 177201.
[5] R. Zhang *et al.*, Phys. Rev. B **78** (2008) 165430.
[6] I. Bihuega *et al.*, Surf. Sci. **602** (2008) L95.
[7] B. Wang *et al.*, J. Phys. Chem. Lett. 2 (2011) 2341.

BL5U

Growth and Electronic Structure of Ultrathin Te Films Grown on Bi_2Te_3

Y. Okuyama[1], Y. Sugiyama[1], S. Ideta[2], K. Tanaka[2] and T. Hirahara[1]
[1]*Department of Physics, Tokyo Institute of Technology, Tokyo 152-8551, Japan*
[2] *UVSOR Facility, Institute for Molecular Science, Okazaki 444-8585, Japan*

Chirality is a geometric property of materials and is mostly discussed in chemistry or biology. A chiral molecule/ion is non-superposable on its mirror image (enantiomers) and individual enantiomers are often called as either “right-” or “left-handed”. Some solid crystals also have chirality such as elements tellurium (Te) and selenium (Se). They are trigonal structures that can be regarded as a hexagonal array of helical chains at ambient pressure. They lack inversion symmetry and possess chirality depending on the rotation direction of the screw axis. Due to this peculiar crystal structure, Te shows intriguing properties such as the circular photon drag effect or the current-induced spin polarization.

It is also well known that the physical properties of Te and Se can be tuned by controlling the lattice constant, which can be achieved by applying pressure. They will eventually undergo a structural transition to the monoclinic or the triclinic phases at very high pressure in the order of ~10 GPa. The electronic structure can also be changed from a semiconductor (the band gap is 0.33eV and 2.0 eV for Te and Se, respectively) to a metal by applying pressure. Recently, based on ab initio calculations, it was predicted that Te undergoes a trivial insulator to a strong topological insulator (metal) transition under shear (hydrostatic or uniaxial) strain in the trigonal phase [1]. Furthermore, it was predicted that the lack of inversion symmetry and spin–orbit interaction leads to the existence of Dirac points or Weyl nodes in the band structure of Te or Se [2]. Such states possess an unconventional spin texture and furthermore, if one can fine-tune the lattice constant by carefully controlling the applied pressure, Te and Se are expected to show the Weyl semimetal phase [3].

In the present work, we have attempted to mimic the lattice constant change by growing a thin Te film on a substrate and utilizing the epitaxy to apply strain. We have adopted Bi_2Te_3 as our substrate since it has been reported as a promising material for Te thin film growth [4]. Figure 1 shows the low-energy diffraction (LEED) pattern of the grown films, and we have found that a six domain Te(10-10) film can be grown on Bi_2Te_3 [5]. We have performed angle-resolved photoemission (ARPES) measurements at BL-5U as shown in Fig. 2. The measurement was performed at 30 K. A Dirac-cone like linear dispersion near the Fermi level was found at the H point of the Brillouin zone. Further work is needed elucidate the entire picture of the band structure.

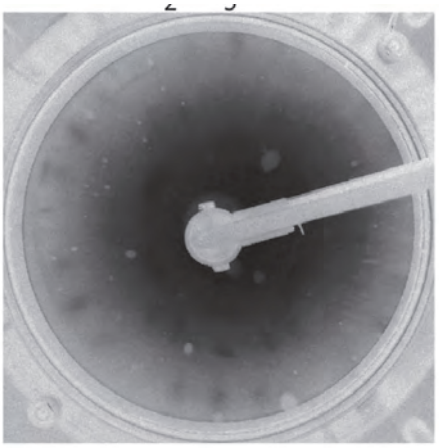

Fig. 1. LEED pattern of the six domain Te(10-10) film grown on Bi_2Te_3.

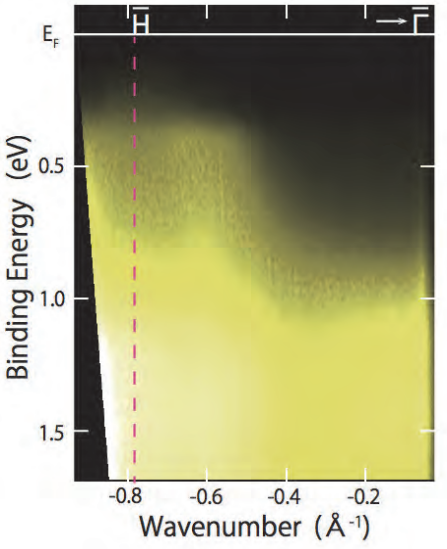

Fig. 2. Band dispersion of the Te(10-10) film near the Fermi level.

[1] L.A. Agapito, N. Kioussis, W.A. Goddard and N.P. Ong, Phys. Rev. Lett. **110** (2013) 176401.
[2] M. Hirayama, R. Okugawa, S. Ishibashi, S. Murakami and T. Miyake, JPS Conf. Proc. **5** (2015) 011024.
[3] M. Hirayama, R. Okugawa, S. Ishibashi, S. Murakami and T. Miyake, Phys. Rev. Lett. **114** (2015) 206401.
[4] K. Hoefer, C. Becker, S. Wirth and L.H. Tjengb, AIP Adv. **5** (2015) 097139.
[5] Y. Okuyama, Y. Sugiyama, S.-I. Ideta, K. Tanaka and T. Hirahara, Appl. Surf. Sci. **398** (2017) 125.

BL5U

Towards Direct Observation of Spatial Modulation on Molecular Orbitals by the Organic–metal Interaction

T. Ueba[1, 2], K. Yonezawa[1], C. Numata[3], R. Shiraishi[2], S. Ideta[1, 2], K. Tanaka[1, 2] and S. Kera[1, 2, 3]

[1]*Department of Photomolecular Science, Institute for Molecular Science, Okazaki 444-8585, Japan*

[2]*School of Physical Sciences, The Graduate University for Advanced Studies (SOKENDAI), Okazaki 444-8585, Japan*

[3]*Department of Nanomaterial Science, Graduate School of Advanced Integration Science, Chiba University, Chiba 263-8522, Japan*

Understanding the weak interaction at the organic-metal interface, including intermolecular interaction and molecule-metal interaction, is of great importance because even such weak interaction can cause the rearrangement of molecular orbitals both in energy and space, which determines the electronic properties at interfaces. Photoelectron angular distribution (PAD) measured by angle-resolved ultraviolet photoelectron spectroscopy (ARUPS) contains information of the spatial distribution and the phase of molecular orbitals (MOs) [1, 2]. Therefore, a careful comparison between experimental and theoretical PADs will enable us to directly discuss a modulation on electronic structures due to the weak interaction. In this work, we performed ARUPS for the perfluoropentacene (PFP, shown in the inset of Figure 1) monolayer film grown on the Ag(111) substrate as a model system, in order to examine how the ARUPS with a photoelectron deflector analyzer in the beam line BL5U shows PAD of MOs.

A PFP monolayer film on Ag(111) was prepared by multilayer deposition on the clean Ag(111) substrate and the following annealing at 400 K, and was kept at 45 ± 5 K during measurements to obtain an ordered structure [3].

Figure 1 (b) shows the k_x-k_y maps converted from ARUPS two-dimensional images measured at $h\nu$ = 60 eV with *p*-polarization, at the respective kinetic energies, as schematically shown in Fig. 1 (a). The momentum k_x is set to be parallel to the Γ-K direction. The energy region I includes merely the *sp*-band of the Ag substrate. In the regions II/III, on the other hand, not only the sharp *sp*-band but also some additional vague structures can be seen. These structures can be attributed to the corresponding MO orbitals, by comparing to the simulated k_x-k_y maps from the PAD simulation [2], as shown Fig. 1 (c).

Unfortunately, even at the lowest photon flux condition (diode current, the pinhole and the exit slit widths were ~350 pA, 4 mm and 100 μm, respectively, at the multi-bunch operation), a radiation damage to the present sample was found, which prevented us to observe clear k_x-k_y maps. For a detailed ARUPS measurement for organic thin films, the photon flux density needs to be further reduced by the use of a defocusing condition or of the single-bunch operation.

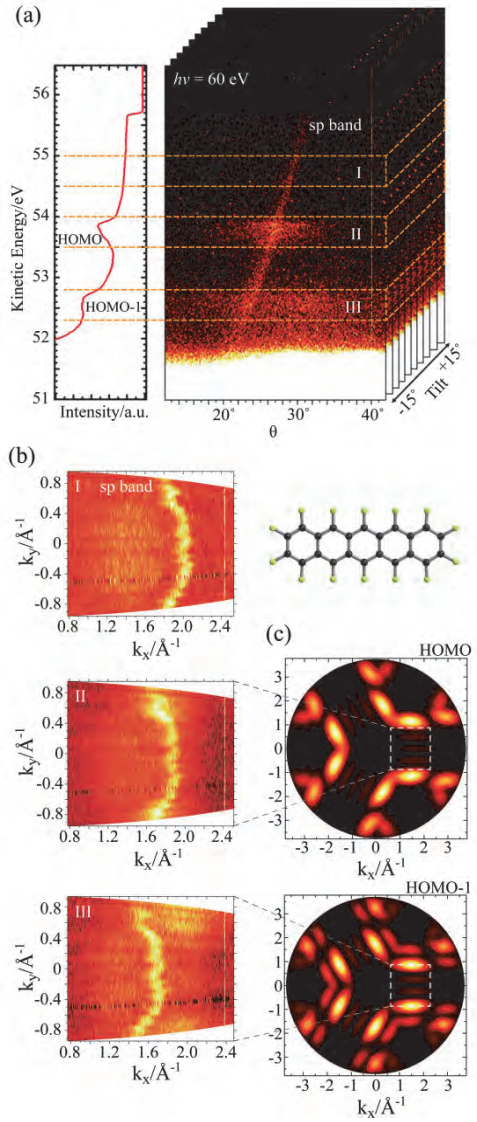

Fig. 1. (a) Angle-resolved UPS image and its angle-integrated spectrum of PFP monolayer on Ag(111). (b) Experimental k_x-k_y maps taken at regions I-III. (c) The corresponding PAD simulation of HOMO/HOMO-1. The three-fold pattern reflects the (111) symmetry. The molecular structure of PFP is also shown in the inset.

[1] P. Puschnig *et al.*, Science **326** (2009) 702.
[2] S. Nagamatsu *et al.*, e-J. Surf. Sci. Nanotechnol. **3** (2005) 461.
[3] M. Marks *et al.*, J, Phys. Chem. C **116** (2012) 1904.

BL5U, BL7U

Two-dimensional Electronic States on InSb(110) Localized in Subsurface Atomic Layers and its Temperature Dependent Energy Shift

Y. Ohtsubo[1, 2], H. Watanabe[1, 2],Y. Yamashita[2], K. Hagiwara[2], S. Ideta[3], K. Tanaka[3] and S. Kimura[1, 2]

[1]*Graduate School of Frontier Biosciences, Osaka University, Suita 565-0871 Japan*
[2]*Department of Physics, Graduate School of Science, Osaka University, Toyonaka 565-0043, Japan*
[3]*UVSOR Facility, Institute for Molecular Science, Okazaki 444-8585, Japan*

On the surface of crystals, two-dimensional (2D) electronic states, so called surface states are formed by two mechanisms as limiting cases [1]. In a localized-bond picture, surface states can be induced by an alternation of the localized chemical bonds due to the reconstruction of the surface atomic structure at the very surface layer. The surface states by such mechanism are usually assumed to have wave functions localized in a few topmost layers. On the other hands, in a perturbed-bulk-band picture, surface states are derived from bulk Bloch states, which are perturbed by the truncation of the periodic potential at the surface and consequently localized at near-surface region. While surface states in general have both characters with varying relative importance, it is sometimes intuitive to consider these two limiting pictures. Recently, there is a renewed interest in the surface states originating from bulk bands, which include the spin-orbital polarized surface states on topological insulators [2] and 2D metallic states on transition-metal oxides [3].

The (110) surface of III-V semiconductors is known to exhibit the well-ordered cleaved surface without any surface reconstruction nor dangling-bond formation [4]. In this project, we observed the surface electronic structure of the InSb(110) cleaved surface. As shown in Fig. 1, two parabolic bands dispersing downwards from the center of surface Brillouin zone was clearly observed by angle-resolved photoelectron spectroscopy (ARPES). Although these band dispersions are quite similar to its bulk-band counterparts, heavy hole and light hole bands, they showed no dispersion along the surface normal checked by changing the incident photon-energy for ARPES. It suggests that these parabolic states have 2D character and derived from the perturbation of the bulk bands by the truncation of the three-dimensional periodicity at the surface. These dispersion of 2D states are similar to the subsurface electronic states on the Ge(111) surfaces covered with various adsorbates [5], suggesting their common origin from subsurface layers of substrates.

Moreover, the 2D states on InSb(110) changed its binding energies depending on the sample temperature. From 13 to 300 K (room temperature), the maximum of the 2D bands moved downwards as large as ~160 meV. Usually, such temperature dependence of semiconductor states are understood due to surface photo-voltage (SPV) effect and surface band bending. However, we have detected a tiny SPV effect by changing the incident photon flux with its sign the opposite to the temperature-driven shift of the 2D bands. Such unusual energy shift can be qualitatively explained by the chemical potential shift due to the low density of states of the conduction bands of InSb [6]. Detailed analysis to understand the temperature-driven energy shifts and further research to use this energy shift to tune energies of the other surface states are in progress.

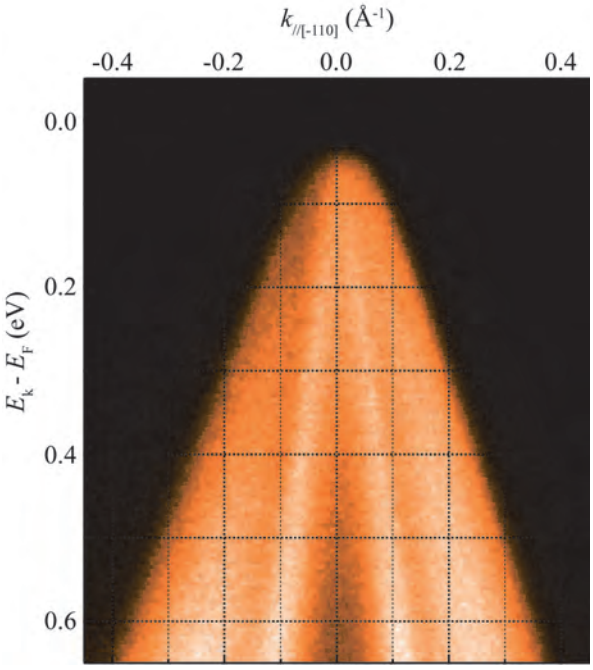

Fig. 1. Surface band dispersion of the InSb(110) cleaved surface observed by ARPES at 13 K ($h\nu$ = 20 eV).

[1] H. Ibarh, *Physics of Surfaces and Interfaces* (Springer-Verlag, Berlin, Heidelberg, 2006).
[2] M. Z. Hasan and C. L. Kane, Rev. Mod. Phys. **82** (2010) 3045.
[3] A. F. Santander-Syro *et al.*, Nature **469** (2011) 189. and K. Yoshimatsu *et al.*, Science **333** (2011) 319.
[4] L. Pfeiffer *et al.*, Appl. Phys. Lett. **56** (1990) 1697.
[5] Y. Ohtsubo *et al.*, Phys. Rev. B **88** (2013) 245310.
[6] L. Walczak *et al.*, Surf. Sci. **608** (2013) 22.

BL5U, BL7U

Surface Electronic Structure of Kondo Insulator SmB_6(111)

Y. Ohtsubo[1, 2], K. Hagiwara[2], C. Wang[2], S. Ideta[3], K. Tanaka[3], F. Iga[4] and S. Kimura[1, 2]
[1]*Graduate School of Frontier Biosciences, Osaka University, Suita 565-0871 Japan*
[2]*Department of Physics, Graduate School of Science, Osaka University, Toyonaka 565-0043, Japan*
[3]*UVSOR Facility, Institute for Molecular Science, Okazaki 444-8585, Japan*
[4]*Department of Physics, Ibaraki University, Mito 310-0056, Japan*

Topological Kondo insulator (TKI) is a new group of topological materials. On the surface of TKI, robust topological surface state (TSS) disperses across a tiny energy gap owing to the strong correlation between itinerant and localized electrons (Kondo effect) [1]. Therefore, TKI phase is realized thanks to the synergetic effect between strong electron correlation and spin-orbit interaction (SOI), which results in the non-trivial parity eigenvalues across the Kondo gap. Since such synergetic effect can cause new exotic physical phenomena, such as superconductivity without inversion symmetry [2], the surface electronic structure of TKI is gathering much attention in these days.

So far, most of the experimental and theoretical studies about TKI have been performed on the (001) cleaved surface of SmB_6 and the surface state exhibits metallic dispersion and spin-polarization, which are the major characteristics of TSS [3-5]. Recently, we found a new TKI, YbB_{12} [6]. On the (001) clean surface of YbB_{12}, angle-resolved photoelectron spectroscopy (ARPES) showed a metallic surface state dispersing across the bulk Kondo gap and its orbital angular momentum (OAM) polarization that is often connected to spin polarization via SOI. For this study, we have established a method to obtain the clean surface of a group of Kondo insulators such as SmB_6 and YbB_{12} in situ without cleaving [7]. The clean surface preparation without cleaving also pave the way to observe the surface electronic states and its topology not only in cleavage planes but in general surfaces of the crystal. It is important to discuss the topological nature of the crystal from its surface states, because the topological order of the bulk crystal should govern the general character of the surface states without regarding detailed atomic structure and mirror indices of the surface plane.

In this project, we studied the electronic structure of the SmB_6(111) clean surface by ARPES. The clean surface of SmB_6(111) cannot be obtained by cleaving but was obtained *in-situ* by heating the single crystal up to 1600 K in an ultra-high vacuum chamber. The quality of the clean surface was evaluated by the sharp and low-background electron diffraction patterns as well as sharp photoelectron spectra itself.

Figure 1 shows the ARPES result indicating the highly dispersive itinerant states which exhibits clear hybridization with nearly localized 4f states lying just below the Fermi level. The hybridized state disperses across the Kondo gap and clearly indicates the metallic dispersion across the Fermi level at the same time. It strongly suggests its topological origin since the similar surface states are expected to appear on different surfaces of the same TKI crystal. Further analysis to understand the topological origin and whole picture of the topological electronic states of SmB_6 is in progress.

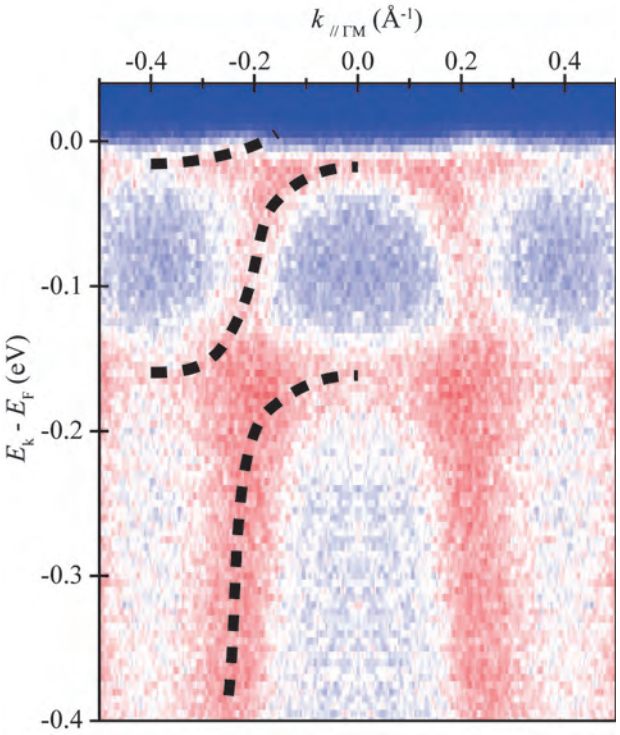

Fig. 1. Surface band dispersion of the SmB_6(111) clean surface observed by ARPES at 13 K ($h\nu$ = 26 eV). Dashed lines are guides to the eye. The ARPES intensities are symmetrized with respect to k = 0 Å^{-1}.

[1] M. Dzero *et al.*, Phys. Rev. Lett. **104** (2010) 106408.
[2] E. Bauer *et al.*, Phys. Rev. Lett. **92** (2004) 027003.
[3] N. Xu *et al.*, Phys. Rev. B **88** (2013) 121102(R).
[4] M. Neupane *et al.*, Nature Commun. **4** (2013) 2991.
[5] J. Jiang *et al.*, Nature Commun. **4** (2013) 3010.
[6] K. Hagiwara, Y. Ohtsubo *et al.*, Nature Commun. **7** (2016) 12690.
[7] K. Hagiwara, Y. Ohtsubo *et al.*, Proc. SCES 2016.

BL5U

Electronic Structure of a (1×1) VO Film on Ag(100): Soft X-ray Photoelectron Spectroscopy Study

Y. Sugizaki[1], H. Motoyama[1] and K. Edamoto[1, 2]
[1]*Department of Chemistry, Rikkyo University, Tokyo 171-8501, Japan*
[2]*Research Center for Smart Molecules, Rikkyo University, Tokyo 171-8501, Japan*

The mechanism of metal-insulator transitions (MITs) in vanadium oxides has been a matter of ongoing controversy for decades. The discussion has been focused on whether the transition is triggered by an electron-lattice interaction (Peierls-type model) or by an electron-electron interaction (Mott-type model), and a vast amount of studies have been performed on the electronic structures of vanadium oxides (mostly VO_2 and V_2O_3). However, very limited information is available on the electronic structure of vanadium monoxide (VO) at present, and it is not clear whether MIT also occurs in VO or not. This is primarily because it is hard to synthesize a VO single-crystal in an atmospheric condition, which makes it difficult to make an experimental study on the electronic structure of VO. Recently we found that a VO(100) single-crystal film can be formed on Ag(100) by reactive deposition of V atoms [1], which would enable the detailed spectroscopic studies on the electronic structure of this substance. In this study, we performed a high-resolution PES study for the VO(100) film on Ag(100).

Experiments were performed at BL-5U of the UVSOR Facility, Institute for Molecular Science. The spectra presented below were measured at the photon energy of 54 eV. In this study, the estimation of the Fermi edge is primarily important, and it was estimated by fitting the spectrum of a gold film attached to the sample holder in the Fermi edge region using Gaussian convoluted Fermi distribution function. The VO(100) film was prepared by electron beam deposition of V atoms in O_2 at 3.0×10^{-7} Pa and subsequent annealing at 450°C for 30 min.

Figure 1. shows the valence band PES spectrum of the VO film on Ag(100) measured at room temperature (red line) and that at 4.86 K (blue line). The band observed at 0 - 4 eV is ascribed to a V 3*d* band, and the band at 4 – 10 eV is ascribed to a V 3*d* – O 2*p* hybrid band (valence band) overlapping with a 4*d* band of the underlying Ag substrate. We measured magnified spectra in the vicinity of the Fermi level (E_F) at both temperatures, and confirmed that there is a clear cut-off in both spectra. The positions of the cut-off were carefully determined by fitting the spectra using Gaussian convoluted Fermi distribution functions, and it was confirmed that the cut-off positions were identical to that observed in the spectrum of the gold film. These results imply that VO in the ground state should have a metallic electronic structure. It has been controversial whether the ground state of VO is a metal or an insulator; for example, Yamazaki et al. made a theoretical study using the energy band calculations utilizing GW approximation and predicted that VO has a metallic nature [2], while Mackrodt et al. proposed that VO in the ground state is a Mott-Hubbard type insulator using a hybrid DFT calculations [3]. We think that the long-standing controversy is settled by the result of the present PES study. In addition, it is found that VO has a metallic nature in the temperature range of 4,86 K – room temperature. This result suggests that MIT does not occur in VO unlikely to the case of other vanadium oxides.

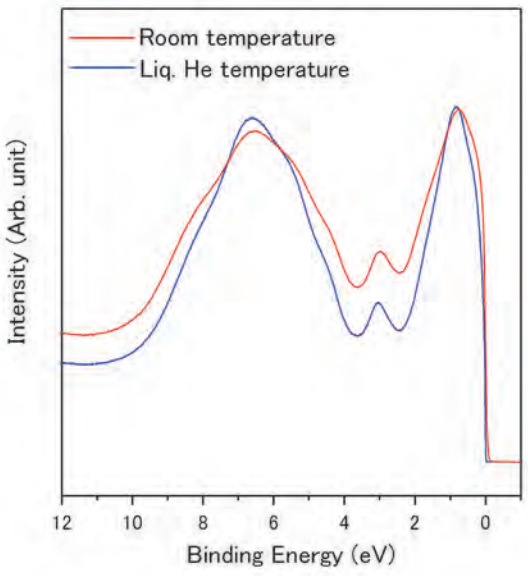

Fig. 1. The PES spectrum of the VO(100) film on Ag(100) measured at room temperature (red line) and that at 4.86 K (blue line) (*hv* = 54 eV).

[1] T. Nakamura *et al.*, Jpn. J. Appl. Phys. **55** (2016) 075501.
[2] A. Yamasaki and T. Fujiwara, Phys. Rev. B. **66** (2002) 245108.
[3] W. C. Markrodt *et al.*, Phys. Rev. B. **69** (2004) 115119.

BL5B

Vacuum Ultra-Violet Absorption Spectra of Amorphous Chalcogenide Semiconductor Thin Films

K. Hayashi

Department of Electrical, Electronic and Computer Engineering, Gifu University, Gifu 501-1193, Japan

Amorphous chalcogenide semiconductor materials, such as a-As_2S_3, a-As_2Se_3 and a-Se etc., show a variety of photo-induced phenomena. Therefore, these materials are expected as materials for optoelectronic devices. A lot of work have been done on the photo-induced phenomena of these amorphous semiconductor materials and various mechanisms have been proposed for these photo-induced phenomena [1-3]. However, the details of the mechanisms are still unknown. For device applications, it is necessary to sufficiently understand the fundamental properties of these materials. These phenomena were studied by exciting outer core electrons with the irradiation of light with the energy corresponding to the optical bandgap or sub-bandgap. The interest has been attracted for the change of the optical properties in the energy region of the visible light. We are interesting for the changes of the optical properties in the higher energy region. To our knowledge, little attention has been given to photo-induced changes at the vacuum ultra-violet (VUV) absorption spectrum. In this report, we measure the VUV absorption spectra on as-deposited evaporated amorphous As_xSe_{1-x} (for x=0.3, 0.4 and 0.5) thin films.

Samples used for the measurement of the VUV absorption spectra were amorphous As_xSe_{1-x} (for x=0.3, 0.4 and 0.5) thin films prepared onto aluminum thin films by conventional evaporation technique. Using different bulk glass of the composition as a source material, different amorphous film of the compositions was prepared. Typical thickness of the amorphous film and the aluminum film were around 200 nm and 100 nm, respectively. The aluminum film of the thickness of 200 nm was also used in order to eliminate the higher order light from the monochromator in the VUV region. The measurements were carried out at room temperature at the BL5B beam line of the UVSOR facility of the Institute for Molecular Science. And the spectrum was measured by using the silicon photodiode as a detector. Two pinholes of 1.5 mm in a diameter were inserted between the monochromator and sample to remove stray light. The intensity of the VUV light was monitored by measuring the total photoelectron yeild of a gold mesh. The positions of the core levels for the samples were calibrated by referencing to the 2*p* core level absorption peak of the aluminum film.

Figure 1 shows the VUV absorption spectra of as-deposited amorphous As_xSe_{1-x} (for x=0.3, 0.4 and 0.5) thin films in the energy region from 40 to 60 eV. Two main absorption peaks were observed in this energy region. One absorption peak around 44 eV corresponds to the 3*d* core level of arsenic atom. Another absorption peak around 56 eV corresponds to the 3*d* core level of selenium atom. The broad structures observed in the absorption spectra consist of two or more components. The origin of each component is not clear now. I would like to clarify the origin of each component in the future. As shown in figure, the ratio of the two main absorption peaks changes depending on composition of the film. The spectrum shape also changes depending on composition of the film. We think that those changes are related to the local structures of the amorphous network. We will observe the composition dependence of the change in the spectrum before and after irradiation of light in future. And we are going to investigate the relations between those changes.

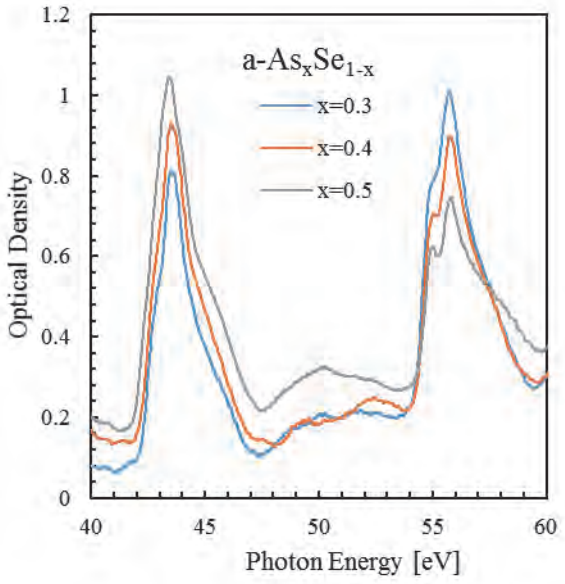

Fig. 1. VUV absorption spectra of as-deposited amorphous As_xSe_{1-x} (for x=0.3, 0.4 and 0.5) thin films in the energy region from 40 to 60 eV.

[1] K. Tanaka, Rev. Solid State Sci. **4** (1990) 641.
[2] K. Shimakawa, A. Kolobov and S. R. Elliott, Adv. Phys. **44** (1995) 475.
[3] K. Tanaka, Encyclopedia of Nanoscience and Nanotechnology **7** (2004) 629.

BL6U

Electronic Structures of Two-dimensional Alloys of Silicon and Germanium

A. Fleurence[1], C. Huet[1], S. Wallace[1], F. Wiggers[3], H. Yamane[2], N. Kosugi[2] and Y. Yamada-Takamura[1]

[1]*School of Materials Science, Japan Advanced Institute of Science and Technology, Nomi 923-1292, Japan*
[2]*Institute for Molecular Science, Okazaki 444-8585, Japan*
[3]*MESA+ Institute for Nanotechnology, University of Twente, 7500 AE Enschede, The Netherlands*

Silicene and germanene are honeycomb lattices made of Si and Ge atoms, respectively, with buckled structures due to the mixed sp^2/sp^3 hybridization in their chemical bondings [1]. The electronic structures calculated for free-standing silicene and germanene both exhibit Dirac cone regardless of the buckling [1].

Although silicon-germanium alloys with diamond structure are known as isomorphous system, up to now, there is no experimental study for their two-dimensional (2D) counterparts.

Silicene and germanene exist only in epitaxial forms. Among them, epitaxial silicene on ZrB_2 thin films grown on Si(111) has the particularity to form in a spontaneous and self-terminating way by segregation of Si atoms from the silicon substrate [2]. Epitaxial silicene forms a ZrB_2(0001)-(2×2) reconstruction and is semiconducting as a 350 meV-wide gap is opened in the Dirac cones.

We had demonstrated by means of low energy electron diffraction (LEED) and scanning tunneling microscopy at our home laboratory that the deposition of germanium on silicene can give rise to silicene-germanene heterostructures, 2D silicene-Ge alloy in the form of Ge incorporation into the silicene lattice, and vertical silicene-germanene heterostack structures, depending on the preparation conditions [3]. The experiments carried out at UVSOR were aimed at getting insights into (i) how Ge atoms are integrated in the silicene lattice and heterostacks, and (ii) what their electronic band structures are.

Water-cooled mini K-cell, which we use for the experiments in our home-based setup, was installed in the preparation chamber of BL6U for evaporating Ge. Epitaxial silicene samples were prepared on-site by annealing ZrB_2/Si(111) samples at 800ºC under ultrahigh vacuum [2]. Ge deposition was realized with a substrate temperature of 350°C.

For low Ge coverages giving rise to silicene-Ge alloy, no significant change in the Si2*p* core-level spectrum are observed and the structure remains ZrB_2(0001)-(2×2)-reconstructed. The Ge core-level (Fig1.(a)) shows a single component which indicates that the Ge atoms are incorporated in a unique site in the silicene lattice. Angle-resolved photoemission spectroscopy (ARPES) spectra (Fig. 1 (b)) indicate that the band structure is essentially the same as that of pristine silicene. In contrast, for coverage beyond 0.2 ML Ge, a complex LEED pattern and a different core-level spectrum (Fig. 1 (c)) suggests a more drastic transformation of the silicene structure related to the growth of a Si-Ge heterostack.

This work was supported by the Joint Studies Program (No. 203, 2016-2017) of the Institute for Molecular Science.

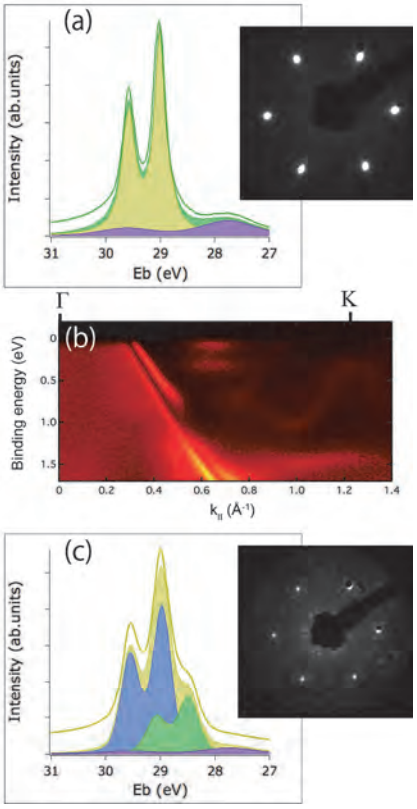

Fig. 1. (a): Ge 3*d* core-level ($h\nu$ = 80 eV) and ZrB_2(0001)-(2×2) LEED pattern (E_B = 40 eV) after deposition of 0.06 ML Ge. (b): ARPES spectra after deposition of 0.04 ML Ge ($h\nu$ = 43 eV). (c): Ge 3*d* core-level ($h\nu$ = 80 eV) and LEED pattern (E_B = 40 eV) after deposition of 0.41 ML Ge. All the measurements were carried out at room temperature.

[1] K. Takeda and K. Shiraishi, Phys. Rev. B **50** (1994) 14916.
[2] A. Fleurence *et al.*, Phys. Rev. Lett. **108** (2012) 245501.
[3] Y. Awatani, A. Fleurence and Y. Yamada-Takamura, Bulletin of the American Physical Society, 2016 March Meeting, T1.307.

BL6U

Bilayer Silicon on ZrB_2(0001)

A. Fleurence[1], F. Wiggers[2], S. Wallace[1], C. Huet[1], H. Yamane[2], N. Kosugi[2] and Y. Yamada-Takamura[1]

[1]*School of Materials Science, Japan Advanced Institute of Science and Technology, Nomi 923-1292, Japan*
[2]*MESA+ Institute for Nanotechnology, University of Twente, 7500 AE Enschede, The Netherlands*
[3]*Institute for Molecular Science, Okazaki 444-8585, Japan*

The experimental observation of silicene provides an evidence that silicon can crystallize in a graphitic form with chemical and physical properties different from those of bulk silicon in which Si atoms are sp^3 hybridized. Even though the graphene-like character of silicene was verified by the observation of π-electronic states [1], the hybridization of the Si atoms in silicene is not pure sp^2 as for C atoms in graphene, but adopts an intermediate sp^2/sp^3 hybridization reflected by the buckling of the honeycomb structure of free-standing silicene [2]. The resulting flexibility of silicene structure makes it less robust than graphene against its environment. Therefore, the possibility of stacking silicene layers in a manner similar to other layered materials such as graphite or chalcogenides is questionable.

It was recently claimed that multilayer silicene can be grown. In our group, we demonstrated that a bilayer silicon can be fabricated on ZrB_2(0001) thin films grown on Si(111) substrates by depositing silicon on the epitaxial silicene sheet that forms spontaneously on the ZrB_2(0001) surface [3]. The resulting bilayer silicon sheet has structural and electronic properties distinct from both silicene and bulk silicon: The bilayer silicon is metallic as the density of states at Fermi level is non zero [3] as shown by tunneling spectroscopy and preliminary characterizations of the band structure by angle-resolved photoemission spectroscopy (ARPES). Low-energy electron diffraction (LEED) pattern shows that the bilayer has a lattice parameter slightly larger than that of silicene. As a consequence, the ($\sqrt{3}\times\sqrt{3}$) unit cell of the bilayer does not commensurate with the (2×2) unit cell of ZrB_2(0001) as that of silicene does.

The purpose of this study was to get a comprehensive picture of the band structure of the Si bilayer by measuring high resolution ARPES spectra along both the Γ-K and Γ-M directions of the Brillouin zone of ZrB_2(0001).

Epitaxial silicene samples were prepared on-site by annealing ZrB_2/Si(111) samples at 800°C under ultrahigh vacuum [1]. Silicon was evaporated by heating a piece of silicon in front of the sample held at a temperature of 320°C. The formation of the bilayer is verified by the observation of features specific to the bilayer silicon in LEED pattern [3]. ARPES spectra were then recorded with a photon energy of $h\nu$=43 eV at a temperature of 20 K.

The parabolic band centered on the M point (which also corresponds to the K point of epitaxial silicene) is reminiscent of the π band observed for epitaxial silicene on ZrB_2(0001).

However, it is shifted upward by 200 meV. In addition, the band structure features several new bands crossing linearly at the Fermi level. The most intense band of these new bands intersect the Fermi level at a position slightly inward with respect to the M point of the Brillouin zone of ZrB_2(0001). This shift is consistent with a silicon structure with a lattice parameter slightly larger than that of epitaxial silicene as previously deduced from LEED patterns [3]. The mismatch between the ZrB_2(0001) unit cell and that of the bilayer silicon causes a back-folding of the linear bands which are replicated near the Γ and M points of the Brillouin zone.

These results may suggest that the silicon layers have slightly different lattice parameters that results in the decoupling of the topmost layer. This hypothesis will be investigated further by *ab-initio* calculations using the conclusions drawn from the experimental data as inputs.

This work was supported by the Joint Studies Program (No. 203, 2016-2017) of the Institute for Molecular Science.

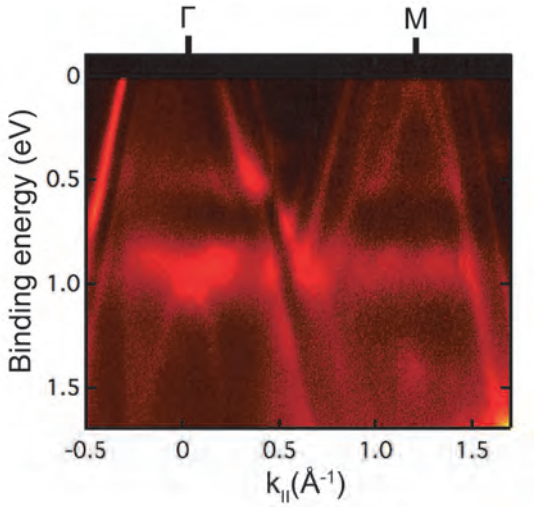

Fig. 1. ARPES spectra of the bilayer silicon along the Γ-M direction of the Brillouin zone of the ZrB_2(0001) recorded with $h\nu$ = 43 eV at 20K.

[1] A. Fleurence *et al.*, Phys. Rev. Lett. **108** (2012) 245501.
[2] S. Cahangirov *et al.*, Phys. Rev. Lett. **102** (2009) 236804.
[3] T. G. Gill *et al.*, 2D Mater. **4** (2017) 021015.

BL6U

Hydrogenation of Epitaxial Silicene on ZrB_2(0001)

A. Fleurence[1], T. Yonezawa[1], S. Wallace[1], S. Horibe[1], T. Kato[1], H. Yamane[2], N. Kosugi[2] and Y. Yamada-Takamura[1]

[1]*Japan Advanced Institute of Science and Technology, Nomi 923-1292, Japan*
[2]*Institute for Molecular Science, Okazaki 444-8585, Japan*

Silicene is a 2D Dirac material made of a Si honeycomb lattice [1]. However, in contrast to its analogue, graphene, for which the sp^2 hybridization of the orbitals makes the structure perfectly planar, the structure of silicene is buckled due to sp^2/sp^3 hybridization [1]. For this reason, it was predicted by theoretical calculations that the hydrogenation of silicene would have an even stronger effect on the structure of silicene than on that of graphene with the opening of a gap as wide as 1.2 eV [2].

ZrB_2 thin films grown on Si(111) has the particularity to promote the spontaneous formation of silicene by segregation of Si atoms from the substrate [3]. This epitaxial form of silicene has a structure in which all atoms but one are laying at the same height and one is protruding. The band structure is also affected as the Dirac cones are turned into parabolic bands [3].

Previous experiments confirmed that the hydrogenation of epitaxial silicene sheets on Ag(111) [4] and ZrB_2(0001) causes structural change of the silicene structures. In the latter case, this is reflected by a different electron energy dependence of the low-energy electron diffraction (LEED) pattern. The surface is ZrB_2(0001)-(2×2)-reconstructed as pristine silicene does, but for an electron energy (E_B) of 30 eV, the inner fractional spots are not visible anymore.

The purpose of the experiments carried out at BL6U was to get insights into the nature of the change induced by hydrogenation in the structure and the band structure of epitaxial silicene, which has not been reported yet. Si2*p* core-level spectra were recorded at different photon energies including a surface-sensitive photon energy of $h\nu$ = 130 eV. For Angle-resolved photoemission spectroscopy (ARPES), a photon energy of $h\nu$ = 43 eV were used.

Epitaxial silicene samples were prepared on-site by annealing ZrB_2/Si(111) samples at 800ºC under ultrahigh vacuum [3]. Silicene was hydrogenated at room temperature by means of a hot W filament used to crack H_2 molecules fed in the chamber through a leak valve. The complete hydrogenation of silicene was verified by the vanishing of the ZrB_2(0001)-(2×2) fractional spots in LEED pattern recorded with E_B = 30 eV. Fig. 1. (a) compares the Si2*p* core-level spectra recorded before and after hydrogenation of epitaxial silicene. It shows that hydrogenation causes a 0.2 eV shift of the Si2*p* core-level towards higher binding energies. The spectrum features two components broader than those of silicene. More surprisingly, the ARPES spectra shown in Figs. 1. (d) and (e) recorded around the K point of silicene show that all the silicene-related bands (visible between the Fermi level and E_B=1.5 eV) have faded upon hydrogenation whereas those of the ZrB_2 remained.

These results although insightful, suggest that further characterizations by scanning tunnel microscopy are required to determine whether the silicon structure remains two-dimensional upon hydrogenation.

This work was supported by the Joint Studies Program (No. 203, 2016-2017) of the Institute for Molecular Science.

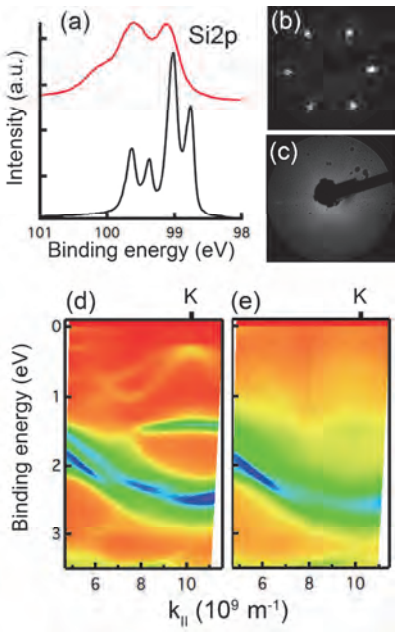

Fig. 1. (a) Si2*p* core-level spectra before (black) and after (red) hydrogenation. (b) and (c): LEED patterns corresponding respectively to the spectra. (d) and (e): ARPES spectra before and after hydrogenation around the K point of silicene. All the measurements were carried out at a temperature of 20K.

[1] K. Takeda and K. Shiraishi, Phys. Rev. B **50** (1994) 14916.
[2] M. Houssa *et al.*, Appl. Phys. Lett. **97** (2010) 112106.
[3] A. Fleurence *et al.*, Phys. Rev. Lett. **108** (2012) 245501.
[4] J. Qiu *et al.*, Phys. Rev. Lett. **114** (2015) 126101.

BL6U

Electronic Structure of GaSe Thin Films Grown on Ge(111) Wafers

T. Yonezawa[1], A. Fleurence[1], H. Yamane[2], S. Wallace[1], S. Horibe[1], T. Kato[1], N. Kosugi[2] and Y. Yamada-Takamura[1]

[1]*Japan Advanced Institute of Science and Technology, Nomi 923-1292, Japan*
[2]*Institute for Molecular Science, Okazaki 444-8585, Japan*

Gallium selenide (GaSe) belongs to a class of material called "metal chalcogenides" which is attracting a lot of interests as a two-dimensional semiconducting material, since a single layer of molybdenum disulfide (MoS_2) was made into a transistor [1]. Like graphite, layers of chalcogenides stack via weak van der Waals interaction, and these layers can be exfoliated easily using adhesive tapes, which is advantageous to prepare atomically-flat and clean surfaces. We are particularly interested in GaSe as a lattice-matching and less-interacting substrate for "silicene" which is a Si-version graphene [2], so that the combination will realize epitaxial silicene with the properties of those of free-standing one.

GaSe thin films used in this study were grown on Ge substrates by molecular beam epitaxy (MBE) method. Ge(111) wafers (undoped) were cleaned ultrasonically with acetone, ethanol, and deionized water. The substrates were then fixed to a molybdenum block with indium, and introduced into the MBE system via a load-lock. Surface oxides were removed by heating the substrates at 600°C under ultrahigh vacuum (UHV). Oxide-free surface kept at growth temperature of 525°C was first exposed to Se vapor for 30 seconds, and then GaSe growth was started by exposing the surface simultaneously to Ga vapor and Se vapor with a flux ratio of Ga/Se = 7/100 for 20 minutes. GaSe growth was monitored *in situ* by reflection high energy electron diffraction, and an epitaxial relationship of GaSe(0001)//Ge(111) and GaSe[11-20]//Ge[1-10] was determined.

For the GaSe thin film surface prepared by cleavage using adhesive tape at UVSOR prior to the introduction to the preparation chamber of BL6U via load-lock, we found traces of carbon in photoelectron spectroscopy results, which are not shown here. Seeing this result, the following measurements were carried out without this preparation process.

Angle-resolved photoemission spectroscopy (ARPES) was carried out on an as-grown GaSe thin film surface using a photon energy of 50 eV at room temperature. GaSe thin film sample was degassed at 300°C under UHV before the measurement. The results are plotted along the Γ-K direction of GaSe(0001), which is shown in Fig. 1. Clear double parabolic bands similar to what has been observed for cleaved GaSe single crystal [3] can be identified, but at larger binding energy indicating possible doping. The lack of feature at K point makes this surface an ideal substrate for free-standing-like silicene.

Raising annealing temperature to 500°C resulted in a change in the low energy electron diffraction (LEED) pattern. As shown in Fig. 2, additional spots appeared around original GaSe(0001)-(1x1) spots which corresponds well with Moiré constructed by GaSe(0001) and Ge(111). This change was associated with loss of oxygen from the surface and change in Ga- and Ge-related states observed by core-level photoelectron spectroscopy, indicating possible change at the film-substrate interface.

This work was supported by the Joint Studies Program (No. 203, 2016-2017) of the Institute for Molecular Science.

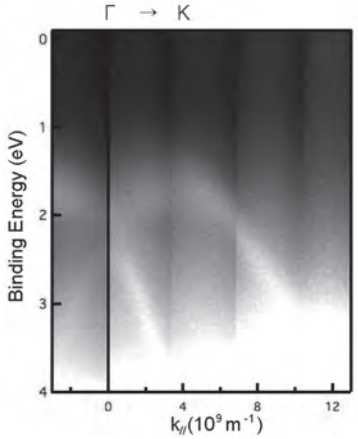

Fig. 1. ARPES spectra of GaSe thin film surface measured along Γ-K direction of GaSe(0001).

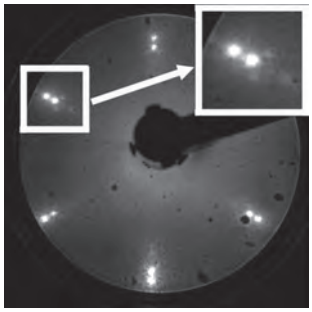

Fig. 2. LEED pattern of GaSe/Ge(111) sample surface showing spots corresponding to Moiré.

[1] B. Radisavijevic *et al*., Nat. Nanotechnol. **6** (2011) 147.
[2] A. Fleurence *et al*., Phys. Rev. Lett. **108** (2012) 245501.
[3] L. Plucinki *et al*., Phys. Rev. B **68** (2003) 125304.

BL6U

Epitaxial Silicene on h-BN Terminated ZrB_2 Thin Films

F. B. Wiggers[1], A. Fleurence[2], K. Aoyagi[2], T. Yonezawa[2], H. Yamane[3], Y. Yamada-Takamura[2], N. Kosugi[3], A. Y. Kovalgin[1] and M. P. de Jong[1]

[1] *MESA+ Institute for Nanotechnology, University of Twente, 7500 AE Enschede, The Netherlands*
[2] *Japan Advanced Institute of Science and Technology, School of Materials Science, Nomi 923-1292, Japan*
[3] *Department of Photo-Molecular Science, Institute for Molecular Science, Okazaki 444-8585, Japan*

Silicene is the silicon analogue of graphene, i.e. a two-dimensional (2D) silicon allotrope featuring an atomically buckled honeycomb-lattice. Theory predicts Dirac electrons and an electrically tunable spin-orbit bandgap of a few meV, leading to the topological quantum spin Hall phase [1]. However, these properties of free-standing silicene remain hypothetical, because so far only epitaxial silicene has been synthesized on metallic substrates such as Ag(111) [2], ZrB_2(0001) [3], Ir(111) [4], and ZrC(0001) [5], introducing non-negligible hybridization of electronic states and denying direct electrical characterization without complex processing.

The synthesis of silicene on insulating, weakly interacting substrates is therefore highly desired. Motivated by this, we studied the growth and properties of 2D silicon layers grown on the h-BN(0001)-terminated surface of a ZrB_2(0001) thin film on a Si(111) substrate. The h-BN terminated substrates were prepared ex-situ using plasma nitridation and annealing of epitaxial ZrB_2 films. Surface cleaning was performed at BL6U prior to silicene growth using annealing at about 800 °C to remove oxides. Silicon was deposited in steps by heating a Si strip by direct current. The resulting highly ordered 2D silicon layer on the h-BN terminated ZrB_2 surface was studied by LEED, ARPES, and core level PES.

It was found that the electronic structure of the so-obtained Si layer is very similar to that of epitaxial silicene on ZrB_2, which has been characterized previously [3]. Figure 1 shows the valence band structure as determined by ARPES measurements recorded with a photon energy of 50.5 eV. Besides ZrB_2 derived bands, characteristic Si-related bands can be identified centered around the K-point of the Si lattice, the most prominent of which is indicated by the dotted line. This particular electronic structure is virtually identical to that of silicene on ZrB_2, strongly suggesting that intercalation underneath the h-BN layer takes place. This conclusion is further supported by the Si 2*p* spectra (not shown). Interestingly, the h-BN layer has a negligible effect on the electronic structure of the silicene that it covers. This is promising for non-destructive capping of silicene, which is required for any analysis or application of silicene outside ultra-high vacuum.

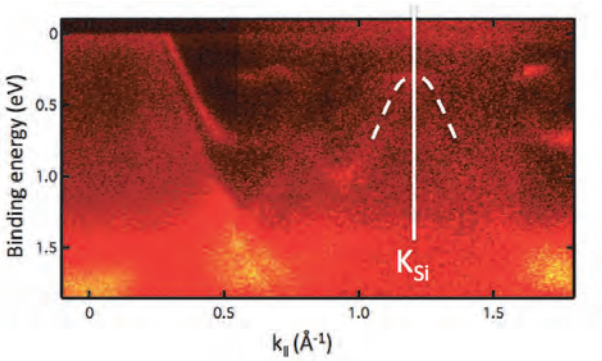

Fig. 1. ARPES spectra measured along the Γ-K direction of the 2D Si layer.

[1] M. Ezawa, New J. Phys. **14** (2012) 33003.
[2] P. Vogt, P. De Padova, C. Quaresima, J. Avila, E. Frantzeskakis, M. C. Asensio, A. Resta, B. Ealet and G. Le Lay, Phys. Rev. Lett. **108** (2012) 155501.
[3] A. Fleurence, R. Friedlein, T. Ozaki, H. Kawai, Y. Wang and Y. Yamada-Takamura, Phys. Rev. Lett. **108** (2012) 245501.
[4] L. Meng, Y. Wang, L. Zhang, S. Du, R. Wu, L. Li, Y. Zhang, G. Li, H. Zhou, W. A. Hofer and H.-J. Gao, Nano Lett. **13** (2013) 685.
[5] T. Aizawa, S. Suehara and S. Otani, J. Phys. Chem. C **118** (2014) 23049.

BL6U

Electronic Structure of Iron Phthalocyanine (I): Temperature-Dependent Interface-Specific Electronic State in Monolayer on Au(111)

H. Yamane[1, 2], A. Carlier[1, 3] and N. Kosugi[1, 2]
[1]*Institute for Molecular Science, Okazaki 444-8585, Japan*
[2]*The Graduate University for Advanced Studies (SOKENDAI), Okazaki 444-8585, Japan*
[3]*Department of Physics, University of Namur, Namur B-5000, Belgium*

Iron phthalocyanine (FePc) is well known as one of important organic semiconductors with unique electronic and magnetic properties. Among them, it was found that FePc molecule on Au(111) exhibits unique Kondo effects depending strongly on the adsorption configuration, e.g., ontop site at 2.6±1.4 K and bridge site at 110~150 K [1]. In the present work, in order to investigate the change in the electronic structure introduced by the Kondo effect, we have applied angle-resolved photoemission spectroscopy (ARPES) to the FePc monolayer on Au(111).

The experiment was performed at the in-vacuum undulator beamline BL6U. The clean Au(111) surface was obtained by the repeated cycles of the Ar^+ sputtering and the subsequent annealing at 700 K, as confirmed by the low-energy electron diffraction (LEED) and the Shockley state in ARPES. The ordered monolayer was obtained by flashing the FePc thin multilayer on Au(111) at 470 K.

Figure 1 shows the photoemission angle (θ) dependence of the ARPES spectra measured for the FePc monolayer on highly oriented pyrolytic graphite (HOPG) and on Au(111) at 20 K using hv = 45 eV. At the FePc/HOPG interface, the C 2*p*- and Fe 3*d*-derived peaks appear at the binding energy of 1.2 eV and 1.5 eV, respectively. The large background observed at θ = 30° originates from the π band of HOPG. The Fe 3*d* intensity is getting stronger than the C 2*p* intensity when $h\nu$ > 60 eV (not shown) as observed for the gas phase [2]. On the other hand, at the FePc/Au(111) interface, the C 2*p* peak at 0.7 eV exhibits the clear θ dependence with the intensity maximum at θ = 32° ($\boldsymbol{k} \approx 1.7$ Å^{-1}), while no clear Fe 3*d*-derived peaks appear below the C 2*p*-derived peak, as observed at the CoPc/Au(111) interface [3], indicating the modification of the Fe 3*d* orbital with the Au(111) surface. It is worthy of note here that a quite weak peak is appeared below the Fermi level (E_F) but is not observed at the clean Au(111) surface.

Figure 2 (a) shows the temperature dependence of ARPES at $\boldsymbol{k} \approx 1.7$ Å^{-1} for the FePc/Au(111) interface. With decreasing the temperature, the Fermi edge is getting sharpened and the interface-specific peak at 0.12 eV is getting visible. The difference ARPES spectrum between 30 K and 240 K shown in Fig. 2 (b) indicates the presence of the temperature-dependent interface states at 0 eV and 0.12 eV, which disappear at *ca.* 160 K. The increase in the density of states at E_F is the indication of the Kondo resonance, as reported in Ref. [1], which may also introduce the formation of the interface state observed at 0.12 eV.

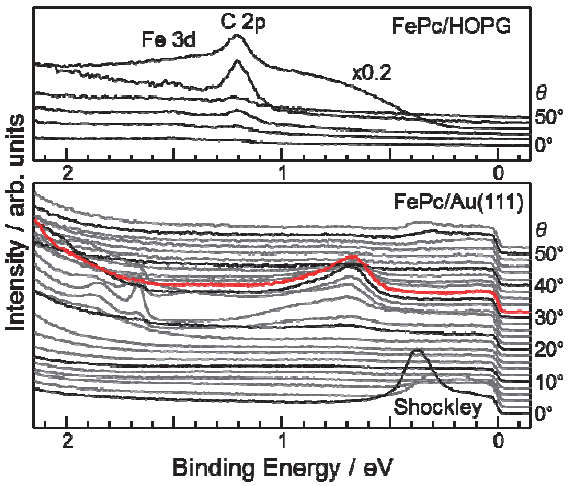

Fig. 1. Photoemission angle (θ) dependence of ARPES ($h\nu$ = 45 eV) measured for the interfaces of FePc/HOPG and FePc/Au(111) at 20 K.

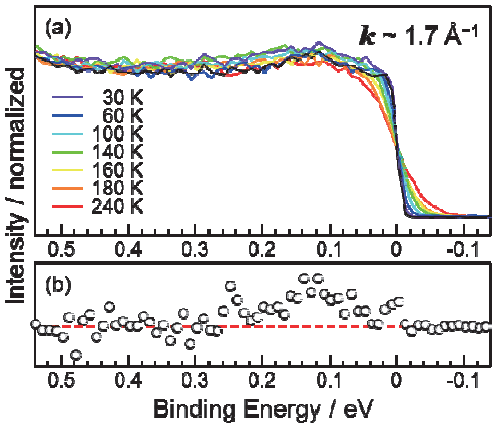

Fig. 2. (a) Temperature dependence of ARPES at $\boldsymbol{k} \approx 1.7$ Å^{-1} measured for the FePc/Au(111) interface. (b) Difference spectrum between 30 K and 240 K, which is obtained after the substrate-background subtraction and the smoothing.

[1] E. Minamitani *et al.*, Phys. Rev. Lett. **109** (2012) 086602.
[2] B. Brena *et al.*, J. Chem. Phys. **134** (2011) 074312.
[3] H. Yamane and N. Kosugi, J. Phys. Chem. C **120** (2016) 24307.

BL6U

Electronic Structure of Iron Phthalocyanine (II): Intermolecular Electronic Band Dispersion in Crystalline Multilayer

H. Yamane[1, 2], A. Carlier[1, 3] and N. Kosugi[1, 2]
[1]*Institute for Molecular Science, Okazaki 444-8585, Japan*
[2]*The Graduate University for Advanced Studies (SOKENDAI), Okazaki 444-8585, Japan*
[3]*Department of Physics, University of Namur, Namur B-5000, Belgium*

The intermolecular electronic band dispersion, originating from the periodicity of the molecular stacking structure, is essential to investigate the charge transport mechanism related to organic electronics. Recently, we have succeeded in precise observation of the quite weak intermolecular band dispersion for crystalline films of phthalocyanines [MPc, M = metal or H_2 (metal free)], such as MnPc, CoPc, ZnPc, F_{16}ZnPc and H_2Pc, by angle-resolved photoemission spectroscopy (ARPES) [1]. In this work, we have investigated the intermolecular band dispersion of the FePc crystalline film, which is difficult to observe precisely with respect to the other MPc films since the C 2*p* and Fe 3*d* energies are close to each other.

The experiment was performed at the in-vacuum undulator beamline BL6U. The cleanliness of the Au(111) surface was confirmed by the low-energy electron diffraction (LEED) and the Shockley state in ARPES, as obtained from the repeated cycles of the Ar^+ sputtering and the subsequent annealing at 700 K. The FePc multilayer is obtained by the vacuum deposition of purified FePc molecules onto the Au(111) as kept at 350 K.

Figure 1 shows the incident angle (α) dependence of N K-edge X-ray absorption spectra for the 300-Å-thick FePc films on Au(111). The sharp $1s \rightarrow \pi^*$ transition peaks appear at $h\nu$ = 398-405 eV. These peaks are strongest at grazing incidence (α = 70°) and are getting weaker with decreasing α, except for peak X at 399 eV due to the hybridization with Fe 3*d* orbital. Other broad $1s \rightarrow \sigma^*$ transition features ($h\nu$ > 405 eV) show the opposite polarization dependence. Furthermore, the FePc multilayer shows the clear LEED pattern as shown in the inset of Fig. 2. These evidences indicate that the FePc molecules on Au(111) form the flat- lying ($\beta \approx 0°$) crystalline film.

Figure 2 shows the photon energy ($h\nu$) dependence of the normal-emission ARPES spectra for the FePc crystalline film. Since the FePc crystalline film on Au(111) shows a Stranski-Krastanov growth mode, there are remanent substrate signals such as the Fermi edge, which we used for the fine $h\nu$ calibration. The topmost peak exhibits two components derived from the C 2*p* and Fe 3*d* orbitals as labeled in Fig. 2. The relative peak intensity between C 2*p* and Fe 3*d* is dependent on $h\nu$, which is slightly different from the case in the gas-phase FePc [2]. This difference can be ascribed to the weak intermolecular orbital overlap between C 2*p* and Fe 3*d*.

The C 2*p* peak shows a dispersive behavior with $h\nu$, while the Fe 3*d*-derived peak does not show such a behavior. This indicates the presence of the relatively strong intermolecular π-π interaction with the transfer integral of 25-30 meV and the localization of the Fe 3*d*-derived electronic state. The detailed lineshape analysis of the ARPES peak for the energy-*versus*-wavevector relation is now in progress.

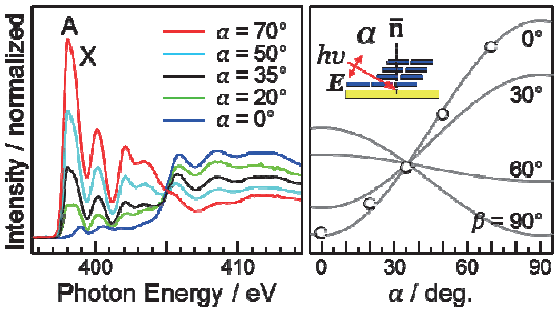

Fig. 1. Incident angle (α) dependence of N K-edge X-ray absorption spectra and the intensity plot of peak A for the FePc crystalline film at 20 K.

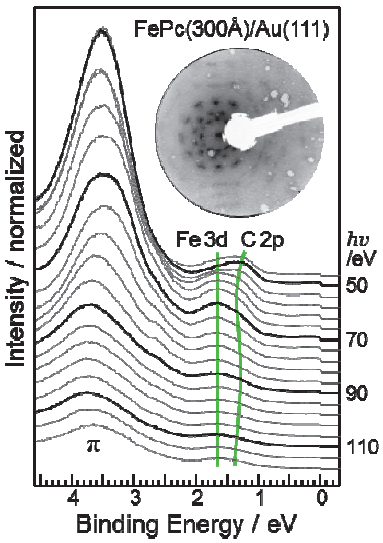

Fig. 2. $h\nu$-dependent ARPES spectra at the normal emission and the LEED image (E = 60 eV) for the FePc crystalline film at 20 K.

[1] H. Yamane and N. Kosugi, Phys. Rev. Lett. **111** (2013) 086602.
[2] B. Brena *et al.*, J. Chem. Phys. **134** (2011) 074312.

BL6U

Large Intermolecular π-Band Dispersion in Crystalline Films of Hexa-Peri-Hexabenzocoronene on Graphite(0001)

H. Yamane[1, 2] and N. Kosugi[1, 2]
[1]*Institute for Molecular Science, Okazaki 444-8585, Japan*
[2]*The Graduate University for Advanced Studies (SOKENDAI), Okazaki 444-8585, Japan*

Polycyclic aromatic hydrocarbons, e.g., hexa-*peri*-hexabenzocoronene (HBC) used in the present work, have attracted attention as a fragment of graphene. It has been reported that the HBC films on a highly oriented pyrolytic graphite (HOPG) exhibit a new substrate-induced polymorph, where all molecules adopt a recumbent orientation with planar π-stacking [1]. In the present work, we have investigated the presence of the intermolecular π-band dispersion in the HBC multilayer grown on a single crystalline graphite(0001) surface by means of angle-resolved photoemission spectroscopy (ARPES).

The experiment was performed at the in-vacuum undulator beamline BL6U. The single crystalline graphite(0001) surface was obtained by heating the nitrogen-doped 6H-SiC(0001) wafer based on the stepwise surface treatment [2]. The crystallinity of the graphite(0001) surface was confirmed by the low-energy electron diffraction (LEED).

The LEED image of the 250-Å-thick HBC crystalline multilayer on graphite(0001), displayed in the inset of Fig. 1, shows a sharp diffraction pattern, together with the incident-energy-dependent multiple scattering spots. We found that the diffraction pattern of the HBC multilayer agrees well with that of the HBC monolayer (not shown), and that the multiple scattering spots are not observable in the HBC monolayer, indicating the highly-ordered layer-by-layer growth of the HBC molecules on graphite(0001).

Figure 1 shows the photon energy (*hv*) dependence of the normal-emission ARPES spectra measured for the HBC multilayer on graphite(0001) at 20 K and 300 K. At 20K, the topmost valence band shows a large dispersion as 220 meV with *hv*. This dispersion is observable even at 300 K, indicating the presence of the stable and strong intermolecular π-stacking.

Figure 2 shows the energy-*vs*.-wavevector (*E*-***k***) map of the HBC multilayer on graphite(0001) at 20 K, which is obtained from the second-derivative curves of the normal-emission ARPES spectra in Fig. 1. The dispersion periodicity gives the intermolecular distance a = 3.369 Å, which is slightly larger than that of the graphite (a = 3.335 Å). The tight-binding fitting to the topmost band dispersion gives the intermolecular transfer integral t = 55 meV. Similar evidence is observable for the case of the HOPG substrate (not shown).

The present observation clearly indicates that the band-like hole transport can be realized in the new polymorphs of HBC on graphite.

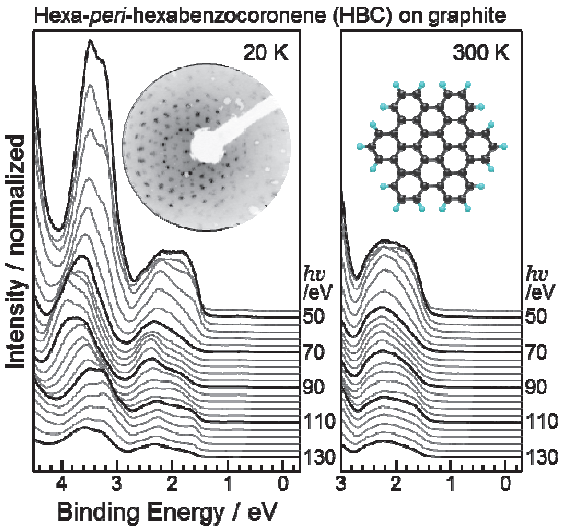

Fig. 1. Photon energy dependence of the normal-emission ARPES spectra for the HBC multilayer on graphite(0001) at 20 K and 300 K. The LEED image measured at E = 40 eV is show in the inset.

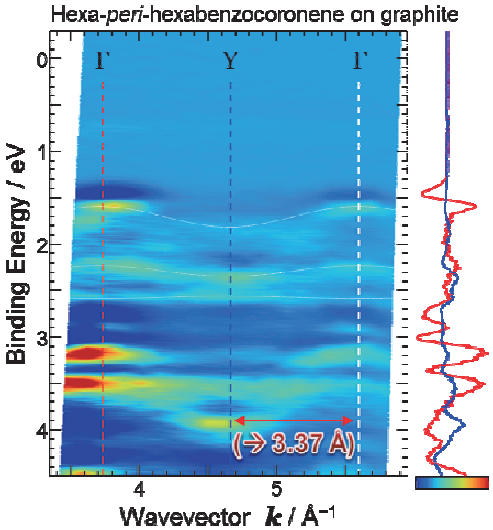

Fig. 2. *E*-***k*** map of the HBC multilayer on graphite (0001) at 20 K, obtained from the second derivatives of the normal-emission ARPES data. For the ***k*** conversion, we used the inner potential V_0 as −3.0 eV.

[1] P. Beyer *et al.*, ACS Appl. Mater. Interfaces **6** (2014) 21484.
[2] I. Forbeaux, J.-M. Themlin and J.-M. Debever, Phys. Rev. B **58** (1998) 16396.

BL6U

Origin of the Interface State at the Tetraphenyldibenzoperiflanthene Monolayer on Ag(111)

R. Shiraishi[1, 2], K. Yonezawa[2], T. Yamaguchi[1, 2], T. Ueba[1, 2], H. Yamane[1, 2], N. Kosugi[1, 2] and S. Kera[1, 2]

[1]*The Graduate University for Advanced Studies (SOKENDAI), Okazaki 444-8585, Japan*
[2]*Department of Photomolecular Science, Institute of Molecular Science, Okazaki 444-8585, Japan*

Strong modification of the electronic property in π-conjugated molecules adsorbed on a metal substrate has been reported, for example, 2D band dispersion, Kondo effect, and so on. These phenomena are induced by the hybridization of the electronic wave function between the molecule and the metal surface. Thus, the formation mechanism of the interface state has attracted attention for a long time.

Tetraphenyldibenzoperiflanthene (DBP, Fig. 1 (a)) is an interesting molecule for investigating the hybridized state between molecule and metal surface, because the molecule is lying-flat on the substrate and its large π-conjugated plane is expected to be far apart from the surface due to its phenyl rings. We reported DBP forms a well-ordered monolayer (ML) film on Ag(111) [1]. Here the interfacial electronic state of DBP(ML)/Ag(111) is investigated by angle-resolved ultraviolet photoelectron spectroscopy (ARUPS).

As shown in Fig. 1 (b), while UPS spectra of the gas phase and the ML film on HOPG show similar features due to weak interaction, the ML on Ag(111) shows the shift and broadening of these features. Moreover, no significant feature around the Fermi level and an additional feature at 1.4 eV are detected for DBP/Ag (111). The secondary cut-off of the DBP ML becomes lower by 0.8–1.0 eV than that of a clean Ag(111). The *negative* shift is more significant than that due to electron push-back effect of Xe/Ag (~0.5 eV) [2]. In general, hybridized states in many organic/metal systems appear as the filled LUMO. However, this assumption is hardly applicable to the case of DBP/Ag (111), because the electron transfer from the substrate to the LUMO would contribute *positive* surface potential shift. Therefore we concluded that these interface states (I_1-I_4) are caused by a hybridization between DBP and Ag(111) , hence the HOMO region is largely affected to give bonding and antibonding features of I_1 and I_2. The features I_3 and I_4 are described to HOMO-1(-2) and HOMO-3(-4) derived states, respectively.

This conclusion is further confirmed by the comparison of photoelectron angular distribution (PAD) between experiment and simulation [3]. In Fig. 1 (c) left, the azimuthal dependence of the I_1 and I_2 region is shown. Fig. 1 (d) shows the calculated PAD for HOMO and LUMO of a free molecule by multiple scattering theory. In Fig. 1 (c) right, the experimental intensities of I_1 and I_2 are compared to the theoretical simulations of HOMO and LUMO taken from Fig. 1 (d). The experimental pattern of I_1 (blue circle) well agrees with the simulation of the HOMO (black line), rather than that of the LUMO (red line). A deviation of experimental data from the simulation might reflect a spatial modulation of the HOMO due to the hybridization with the substrate band which is not taken into account for the present calculation.

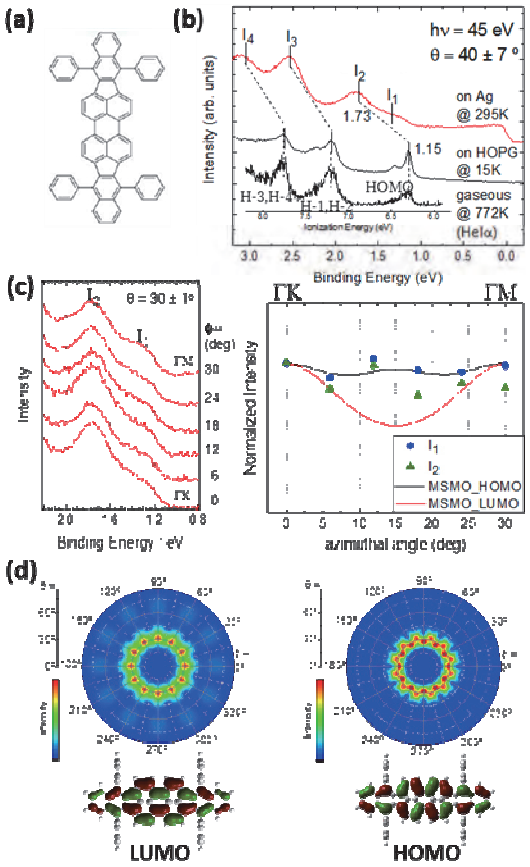

Fig. 1. (a) Chemical structure of DBP. (b) UPS of gaseous DBP (bottom), ML on graphite (middle), and ML on Ag(111) (top). (c) azimuthal ARUPS (left) and a comparison between experimental and theoretical pattern of HOMO and LUMO. All the intensity were normalized at φ = 0° for comparison. (d) PAD simulation of HOMO/LUMO for an isolated DBP. Two differently oriented molecules in a unit cell [1] and the (111) surface symmetry were considered.

[1] T. Kirchhuebel *et al.,* Langmuir **32** (2016) 1981.
[2] K. Wandelt *et al.,* Surf. Interf. Anal. **12** (1988) 15.
[3] S. Nagamatsu *et al*., e-J. Surf. Sci. Nano. **3** (2005) 461.

BL7U

On the Long-wavelength Approximation in the Photoelectric Effect

Y. Ishida[1], S. Ideta[2], K. Tanaka[2] and S. Shin[1]
[1]*ISSP, University of Tokyo, Chiba 444-8585, Japan*
[2]*UVSOR, Institute for Molecular Science, Okazaki 444-8585, Japan*

A long-wavelength approximation is often assumed *a priori* when the interaction between light and matter is concerned. The assumption, however, may be strongly invalidated in the surface region at the atomic scale particularly when the photon energy is low [1]. Here, we test the validity of the assumption in the photoelectric effect.

When the long-wavelength approximation is valid, the electrons subjected to the photon field $\boldsymbol{A}$ cannot sense the direction of the light propagation. The validity can thus be tested by investigating whether or not the angular distribution of photoelectrons depends on the direction of the incident light. Figure 1 (a) shows the setup for the test. The incident light is *s*-polarized, and the angular distribution of the photoelectrons are investigate by the analyzer [2]. In this configuration, it is only the direction of the light that breaks the mirror symmetry of the setup with respect to the plane spanned by the *s*-polarization vector and surface normal of the sample. The photoelectron distribution thus becomes asymmetric (symmetric) with respect to the geometrical mirror plane when the photoelectric effect is susceptible (unsusceptible) to the propagation vector. Note, we adopt the scalar gauge.

In the setup, the following two conditions are also imposed on the sample side: (1) The sample should not break the mirror symmetry of the geometry; (2) Near the surface Γ point, the sample has to have surface localized states, because they can strongly overlap to the photon field in the surface region that is under investigation. To this end, we chose highly-oriented Bi microcrystals grown on a highly-oriented pyro-graphite for the sample [3]. The Bi microcrystals are randomly oriented in plane with their 111 face oriented normal to surface, so that the effect of the crystal symmetry is averaged out in the azimuth. In other words, the sample has a high symmetry of C_∞. In addition, Bi(111) harbors Rashba-split surface states around the surface Γ point.

Figure 1 (a) shows the angular distribution of photoelectrons $I(E_B, \alpha)$ emitted from the highly-oriented Bi(111) microcrystalline thin film with the incidence of 17 eV light. Here, E_B and α are the binding energy and the emission angle, respectively. Clear dispersions are observed: The structures in [~0.1, 0 eV] are mainly due to the Rashba-split surface states. In order to investigate whether the distribution is symmetric about $\alpha = 0$, we show in Figure 2 (b) $\Delta_{sym}(E_B, \alpha) \equiv I(E_B, \alpha) - I(E_B, -\alpha)$. We observe some asymmetric distributions from the photoelectrons emitted from the Rashba bands, as well as those from the states occurring below 0.3 eV. Thus, the photoelectron distribution senses the direction of the incident light.

Based on the jellium model, the breakdown occurs only for *p*-polarized component of $\boldsymbol{A}$ [1]. The present results indicating that the approximation is broken even in the *s*-polarized case thus calls for a description beyond. We note that the three-slab model often used in the field of surface nonlinear optics can qualitatively explicate the phenomena.

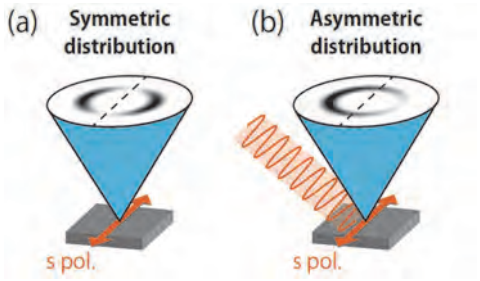

Fig. 1. Experimental geometry for testing the long-wavelength approximation in the photoelectric effect. When the long-wavelength approximation is valid, a mirror-symmetric photoelectron distribution is expected (a); if not valid, or when the direction of the incident light matters, the angular distribution becomes asymmetric (b).

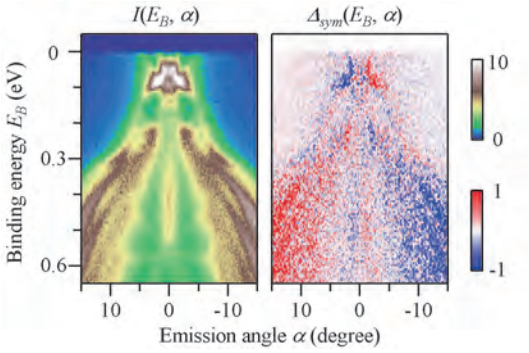

Fig. 2. Angular distribution of photoelectrons from highly-oriented Bi(111) thin film (a) and the asymmetry in the distribution (b).

[1] H. J. Levinson, E. W. Plummer and P. J. Feibelman, Phys. Rev. Lett. **43** (1970) 952.
[2] S. Kimura *et al.*, Rev. Sci. Instrum. **81** (2010) 053104.
[3] Y. Ishida *et al.*, Rev. Sci. Instrum. **87** (2016) 123902.

BL7U

Interfacial Interaction between Coronene Thin Film and Graphite

T. Yamaguchi[1, 2], T. Ueba[1, 2], M. Meissner[2], K. Yonezawa[2], R. Shiraishi[1, 2], S. Ideta[1, 2], K. Tanaka[1, 2] and S. Kera[1, 2]

[1] *The Graduate University for Advanced Studies (SOKENDAI), Okazaki 444-8585, Japan*
[2] *Institute for molecular science, Okazaki 444-8585, Japan*

Interactions between organic thin films and solid surfaces strongly affect the electronic structure at the interface which contributes to the performance of organic-based devices. Tanaka *et al.* observed a replica of a π-band of the highly oriented pyrolytic graphite (HOPG) surface appearing at the Γ-point below a critical temperature of 29 K [1]. The intensity of the replica band is enhanced at a low-energy photon ($h\nu \approx 11.5$ eV), indicating that the transition occurs resonantly via unoccupied states at 11.5 eV above the Fermi level. The authors suggested that the origin of the band is a superstructure due to surface defects, a charge density wave transition, or the adsorption of residual gas molecules [1, 2]. We observed similar replica bands for a coronene thin film on HOPG which, however, differ in the critical temperature and the resonance energy.

A clean surface of HOPG was obtained by cleaving in air and subsequent annealing in UHV. Coronene was purified twice by sublimation. The sample preparation was performed in a custom UHV chamber designed for organic molecules, with a base pressure of 2×10^{-7} Pa. A coronene layer with a nominal thickness of 2.5 Å was deposited at room temperature (RT) at a rate of 1 Å/min.

Figures 1 (a) and 1 (b) depict temperature dependences of $E(k)$ intensity maps at RT and 50 K. Fig. 1 (c) shows energy distribution curves (EDCs) derived from the $E(k)$ images. In Fig. 1 (b), the replica bands appear not only at the Γ-point as in the case of the pristine HOPG but also at 0.63 Å^{-1}, 1.11 Å^{-1}, and 1.26 Å^{-1} (not shown). Upon cooling, the shape of the highest occupied molecular orbital (HOMO) is markedly changed, namely the intensity decreases and the energy is higher by 60 meV as shown in Fig. 1 (c). The $h\nu$ dependence of the intensity at the Γ-point around the Fermi level is shown in Fig. 1 (d). An intensity maximum is observed at 12.8 eV, which is clearly different from the case of pristine HOPG, indicating a strong modification of the unoccupied state due to weak hybridization at the interface.

We observed similar multi-replica bands below 180 K. The critical temperature of 180 K is much higher than that of the pristine HOPG. The coronene molecules form a superstructure on HOPG at RT [3], however, there is no clear features of the replica band at RT, which may be smeared out by nuclear motions and/or weak wavefunction overlap. The occupied and unoccupied states are strongly modified by the weak interaction at the physisorbed interface nontrivial way and the impact may possibly enhanced at low temperature due to larger wavefunction overlap. A gap-opening and a change in effective hole mass should occur due to the interaction. They may be observed by more precise experiments.

[1] S. Tanaka *et al.*, Phys. Rev. B **84** (2011) 121411.
[2] S. Tanaka *et al.*, private communications.
[3] K. Walzer *et al.*, Sur. Sci. **415** (1998) 37.

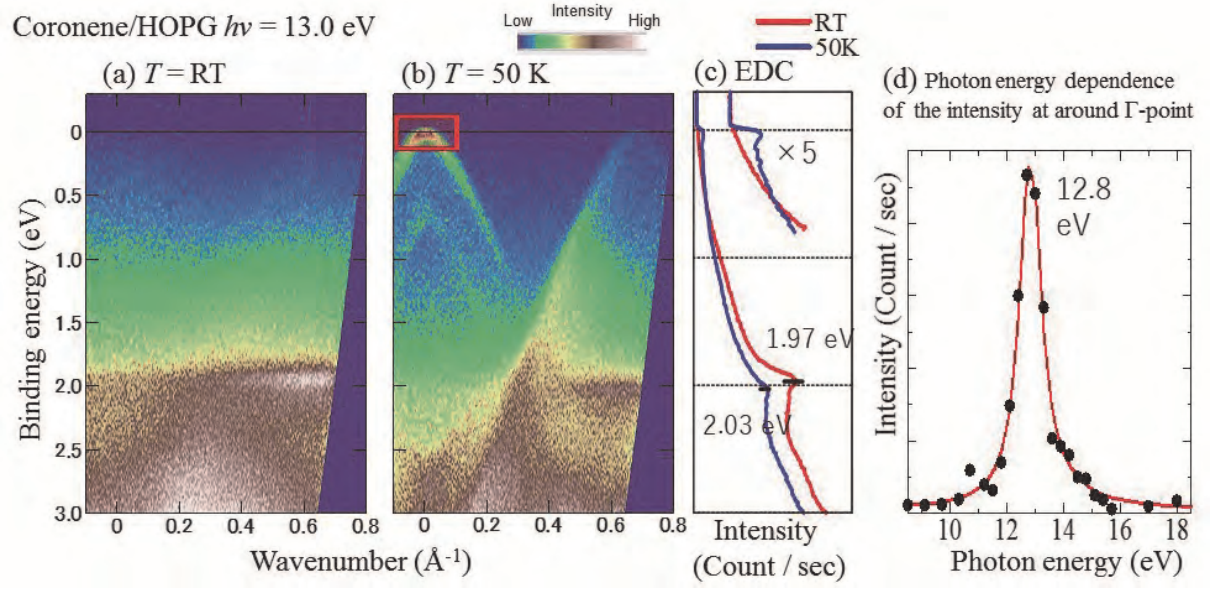

Fig. 1. $E(k)$ intensity maps of coronene/HOPG at (a) RT and (b) 50 K taken at 13.0 eV. (c) Momentum-integrated EDCs at RT (red) and 50 K (blue). (d) Intensity plot in red area in (b) as a fucnction of hv. The intensity of each energy is nomalized by photon flux. The red curve is a fitted curve using two Lorentzian functions.

UVSOR User 8

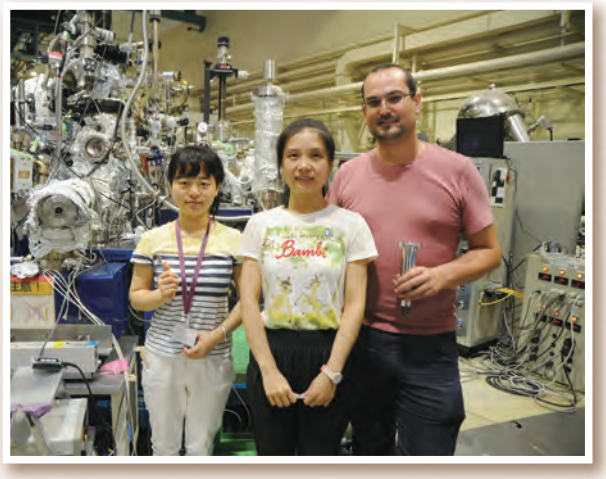

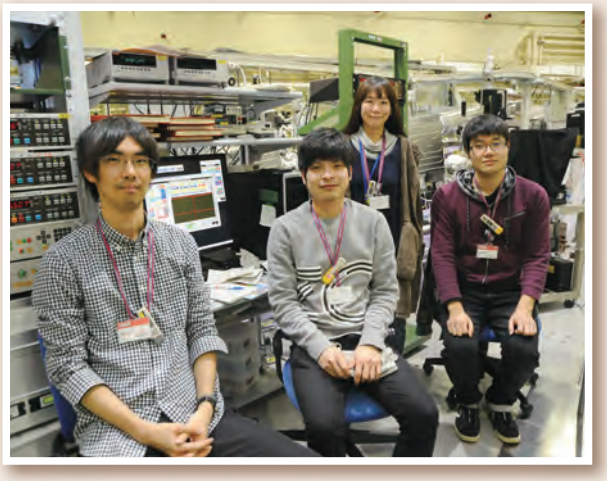

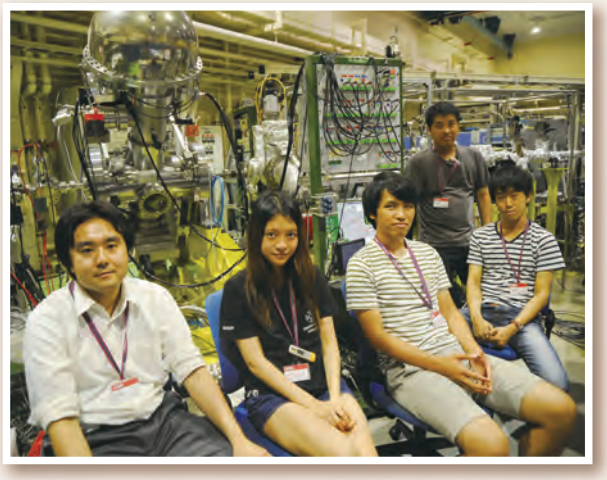

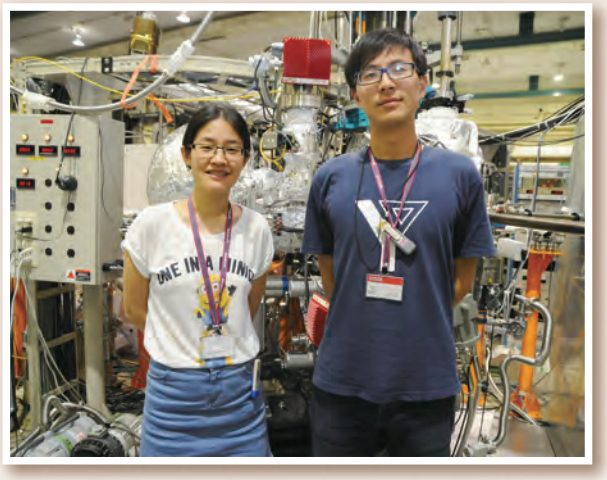

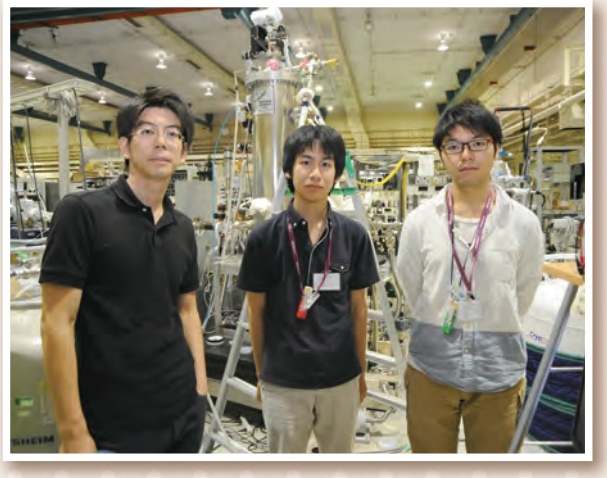

Ⅲ-5

Life, Earth and Planetary Sciences

Highlight

BL4U

Drug Release and Probing of Thermoresponsive Nanogels in Human Skin by Soft X-Ray Spectromicroscopy

K. Yamamoto[1], A. Klossek[1], T. Ohigashi[2], F. Rancan[3], R. Flesch[1], M. Giulbudagian[1], A. Vogt[3], U. Blume-Peytavi[3], P. Schrade[4], S. Bachmann[4], M. Calderón[1], M. Schäfer-Korting[5], N. Kosugi[2] and E. Rühl[1]

[1]*Institute for Chemistry and Biochemistry, Freie Universität Berlin, Takustr. 3, 14195 Berlin, Germany*
[2]*UVSOR Synchrotron Facility, Institute for Molecular Science, Okazaki 444-8585, Japan*
[3]*Charité Universitätsmedizin, 10117 Berlin, Germany*
[4]*Abteilung für Elektronenmikroskopie at CVK, 13353 Berlin, Germany*
[5]*Institut für Pharmazie, Freie Universität Berlin, 14195 Berlin, Germany*

The transport of drugs into human skin facilitated by triggered drug release from polymeric nanocarriers is reported. Label-free detection by X-ray microscopy is used to probe both, the drug and the drug nanocarriers. Dexamethasone (DXM) is used as a drug and the thermoresponsive gel was Poly(N- isopropylacrylamide) (nanogel). The stratum corneum (SC) is the top skin layer. It is the main barrier, which hinders drugs to penetrate into the viable epidermis. We recently published first results using X-ray microscopy for selectively probing DXM [1, 2] and core-multishell nanocarriers penetrating human skin [3]. It was shown that nanocarriers release the drug in the SC without penetrating into deeper skin layers. This yields higher local drug concentrations in the viable epidermis than for conventional drug formulations [3].

The experiments made use of excised human skin, which was exposed to DXM-loaded nanogels for penetration times of 100 and 1000 min. The nanogels were dissolved in water with a concentration of 33.5 mg/mL and had a drug load of 10%. Excised human skin was tape-stripped 30 times prior to topical drug application. In total 120 µL of this nanogel suspension containing 400 µg of DXM was applied per cm² of skin. Triggered drug release was initiated after 10 min by exposure of the skin samples to infrared radiation for 30 s, leading to a contraction of the nanogel and drug release.

Spectromicroscopy studies were performed at the BL4U beamline at UVSOR III using a scanning X-ray microscope. The chemical selectivity for probing either the thermoresponsive nanogel or DXM in fixed skin was achieved by exciting the samples selectively at the oxygen K-edge in the pre-edge regime (cf. [1-3]). Differential absorption maps were derived, similar to our previous work (see Fig. 1).

Figure 1 shows a compilation of the results, where only the top skin layers are shown (SC and top part of the viable epidermis). Fig. 1 (a) - (d) show results for the nanogel distribution, whereas Fig. 1 (e) - (h) show the drug distribution. Triggered and non-triggered conditions result in distinct differences for both, the drug and the drug nanocarrier distributions. The nanogel appears to penetrate only efficiently the SC, if triggered by IR radiation (Fig. 1 (b), (d)), but cannot reach the viable epidermis. Moreover, significant drug release and penetration into deeper layers only occurs, if the release is thermally triggered (Fig. 1 (f), (h)). The nanogel also provides in the SC access for the drug into the corneocytes, which has not been observed before using other vehicles, then DXM remained in the lipid regions between the corneocytes [1-2]. This nanogel-induced effect goes along with swelling of the corneocytes, which has been recently observed by electron microscopy [4]. Stimulated Raman studies provide additional evidence that this is related to changes the organization of proteins and lipids [4]. These results underscore that label-free detection at high spatial resolution provides novel insights that are required for the optimization of topical drug delivery strategies facilitated by polymeric drug nanocarriers.

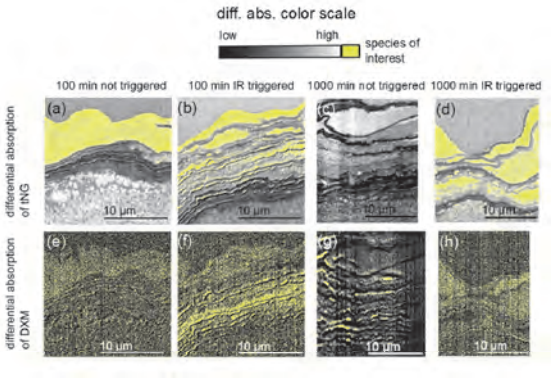

Fig. 1. The differential absorption of dexamethasone loaded nanogels penetrating the top skin layers for 100 and 1000 min, respectively: (a) - (d) selective probing of the nanogel; (e) - (h) selective probing of dexamethasone. Triggered ((b), (d), (f), (h)) and non-triggered ((a), (c), (e), (g)) drug release conditions show different distributions of the selected species.

[1] K. Yamamoto *et al.*, Anal. Chem. **87** (2015) 6173.
[2] K. Yamamoto *et al.*, Eur. J. Pharm. Biopharm., in press (2017). DOI: 10.1016/j.ejpb.2016.12.005.
[3] K. Yamamoto *et al.*, J. Control. Release **242** (2016) 64.
[4] M. Giulbudagian *et al.*, J. Control. Release **243** (2016) 323.

BL1U

Optical Activity Emergence in Glycine by Circularly Polarized Light

J. Takahashi[1, 2], N. Suzuki[1], Y. Kebukawa[1], K. Kobayashi[1], Y. Izumi[3], K. Matsuo[3], M. Fujimoto[4] and M. Katoh[4]

[1]*Fucalty of Engineering, Yokohama National University, Yokohama 250-8501, Japan*
[2]*Institute of Laser Engineering, Osaka University, Suita 565-0871, Japan*
[3]*Hiroshima Synchrotron Radiation Center, Higashi-Hiroshima 739-0046, Japan*
[4]*UVSOR Facility, Institute for Molecular Science, Okazaki 444-8585, Japan*

The origin of homochirality in terrestrial bioorganic compounds (L-amino acid and D-sugar dominant) is one of the most mysterious issues that remain unresolved in the study of the origin of life. Because bioorganic compounds synthesized in abiotic circumstances are intrinsically racemic mixtures of equal amounts of L- and D-bodies, it is hypothesized that chiral products originated from asymmetric chemical reactions induced by a "chiral impulse". These types of asymmetric reactions could have possibly been derived from physically asymmetric excitation sources in space and the chiral products would have been transported to primitive Earth resulting in terrestrial homochirality (Cosmic Scenario) [1]. In space, asymmetric excitation would be mainly effectuated by polarized photons of synchrotron radiation (SR) from kinetic electrons captured by strong magnetic field around neutron stars or white dwarfs in supernova explosion area, or by polarized photons scattered by interstellar dust clouds in star formation areas. Eventually, several terrestrial observations of polarized photon radiation from space due to scattering by interstellar dust clouds in star formation regions have been reported [2].

Several experiments have already examined asymmetric photochemical reactions in simple biochemical molecules by using circularly polarized light (CPL). We have reported optical activity emergence in solid-phase films of racemic mixtures of amino acids by using CPL from UVSOR-II free electron laser (FEL) [3].

In this paper, optical activity emergence into the achiral (optically inactive) amino acid film by using CPL is reported. We formed thin solid films of glycine on fused quartz substrates from crystal powders of glycine using a thermal-crucible vacuum evaporator. Sublimation temperature was 150 ~ 200 °C and pressure of the vacuum chamber was approximately 10^{-2} Pa throughout the evaporation process. To introduce optical asymmetry into the racemic film, we irradiate them with CPL introduced from undulator beam line BL1U of UVSOR-III (Fig.1). The irradiated CPL wavelength was 215 nm and total irradiation energies were 12 and 20 mW hour.

In order to clarify the optical anisotropy of the films, we measured the circular dichroism (CD) and photo absorption spectra using a commercial CD spectrometer (JASCO J-720WI). As a result, almost completely symmetric spectra were observed with left- and right-handed CPL irradiation. The dependence on sample rotation angle of the spectra of 0- and 90-degree rotation was measured. If linear dichroism (LD) and/or linear birefringence (LB) components are dominantly effective, the signs of appearance CD peaks should be inverted. We ensured that rough spectrum profile and at least signs of two CD peaks were not changed. Therefore, observed appearance CD should be derived dominantly from chiral CD component. We are planning CD spectra measurement over the shorter wavelength region using SR-CD beamline of Hiroshima Synchrotron Radiation Center (HiSOR).

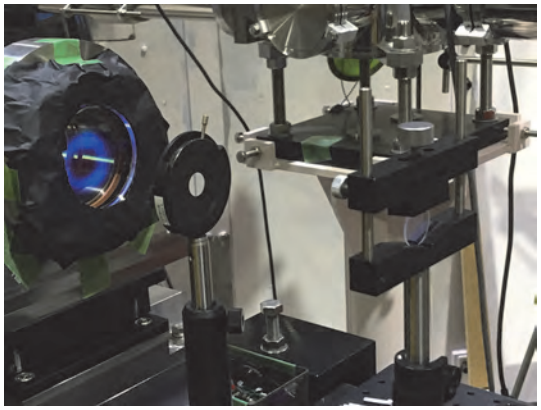

Fig. 1. Photo of the irradiation experiment of circularly polarized light on BL1U.

[1] Bonner, Origins Life Evol. Biosphere **21** (1991) 59.
[2] T. Fukue *et al.*, Origins Life Evol. Biosphere **40** (2010) 335.
[3] J. Takahashi, H. Shinojima, M. Seyama, Y. Ueno, T. Kaneko, K. Kobayashi, H. Mita, M. Adachi, M. Hosaka and M. Katoh, Int. J. Mol. Sci. **10** (2009) 3044.

BL1U

Emergence of Biological Homochirality by Irradiation of Polarized Quantum Beams

K. Matsuo[1], Y. Izumi[1], J. Takahashi[2], M. Fujimoto[3] and M. Katoh[3]

[1]*Hiroshima Synchrotron Radiation Center, Hiroshima University, Higashi-Hiroshima 739-0046, Japan*

[2]*Faculty of Engineering, Yokohama National University, Yokohama 240-8501, Japan*

[3]*UVSOR Facility, Institute for Molecular Science, Okazaki 444-8585, Japan*

Origin of homochirality in terrestrial biomolecules (L-amino acids and D-sugars dominant) remains an unresolved problem. One of the hypotheses for the emergence of homochirality is Cosmic Scenario, in which the space materials on the surface of meteorites are transformed into the complex organic molecules (for example amino acid precursors) by the asymmetric reactions due to the irradiation of circularly polarized light (CPL). To validate this scenario, as a pioneer research, Takahashi et al. investigated the emergence of optical anisotropy in solid films of racemic amino acids (L/D = 1) with the left- and right-CPL (LCPL and RCPL) irradiation of 215 nm, and suggested that the CPL caused the preferential conformational changes between the two enantiomers in racemic amino acid films [1].

Circular dichroism (CD) spectroscopy can easily detect the emergence of optical anisotropy due to the asymmetric reaction because it sensitively reflects the steric structures of chiral molecules such as amino acids. Further the theoretical calculation of CD spectrum of L-alanine molecule revealed that the chromophores such as carboxyl and amino groups had many characteristic electronic transitions (n-π^*, π-π^* and n-σ^*) below 230 nm [2], suggesting that the photoreaction might depend on the irradiation energy. In this study, the thin solid films of racemic alanine (L/D = 1) were irradiated by the two types of CPL wavelengths (230 and 202 nm) and the emergence of amino acid homochirality were investigated by the CD measurements.

The thin solid films on SiO_2 substrates were produced by evaporating the powder of DL-alanine using the vacuum-evaporation system in Hiroshima Synchrotron Radiation Center (HiSOR). Sublimation temperature was about 150 ~ 200 °C and the pressure in the vacuum chamber during the evaporation was approximately 5 x 10^{-2} Pa. The CD spectra of these thin solid films were measured from 260 to 170 nm using a vacuum-ultraviolet circular dichroism instrument in HiSOR and confirmed to be mostly zero before the irradiation, showing that the spurious CD due to the contamination of film surface were negligible. The LCPL and RCPL irradiation for these films were carried out in the BL1U of UVSOR at the wavelengths of 230 and 202 nm. After the irradiation, these CD spectra were measured again, in order to confirm the emergence of homochirality.

Figure 1 shows the CD spectra of thin films after the LCPL and RCPL irradiation of two wavelengths. As shown in Fig. 1, the LCPL and RCPL irradiation exhibited symmetrically inverted spectra in the both irradiation wavelengths (230 and 202 nm), indicating the emergence of homochirality at the both irradiation wavelengths. Further, the spectral shape observed in Fig.1a were largely different from those in Fig.1b, suggesting that the asymmetric reactions of DL-alanine thin solid film depend on the irradiation wavelength.

To further validate these results, we are planning to irradiate the CPL in the vacuum-ultraviolet region. Accumulations of these experimental results would be useful for determining the effective emergence of homochirality in solids by the CPL irradiation.

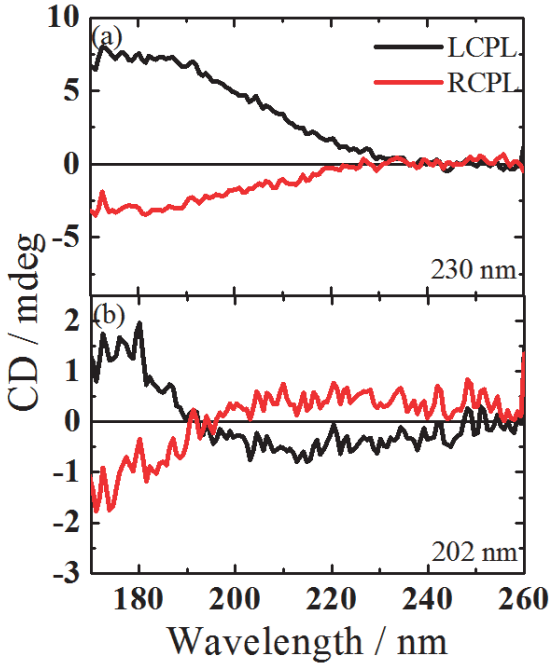

Fig. 1. CD spectra of DL-alanine thin films after the LCPL and RCPL irradiation at 230 nm (a) and 202 nm (b).

[1] J. Takahashi, H. Shinojima, M. Seyama, Y. Ueno, T. Kaneko, K. Kobayashi, H. Mita, M. Adachi, M. Hosaka and M. Katoh, Int. J. Mol. Sci. **10** (2009) 3044.
[2] T. Fukuyama, K. Matsuo and K. Gekko, J. Phys. Chem. A **109** (2005) 6928.

BL4U

STXM Study on the Microbial Alteration of Iron Sulfide Mineral at the Submarine Seafloor

S. Mitsunobu[1, 2], Y. Ohashi[2] and T. Ohigashi[3]

[1]*Department of Agriculture, Ehime University, Matsuyama 790-8566, Japan*
[2]*Institute for Environmental Sciences, University of Shizuoka, Shizuoka 422-8526, Japan*
[3]*UVSOR Facility, Institute for Molecular Science, Okazaki 444-8585, Japan*

Recent studies have revealed that various microorganisms are alive on the submarine seafloor and contribute alteration of oceanic crust [1, 2]. It is considered that the microorganisms (e.g., bacteria, archaea) gain their life-energy from the redox reaction using inorganic active elements such as ferrous iron and sulfur involved in the oceanic crust (basaltic rocks and sulfidic minerals). The microbial activities would accelerate the alteration of the oceanic crust, which would influence the carbon dynamics in the earth significantly. However, little is known on mechanism of the microbial alteration of the minerals, because direct chemical speciation of both metals and biomolecules at mineral-microbe interface has been crucial due to high spatial resolution in analysis. Moreover, difficulty on the field access is also an obligate reason that no enough studies on that has been done so far.

Here, we performed *in situ* bio-alteration experiment using mineral substrates composed of the ocean crust, fresh sulfidic mineral (pyrite) and basalt rock, at oxidative submarine seafloor in Izu-Bonin region, where oxidative alteration of the basalt and pyrite naturally occur. Then, we investigated the mechanisms of the bio-alteration process using scanning transmission X-ray microscopy (STXM) based C and Fe near edge X-ray absorption fine structure (NEXAFS) analyses at UVSOR BL4U.

Before STXM analysis, bacteria attached on the pyrite were stained with a minimum fluorescent dye and marked for the STXM analysis. In the analysis, we applied the STXM analysis to determine in situ carbon (C) and iron (Fe) species at the interface of target bacteria cell and mineral (pyrite). STXM-based imaging and C 1s NEXAFS analysis directly showed that the attached bacterial cell produce some polysaccharide-rich extracellular polymeric substances (EPS) at the cell-pyrite interface (data not shown). The polysaccharide substances generally have a metal-chelating effect and enhance the dissolution of mineral involving the metals [3]. Hence, the bacteria may produce the polysaccharide-rich EPS on the pyrite actively to dissolve the pyrite and gain energy efficiently.

Furthermore, we measured STXM-based Fe imaging and Fe 4p NEXAFS at the same area. Figure 1 (a) shows the STXM-based merged Fe/C image. The image shows the several particles yielding Fe with diameter of 50-100 nm on the cells (orange circles in Fig. 1 (a)). The Fe NEXAFS analysis of the particles indicate that Fe species in these particles were Fe(III) hydroxides such as ferrihydrite and schwertmannite on the whole (Fig. 1 (b)). Because the Fe species in substrate (pyrite) is Fe(II), observed Fe(III) results from oxidation of Fe(II) originally involved in pyrite. These findings indicate that some of bacteria attached on the pyrite gain energy by Fe oxidation at the submarine seafloor and that have a metabolic mechanism to excrete subsequent insoluble-Fe(III) formed by oxidizing reaction.

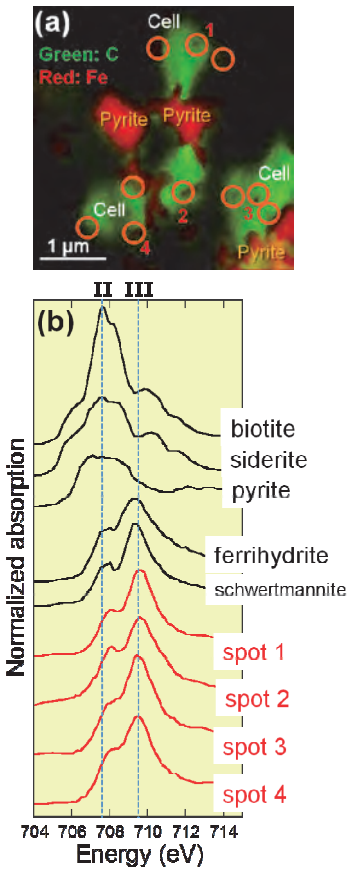

Fig. 1. STXM-based C and Fe images (a) and Fe 4p NEXAFS spectra (b).

[1] T. M. McCollom, Deep-Sea Res. **47** (2000) 85.
[2] K. J. Edwards *et al.*, Geochim. Cosmochim. Acta **67** (2003) 2843.
[3] S. Mitsunobu *et al.*, Microbes Environ. **31** (2016) 63.

BL4U

NEXAFS Measurements of Biomolecules at the C-K edge for Molecular Mapping in Biological Specimens by STXM

A. Ito[1], T. Ohigashi[2, 3], K. Shinohara[1], S. Tone[4], M. Kado[5], Y. Inagaki[2] and N. Kosugi[2, 3]

[1]*School of Engineering, Tokai University, Hiratsuka 259-1292, Japan*
[2]*UVSOR Synchrotron, Institute for Molecular Science, Okazaki 444-8585, Japan*
[3]*The Graduate University for Advanced Studies (SOKENDAI), Okazaki 444-8585, Japan*
[4]*Graduate School of Science & Engineering, Tokyo Denki University, Hatoyama 350-0394, Japan*
[5]*Kansai Photon Science Institute, Nat. Inst. Quantum and Radiological Sci. Technol., Kizugawa 619-0215, Japan*

Spectromicroscopy using scanning transmission X-ray microscope (STXM) has been applied to DNA and protein distributions in biological specimens such as chromosome and sperm at the C-K absorption edge [1, 2]. In our previous studies using STXM at BL4U, we obtained DNA and histone, a nuclear protein, distributions in mammalian cells using characteristic NEXAFS peaks of DNA and histone which can be clearly observed at the N-K absorption edge [3]. Furthermore quantitative mapping of these molecules was developed [4], but the results showed that the contribution of biomolecules other than DNA and histone should be taken into account.

In this study we measured NEXAFS of phospholipids, a major component of cellular membrane, in addition to nucleic acids and various kinds of proteins at the C-K absorption edge. Figure 1 shows NEXAFS for typical biomolecules of nucleic acid, protein and phospholipid at the C-K absorption edge.

Ade *et al*. used the slight shift of a peak as shown by 1 and 2, which was assigned to 1s to π* transition of C=C bond, to image of DNA and protein in chromosome separately [1]. The significant difference in peaks among nucleic acid, protein and phospholipid can be observed at the peak 6, 7 and 8 as indicated in Fig. 1. These peaks were assigned to 1s to π* transition of C=O bond [5, 6]. Peak 6 and 8 corresponds to N-C(=O)-C and N-C(=O)-N, respectively. On the other hand phospholipid does not have such amide bonds, but has O-C=O. This bond may result in the unique peak 7. The different location of peaks due to C=O bond may be applicable to separate imaging of these molecules.

Figure 2 shows the comparison of DNA and RNA in the NEXAFS at the C-K edge. Peaks 5 and 6, 1s to π* transition of C=O bond, exhibits a slight difference, suggesting the possibility for imaging nucleic acids separately.

For the difference among proteins, we measured spectra of bovine serum albumin (BSA), histone, cytochrome C and actin. NEXAFS peaks have the same energies except actin. Interestingly actin has the significant peak shift to higher energies. This finding needs to be confirmed in future experiments.

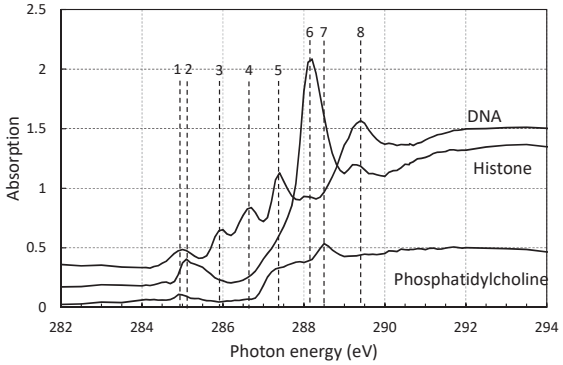

Fig. 1. NEXAFS spectra of DNA, histone and phosphatidylcholine at the C-K absorption edge.

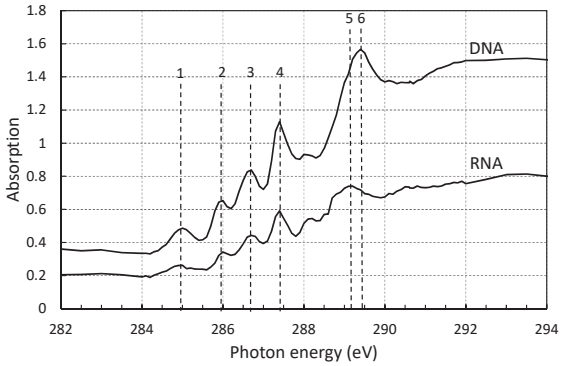

Fig. 2. NEXAFS spectra of DNA and RNA at the C-K absorption edge.

[1] H. Ade *et al*., Science **258** (1992) 972.
[2] X. Zhang *et al*., J. Struct. Biol. **116** (1996) 335.
[3] A. Ito,T. Ohigashi, K. Shinohara, S. Tone, M. Kado, Y. Inagaki and N. Kosugi, UVSOR Activity Report **43** (2016) 143.
[4] K. Shinohara, T. Ohigashi, S. Tone, M. Kado and A. Ito, Proc. 13th Intl. Conf. X-Ray Microsc. (XRM2016) (in press).
[5] Kummer *et al*., J. Phys. Chem. B **114** (2010) 9645.
[6] Stewart-Ornstein *et al*., J. Phys. Chem. B **111** (2007) 7691.

BL4U

Chemical Speciation of Single Aerosol Particles: A Reconstruction of Hygroscopicity for Sulfate Aerosols

Y. Takahashi[1], C. Miyamoto[1] and K. Sakata[2]

[1]*Department of Earth and Planetary Science, Graduate School of Science, the Univ. of Tokyo, Tokyo 113-0033, Japan*

[2]*Department of Earth and Planetary Systems Science, Graduate School of Science, Hiroshima Univ., Higashi-Hiroshima 739-8526, Japan*

Hygroscopic sulfate aerosol such as ammonium sulfate (AS: $(NH_4)_2SO_4$) contributes to indirect cooling effect by acting as cloud condensation nuclei (CCN) [1]. On the other hand, gypsum (Gyp: $CaSO_4 \cdot 2H_2O$), non-hygroscopic sulfate, suppresses CCN activity of AS, which are formed by chemical reaction of calcite (Cal: $CaCO_3$) in mineral dust with H_2SO_4 in atmosphere [2]. Thus, non-sea-salt sulfate ($nssSO_4^{2-}$) species is one of the important information for estimation of CCN activity of sulfate aerosol.

Ice sheet in polar region preserves atmospheric particles and gases at the time of its deposition [3]. In the case of Greenlandic ice sheet, they preserve mineral dust and anthropogenic aerosol from continental region in the Northern hemisphere [3]. In this study, chemical speciation experiments of trapped particles in ice sheet were conducted. In addition, chemical speciation in sea spray aerosol (SSA) with high CCN activity was also conducted to distinguish non-sea-salt sulfate ($nssSO_4^{2-}$: AS and Gyp) and SO_4^{2-} from seawater. The aim of this study is to determine Gyp/AS ratio in trapped particles in ice sheet to estimate CCN activity of $nssSO_4^{2-}$ aerosols in the past.

Trapped particles in Greenlandic ice sheet were extracted by sublimation of ice samples in low temperature room (-20°C), which can extract trapped particles with minimal chemical alteration by water from melting ice samples [4]. Trapped particles in ice sheet with ages of 1987, which is a part of ice core drilled at SE-Dome (67.2°N, 36.4°W, 3170 m above sea level), were analyzed. SSA sampling were conducted at the Antarctic Ocean to obtain non-alteration SSA by anthropogenic gases (*R/V Hakuho-Maru* cruise, KH-14-6, GEOTRACES). Chemical speciation experiments were conducted by STXM/NEXAFS with image stack [5].

Sulfate and Ca in SSA were enriched in edge position of aerosol particles (Fig. 1). Carbonate distribution in single SSA particles, for which we measured carbon K-edge NEXAFS, were similar between sulfate and Ca (Fig. 1). The spectral analysis showed that Ca species were aragonite (Arg: $CaCO_3$) and Gyp. Sulfate in SSA was also present as Na_2SO_4, which was hygroscopic sulfate. Considering that Na and Ca concentration in SSA, Na concentrations is much higher than that of Ca. Therefore, dominant sulfate species in SSA can be Na_2SO_4. On the other hand, center part of SSA was composed of NaCl, which result is consistent with a previous study [5]. Thus, SSA surface and center were composed of sulfate with Ca, Na and C, and NaCl, respectively (Fig. 1).

Sulfate and Ca are distributed heterogeneously in trapped particle in Greenlandic ice sheet (Fig. 2). Distributions of sulfate and Ca in trapped particles were different from those in SSA (Figs. 1 and 2). Therefore, mineral dust and SSA can be distinguished based on distributions of sulfate and Ca. Unfortunately, AS-bearing particles cannot be detected from Greenlandic ice sheet due to the small number of measured particles. Previous studies reported that AS particle contains sulfate homogeneously in the single particle [6]. Thus, SSA, mineral dust, and AS particles can be distinguished by sulfate distributions in their single particles. Therefore, S speciation for trapped particles by STXM/NEXAFS and estimation of AS and Gyp amount of based on optical density (OD) of SO_4^{2-} lead to reconstruction of CCN activity of sulfate aerosol in the past.

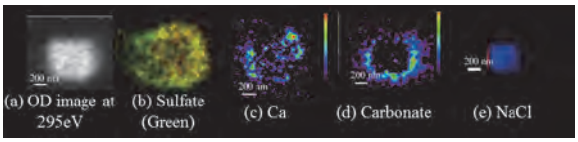

Fig. 1. Results of image stack of SSA. (a) OD image at 295 eV, (b-e) sulfate, Ca, carbonate, and NaCl distributions, respectively.

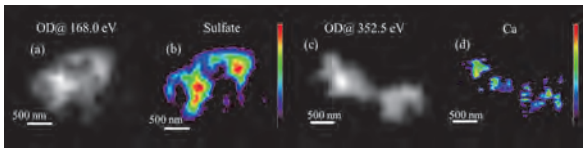

Fig. 2. Results of image stack of two trapped particles in Greenlandic ice sheet: (a) OD image at 168.0 eV, (b) sulfate distribution, (c) OD image at 352.5 eV, and (d) Ca distribution.

[1] C. D. O'Dowd *et al*., Atmos. Environ. **31** (1997) 73.
[2] Y. Takahashi *et al*., Environ. Sci. Technol. **43 (17)** (2009) 6535.
[3] R. J. Delmas, Rev. Geophys. **30 (1)** (1992) 1.
[4] Y. Iizuka *et al*., J. Glaciology **55 (191)** (2009) 552.
[5] R. C. Moffet *et al*., Anal. Chem. **82** (2010) 7906.
[6] W. Li *et al*., J. Clean. Prod. **112** (2016) 1330.

BL4U

Evaluation of Influence on Organic Matters by Dehydration of Hydrous Asteroids

A. Nakato[1] and M. Uesugi[2]
[1] *Division of Earth and Planetary Sciences, Kyoto University, Kyoto, 606-8502, Japan*
[2] *SPring-8/JASRI, Sayo,679-5198, Japan*

Extraterrestrial organics in the carbonaceous chondrites show wide variety and complex structures. Those characteristics of the structure could be evidences of the evolution of parent body since the structure would be modified due to thermal metamorphism and aqueous alteration [*e.g.*, 1, 2]. Many previous studies have investigated the structural change of the insoluble organic matters (IOM) extracted from the meteorites, but lacked '*in situ*' investigation of organics in meteorites. XANES and high resolution STXM installed in UVSOR BL4U are useful tools for such '*in-situ*' analysis of molecular structure of the organics in bulk rock of unknown carbonaceous chondrites, and observation of their micro- distribution. We prepared two types carbonaceous chondrites, one is Murchison that experienced aqueous alteration, and the other is Allende that was suffered thermal metamorphism on the parent body, respectively. Both samples were made by focused ion beam (FIB), and analyzed by STXM/XANES. In addition, we examined that sample contamination during the storage [3], and sample damage due to sample preparing methods [4] suggested by previous studies.

We fibbed 8 samples from the matrix of Murchison polished thick section. The size is about 15x10 μm and 100 nm thickness. An Allende fragment was embedded into sulfur and then sliced about 70 nm thick each by ultramicrotome. After that, the remaining portion was picked up from the sulfur and embedded in epoxy to be fibbed into 5x5 μm and 100 nm thickness sections. These processes of Allende were performed for comparison of the sample damage between the preparing methods. STXM and C, N, O-NEXAFS was carried out for all samples formed by FIB and ultramicrotome.

For evaluation of the sample contamination during the storage, Murchison samples were kept in 4 different conditions for 6-8 months. The storage atmospheres were pure Nitrogen and approximately 10^2 Pa vacuumed conditions. The sample holder made by Si and metal, respectively.

Several characteristic peaks of aromatic carbon at 285 eV, aliphatic carbon at 287.5 eV, carboxyl at 288.5 eV, and carbonate 290.5 eV were detected from Murchison samples as same as the previous studies of IOM [*e.g.*, 5]. Most of the Murchison samples show similar peaks except for those of carbonate. It suggests that the molecular structure of organics in Murchison is relatively primitive and homogeneous. On the other hand, it is well known that Allende IOM shows unique chemical structure of 1s-σ* exciton at 291.7 eV of graphene structures, that is a characteristic of thermally metamorphosed meteorites [5]. However, we could not detect the peak in both fibbed and microtomed samples in this study (Fig. 1). It may reflect that the graphene can be concentrated in extracted sample, or apparently masked by features of other organic components in in situ observation of bulk sample. In other words, we found fine–scaled heterogeneity of organic matter in Allende matrix using XANES and high resolution STXM, though further investigation is required. C-XANES of Murchison and Allende did not show any differences of the organic molecular structures. Thus, any influences on the organic matter by thermal metamorphism were not found in our '*in-situ*' bulk analysis and observation so far.

C-XANES spectrum of Murchison samples stored for 6-8 months do not show any changes irrespective of the storage environment. In addition, we can not detect clear N-XANES transition in all samples, even some samples were kept in pure N_2 atmosphere. We can conclude from these results that sample storage does not give any contaminations, under the conditions tested in our study.

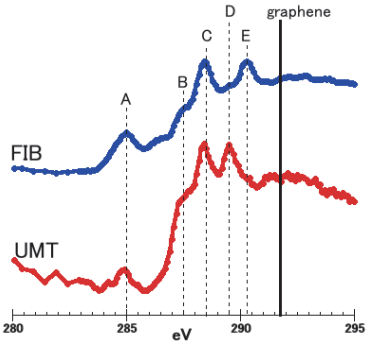

Fig. 1. C-XANES spectra of Allende.
Peaks indicated with letters A-E. A: aromatic carbon, B: aliphatic carbon, C: carboxyl moiety, D: alcohol or ether moieties, E: carbonate.

[1] Y. Kebukawa and G. D. Cody, Icarus **248** (2015) 412.
[2] H. Yabuta *et al*., Meteorit. Planet. Sci. **42** (2007) 37.
[3] M. Uesugi and A. Nakato, UVSOR activity report (2015)
[4] N. D. Bassim *et al*., J. Microsc. **245** (2012) 288.
[5] G. D. Cody *et al*., Earth Planet. Sci. Lett. **272** (2008) 446.

BL4U

Carbon Materials and Alteration Products in Martian Meteorites

H. Suga[1], N. Sago[1], M. Miyahara[1], T. Ohigashi[2], Y. Inagaki[2], A. Yamaguchi[3] and E. Ohtani[4]
[1]*Department of Earth and Planetary Systems Science, Graduate School of Science, Hiroshima University, Higashi-Hiroshima 739-8526, Japan*
[2]*UVSOR Facility, Institute for Molecular Science, Okazaki 444-8585, Japan*
[3]*National Institute of Polar Research, Tokyo 190-8518, Japan*
[4]*Department of Earth Sciences, Graduate School of Science, Tohoku University, Sendai 980-8578, Japan*

It is now widely accepted that water existed on the Mars. Martian surface materials were launched from the Mars by an impact event, and only a few of them were delivered to the Earth, which are so called Martian meteorites. It is expected that one group of Martina meteorite, nakhlite records a water-rock reaction (alteration) occurred on the Mars [*e.g.*, 1]. Iddingsite is one of pervasive alteration textures found in nakhlites. A small amount of carbon materials is accompanied with the iddingsite texture [2]. The constituents, chemical species, and theirs coordination in the iddingsite textures strongly depend on pH, temperature, rock/water ratio, and pressure during the alteration process. The scrutiny of iddingsite in nakhlites will become a clue for elucidating environment on the Mars during a wet-period. However, the sample volume of nakhlite available for a study is limited because nakhlite is very a precious sample. Iddingsite texture is only about several 10 μm across. Accordingly, we adopted a FIB-assisted site-specific carbon/water-free STXM/NEXAFS technique [3] to investigate iddingsite texture in naklite.

Yamato 000593 and Nakhlite samples were prepared for this study. We observed the Yamato 000593 and Nakhlite using a FE-SEM. A laser micro-Raman spectroscopy was employed for phase identification. Several target portions for a STXM analysis were excavated by a FIB technique and became ultra-thin foils. A STXM analysis was conducted at BL4U. Finally, the foils were observed with a FE-STEM.

Both Nakhla and Yamato 000593 consist mainly of augite and minor olivine [$(Mg,Fe)_2SiO_4$]. FE-SEM observations revealed that iddingsite textures were observed in and around the olivine grains. Based on Raman spectroscopy analysis, the iddingsite textures in the olivine grains mainly appear to consist of a nonstoichiometric distorted olivine-type mineral, laifunite [$(Fe^{2+}Fe^{3+})_2(SiO_4)_2$], which is the alteration product of original olivine. The iddingsite textures around the olivine grains are complex and varied. Silica-rich, sulfur-rich, and chlorine-rich veinlets in addition to laifunite occurred around the olivine grains. Slices for STXM measurements were excavated from these iddingsite textures. Fe- and O-XANES indicate that most iron in original olivine is ferrous (Fe^{2+}/Fe^{3+} = 0.72), whereas most iron in laifunite is ferric (Fe^{2+}/Fe^{3+} = 0.52). Fe^{2+}/Fe^{3+} ratio decreases discontinuously from olivine to laifunite (Fig. 1). Combined FE-SEM, XANES, and STEM analysis allowed us to follow the alteration sequence from olivine to laifunite for the first time. S-XANES revealed that sulfur in the sulfur-rich veinlet existed as hexavalent rather than zero-valent by comparing with reference materials (sulfur, iron sulfate (iii) hydrate, and iron (II) sulfate heptahydrate). Although Si-XANES was obtained from the silica-rich veinlet, the spectrum was ambiguous (probably due to strong adsorption). Cl-XANES could not be obtained from the Cl-rich veinlet due to lack of an adequate reference material. Alternatively, C- and O-XANES taken showed that the Cl-rich veinlet included both carbon and oxygen, and aromatic hydrocarbons (C=C) was detected. Although we have not completed all measurements, our site-specific STXM/NEXAFS technique is now uncovering complex and varied alteration processes occurred on the early Mars.

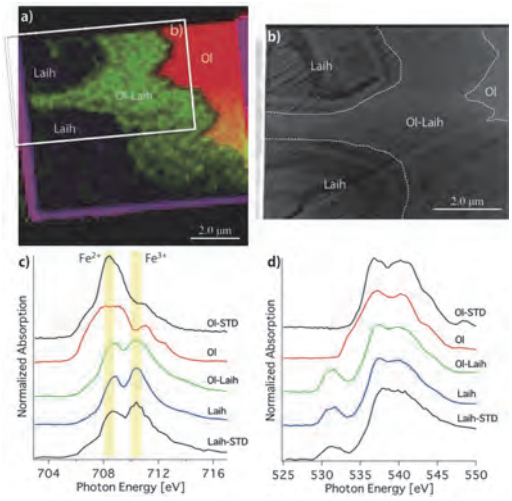

Fig. 1. a) Fe^{2+}/Fe^{3+} ratio distribution in iddingsite texture, b) STEM image of a box in a), c) and d) are the Fe- and O-XANES for olivine (Ol), olivine-laifunite intermediate (Ol-Laith), and laifunite (Laih) domains with standard (STD) materials, respectively.

[1] T. Noguchi *et al.*, J. Geophy. Res. **114** (2009) E10004.
[2] L. M. White *et al.*, Astrobiology **14** (2014) 170.
[3] H. Suga *et al.*, in prep.

BL4U

Chemical Evaluations of Sample Preparation Methods for C-, N-, O-XANES/STXM

Y. Kebukawa[1], E. Uchimura[2], T. Ohigashi[3], Y. Inagaki[3] and K. Kobayashi[1]

[1] *Faculty of Engineering, Yokohama National University, Yokohama 240-8501, Japan*

[2] *School of Engineering Science, Yokohama National University, Yokohama 240-8501, Japan*

[3] *UVSOR Synchrotron, Institute for Molecular Science, Okazaki 444-8585, Japan*

Carbon, nitrogen, oxygen X-ray absorption near edge structure (XANES) with scanning transmission X-ray microscope (STXM) became a powerful tool for extraterrestrial organic matter analyses in this decade. Some problems may still exist due to small amount of organic matter that usually exists in extraterrestrial samples, such as meteorites, and its susceptibility to damage, degradation and contamination. Here we compared the sample preparation methods for STXM and evaluate whether correct organic chemistry would be reflected and reproduced.

We prepared ~100 nm-thick thin sections of Murchison meteorite and humic acid (IHSS standard Leonardite humic acid, as an analog of organic matter in meteorites) using a focused ion beam (FIB) and an ultramicrotome (UMT) equipped with a diamond knife. For UMT, the sample grains were mixed with sulfur powder and heated to melt the sulfur (~150°C for less than one minute). Solidified sulfur droplet was attached to an epoxy stub. The ultramicrotomed sections were transferred to SiO-coated TEM grids and gently heated until the sulfur sublimed off. C, N, O-XANES spectra were obtained at BL4U, UVSOR.

Figure 1 shows C-XANES spectra of the Murchison and humic acid prepared with UMT and FIB. C-XANES spectra of the Murchison show some differences between UMT and FIB. Ketone C=O appeared only in FIB sample and C-O (alcohol, ether) appeared only in UMT sample. Ketone might be increased due to FIB beam damage, while C-O in UMT sample might be a contamination during sample preparation. Note that the Murchison has some heterogeneity so we examined C-XANES from several different locations. While humic acid prepared in either UMT or FIB showed no significant difference in C-XANES, indicating that slight damage/contamination affects when one intend to detect small amount of organic matter embedded in mineral matrix. Figure 2 shows elemental abundances calculated using computational fit of C-, N-, and O-XANES spectra [1]. The O/C ratio obtained with XANES are underestimated compared to elemental composition data for the humic acid standard provided by International Humic Substances Society (IHSS) [2]. These results indicate that XANES data interpretations must be made with cautions.

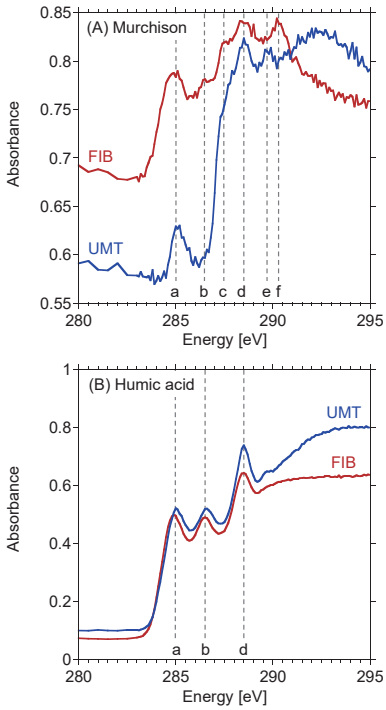

Fig. 1. C-XANES spectra of (A) Murchison and (B) humic acid. Peak assignments [1]; a: 285.0 eV, aromatic C=C, b: 286.5 eV, ketone C=O, c: 287.5 eV, aliphatic C-C, d: 288.5 eV, carboxyl O=C-O, e: 289.7 eV, alcohol, ether C-O, f: 290.3 eV, carbonate CO_3.

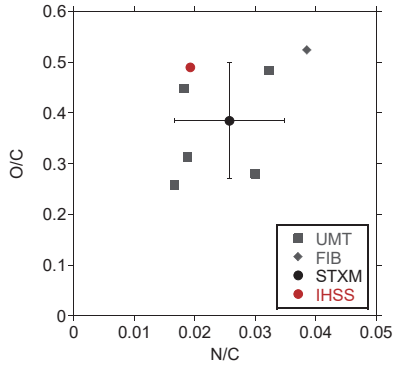

Fig. 2. Atomic N/C versus O/C derived from C-, N-, and O-XANES of humic acid. An average of 5 UMT data points and one FIB data point is plotted in a black circle. IHSS reference data [2] is included in the plot (red circle).

[1] G. D. Cody *et al.*, Meteorit. Planet. Sci. **43** (2008) 353.
[2] http://www.humicsubstances.org

BL4U

Speciation of Carbon in Prokaryotic Organelles of *Pseudanabaena foetida* (*Phormidium tenue*)

K. Takemoto[1], M. Yoshimura[2], Y. Inagaki[3] and T. Ohigashi [3]
[1]*Department of Physics, Kansai Medical University, Hirakata 573-1010, Japan*
[2]*SR center, Ritsumeikan University, Kusatsu 525-8577, Japan*
[3] *UVSOR Synchrotron, Institute for Molecular Science, Okazaki 444-8585, Japan*

Lake Biwa is the most important water reservoir in Kyoto-Osaka-Kobe region in Japan. In 1969, the musty-odor occurred due to sudden propagation of a certain cyanobacterium in Lake Biwa. Since then, the musty-odor problem in Lake Biwa is reported almost every year. The matter of the musty-odor was identified as 2-methylisoborneol (2-MIB) [1]. Although the musty-odor-causing cyanobacterium was reported as *Phormidium tenue* (Menegh.) Gomont, in 2016, the cyanobacterium was proposed as a new species producing 2-MIB: *Pseudanabaena foetida Niiyama*, Tuji *et* Ichise sp. nov. [2]. Now, the study how the microstructure and growth condition are related to the 2-MIB productivity has proceeded. In our previous study based on full field transmission soft X-ray microscope observation, two interesting intracellular structure were observed. One is oxygen-enriched granules and the other is carbon-enriched structures. Oxygen distribution and K-edge XANES spectra were collected on the scanning transmission X-ray microscope (STXM) at UVSOR BL4U [3]. Several oxygen-enriched granules were confirmed. Though the pre-peak intensity of oxygen-enriched granules was smaller than that of cytoplasm, the pre-peak energies were almost similar.

However, the main edge energy of the granule shifted toward lower than that of cytoplasm. In this study, the carbon-enriched structures were examined using STXM.

P. foetida sp. collected from Lake Biwa were subcultured. The culture was maintained on CT medium (pH 8.0) under a 12 h light/12 h dark cycle at 20 °C. The cultures were illuminated with fluorescent lamps, which provided about 20 μmol photons m^{-2} s^{-1} of photosynthetically active radiation.

Figures 1 a and b show XM images of air-dried *P. foetida* cells. Oxygen was localized around the center of the cells like a belt (Fig. 1a). Since a blank area was seen in the belt-like oxygen localizing area, black arrow, a carbon image was taken at 285 eV (Fig. 1b). At the oxygen blank area, area 1, a structure with high X-ray absorption characteristic was seen. As shown in Fig. 1c, the carbon XANES spectra were similar, but only the spectrum from area 1 showed a peak at 297 eV assigned to potassium, asterisk. It is well known that in bacteria, sodium, potassium, calcium, and magnesium have all been shown to effect cell division [4]. This result suggests that localization of potassium is implicated as the site of regulation of cell division of *P. foetida*.

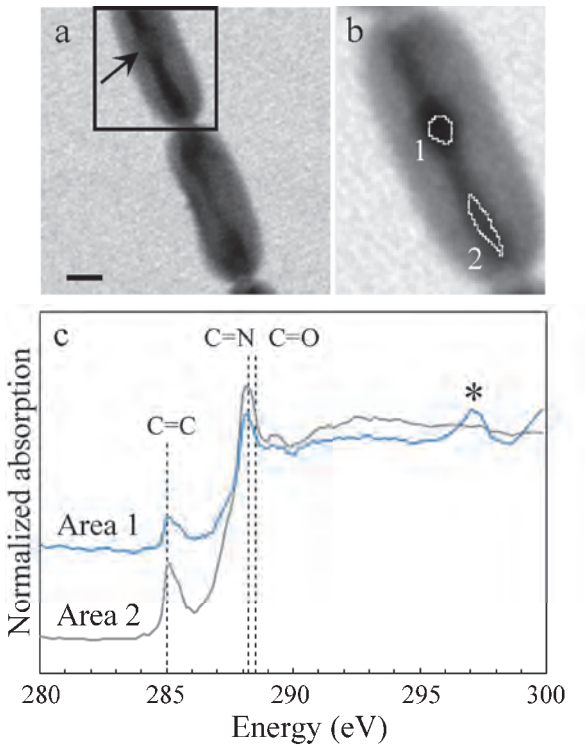

Fig. 1. STXM images of *P. foetida* cell taken at 532 eV (a) and 285 eV (b) and carbon XANES spectra (c). The blue and grey spectra correspond to the area 1 and 2 in (b). The peak around 285 eV, 288.2 eV and 288.5 eV were assigned to C=C, C=N and C=O, respectively. Scale bar is 1 μm.

[1] M. Yagi *et al*., Water Sci. Technol. **15** (1983) 311.
[2] Y. Niiyama *et al*., Fottea **16** (2016) 1.
[3] T. Ohigashi *et al*., J. Phys. Conf. Ser. **463** (2013) 012006.
[4] L. O. Ingram *et al*., J. Bacteriol. **125** (1976) 369.

BL6B

Observation of Infinitesimal Optical Isomers in Homochiral Aspartic Acid Films by Infrared MicroMicro-Spectroscopic Imaging

J. Hibi[1], S. Kamei[1] and S. Kimura[1, 2]

[1]*Graduate School of Frontier Biosciences, Osaka University, Suita 565-0871, Japan*

[2]*Department of Physics, Graduate School of Science, Osaka University, Toyonaka 560-0043, Japan*

Proteins, which play an important role in living bodies, are composed of many kinds of amino acids. Among amino acids except for glycine, there are two types of optical isomers, L- and D-types, whose physical and chemical properties are equal to each other, but, most of amino acids in living bodies are L-type. However, in recent years, it has been revealed that L-amino acids change to D-amino acids in proteins by aging and the change from L- to D-type (racemization) is considered to be related to aging diseases such as cataract and Alzheimer's disease. Even among amino acids, racemization of aspartic acid (Asp) is relatively easy to occur in proteins of aged human lens [1]. In crystallin that is a protein in Human lens, for example, the amount of D-Asp increases by aging but is infinitesimal in comparison with L-Asp [1]. To detect the D-Asp as well as D-amino acid in L-type one, special complex techniques are needed, for instance, a special chromatography with asymmetric catalysts, are used at present. In addition, the spatial distribution of D-Asp cannot be detected easily.

To verify whether we can detect infinitesimal D-Asp in the majority of L-Asp and also the spatial distribution, we performed an infrared micro-spectroscopic imaging of aspartic acids thin film.. Thin film samples of L- and D-Asp on potassium bromide (KBr) substrates were fabricated by a vacuum evaporating method. We made two kinds of samples, one is a pure L-Asp film (namely D:0%) and the other contains D-Asp by 1% (namely D:1%). The D:1% thin film of was fabricated by the mixture using a pestle in a mortar beforehand. Infrared micro-spectroscopic imaging (IR imaging) were performed by a reflection mode at BL6B using the infrared microscope (FT/IR 6100 + IRT 7000, JASCO Co., Ltd.) Wavenumber and spatial resolutions were set as 2 cm^{-1} and 100 μm, respectively. The interval of each step was set to the same as the spatial resolution. The wavenumber range was 600-4000 cm^{-1}.

Figure 1a indicates normalized reflectivity spectra of D:0% and D:1% in the wavenumber range at around 1400 cm^{-1}. The observed peak shifts to the higher wavenumber side by the mixture of D-type. This result suggests that we can detect a tiny amount of D-Asp (1%) mixed in the majority of L-Asp by infrared spectroscopy. To check whether the spatial image of D-Asp can be detected, we measured reflectivity imaging of the sample that contains the D:0% and D:1% areas (Fig. 1b) and obtained the peak wavenumbers at each point by the fitting using the Lorentz model. Figure 1c shows the spatial distribution of peak wavenumber. Comparing with visible image of Fig. 1b, the border of the areas of D:1% and D:0% can be observed. Therefore, we can conclude that the presence of the tiny amount of D-Asp can be visualized by the IR imaging. Moreover, we can perform the IR imaging with the high spatial resolution and high contrast using infrared synchrotron radiation (IRSR). Therefore, more detailed information will be expected by using IRSR.

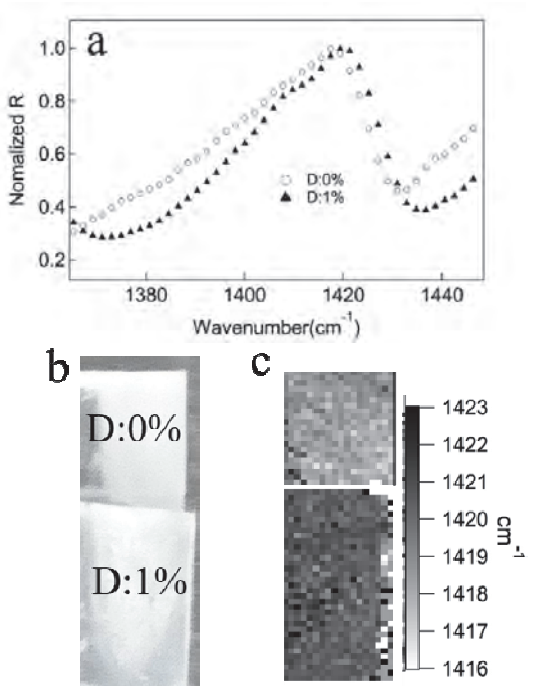

Fig. 1. (a) Normalized reflectivity spectra of thin film samples of pure L-Asp (D:0%) and 1-% D-Asp in L-Asp (D:1%). (b) Photo of the sample (D:0% and D:1% films on KBr). (c) Spatial distribution of peak wavenumber of the sample. The peak position corresponds to that of (a).

[1] N. Fujii *et al.,* Biol. Pharm. Bull. **28** (2005) 1585.
[2] S. Kimura and Y. Ikemoto, Hoshako **18** (2005) 5 [in Japanese].

UVSOR User 9

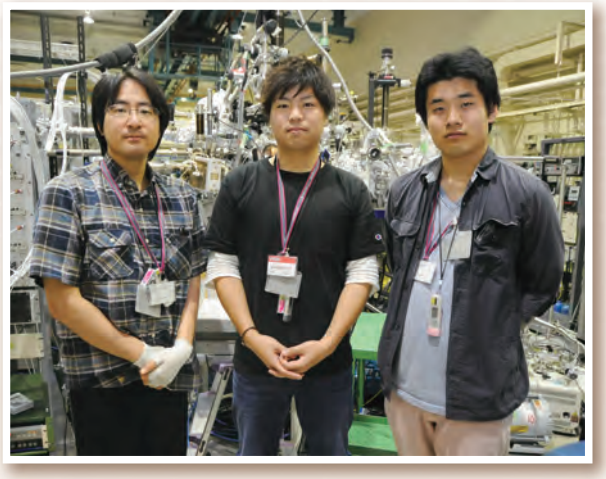

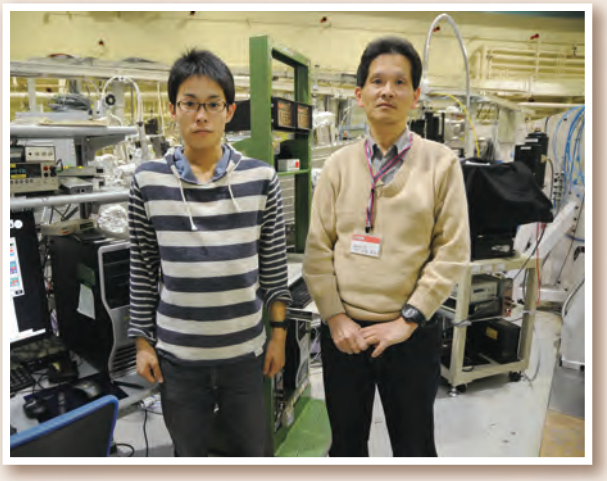

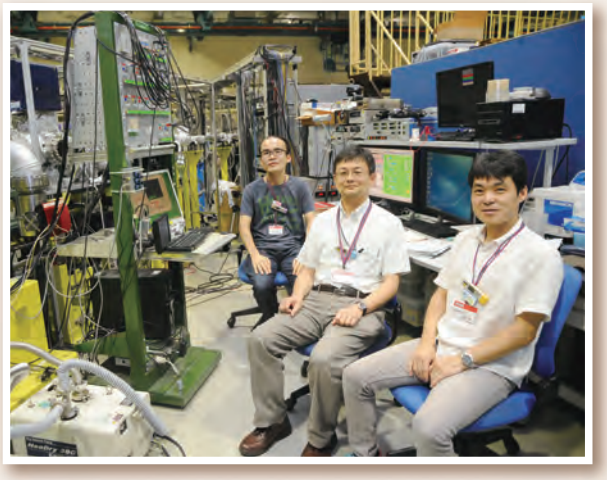

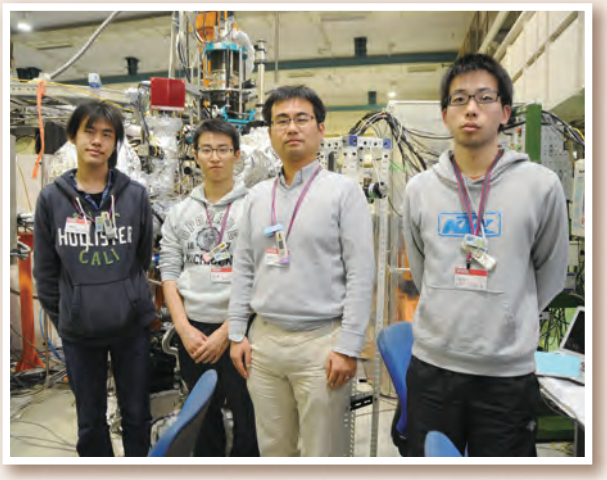

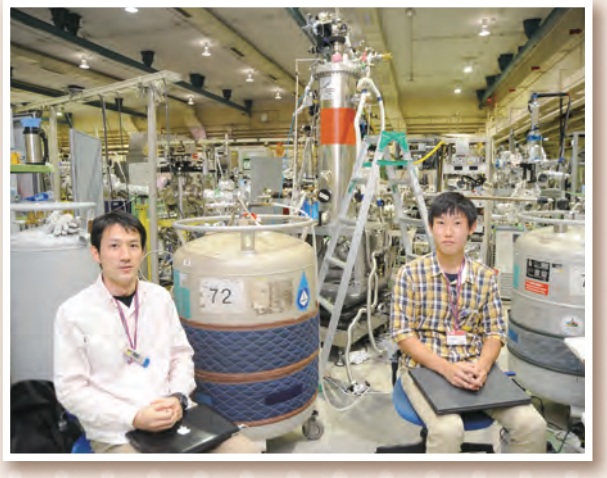

Ⅳ

List of Publications

List of Publications

P. Ayria, S. Tanaka, A. R. T. Nugraha, M. S. Dresselhaus and R. Saito
"Phonon-assisted Indirect Transitions in Angle-resolved Photoemission Spectra of Graphite and Graphene", Phys. Rev. B, **94** (2016) 075429.

K. Hagiwara, Y. Ohtsubo, M. Matsunami, S. Ideta, K. Tanaka, H. Miyazaki, J. E. Rault, P. L. Fèvre, F. Bertran, A. Taleb-Ibrahimi, R. Yukawa, M. Kobayashi, K. Horiba, H. Kumigashira, K. Sumida, T. Okuda, F. Iga and S. Kimura
"Surface Kondo Effect and Non-Trivial Metallic State of the Kondo Insulator YbB_{12}", Nat. Commun., **7** (2016) 12690.

Y. Hikosaka, R. Mashiko, Y. Konosu, K. Soejima and E. Shigemasa
"Electron Emission Relevant to Inner-shell Photoionization of Condensed Water Studied by Multi-electron Coincidence Spectroscopy", J. Electron Spectrosc. Relat. Phenom., **213** (2016) 17.

T. Horiai, S. Kurosawa, R. Murakami, J. Pejchal, A. Yamaji, Y. Shoji, V. I. Chani, Y. Ohashi, K. Kamada, Y. Yokota and A. Yoshikawa
"Crystal Growth and Luminescence Properties of $Yb_2Si_2O_7$ Infra-red Emission Scintillator", Optical Materials, **58** (2016) 14.

A. Ito, T. Inoue, M. Kado, T. Ohigashi, S. Tone and K. Shinohara
"Biomedical Application of Soft X-ray Microscopy with Special Reference to Spectromicroscopy", A. Phys. Pol. A, **129** (2016) 260.

H. Iwayama, T. Kaneyasu, Y. Hikosaka and E. Shigemasa
"Stability and Dissociation Dynamics of N_2^{++} Ions Following Core Ionization Studied by an Auger-electron-photoion Coincidence Method", J. Chem. Phys., **145** (2016) 034305.

T. Kaneyasu, Y. Hikosaka, M. Fujimoto, T. Konomi, M. Katoh, H. Iwayama and E. Shigemasa
"Limitations in Photoionization of Helium by an Extreme Ultraviolet Optical Vortex", Phys. Rev. A, **95** (2017) 023413.

M. Katoh, M. Fujimoto, H. Kawaguchi, K. Tsuchiya, K. Ohmi, T. Kaneyasu, Y. Taira, M. Hosaka, A. Mochihashi and Y. Takashima
"Angular Momentum of Twisted Radiation from an Electron in Spiral Motion", Phys. Rev. Lett., **118** (2017) 094801.

S. Kimura, Y. S. Kwon, Y. Matsumoto, H. Aoki and O. Sakai
"Optical Evidence of Itinerant-Localized Crossover of 4*f* Electrons in Cerium Compounds", J. Phys. Soc. Japan, **85** (2016) 083702.

S. Kimura, H. Takao, J. Kawabata, Y. Yamada and T. Takabatake
"Doping Effects on the Electronic Structure of an Anisotropic Kondo Semiconductor $CeOs_2Al_{10}$: An Optical Study with Re and Ir Substitution", J. Phys. Soc. Jpn., **85** (2016) 123705.

M. Kitaura, K. Kamada, S. Kurosawa, J. Azuma, A. Ohnishi, A. Yamaji and K. Hara
"Probing Shallow Electron Traps in Cerium-doped $Gd_3Al_2Ga_3O_{12}$ Scintillators by UV-induced Absorption Spectroscopy", Appl. Phys. Express, **9** (2016) 072602.

M. Koshimizu, T. Yanagida, Y. Fujimoto and K. Asai
"Luminescence Properties of $Gd_2Si_2O_7$:Ce and $Gd_2Si_2O_7$:La, Ce under Vacuum Ultraviolet Irradiation", J. Rare Earths, **34** (2016) 782.

M.-W. Lin, K.-C. Wang, J.-H. Wang, M.-H. Li, Y.-L. Lai, T. Ohigashi, N. Kosugi, P. Chen, D.-H. Wei, T.-F. Guo and Y.-J. Hsu
"Improve Hole Collection by Interfacial Chemical Redox Reaction at a Mesoscopic NiO/$CH_3NH_3PbI_3$ Heterojunction for Efficient Photovoltaic Cells", Adv. Mater. Interface, (2016) 1600135.

T. Morimoto, M. Harima, Y. Horii and Y. Ohki
"Involvement of Crystallinity in Various Luminescent Bands in Yttrium Aluminate", Nucl. Instrum. Methods Phys. Res. B, **366** (2016) 198.

T. Morimoto, Y. Kuroda and Y. Ohki
"Electronic Excitation and Relaxation Processes of Oxygen Vacancies in YSZ and their Involvement in Photoluminescence", Appl. Phys. A, **122** (2016) 790.

S. Nagaoka, T. Kakiuchi, J. Ohshita, O. Takahashi and Y. Hikosaka
"Site-Specific Electron-Relaxation Caused by Si:2p Core-Level Photoionization: Comparison between $F_3SiCH_2CH_2Si(CH_3)_3$ and $Cl_3SiCH_2CH_2Si(CH_3)_3$ Vapors by Means of Photoelectron Auger Electron Coincidence Spectroscopy", J. Phys. Chem. A, **120** (2016) 9907.

D. Nakauchi, G. Okada, M. Koshimizu and T. Yanagida
"Optical and Scintillation Properties of Nd-doped $SrAl_2O_4$ Crystals", J. Rare Earths, **34** (2016) 757.

D. Nakauchi, G. Okada, M. Koshimizu and T. Yanagida
"Evaluation of Ce : $SrAl_2O_4$ Crystal Scintillators", Nucl. Instrum. Methods Phys. Res. B, **377** (2016) 89.

Y. Nakayama, Y. Mizuno, M. Hikasa, M. Yamamoto, M. Matsunami, S. Ideta, K. Tanaka, H. Ishii and N. Ueno
"Single-Crystal Pentacene Valence-Band Dispersion and Its Temperature Dependence", J. Phys. Chem. Lett., **8** (2017) 1259.

T. Ohigashi, M. Nagasaka, T. Horigome, N. Kosugi, S. M. Rosendahl and A. P. Hitchcock
"Development of In-situ Sample Cells for Scanning Transmission X-ray Microscopy", AIP Conf. Proc., **1741** (2016) 050002.

Y. Okuyama, Y. Sugiyama, S. Ideta, K. Tanaka and T. Hirahara
"Growth and Atomic Structure of Tellurium Thin Films Grown on Bi_2Te_3", Appl. Surf. Sci., **398** (2017) 125.

T. Senden and A. Meijerink
"The d-f Luminescence of Eu^{2+}, Ce^{3+} and Yb^{2+} Ions in $Cs_2MP_2O_7$ (M = Ca^{2+}, Sr^{2+})", J. Lumi., **177** (2016) 254.

I. Song, J. S. Goh, S.-H. Lee, S. W. Jung, J. S. Shin, H. Yamane, N. Kosugi and H. W. Yeom
"Realization of a Strained Atomic Wire Superlattice", ACS Nano, **9** (2015) 10621.

C. X. Trang, Z. Wang, D. Takane, K. Nakayama, S. Souma, T. Sato, T. Takahashi, A. A. Taskin and Y. Ando
"Fermiology of Possible Topological Superconductor $Tl_{0.5}Bi_2Te_3$ Derived from Hole-doped Topological Insulator", Phys. Rev. B, **93** (2016) 241103.

E. Tsuda, Y. Mitsumoto, K. Takakura, N. Sunaga, T. Akitsu, T. Konomi and M. Katoh
"Electrochemical Tuning by Polarized UV Light Induced Molecular Orientation of Chiral Salen-type Mn(II) and Co(II) Complexes in an Albumin Matrix", J. Chem. Chem. Eng., **2** (2016) 53.

J. Ueda, A. Meijerink, P. Dorenbos, A. J. J. Bos and S. Tanabe
"Thermal Ionization and Thermally Activated Crossover Quenching Processes for 5*d*-4*f* Luminescence in $Y_3Al_{5-x}Ga_xO_{12}$: Pr^{3+}", Phys. Rev. B, **95** (2017) 014303.

K. Yamamoto, A. Klossek, R. Flesch, T. Ohigashi, E. Fleige, F. Rancan, J. Frombach, A. Vogt, U. Blume-Peytavi, P. Schrade, S. Bachmann, R. Haag, S. Hedtrich, M. Schäfer-Korting, N. Kosugi and E. Rühl
"Core-multishell Nanocarriers: Transport and Release of Dexamethasone Probed by Soft X-ray Spectromicroscopy", J. Control. Release, **242** (2016) 64.

H. Yamane and N. Kosugi
"Systematic Study on Intermolecular Valence-Band Dispersion in Molecular Crystalline Films", J. Electron Spectrosc. Relat. Phenom., **204** (2015) 61.

H. Yamane and N. Kosugi
"Site-Specific Intermolecular Valence-Band Dispersion in α-Phase Crystalline Films of Cobalt Phthalocyanine Studied by Angle-Resolved Photoemission Spectroscopy", J. Chem. Phys., **141** (2014) 224701.

H. Yamane, N. Kosugi and T. Hatsui
"Transmission-Grating Spectrometer for Highly Efficient and High-Resolution Soft X-Ray Emission Studies", J. Electron Spectrosc. Relat. Phenom., **188** (2013) 155.

H. Yamane and N. Kosugi
"Site-Specific Organic/Metal Interaction Revealed from Shockley-Type Interface State", J. Phys. Chem. C, **120** (2016) 24307.

M. Yoshida, S. Onishi, Y. Mitsutomi, F. Yamamoto, M. Nagasaka, H. Yuzawa, N. Kosugi and H. Kondoh
"Integration of Active Nickel Oxide Clusters by Amino Acids for Water Oxidation", J. Phys. Chem. C, **121** (2017) 255.

H. Zen, Y. Taira, T. Konomi, T. Hayakawa, T. Shizuma, J. Yamazaki, T. Kii, H. Toyokawa, M. Katoh and H. Ohgaki
"Generation of High Energy Gamma-ray by Laser Compton Scattering of 1.94-μm Fiber Laser in UVSOR-III Electron Storage Ring", Energy Procedia, **89** (2016) 335.

UVSOR Symposium 2016 1

V

Workshops

UVSOR Symposium 2016

Date: October 29-30, 2016

Place: Okazaki Conference Center

October 29th (Sat.)

<Session 1, Chair: **M. Katoh**>

13:00 - 13:05 Opening remarks
S. Ideta (UVSOR)

13:05 - 13:25 Present Status of UVSOR and Other Synchrotron Facilities in Japan and the World
N. Kosugi (UVSOR)

13:25 - 13:45 Photoionization Study of Rare Gas Atoms by Extreme Ultraviolet Vortex
T. Kaneyasu (SAGA Light Source)

13:45 - 14:05 Dissociation Dynamics of Isolated Molecules Driven by Core Excitation and Ionization
H. Iwayama (UVSOR)

14:05 - 14:25 Development of Application Technology of Coherent Light Source and Solid-State Spectroscopy
S. Kimura (Osaka Univ.)

14:25 - 14:45 Coffee Break

14:45 - 15:30 Poster Short Presentation

<Session 2, Chair: **K. Tanaka**>

15:30 - 16:00 [invited] Development of Gadolinium-Pyrosilicate-type Scintillators and Its Applications Using UVSOR Beam Line
S. Kurosawsa (Tohoku Univ.)

16:00 - 16:30 [invited] Present Status and Future Prospect of Soft X-ray Absorption Spectroscopy of Liquid
M. Nagasaka (IMS)

16:30 - 18:30 Poster Session

18:30 - 20:00 Banquet

October 30th (Sun.)

<Session 3, Chair: **T. Ito**>

9:00 - 9:30 [invited] Hidden Spin-Polarized State Revealed by Spin-Resolved Photoemission
T. Okuda (Hiroshima Univ.)

9:30 - 9:50 Current Status and Future Plans of BL5U
K. Tanaka (UVSOR)

9:50 - 10:10 Strongly Correlated Electronic States of Pyrochlore Iridates Revealed by Angle-Resolved Photoemission Spectroscopy
T. Kondo (ISSP, The Univ. of Tokyo)

10:10 - 10:30 Coffee Break

<Session 4, Chair: **E. Shigemasa**>

10:30 - 10:50 Atomic Scale Surface Magnetism Studied by X-ray Absorption Spectroscopy/X-ray Magnetic Circular Dichroism and STM
T. Miyamachi (ISSP, The Univ. of Tokyo)

10:50 - 11:10 Four Years Left till the Return of Hayabusa2: Analytical Strategy Using STXM, TEM, and SIMS for Understanding of Association among the Asteroidal Organics, Water, and Minerals
H. Yabuta (Osaka Univ.)

11:10 - 12:00 Discussion and closing remarks
K. Fukui (Fukui Univ.)

<Poster Presentation>

P01 Optical Vortex UV Light Irradiation to Zn(II) Complex-PVA Hybrid Materials
M. Takase (Tokyo Univ. of Science)

P02 Emergence of Optical Activity in Achiral Amino Acids by Irradiation of Circularly Polarized Light from Undulator
J. Takahashi (Yokohama Natl. Univ., Osaka Univ.)

P03 Temporal Response Measurement with Transmission-Type Spin-Polarized Photocathodes
K. Yamaguchi (Nagoya Univ.)

P04 Two Dimensional Isotope Imaging Using LCS Gamma-ray
H. Zen (Kyoto Univ.)

P05 Evaluations of the Optical Components Mounted on the Sounding Rockets for the Solar Observations
N. Narukage (National Astronomical Observatory of Japan)

P06 Site Preference of Gd^{3+} Ions in $Gd_3Al_5(1-x)Ga_{5x}O_{12}$ Crystals
C. Oyama (Yamagata Univ.)

P07 Investigation of Persistent Luminescence Mechanism in $SrAl_2O_4:Eu^{2+}$-Dy^{3+} by Vacuum Referred Binding Energy Diagram
J. Ueda (Kyoto Univ.)

P08 Stability of Photoexcited States in Alanine Single Crystals
S. Tanaka (Yamagata Univ.)

P09 Investigation of Quenching and Persistent Luminescence Process by Construction of Energy Diagram in Ce^{3+} Doped $Gd_3(Al,Ga)_5O_{12}$
K. Asami (Kyoto Univ.)

P10 Study on Nickel Oxygen Evolution Catalysts Containing Organic Molecules
S. Onishi (Keio Univ.)

P11 Direct Observation of Active Species in the Efficient Cobalt Catalysts
M. Yoshida (Keio Univ.)

P12 Local Structure Observation of Aqueous Solution of Cation-Crown ether Complex by Soft X-ray Absorption Spectroscopy
H. Yuzawa (IMS)

P13 Direct Observation of Modified Molecular Orbital Caused by Weaker Interfacial Interaction
K. Yonezawa (IMS)

P14 Angle-Resolved Photoemission Spectroscopy Study of NdFeAs(O, F) Single Crystal
Z.- H. Tin (Osaka Univ.)

P15 Three-Dimensional Angle-Resolved Photoemission Study of MAX Phase Compounds (Cr_2AlC)
T. Fujita (Nagoya Univ.)

P16 UV-Induced Infrared Absorption Change in $SrAl_2O_4$: Eu^{2+} Crystals: Influence of Eu^{2+} Concentration on Trap Filling Process
M. Kitaura (Yamagata Univ.)

P17 Infrared Absorption of Trapped Electron Centers in Ce:$Gd_3Al_1Ga_4O_{12}$ and Ce:$Gd_3Ga_5O_{12}$ Crystals
R. Inaba (Yamagata Univ.)

P18 Observation of tiny amount of D-Asp in aspartic acid films by infrared micro-spectroscopic imaging
J. Hibi (Osaka Univ.)

P19 Stabilization of BL6B Optical Path by a Feedback Control
H. Zen (IAE, Kyoto Univ.)

P20 Chemical Shift of Inner-Shell Electron Binding Energies in Primary Bromoalkanes
H. Fujise (The Graduate University for Advanced Studies)

P21 Angular Dependence of the PCI Recapture of Photoelectron Originating from Xe $4d^{-1}_{5/2}$ Photoionization
S. Kosugi (Sophia Univ.)

P22 Recapture of Kr $3d^{-1}_{5/2}$ Photoelectron Due to Post Collision Interaction (PCI) Studied by High Resolution Measurements of Auger Electrons
N. Kumagai (Sophia Univ.)

P23 Time Resolved Fluorescence Spectroscopy of Ne with Single Bunch Synchrotron Radiation
N. Suzuki (Sophia Univ.)

P24 Origin of the Interfacial State Observed at Tetraphenyldibenzoperiflanthene Thin Films on Ag(111)
R. Shiraishi (SOKENDAI)

P25 Dissociation Dynamics of Dication States in Water Molecule
F. Kumaki (Niigata Univ.)

P26 The Change of Electronic Structure Accompanied with Cl Bonding to Central Metal of Tin-Phthalocyanine
C. Numata (Chiba Univ.)

P27 Dissociation Dynamics of Methanol Dication Studied by an Electron-Ion Coincidence Method
M. Higuchi (Niigata Univ.)

P28 Temperature Dependence of the Emission Spectra of Laser Irradiated a-CNx Thin Films
K. Nakamura (Univ. of Fukui)

P29 The Localized Exciton Model in AlGaN Alloys
K. Watanabe (Univ. of Fukui)

P30 Improvement of Spectroscopic Ellipsometry for VIS-VUV Region and Measurements of Complex Refractive Index of AlN Wafer
Y. Fujii (Univ. of Fukui)

P31 Optical Property of Compound Fluoride Materials Ca_xSr_1-xF_2 at Low Temperature
R. Yamazaki (Nagoya Institute of Tec.)

P32 Angle-resolved Photoemission Study of the Quasi-one-dimensional Organic Conductors $(TMTTF)_2X(X=AsF_6, SbF_6)$
T. Ito (NUSR, Nagoya Univ.)

UVSOR Symposium 2016 2

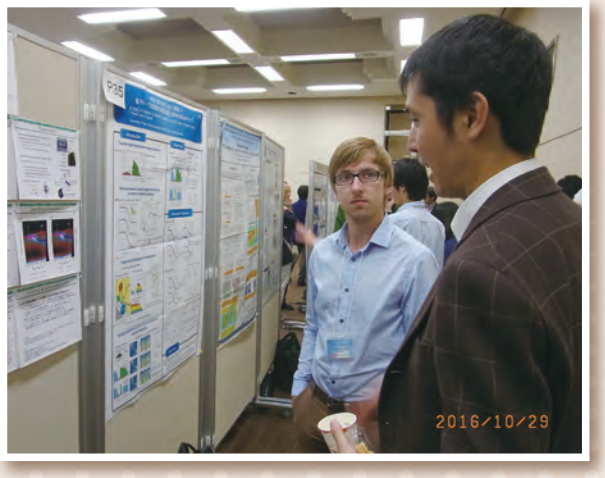

Editorial Board：S. Ideta　M. Fujimoto　M. Sakai　H. Hagiwara　I. Inagaki